Full-spectrum Solar Energy Harvesting for Power and Heat Production using Dichroic Mirror

A thesis submitted to Cardiff University in the candidature for the degree of

Doctor of Philosophy

By

Abdullah Mohammed Altuwairgi

School of Engineering
Cardiff University
March 2022

إذا هبت رياحك فاغتنمها

فعقبى كل خافقة سكون

"الإمام الشافعي"

Abstract

Solar energy has the potential to fulfil the world's energy needs if it is exploited efficiently. Energy from the sun can be converted directly to electricity by photovoltaic cells (PV) or it can be converted thermally by concentrated solar power. In recent years, PV technology has become more attractive thanks to the considerable reduction in its costs. However, PV cells cannot convert all of the energy in the solar spectrum, due to their inability to utilise low energy photons and the thermal energy produced through thermalization by high-energy photons. This leads to lower harvesting of the full solar spectrum energy. Under continuous illumination, the temperature of PV cells can increase up to 40°C above ambient, which affects their performance and durability. Therefore, integrating a PV cell with a thermal collector in a PV/Thermal hybrid system that can supply both electrical and thermal energy is an attractive solution. Over the past few decades, research has focused on coupling photovoltaic systems with solar concentrators, such as parabolic trough and parabolic dish systems. Effective thermal management of photovoltaic cells will enhance their conversion efficiency and prevent material deterioration. Given that commercial PV cells have an efficiency of 15–20%, a large proportion of solar energy dissipates as heat in the cells, which can be collected by a thermal receiver. The overall performance of these cells can be enhanced using a thermoelectric generator (TE) to capture waste heat that cannot be utilised by the PV cells. In this study, new designs of hybrid PV-TE systems based on spectral beam splitting and solar concentration are proposed. Experimental investigations using the beam splitting technique show that there is an improvement in the overall power generation of the PV-TE hybrid systems compared to the bare cell. Two designs were investigated and compared in terms of their design, performance, and economic viability. The comparison reveals that the dish hybrid system is better than the trough system because it facilitates the use of a smaller thermal absorber. Insulating the thermal absorber of the hybrid system was also investigated to examine the effect of reducing heat loss to the surroundings on the thermoelectric power generation. The results show that a 13.3% improvement in the thermoelectric power generation can be achieved. A theoretical model was developed to optimize the geometry of the thermoelectric generator to maximise the power output of the PV-TE hybrid systems. The results of the model calculation show that a significant improvement of the thermoelectric performance can be achieved under a vacuum environment. Finally, recommendations based on the outcomes of this research to improve the performance of these hybrid systems are presented.

Dedication

I dedicate this work to my beloved Father, Mohammed, who passed away in the first year of my study, may Allah have mercy on his soul.

Acknowledgments

All praises to Allah, the Ever-magnificent, the Ever-Thankful for giving me the patience and strength to complete this thesis. All praise is due to You alone, until You are pleased. And all praise is due to You alone when You are pleased. And all praise is due to You alone after You are pleased. Prayers and peace be upon our Prophet, Muhammad, his family, and all of his companions, whose way of life has been a continuous guidance for me.

I am overwhelmed in all humbleness and gratefulness to acknowledge all those who have helped me to complete this task. First, I would like to express my special thanks of gratitude to my supervisor, Prof. Gao Min, for his invaluable advice, continuous support, and patience during my PhD study. I will never forget his assistance during the difficult times that I faced in my first year of study. I am really thankful to him.

I would like to thank my family members, without their tremendous understanding and encouragement in the past few years, it would have been impossible for me to complete my study. I would like to thank my dearest mother, ***Rahmah***; my brothers ***Mansour***, ***Yousef,*** and ***Abdulaziz***; and my sisters ***Fatto*** and ***Hanan***. I wish to thank my loving and supporting wife, ***Samihah***; my beloved daughters, ***Dina***, ***Dania***, ***Nailah***, ***Lujain***, ***Lama***, ***Lamees***; and my lovely son ***Omar***, who all provide unending inspiration.

I would also like to extend my deepest gratitude to the Ministry of Higher Education (MOHE) in Saudi Arabia for providing financial support for my research. Special thanks also go to the Royal Embassy of Saudi Arabia Cultural Bureau in London for their assistance during my study.

I am grateful to the research office staff at the School of Engineering, Cardiff University for their help during my study. Special thanks go to Aderyn Reid for her prompt assistance and guidance. I would also like to thank the Mechanical and Electrical Workshop staff for their technical support, in particular, Mr. Kamaljit Lyall.

I would like to extend my sincere thanks to my colleagues in the Solar Energy group in the School of Engineering at Cardiff University. Also, my special thanks go to my friends who supported me in my study with their useful suggestions and advice.

Contents

Abstract i

Dedication iii

Acknowledgments iv

Contents vi

List of Figures x

List of Tables xv

List of Symbols xvii

Abbreviations xix

Chapter One: Introduction 1

- 1.1 Background 1
- 1.2 Research Motivation 2
- 1.3 Aims and Objectives 2
- 1.4 Thesis Outline 4

Chapter Two: Literature Review 6

- 2.1 Introduction 6
- 2.2 Renewable Energy 6
- 2.3 Solar Energy 7
  - 2.3.1 Photovoltaic Cells 9
  - 2.3.2 Photovoltaic Technologies 11
    - 2.3.2.1 Wafer-based Crystalline Silicon Technology (First Generation) 11
    - 2.3.2.2 Thin Film Technology (Second Generation) 13
    - 2.3.2.3 Emerging Technologies (Third Generation) 15
  - 2.3.3 Concentrated Photovoltaic Technology 17
  - 2.3.4 Concentrated Solar Power 17
    - 2.3.4.1 Geometrical Considerations of Parabolic Concentrators 24
- 2.4 Spectral Splitting 27
- 2.5 Thermoelectric Technology 32
  - 2.5.1 Thermoelectric Effect 33
    - 2.5.1.1 Seebeck Effect 34
    - 2.5.1.2 Peltier Effect 34
    - 2.5.1.3 Thomson Effect 35
  - 2.5.2 Thermoelectric Figure-of-Merit (ZT) 35
  - 2.5.3 Advantages of Thermoelectric Devices 36

2.6 PV-TE Hybrid Systems 37
2.7 Conclusion 41
Chapter Three: Research Methodology 43
3.1 Introduction 43
3.2 Research Concept 43
3.3 Experimental System 44
  3.3.1 Trough Hybrid System 45
    3.3.1.1 Parabolic Trough Design 45
    3.3.1.2 Simulation Studies 48
      3.3.1.2.1 Trough Concentrator 48
      3.3.1.2.2 Thermal Absorber End Size 52
      3.3.1.2.3 Optimum Diameter for the Copper Rod 54
      3.3.1.2.4 TracePro Simulation to Verify the Parabolic Trough Design 54
    3.3.1.3 Trough System Construction 57
      3.3.1.3.1 Parabolic Trough Concentrator 57
  3.3.2 Dish Hybrid System 61
    3.3.2.1 Parabolic Dish Design 62
    3.3.2.2 Parabolic Dish Concentrator 63
3.4 Experimental Instrumentation 66
  3.4.1 Solar Simulator 66
  3.4.2 Autolab System 70
  3.4.3 Thermocouple Data Logger 70
3.5 PV Cell Characterisation and Parameters 71
3.6 Determining Heat Absorption 75
3.7 Power Generated by TEG Modules 79
3.8 Energy Distribution by Beam Splitter 83
3.9 Conclusion 85
Chapter Four: PV-TE Hybrid System Using a Dichroic Mirror and a Parabolic Trough Concentrator 87
4.1 Introduction 87
4.2 Electrical Power Output of the PV Cell 87
  4.2.1 Splitting Effect 88
    4.2.1.1 Power and I-V Curves 88
    4.2.1.2 Temperature Effect 92
4.3 Thermal Output of the Parabolic Trough Concentrator 97
  4.3.1 Heat Produced by the Copper Absorber 97

4.3.2 Convective Heat Transfer Coefficient 100
4.4 Thermoelectric Module Characterisation 101
4.4.1 Power Output and Matched Load 102
4.4.2 Simulation and Theoretical Calculation 110
4.5 Power Production of the Hybrid System 115
4.6 Further Optimisation 117
4.6.1 Optimising Thermoelement Length for Maximum Power Output 119
4.6.2 Optimising Thermoelement Width for Maximum Power Output 122
4.6.3 Optimisation Considering Thermoelement Length and Width 123
4.6.4 TEG Power Output in Ambient and Vacuum Environments 125
4.6.4.1 Effect of a Vacuum on Power Output for Commercial TEGs 126
4.6.4.2 TEG Modules Optimised for Thermoelement Length 127
4.7 Advantage of an InGaP Cell for the Hybrid System 128
4.8 Conclusion 129
Chapter Five: PV-TE Hybrid System using Dichroic Mirror and Parabolic-Dish Concentrator 131
5.1 Introduction 131
5.2 Performance of the dish-hybrid system 131
5.2.1 First receiver (PV cell) 132
5.2.2 Second receiver (TEG module) 132
5.2.2.1 Thermal output of the parabolic-dish concentrator 132
5.2.2.2 Convective heat transfer coefficient 135
5.2.2.3 Power output of the TEG module during transit state 136
5.2.2.4 Power output of the TEG module at steady state 138
5.2.2.4.1 The power output of the hybrid system 139
5.3 Comparison of the two hybrid systems (trough and dish) 140
5.3.1 Performance comparison 141
5.3.1.1 The final temperature of the absorber with and without splitting 141
5.3.1.2 TEG power output 142
5.3.1.3 Total power output of the hybrid system 143
5.3.2 Design comparison 143
5.3.2.1 Trough design vs. dish design 144
5.3.3 Economic comparison: trough vs. dish 146
5.4 Further dish geometry optimisation 148
5.4.1 Actual dish design vs. different dish geometries 148
5.4.2 Actual dish copper rod diameter vs. thinner copper rod diameter 152

5.5 Conclusion 154

Chapter Six: Minimising Convective Heat Loss in the Copper Rod by Insulation 156

6.1 Introduction 156

6.2 Insulation for the Trough Hybrid System 156

6.2.1 Insulation: Experimental Setup 157

6.2.1.1 Glass Cover for the Copper Rod 158

6.2.1.2 Absorber Cover 160

6.2.2 Absorber Temperature Measurements 162

6.2.2.1 Improvement Without Attaching the TEG 162

6.2.2.2 Improvement After Attaching the TEG 164

6.2.2.3 The Effect of Insulation on the TEG’s Power Output 166

6.3 Investigating the Insulation Effect by Thermal Simulation 167

6.3.1 Simulation Procedure 167

6.3.2 Further Investigations Using the Simulation Model 171

6.4 Conclusion 174

Chapter Seven: Conclusion and Future Work 175

7.1 Conclusion 175

7.2 Future Work 177

References: 180

Appendices: 190

List of Figures

Figure 2.1: Estimated renewable energy share of global electricity production, end-2019 7
Figure 2.2: Basic structure of a PV solar cell 9
Figure 2.3: Equivalent circuit of PV cell 10
Figure 2.4: Classification of solar cell technologies 11
Figure 2.5: Monocrystalline solar cell. 12
Figure 2.6: Polycrystalline solar cell. 12
Figure 2.7: Amorphous silicon solar cell. 14
Figure 2.8: Line focusing and point focusing solar concentrators 18
Figure 2.9: Schematic of parabolic trough concentrator with a tube thermal absorber 19
Figure 2.10: Parabolic trough collector 20
Figure 2.11: Central receiver tower 21
Figure 2.12: liner Fresnel reflector (LFR) 22
Figure 2.13: *Parabolic dish collector* 23
Figure 2.14: *Collector aperture area and receiver aperture area for (a) parabolic trough and (b) parabolic dish* 24
Figure 2.15: Rim angle in a cross-section of a paraboloid 25
Figure 2.16: Relationship between the focal length and the rim angle for a constant reflector diameter. 26
Figure 2.17: Schematic of the CPVT system, (a) the WHR CPVT system; (b) the SBS CPVT system 28
Figure 2.18: Basic design of the hybrid system 29
Figure 2.19: Diagram of the designed thin film filter structure and a simple illustration of the interference of the lights reflected from a random layer's two sides 30
Figure 2.20: Schematic diagram of the concentrating beam splitting solar system, shown in two dimensions 32
Figure 2.24: a) Power generation and b) cooling/heating by thermoelectric device 33
Figure 2.25: ZT of many typical thermoelectric materials as a function of year 36
Figure 2.21: *Schematic diagram of CSSPV-TE hybrid system* 38
Figure 2.22: *Schematic diagram of CSSPV-TE hybrid system* 40

***Figure 2.23:** Schematic diagram of the PV-TE hybrid system* 41
***Figure 3.1:** Schematic of the conceptual hybrid PV-TE system.* 44
Figure 3.2: Parameters of parabolic reflector. 46
***Figure 3.3:** Focal points for different parabolic curves.* 47
***Figure 3.4:** a) Final design of the trough system and b) assembly drawings.* 47
***Figure 3.5:** Straight-forward simulated design (copper plate).* 49
***Figure 3.6:** Steady-state temperature of copper plates simulated with SolidWorks thermal simulation.* 51
***Figure 3.7:** Simulated ΔT obtained by trough design and copper plate design for all modules.* 52
***Figure 3.8:** Simulated fixed absorber vs. variable absorber for TEGs (15x15mm).* 53
***Figure 3.9:** Delta temperature across the five TEGs attached to absorbers with variable and fixed sizes.* 53
***Figure 3.10:** Eight different designs simulated by TracePro.* 55
***Figure 3.11:** Parabola parameter entry in SolidWorks.* 57
***Figure 3.12**: The trough after extruding to the required trough length using extruding feature in SolidWorks.* 58
***Figure 3.13:** Ultimaker 2 GO 3D printer that was used to print the parabolic trough.* 58
***Figure 3.14:** Parabolic trough printed using the Ultimaker 2 3D printer.* 59
***Figure 3.15:** High reflectivity reflector fixed on the inner surface of the parabolic trough.* ..59
***Figure 3.16:** Completed setup of the hybrid trough system.* 60
***Figure 3.17:** Schematic of the experimental setup of the dish design.* 61
***Figure 3.18:** a) Final design of the dish system and b) assembly drawings.* 63
***Figure 3.19:** Parabolic dish that was printed using a 3D printer.* 63
***Figure 3.20:** Parabolic dishes covered with different numbers of reflector pieces.* 64
***Figure 3.21:** Polished aluminium dish.* 65
***Figure 3.22:** Hybrid dish system complete setup.* 66
***Figure 3.23:** Spectral irradiance of the reference solar spectrum (AM1.5G) and the solar simulator (LCS-100).* 67
***Figure 3.24:** Instrumentation and equipment used for measurements in this study.* 68
***Figure 3.25:** Solar simulator illumination area divided into nine squares for irradiance measurement.* 69
***Figure 3.26:** The irradiance measurement results for the nine squares.* 69

Figure 3.27: *Temperature measurement, monitoring and recording sequence.*......................71

Figure 3.28: *Typical I-V and P-V curves of a solar cell* 71

Figure 3.29: *I-V curves for the three PV cells measured under STC.*....................................74

Figure 3.30: *Energy flow in the experimental system.*..75

Figure 3.31: *The heating curve of the copper rod and absorber illuminated under solar simulator (1000 W/m^2). The inset shows the slope of the curve at the initial period of illumination.*...77

Figure 3.32: *Energy flow in the experimental system with TEG attached*..............................78

Figure 3.33: *Typical thermoelectric generator.*..80

Figure 3.34: *Schematic of the experimental setup for characterising the performance of a dichroic mirror using a spectroradiometer.* 84

Figure 3.35: *Transmission and reflection characteristics of the dichroic mirror measured using spectroradiometer.* 85

Figure 4.1: I-V and P-V curves for the three solar cells: (A) Si cell, (B) GaAs cell, and (C) InGaP cell with/without splitting..90

Figure 4.2: The setup for testing the spectral splitting effect on the temperature of the PV cell. A dichroic mirror (not shown in the photograph) was placed between the solar cell and the solar simulator (not shown in the photograph). 92

Figure 4.3: The effect of spectral splitting on the temperature and power output of the InGaP cell...93

Figure 4.4: Splitter reflected rays for the three PV cells (InGaP, GaAs & c-Si)...................94

Figure 4.5: The effect of spectral splitting on the temperature and power output of the GaAs cell...95

Figure 4.6: The effect of spectral splitting on the temperature and power output of the Si cell. 95

Figure 4.7: InGaP cell temperature coefficient of: (a) short circuit current, (b) open circuit voltage, and (c) power...96

Figure 4.8: Temperature profiles for four cases of light irradiance..98

Figure 4.9: Heat retained by the copper absorber (Qa) determined using the slope technique for four cases. The curves are extrapolated to the y-axis to find the heat absorbed by the copper absorber...99

Figure 4.10: TEG module power output as a function of load resistance. 103

Figure 4.11: Theoretical and experimental power output for the 5 TEG modules as a function of ΔT with/without splitting....104
Figure 4.12: Absorber temperature of TEG modules classified by its aspect ratio....105
Figure 4.13: Temperature difference across the five TEG modules vs. their aspect ratio....106
Figure 4.14: TEG modules power output as a function of aspect ratio....107
Figure 4.15: Voltage vs. load resistance for the five TEG modules....108
Figure 4.16: I-V curves and P-V curves for the five TEG modules....110
Figure 4.17: Thermal load addition in SolidWorks....111
Figure 4.18: TEG module 6x6 hot side simulation under concentration (a) without splitting, (b) with splitting....113
Figure 4.19: ΔT across TEG modules obtained from simulation, experiments, and theoretical calculations: (a) without splitting, (b) with splitting....114
Figure 4.20: The temperature difference across thermoelectric module as a function of thermoelement length for all 5 TEG modules without spectral splitting....120
Figure 4.21: Power output as a function of thermoelement length for all TEG modules without splitting....121
Figure 4.22: Power production as a function of thermoelement width for all TEG modules without splitting....123
Figure 4.23: Thermoelement volume increase compared to power increase at optimum length for all modules....125
Figure 4.24: Power output vs. aspect ratio in ambient and vacuum for 5 modules with actual thermoelement length....126
Figure 4.25: TEG modules theoretical power output vs. the aspect ratio in ambient and vacuum environment at optimum thermoelement length....127
Figure 5.1:*Temperature profiles of the dish system for all cases without attaching the TEG.* 133
Figure 5.2: *Heat retained by the copper absorber (Qa) extrapolated to hit the y-axis for all cases.*....134
Figure 5.3: *Theoretical and experimental power output of the TEG module (15x15) as a function of ΔT: (a) without splitting, (b) with splitting.*....137
Figure 5.4: *Power and current curves vs. voltage for the TEG module (15x15) with and without splitting.*....138

Figure 5.5: *The temperature profile of the copper absorber attached to a TEG module with and without splitting.* 139

Figure 5.6: *Comparing the absorber steady state temperature for illumination with concentration without and with splitting for the trough and dish concentrators.* 141

Figure 5.7: *The power output of module (15x15) for both trough and dish systems with and without splitting.* 142

Figure 5.8: *Dimensions of the copper absorber: (a) trough design and (b) dish design.*......144

Figure 5.9: Simulation results of the four dish geometries. 149

Figure 5.10: *Absorber steady state temperature for the four dish geometries with and without splitting.* 150

Figure 5.11: *Thinner copper rod diameter simulated absorber steady state temperature vs. actual copper rod diameter: (a) without splitting, (b) with splitting.* 153

Figure 6.1: *Schematic diagram of the insulation setup.* *157*

Figure 6.2: *borosilicate glass tube that was used to cover the copper rod.* *158*

Figure 6.3: *Optical transmission of borosilicate glass in visible and near-infrared ranges (the data shown above is obtained from https://asgs-glass.org/optical-transmission/,).* *159*

Figure 6.4: *Photograph of the glass tube and square absorber cover sealed to the holder using silicone sealant.* *160*

Figure 6.5: *The 3D printed cover for the copper absorber end for insulation experiments.* 161

Figure 6.6: *Copper insulation experiment setup: (a) front side, (b) back side.* 162

Figure 6.7: *The temperature profiles of the copper absorber for the four cases (No TEG attached).* 163

Figure 6.8: *Copper absorber steady state temperature for the four cases after attaching the TEG.* 165

Figure 6.9: *The steady state temperature distribution of the copper absorber without insulation: (a) without splitting, (b) with splitting.* 168

Figure 6.10: *The steady state temperature distribution on the insulated copper absorber covered by a glass tube and an absorber end cover: a) without splitting, b) with splitting.* ..169

Figure 6.11: *Simulated temperature of the absorber at steady state for different vacuum levels: (a) without the TEG, (b) with the TEG.* 172

Figure 6.12: *TEG power output for different vacuum levels with and without splitting.* 172

Figure 6.13: *TEG power output as a function of different irradiance with and without splitting.* 173

List of Tables

Table 3.1: *Parabolic troughs structure advantages and disadvantages.* 45

Table 3.2: *Dimensions of the commercial thermoelectric modules that were selected for this study.* 49

Table 3.3: *Simulation results for the parabolic trough designs.* 56

Table 3.4: *PV cell parameters from the provider and from the literature.* 73

Table 3.5: *PV cell parameters from measurements conducted at Cardiff University's laboratory.* 74

Table 4.1: PV cell (Si, GaAs & InGaP) results: (a) without splitting, and (b) with splitting. 91

Table 4.2: InGaP calculated temperature coefficients versus the literature. 97

Table 4.3: Comparing heat generated by the copper absorber (Qu) with solar simulator irradiance for all cases. 100

Table 4.4: Convective heat coefficient predicted based on theoretical model built to match experimental heat generated (Qu) with theoretical calculated. 101

Table 4.5: TEG module geometry with internal resistance measured by matched load experiments. 103

Table 4.6: The simulation results of the hot and cold side temperatures and temperature difference across the TEG modules with and without splitting. 113

Table 4.7: Power output of large PV cell compared to small PV cell with and without splitting. 116

Table 4.8: Bare PV cell, TEG module (15x15) and hybrid system power production. 117

Table 4.9: Parameters used in geometrical optimisation of TEG modules [173-176]....................... 118

Table 4.10: The optimum thermoelement length for all modules. Note that power is based on the full spectrum illumination (without splitting). 120

Table 4.11: Optimum thermoelement width for the selected modules. 122

Table 4.12: The optimum thermoelement length for all modules and the percent increase in power production.. 124

Table 4.13: Solar energy in PV and TE spectrums after spectral splitting for different semiconductor materials. 128

Table 5.1: *Comparing the heat generated by the copper absorber (Qu) with solar simulator irradiance for all cases.* 135

Table 5.2: *Convective heat coefficients determined from the best fitting between the calculated and experimental values of absorbed heat (Qu) by the copper absorber.* 136

Table 5.3: *Dish system bare PV cell, TEG module (15x15) and hybrid system power production.* 140

Table 5.4: *A power and efficiency comparison of the trough and dish-hybrid systems.* 143

Table 5.5: *Comparison of the hot side temperature and TEG power output for trough and dish-hybrid systems.* 145

Table 5.6: *Cost evaluation of the trough and dish-hybrid system components.* 147

Table 5.7: *Cost per watt for two hybrid systems.* 147

Table 5.8: *Comparison of dish experimental results with simulated results.* 149

Table 5.9: *Actual and proposed dish geometry details and absorber steady state temperature obtained by simulation.* 151

Table 5.10: *Actual and proposed dish geometry details and absorber steady state temperature obtained by simulation.* 152

Table 5.11: *Thinner copper rod simulation results.* 154

Table 6.1: *The steady state temperatures of copper absorber for the four cases.* 164

Table 6.2: *Insulation effect on the copper steady state temperature for the four cases (TEG attached).* 166

Table 6.3: *TEG (15x15) power output for the four cases.* 166

Table 6.4: *Measured and simulated results of the steady state temperature of the copper absorber, both with and without TEG.* 170

List of Symbols

Symbol	Description	Unit
Aa	Area of the absorber	m^2
A_{ap}	Collector aperture area	m^2
A_{im}	Area of the Sun image	m^2
A_{pv}	Area of the solar cell	m^2
C_{geo}	Geometric concentration ratio	
C_p	Specific heat capacity	J/kg.K
CR_{opt}	Optical concentration ratio	
E_{gap}	Band gap of the semiconductor	e.V
f	Focal point of concentrator	m
G	Solar irradiance	W/m^2
h	Convection heat transfer coefficient	$W/m^2.K$
h	Height of reflector	m
I	Electrical current	mA
I_0	Dark saturation current	A
I_D	Diode current	A
I_L	Light generated current	A
I_{SC}	Short circuit current	mA
I_{SH}	Shunt current	A
K	Thermal conductivity	W/m.K
Lc	Thickness of the ceramic	m
L_{TE}	Thermoelement length	mm
n	Electrical contact parameter	mm
N	Number of thermocouples	
P	Electrical Power Output	W
P_{PV-TE}	Hybrid system total power output	W
Q	Heat losses	W
Q_a	Q_a The heat retained by the absorber	W
Q_C	Liberated heat from the thermoelectric generator	W
Q_{in}	Light radiation on the absorber	W
Q_l	The heat lost by the absorber to the surroundings	W

Q_r	The heat reflected by the absorber	W
Q_{TEG}	The heat transferred through the thermoelectric generator	W
Q_u	The useful heat flux generated by the absorber	W
r	Thermal contact parameter	
R	Resistance	Ohm
R_{Load}	Load resistance	Ohm
R_s	Series resistance	Ohm
R_{sh}	Shunt resistance	Ohm
R_{TEG}	Internal resistance of thermoelement	Ohm
T_{amb}	Ambient temperature	^oC
T_{cold}	Cold side temperature of the thermoelectric generator	^oC
T_{final}	The steady state temperature of the absorber	^oC
T_{Hot}	Hot side temperature of the thermoelectric generator	^oC
V_{OC}	Open circuit voltage	Volt
ZT	Figure of merit	
α	Seebeck coefficient	µV/K
β	Thomson coefficient	V/K
ΔT	Temperature difference	K
Δt	Time difference	sec
ε	Emissivity	
η_{PV}	Efficiency of PV cells	%
η_{TE}	Efficiency of TEG	%
$\eta_{PV\text{-}TE}$	Hybrid system total efficiency	%
ρ	The electrical resistivity	$\Omega \cdot m$
σ	Stefan and Boltzmann Constant	$W/m^2.K^4$
ψ	Rim angle	Degree

Abbreviations

AM	Air mass
a-Si	Amorphous silicon
CdTe	Cadmium Telluride
CIGS	Copper Indium Gallium Selenide
CIS	Copper Indium Diselenide
c-Si	Crystalline Silicon
CSP	Concentrating solar power
DC	Direct current
DNI	Direct solar radiation
DSSC	Dye-sensitized solar cells
FF	Fill factor
GaAs	Gallium Arsenide
HCE	Heat collection element
HTF	Heat transfer fluid
I_{MP}	Maximum current
InGaP	Indium gallium phosphide
IR	Infrared
I-V	Current-Voltage curve
LFR	Linear Fresnel reflector
NIR	Near- infrared
OPV	Organic photovoltaics
PLA	Polylactic acid
PTC	Parabolic trough concentrator
P-V	Power-Voltage curve
PV cell	Photovoltaic cell
SBS	Spectral beam splitting
STC	Standard test condition
TE	Thermoelectric
TEG	Thermoelectric generator
TES	Thermal energy storage

UV	Ultraviolet
V_{MP}	Maximum voltage
WHR	Waste heat recovery

Chapter One: Introduction

1.1 Background

Global warming and the rapid depletion of fossil fuels are driving the global shift towards alternative sources of energy, such as renewable energy and particularly solar energy. In 2020, about 30% of electricity production came from renewable energy [1]. The U.S. Energy Information Administration (EIA) estimates that the world energy consumption will increase by approximately 50% by 2050 [2].

Solar energy is one of the most promising energy sources thanks to its sustainable and inexhaustible nature [3, 4]. It can be exploited by direct conversion into electrical energy through the photovoltaic effect or through thermal conversion (i.e., solar thermal power). The amount of solar energy hitting the Earth’s surface is 10,000 times larger than the global energy demand for the whole planet [5]. Consequently, if it is efficiently harnessed, solar energy has the potential to fulfil the Earth's energy demand.

A photovoltaic (PV) cell is a device that can convert sunlight directly to electricity. It has no moving parts, and hence needs minimum maintenance. However, because it uses only a part of the solar spectrum (uv-vis), the theoretical conversion efficiency limit is approximately 34% for single-junction cells. PV cells are distinguished by their versatility—they are very flexible and can be installed anywhere. They can also work independently or attached to a grid [6].

Concentrating solar thermal power is another method of harvesting solar energy. Concentrating solar power (CSP) technologies include parabolic troughs, parabolic dish collectors, linear Fresnel reflectors, and heliostat fields. In these technologies, the concentrated solar radiation is reflected onto a heat collection element (HCE) that is placed in a flux line. The heat transfer fluid (HTF) that passes through the HCE will then exchange its high absorbed heat through a series of heat exchangers to generate a superheated high-pressure steam that is used to run turbines for electricity generation [7]. The heat can also be used directly to power an engine (e.g., Stirling engine) to generate electricity. Moreover, CSP has the advantage of being able to store heat for use during the absence of sunlight, such as in cloudy weather [8].

1.2 Research Motivation

PV cells only use part of the spectrum. The rest of the spectrum causes thermalisation of the cell, which results in cell performance reduction. Meanwhile, a thermoelectric (TE) device can convert the waste heat into electricity based on the Seebeck effect if a temperature difference is maintained between the device’s hot and cold sides. Therefore, it is worthwhile considering a design that integrates the two devices (PV and TE) for full spectrum solar energy harvesting. A PV-TE hybrid system can be achieved by directly coupling two devices or by decoupling them via a spectral splitting method.

To improve the performance of PV cells and to better use the waste heat, a hybrid system combining the two devices was designed and tested. This thesis experimentally and theoretically explores the potential to exploit the unused part of the solar spectrum to increase power production.

1.3 Aims and Objectives

This project aims to improve the energy harvesting of the solar spectrum by developing a laboratory-scale PV-TE hybrid system for experimental investigation. The hybrid system that was developed involves a novel design that incorporates a solar concentrator to reduce the absorber’s area and reduce heat loss to surroundings, which will result in higher power production. The hybrid system also involves a spectral beam splitter that directs only a suitable band of the spectrum to the PV cell, which results in low temperature cell operation and prevents the need for cell cooling.

The main objectives of this study are as follows:

- Characterise the different types of solar cells (e.g., c-Si, GaAs and InGaP) and examine the split effect on their performance.
- Establish a theoretical model for thermoelectric generator (TEG) geometry optimisation in terms of thermoelements length and width to maximise the hybrid system’s power output.
- Design and construct a prototype PV-TE hybrid system using a parabolic trough concentrator.
- Design and construct a prototype PV-TE hybrid system using a parabolic dish concentrator.
- Conduct an experimental investigation of the performance of the two hybrid systems and then compare their performance in relation to their contribution to the total power production of the hybrid system.
- Perform thermal simulation studies. Examine different geometries of the dish concentrator and the thermal absorber, and then study the effect of these geometries on the power output of the hybrid system.
- Design and construct an insulation media for the thermal absorber of the trough hybrid system and experimentally investigate the effect of insulation on the heat and power production of the hybrid system.

1.4 Thesis Outline

This thesis has seven chapters, a brief outline of each chapter follows:

Chapter One: This chapter briefly introduces the subject of the thesis. It emphasises the importance of beam splitting to improve cell efficiency by directing a suitable band of the spectrum to the cell and then using the other part of the spectrum in the TEG to boost power production. The motivation to hybridise a PV cell with thermoelectric generator is presented in this chapter. This chapter concludes with the thesis outline.

Chapter Two: This chapter starts with an overview of renewable energy and its role in climate change mitigation strategies. In particular, this chapter explores the technologies in solar power harvesting as pertains to photovoltaic cells and solar concentrated power. It describes beam splitting techniques and research done in spectral splitting. The working principles and effects of TEGs, and their potential in waste heat harvesting are detailed. Finally, the advantages and disadvantages of TEGs are addressed.

Chapter Three: This chapter describes the research concept with an illustration of the proposed hybrid system. The idea of spectral beam splitting is introduced with wavelengths directed to the two receivers (i.e., PV cell and TEG). The design and construction of the experimental setup of the two proposed hybrid systems are detailed. The characterisation of PV cells in terms of I-V curves and power output for three PV cells under investigation is detailed, together with a comparison of results to values in the literature. The slope technique to determine heat absorbed by a copper absorber is also described. The procedures to calculate the power output of the TEG modules are explained. Finally, the use of a spectroradiometer to determine the spectral energy distribution after beam splitting is described and the results are presented.

Chapter Four: This chapter presents the experimental and theoretical characterisation of the parabolic trough hybrid system. It starts by determining the splitting effect on the three PV cells under consideration. The thermal output of the parabolic trough concentrator was then determined by utilising the slope technique. This chapter explains the selection of thermoelectric modules of different geometries for power output optimisation. The power outputs of the modules were measured at matched-load conditions and their performance was compared with the theoretical calculation. The power outputs and efficiencies of the hybrid system were determined and compared to a bare cell. A theoretical model was then developed to optimise the geometry of the thermoelectric modules. The model was validated using the experiment results obtained from the five modules used in the experiments and was then employed to study the geometry of optimisation of the modules for the hybrid system. Finally, the advantage of InGaP cell for hybrid system is presented.

Chapter Five: This chapter presents the experimental and theoretical characterisation of the parabolic dish hybrid system. The thermal output of the parabolic dish concentrator was determined using the slope technique. A comparison of the two hybrid systems (trough and dish) was performed in terms of their performance, design, and economic viability. Finally, simulation studies were carried out to examine the effect of different dish and absorber geometries on total heat generation.

Chapter Six: This chapter investigates the insulation effect of the thermal absorber of the trough hybrid system. Thermal simulation by SolidWorks was carried out to investigate the potential benefit of different levels of vacuum in the glass tube of a thermal absorber. Different concentration ratios were also simulated to investigate the power output of the hybrid system.

Chapter Seven: This chapter presents the conclusions of the major outcomes from this research, together with recommendations for future work.

Chapter Two: Literature Review

2.1 Introduction

The chapter will begin with an overview of renewable energy as a promising alternative source of energy. Special focus is given to solar energy because it represents the core of this study. First, harvesting solar energy using photovoltaic (PV) technology will be reviewed. Second, thermal solar power harvesting will then be reviewed, with a focus on trough and dish solar concentrators. Third, solar beam splitting for full spectrum power harvesting will be reviewed and thermoelectric waste heat harvesting will be elaborated. Finally, any research gaps that have been identified by this review will be described.

2.2 Renewable Energy

The rapid depletion of fossil fuels (i.e., coal, oil, and gas) and concern about their effect on global warming have led to increased interest in the use of renewable energy for electricity production. As a promising alternative source of energy, renewable energy (e.g., solar, wind, wave, geothermal, biomass and hydro) has gained a lot of interest in the past few decades [9-11]. Renewable energy will also play an important role in minimising the adverse environmental impact of fossil fuels, which are the main source for greenhouse emissions, and they are also expected to meet the rapidly increasing demand for energy supply. The global energy demand is predicted to increase by 30–50 % by 2050 [12, 13].

Renewable energy is a clean source of energy, has low maintenance cost and reduces the dependence on fossil fuel. However, its main advantage is that it is an infinite resource [14].

Despite the tiny share that renewable energy currently contributes to the total energy mix, it is expected to provide a significant share in the future electricity demand [15]. The relatively high cost of renewable energy compared to conventional fossil fuels is the main obstacle to its widespread use. Consequently, considerable efforts are being made by researchers to develop renewable technologies to make them more competitive [13].

According to the "Renewables 2020 Global Status" report, REN21, more than 27% of global electricity production comes from renewable energy, with more than half of that amount coming from hydropower [16]. In fact, renewable power capacity installation in 2020 was more than that from conventional fossil fuel and nuclear power combined [17]. As shown in Figure 2.1, solar represents only 2.8% of this amount. However, the new trends in solar installation capacity in the last few years (e.g., 135 GW or 52% of all renewables installation in 2020) are predicted to increase its share in coming years [18].

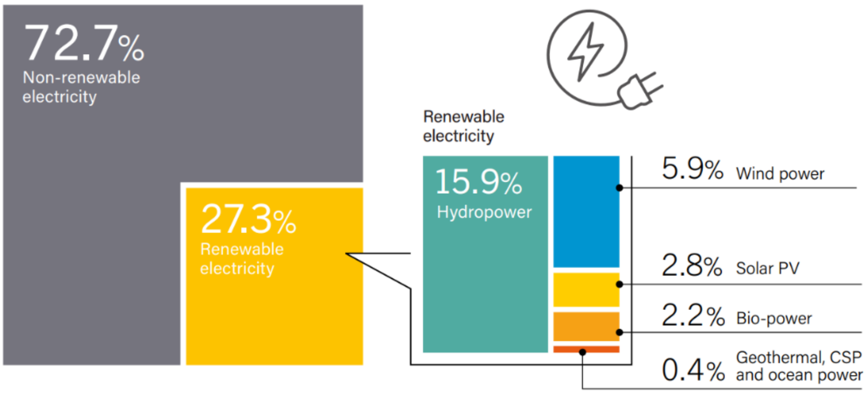

Figure 2.1: *Estimated renewable energy share of global electricity production, end-2019* [19].

2.3 Solar Energy

Among the renewable energy alternatives that are currently being explored, solar energy is recognised as the most promising source of energy. Compared to other renewable energy sources, solar energy is the most abundant and the most exploited source of power generation [20]. For example, Moluguri et al. stated that the amount of solar energy strikes the earth's surface yearly is about 10,000 times the world's annual consumption of energy [21].

There are two main ways to exploit solar energy, namely: solar thermal, which harnesses the heat from the sun, and solar PV, which converts sunlight directly to electricity. Solar thermal technology is used in desalination, heating, cooling, cooking, and power generation [22]. Meanwhile, solar thermal power for electricity generation concentrates sunlight on a heat-transfer fluid to increase its temperature to a high level. The heat-transfer fluid is then used to generate electricity through turbines [23].

In contrast, PV solar cells can directly convert absorbed sunlight energy to electricity based on the PV effect [24]. Compared to the other renewable energy systems, the operating and maintenance costs of PV technology are almost negligible [25]. Except for sun-tracking machines, PV systems have no moving parts and hence they have far less breakages and lower noise compared to other renewables systems. However, like wind power, one of the major drawbacks of solar energy is its intermittency and unpredictability compared to other renewable systems (e.g. hydro and marine) [26].

With more than 773 GW of installed capacity, solar energy accounts for more than 28% of renewable power installed capacity in 2020 [18]. This puts solar energy in the third place worldwide after hydro and wind power, with PV technology being dominant. The global installed concentrated solar power (CSP) capacity is also rising—at the end of 2020, the total installation capacity reached 6.0 GW [27].

2.3.1 Photovoltaic Cells

PV cells convert sunlight directly to electrical power by the PV effect [28]. A PV cell is made from semiconductor materials with a p-n junction, as illustrated in Figure 2.2. A p-n junction is created when two different types of semiconductor materials are joined together. For example, in silicon semiconductors, the P-type layer is created by doping the silicon with Boron and the N-type layer is created by doping with phosphorus [29]. Doping is accomplished by adding a foreign element either from group-III element (Boron (B)) having three electrons in the outermost orbits to make the P-type layer or from group-V (Phosphorus (P)) having five electrons to make the N-type layer [22].

Electron-hole pairs are created when sunlight strikes semiconductor materials, which can be separated under the influence of internal electric fields in the depletion region of the PN junction. If the solar cell is short circuited, as shown in the following figure, then a current proportional to the incident radiation will flow to the external load [30-32].

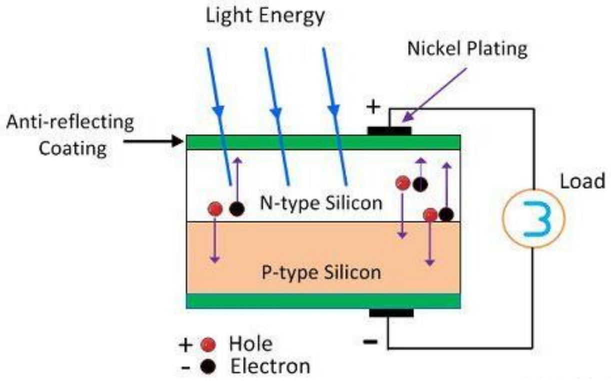

Figure 2.2: *Basic structure of a PV solar cell* [33]

Figure 2.3 shows an equivalent electrical circuit of a PV cell, where the current is represented at the output terminals. This current equals the light generated current, I_L, minus the diode current, I_D, and the shunt current, I_{sh}. The internal resistance of the PV cell consists of the series resistance, Rs, and the shunt resistance, R_{sh}. For an ideal PV cell, Rs = 0, which means that there is no series loss, and $R_{sh} = \infty$, which means that there is no leakage to the ground.

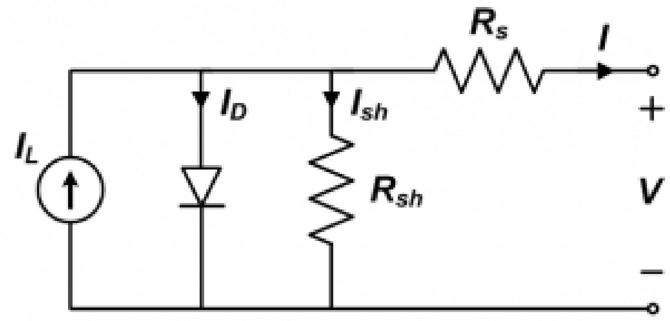

Figure 2.3: *Equivalent circuit of PV cell* [34].

The parameters that characterise the ideal solar cell are given by:

$$I = I_L - I_0\left[e^{\frac{qV}{nkT}} - 1\right] \tag{2.1}$$

where, I_0 is dark saturation current, n is the ideality factor (for ideal diode n = 1), T is the cell temperature, V is the cell voltage, q is the electron charge, and k is Boltzmann's constant. Equation 2.1 can be rearranged to give the voltage in terms of current:

$$V \approx \frac{nkT}{q} ln\left[\frac{I_L - I}{I_0}\right] \tag{2.2}$$

The short circuit current, I_{SC}, is the highest current that a PV cell can produce when the cell is short circuited. Meanwhile, the open circuit voltage, V_{OC}, is the highest voltage at zero current flow when the two terminals of the PV cell are disconnected [35]. Since V_{OC} occurs when the current equals zero, Equation 2.2 for V_{OC} can be written as (n = 1 for ideal cell):

$$V_{oc} = \frac{kT}{q} ln\left[\frac{I_L}{I_0}\right] \tag{2.3}$$

2.3.2 Photovoltaic Technologies

PV cell technologies are generally classified into three main categories: wafer-based crystalline silicon technology, thin film technology, and other emerging technologies. Among the various technologies of PV cells, only two are commonly commercialised: wafer-based solar cells (single or polycrystalline wafers) and thin film cells [36]. Figure 2.4 illustrates the classification of the solar cell technologies:

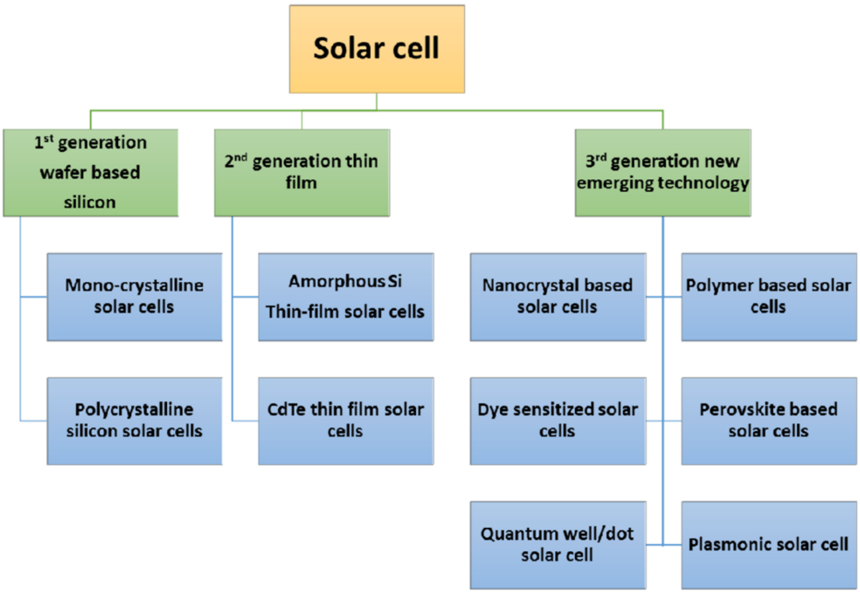

Figure 2.4: *Classification of solar cell technologies [37].*

2.3.2.1 Wafer-based Crystalline Silicon Technology (First Generation)

The first generation of PV cells used wafer-based crystalline silicon technology, as follows:

1) Monocrystalline Si cells, (see Figure 2.5): This technology is currently the market leader and accounts for 80% of the PV solar cell market [38]. The conversion efficiency for this type of cell can reach more than 20%, but for commercialisation the manufacturers claim efficiencies from 15% to 17% [39]. This is the most efficient PV cell in good light

conditions and is fabricated from a single crystal or cast polycrystalline silicon that is sliced into thin chips (wafer) of 10 × 10 cm area and 350 µm thickness [36]. These types of cells have a typical lifespan 25 to 30 years. They can convert solar radiation of 1000 W/m^2, air mass (AM1.5) to 140 W of electricity for each square metre of surface.

Figure 2.5: *Monocrystalline solar cell.*

2) Polycrystalline cells (see Figure 2.6): This type of cell is produced by melting silicon and solidifying it to orient the crystals of silicon in a fixed direction. The product is a rectangular polycrystalline ingot, which is sliced into blocks and finally cut into a thin wafer [40]. In comparison to monocrystalline cells, the production of these cells is more cost effective. These cells exhibit slightly lower conversion efficiencies compared to monocrystalline cells, generally from 13 to 15 % [36]. The expected lifespan for polycrystalline cells is between 20 and 25 years.

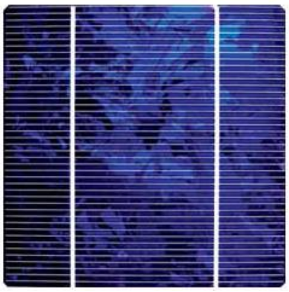

Figure 2.6: *Polycrystalline solar cell.*

3) Bar-crystalline silicon cells: These Si wafers are grown by pulling a ribbon vertically from a bath of molten silicon, which produces low-cost Si due to the high utilisation of the Si feedstock. Their low cost is due the absence of ingot sawing and wafer etching [41]. Because no kerf losses occur in Ribbon Si wafer production, these cells represent a promising cost-effective alternative to c-Si wafers that are sliced from cast ingots. Wafer cutting results in a loss of up to 50% of the ingot material [42]. However, in the near future, this technology will not be a leader with an efficiency of only around 11%.

2.3.2.2 Thin Film Technology (Second Generation)

Thin-film PV cells are fabricated by depositing extremely thin layers of PV materials onto a low-cost substrate, such as glass, stainless steel, or plastic. Thin film PV cells have an output efficiency range of 14–23% [43]. Furthermore, thin film cells consume significantly less materials, exhibit good performance at high ambient temperature and reduced sensitivity to overheating. Their main drawback is their limited efficiency, and little experience of stability and lifetime. Two technologies fall under this category: amorphous thin film and compound semiconductors.

1) Amorphous silicon: Amorphous silicon (a-Si) is a non-crystalline, allotropic form of silicon and is considered to be a well-developed thin film technology. The manufacturing process of this technology is carried out by depositing a thin photoactive film onto a substrate of glass or a transparent film. The film is then structured into cells [40]. An example is shown in Figure 2.7.

Figure 2.7: *Amorphous silicon solar cell.*

Thin film solar cells are both thin and flexible. In addition, much less semiconductor material is required to manufacture them compared to crystalline solar cells. In fact, they can reach up to 99% less material than crystalline solar cells [38]. This type of cell technology has evolved from an efficiency in a range of 2–5 % to above 12 %, and has a service life of 25 years [36].

2) Compound semiconductors (CdTe, CIS and CIGS): Among the most favourable materials for thin film compound semiconductors are cadmium telluride (CdTe), copper indium diselenide (CIS) and copper indium gallium diselenide (CIGS) [36]. Thin film compound semiconductors are PV devices that contain semiconductor elements of groups I, III and VI of the periodic table. Their high optical absorption coefficients and electrical characteristics enable the device to be tuned. The main drawbacks of these technologies are that they require the production process to be expanded to provide high yield and low cost, and degradation under wet conditions (which promote changes in the properties of the material) [38].

3) Compounds of Group III-V (GaAs and GaInP): These semiconductor materials are alloys that are composed of elements from Groups III and V in the periodic table. Cells made from Groups III-V have high power to weight ratio compared to silicon and other PV materials.

Furthermore, they perform excellently in extreme conditions, such as high radiation, high temperatures, and weak light. However, the cost of electricity generation per watt by Group III-V solar cells is about 400 times that for using silicon cells [44]. The most widespread solar cells made from this group are gallium arsenide (GaAs) and indium gallium phosphide (InGaP) cells. GaAs has many features that make it an excellent candidate material for fabrication of solar cells, with efficiencies twice those of silicon. GaAs has high optical absorption coefficients, a near optimum direct bandgap and mobility that is perfectly appropriate to the solar spectrum [45]. However, the performance of these PV cells suffers from fast surface oxidation [46]. The highest efficiency obtained for a single-junction GaAs solar cell is 32.2%. InGaP is a semiconductor made of indium, gallium and phosphorous, with a lattice structure similar to GaAs [47]. The highest conversion efficiency achieved for the InGaP single-junction solar cells was 15.4%, measured under air mass 1.5 global solar spectrum [48].

2.3.2.3 Emerging Technologies (Third Generation)

The emerging PV technologies that are currently in development have good potential to overcome and replace the dominant market incumbent crystalline silicon (c-Si) technology in the future. For example, cell efficiencies of more than three times that of typical commercial c-Si PV have been achieved using these technologies [49]. The most potentially disruptive emerging PV technologies in the near future are as follows:

1) Multi-junction solar cells: These solar cells use several materials stacked in multiple layers, or junctions. Typical multi-junction cells use two or more junctions and have the potential to achieve high conversion efficiencies of over 40% [50]. Solar cells with different bandgaps are stacked on top of each other, so that the solar cell with largest bandgap faces

solar radiation. The high-bandgap top cell absorbs high-energy photons of the spectrum, while allowing the lower-energy photons to pass through. A semiconductor material with a slightly lower bandgap is placed below the top cell to absorb photons with slightly less energy (longer wavelengths), which allows the absorbance of a broader range of solar spectrum. The efficiency of the multi-junction solar cells increases with the number of junctions [51].

2) Organic photovoltaics (OPVs): This technology uses organic polymer semiconductor layers as photoactive materials. Their main features are that they are flexible, lightweight, nontoxic and transparent [52]. OPV solar cells have recently achieved 13% efficiency. Their main drawbacks are their efficiency limitations and poor long-term reliability [53].
3) Dye-sensitised solar cells (DSSCs): These semiconductor structures are formed between a photosensitised anode and an electrolyte [54]. These types of cells are easy to manufacture and are semi-transparent and semi-flexible. They can produce electricity both indoors and outdoors, which enable the user to convert both artificial and natural light into electricity. The latest highest reported efficiency of these type of cells is 11.9% [55].
4) Quantum-dot PVs: Quantum-dot solar cells are PV cells that use quantum dots (semiconductor particles) as the light absorbing PV material. The semiconductor particles are on the nanoscale, which exhibit quantum mechanical properties. The highest efficiency of quantum-dot solar cells is reported to be 16.6% [56].
5) Perovskite solar cells: Perovskite cells are named after their crystal structure, which is the main active layer of these solar cells. These cells are primarily lead-halide based [57]. Perovskite cells can be fabricated using an easy and low-cost fabrication process. They have high extinction coefficients and high carrier mobility, with efficiency reaching 25% [58].

2.3.3 Concentrated Photovoltaic Technology

Concentrated photovoltaic (CPV) systems are based on the use of optical devices, such as lenses and mirrors, to concentrate the sunlight on a small-size solar cell. This technology is primarily developed to lower the cost of the PV system by reducing the amount of semiconductor material used, which is the most expensive part in a PV system [59].

CPV systems are usually classified according to the concentration ratio of the solar radiation incident onto the cell. The concentration ratio is calculated by dividing the lens area by the solar cell area. This ratio indicates how many times the solar light has been concentrated and is usually expressed in ‘suns’. CPV systems can be classified based on the concentration ratio, as follows [60]:

- Low concentrator photovoltaics (LCPVs), with a concentration ratio from 1 to 40 suns.
- Medium concentrator photovoltaics (MCPVs), with a concentration ratio from 40 to 300 suns.
- High concentrator photovoltaics (HCPVs), with a concentration ratio from 300 to 2000 suns.

2.3.4 Concentrated Solar Power (CSP)

Unlike CPV, CSP technologies convert solar radiation indirectly into electricity. In general, CSP plants consists of two main components: a solar field and a power generation field. In the solar field, mirrors direct sunlight onto a receiver. Heat transfer fluid (HTF) flows through the receiver, which increases the HTF temperature to high levels. In the power generation field, the heated fluid is used to drive a turbine or a heat engine to generate electricity [61]. This technology, combined with thermal energy storage (TES), enables power to be produced even when there is not enough sunlight. Despite the advantages of CSP, the conversion efficiency (except for large scale plants) is low, while construction and installation costs are high [62]. Although the contribution of the CSP is limited for the time being, it is anticipated to represent 12% of global energy demand by 2050 [63].

Compared to solar PV systems that uses both direct and diffuse solar radiation, CSP technology can only use the direct solar radiation (DNI) for efficient operation [64]. Partially clouded skies normally have more diffuse radiation than clear skies. Depending on the position of the sun, direct radiation can vary in a single day from 15%–40%, with an average of 30% of the global solar radiation [65, 66].

Figure 2.8 illustrates line focusing and point focusing CSP technologies, which can be classified into four types of systems. A brief description of each type follows [67, 68]:

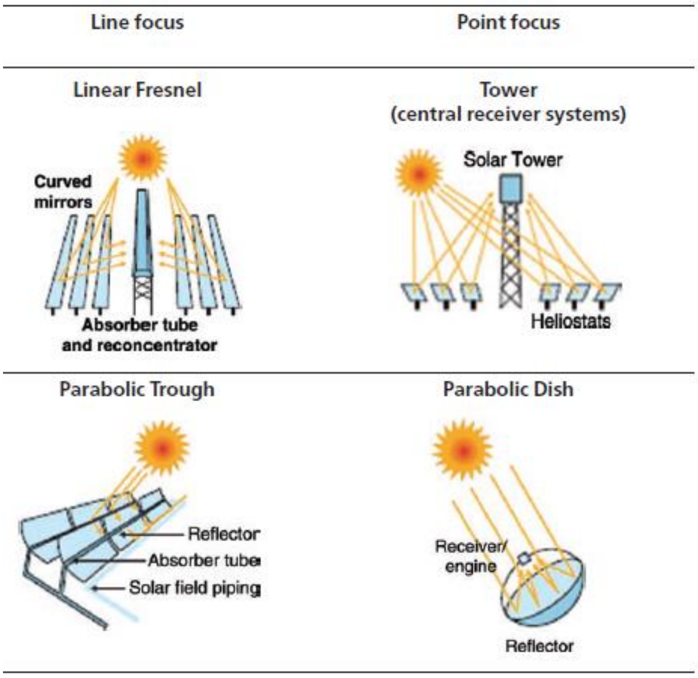

Figure 2.8: Line focusing and point focusing solar concentrators [69].

1) Parabolic Trough

The parabolic trough system is the most proven, widespread and commercially mature among all of the technologies of CSP [30]. Parabolic trough technology has the highest market share, more than 90% among the various types of CSP technologies [70]. Parabolic trough solar collectors are a line focusing solar collector, which is a long parabolic trough shape collector lined with high reflectivity mirrors. As shown in Figure 2.9, the parabolic mirrors concentrate the parallel incoming solar radiation towards a cylindrical tube, which is called the absorber, where the solar energy is absorbed [8]. The tube is typically covered with a selective coating to reduce radiation losses to the environment. An HTF—commonly oil, molten salt, or water—flows through the receiver and absorbs the thermal energy from incoming solar radiation. The HTF can effectively produce heat with high temperatures as high as 400 °C. A cylindrical glass envelope surrounding the absorber tube, as shown in Figure 2.10, is evacuated to minimise heat loss to the environment [64, 71, 72].

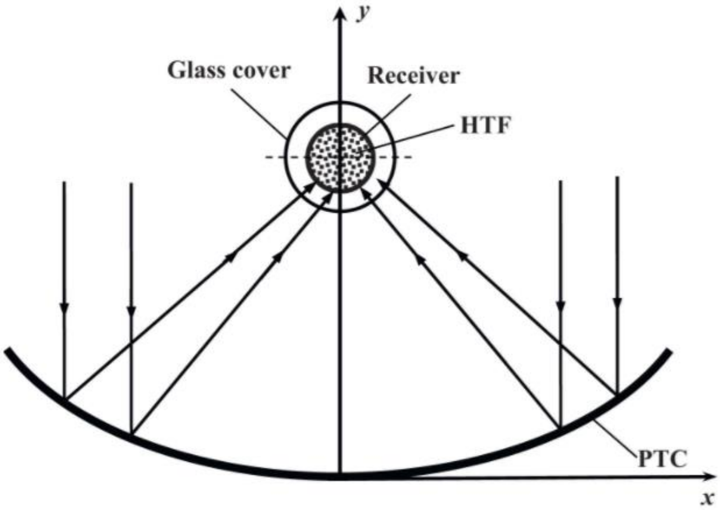

Figure 2.9: *Schematic of parabolic trough concentrator with a tube thermal absorber [64].*

Parabolic trough applications can be classified as high HTF temperature (300–400 C), which are used for power generation, and low HTF temperature (100–250 C), which are used for domestic hot water, space heating and heat-driven refrigeration [73]. A single-axis tracker system, usually aligned north-south, is employed to track the sun for maximum solar radiation absorption.

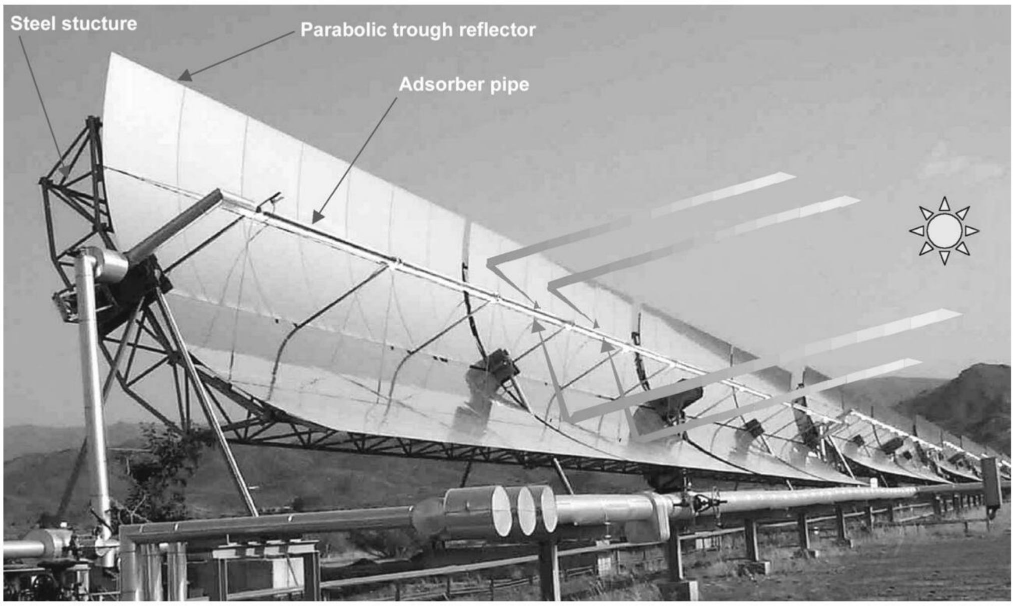

Figure 2.10: *Parabolic trough collector* [7].

Vacuum applied between the glass cover and the absorber is intended to reduce the heat loss to the environment; however, conduction heat losses are still possible via thermal contacts between the glass cover and the absorber pipe, which can be eliminated or at least reduced by preventing this contact [74]. To reduce the reflection of the incident rays by the glass cover, the glass is usually covered with an anti-reflecting layer, which enhances the overall transmissivity of the glass from 90–92% to 94–96% [75].

2) Central Receiver System

The central receiver tower achieves high temperatures by concentrating sunlight onto a central receiving system (tower). Its technology is based on the use of an array of flat, movable mirrors, also known as heliostats, to focus and concentrate the sunlight onto the fixed receiver. As a result of using a huge number of reflectors (mirrors), and hence a high level of concentration, very high temperatures are generated. The HTF, usually molten salt (40% potassium nitrate and 60% sodium nitrate), is heated by reflected rays. HTF liquid with high heat capacity can be used to store the energy before it is used to boil water to drive turbines.

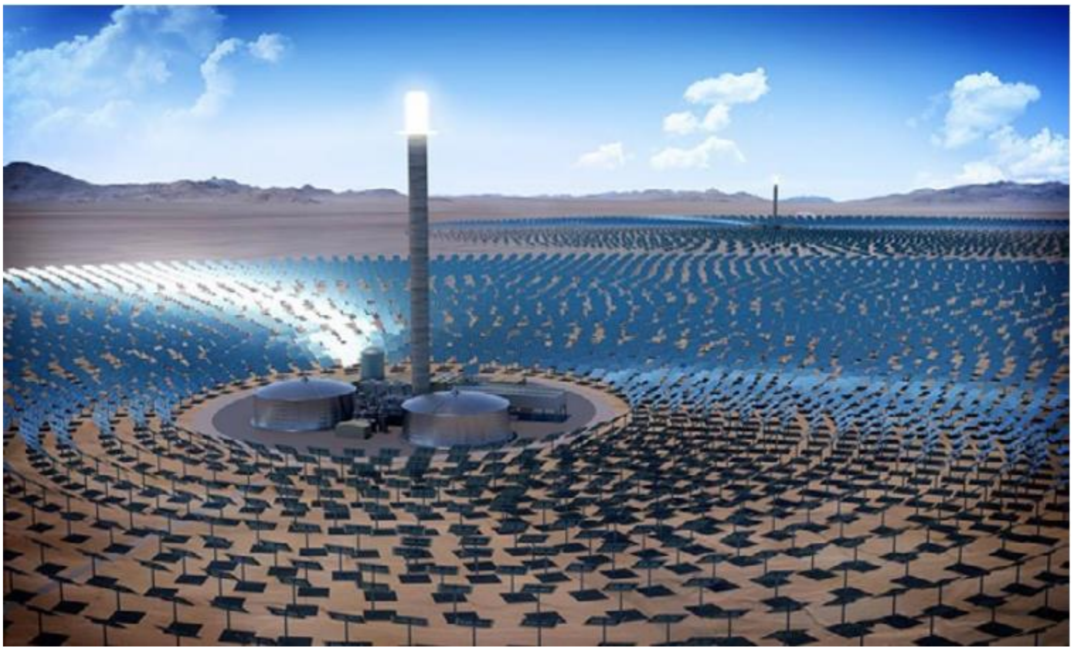

Figure 2.11: *Central receiver tower* [70].

A typical central receiver system, as shown in Figure 2.11, consists of three main subsystems: the heliostat field, the receiver, and the power-conversion station. In the heliostat field, a large number of controlled mirrors track the sun using a two-axis tracking system and they then reflect the solar radiation onto the receiver located on the top of the tower. The receiver absorbs the heliostat reflected solar radiation and converts it into heat that is absorbed by an HTF. In the power-conversion station, the water is heated by the HTF through exchangers to produce steam that drive turbines for electricity generation [76].

3) Linear Fresnel Reflector

The linear Fresnel reflector (LFR) is considered to be a promising technology due to its simple, robust, and inexpensive design. LFRs use flat mirror elements of equal width, as shown in Figure 2.12, to focus sunlight onto a fixed absorber that is located at a common focal point of the reflectors [77]. The mirrors can follow the sun on a single or two axis tracking system[78]. In addition, the mirrors have the capability to concentrate the sun's energy to approximately 30 suns. This concentrated energy is transferred through the absorber to the HTF, which exchanges heat with water to generate steam to run a turbine to produce electricity. LFRs are classified as a low efficiency technology because of their low concentration ratio [78, 79].

Figure 2.12: *liner Fresnel reflector (LFR)* [80].

Despite the advantages of LFRs, such as their low cost and simpler structure compared to other CSP technologies, their main disadvantage is the low thermal efficiency conversion when compared to parabolic trough and dish. The main reasons for lower optical performance of this technology are the spaces between the primary reflectors, the shape of the primary reflectors, the shading effects and the need for a secondary reflector [81].

4) Parabolic Dishes

A parabolic dish is a point-focus collector, which concentrates solar energy onto a receiver that is located at its focal point. To achieve the highest concentration, the dish must fully track the sun to reflect the beam into the thermal receiver using a two-axis tracking system. The receiver located at the focal point of the dish, as shown in Figure 2.13, absorbs the thermal energy from solar radiation and transfers it to a circulating fluid. The captured thermal energy can then be converted to electricity using an engine-generator coupled directly to the receiver, or it can be transported through pipes to a central power-conversion system. Temperatures achieved at the focal point of a parabolic dish can reach up to 1500 ^{o}C [82].

Figure 2.13: *Parabolic dish collector [83].*

The typical concentration ratio of parabolic dishes ranges from 600–2000, and hence they are highly efficient when used as thermal energy absorption and power-conversion systems. They can either function independently or as part of a larger system of dishes. Among all of the mentioned CSP technologies, parabolic dish systems are considered to be the most effective in terms of concentration ratio [84].

2.3.4.1 Geometrical Considerations of Parabolic Concentrators

In imaging parabolic concentrators, direct solar radiation is concentrated on a focal line (troughs) or focal point (dishes), as shown in Figure 2.14. One of main parameters of these concentrators is the geometrical concentration ratio (C_G), which can be defined as the ratio of the projected collector aperture area (A_{ap}) to the focal line or spot area or the area of the Sun image (A_{im}) [85]:

$$C_G = \frac{A_{ap}}{A_{im}} \tag{2.4}$$

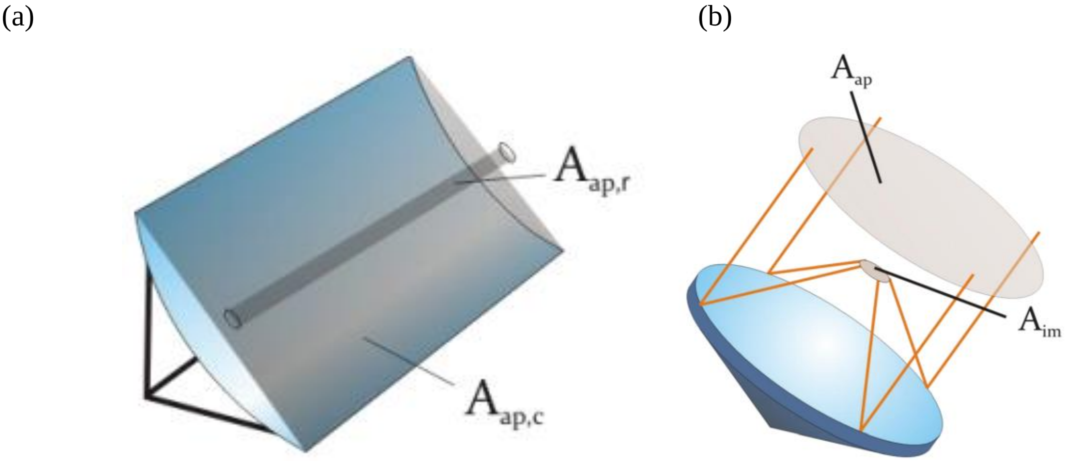

Figure 2.14: *Collector aperture area and receiver aperture area for (a) parabolic trough and (b) parabolic dish [85].*

It is to be noted that the geometrical concentration ratio is only an approximation of the real mean radiation concentration because the reflectivity of the mirror is not taken into consideration. In addition, the imperfections of the mirror may scatter part of the incident light away from the receiver aperture, they may also neglect the shading effects of the receiver and the bearing structure on the collector.

The parameter that determines the shape of a collector is called the rim angle (ψ). The rim angle is correlated to the ratio of the focal length to the aperture diameter. The parabola in Figure 2.15 is an algebraic representation of $y = \frac{x^2}{4f}$, so that the following relation applies [86]:

$$tan\psi = \frac{x_0}{f - \frac{x_0^2}{4f}} \tag{2.5}$$

where *f* is the focal length and x_0 is half of the parabola aperture diameter (*d*).

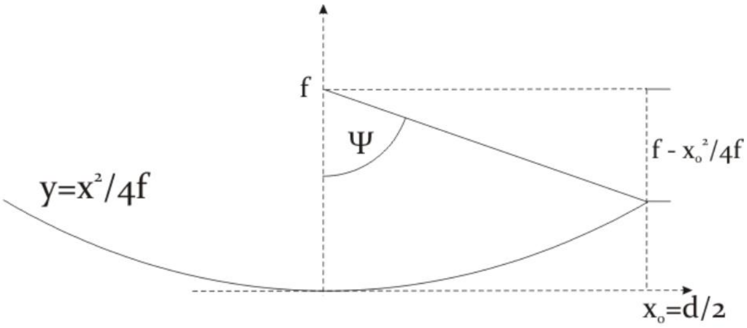

Figure 2.15: *Rim angle in a cross-section of a paraboloid* [86].

For a fixed diameter, the relationship between the focal length and the rim angle is illustrated in Figure 2.16:

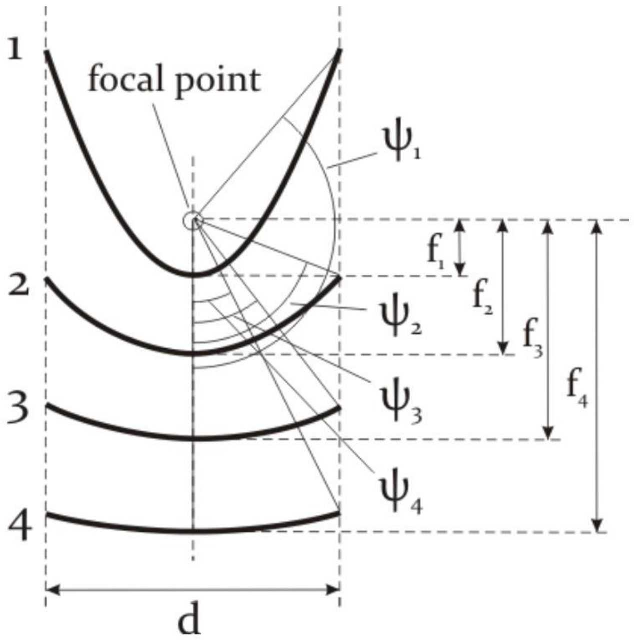

Figure 2.16: *Relationship between the focal length and the rim angle for a constant reflector diameter.*

At a given aperture diameter, small rim angles correspond to a long focal length, and vice versa. With a given diameter, the focal point is far away from the mirror when the rim angle is small [86]. This indicates that the spread of the beam radiation, which is inevitable because the sun is not really a point source, will cause a larger sun image. Therefore, the concentration ratio must be lower for small rim angles at a given collector diameter. Hence, mirrors with a very small rim angle are not favourable for high radiation concentration ratios. Meanwhile, mirrors with a very large rim angle have a negative effect on the concentration, which causes a widening of the focal spot because of the tilted incidence of the reflected rays on the focal plane [87]. In the same way, mirrors with a very big rim angle are not favourable for high radiation concentration ratios. Given that too small and too large rim angles are not favourable, there must be an ideal intermediate rim angle, which was found to be about 45° [88].

2.4 Spectral Splitting

PV cells have a fixed material dependent spectral response and are efficient in converting photons of energies close to the PV cell bandgap energy. However, photons with energies below the bandgap are dissipated as heat in the cell material, resulting in increased cell temperature. Meanwhile, photons with energies higher than the band gap energy are partially absorbed by the cell and the excess energy is dissipated as heat [89].

The conversion efficiency of the solar cell drops because of the mismatch between the spectral response of the cell and the solar spectrum, which leads to conversion losses and increases the cell temperature [90]. Employing spectral beam splitting using optical filters to direct the suitable part of the spectrum to the PV cell is a promising solution to this problem. In addition, the split part (i.e., IR) can be utilised for further energy generation [91, 92].

Ju et al. [93] described two different methods that are typically developed to improve the overall conversion efficiency of solar cell modules by reducing the solar cell operating temperature and spectral splitting. These two methods are waste heat recovery (WHR) and spectral beam splitting (SBS). In the WHR method, a cooling system (thermal receiver) is used to control the solar cell's operating temperature and then harvest the thermal energy dissipated from the solar cells. The SBS method attempts to use the solar energy over its full spectrum. The visible spectrum of the light, consisting of photons with energy larger than the bandgap of the cells, is directed to the PV cells to produce electricity. Meanwhile, the infrared irradiation, consisting of photons with energy below the PV cell bandgap, is directed to a thermal absorber. SBS is achieved with the help of the spectral beam filter. Figure 2.17 illustrates the WHR and the SBS methods.

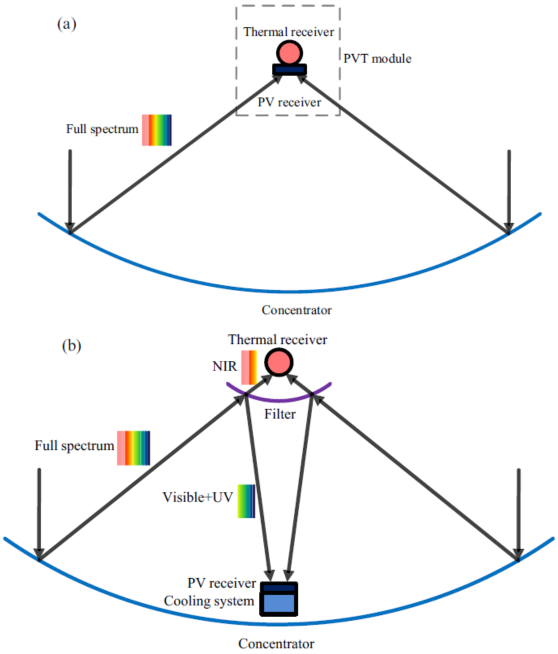

Figure 2.17: *Schematic of the CPVT system, (a) the WHR CPVT system; (b) the SBS CPVT system* [93].

In 1955, Jackson [94] was the first to suggest the concept of splitting the solar spectrum and directing each band of radiation to the most efficient converter. Moon et al. carried out the first experiment of splitting the spectrum in 1978 [95]. SBS is an attractive approach to decrease the PV cell's operating temperature by thermally decoupling the PV and thermal receivers in PV/T hybrid systems, which allows the PV cells to operate at low temperature and the thermal receiver to operate at high temperature. By applying this approach to any energy conversion for solar energy applications, a remarkable increase in efficiency is anticipated [96].

Shou et al. [97] proposed a CPV system based on a parabolic dish collector, as shown in Fig. 2.18. A TiO_2/SiO_2 filter consists of 78 layers (42 front layers and 36 back layers) and a substrate is used to separate the reflected solar beams from the collector. Radiation in the range of 600–

1050 nm reached the silicon solar cells after filtration. The results showed efficiency as high as 25% for the hybrid system, with a concentration ratio of 600 suns.

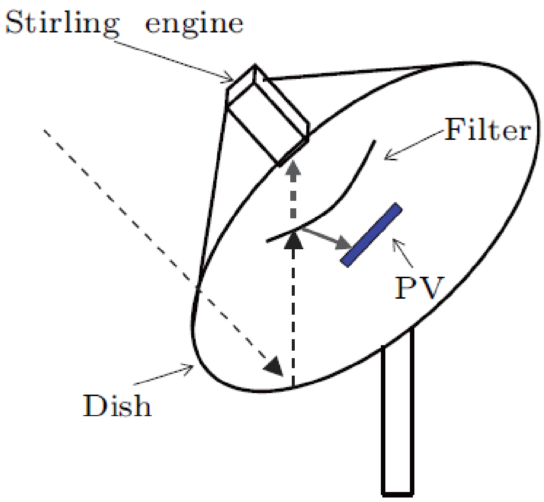

Figure 2.18: *Basic design of the hybrid system [97].*

Shou et al. [98] also designed an 82-layer broadband optical interference thin film filter fabricated by TiO_2 and SiO_2 materials, as shown in Figure 2.19. The authors achieved high reflectance in the range from 400–1100 nm and a high transmittance from 1100–2500 nm over the broadband of solar spectrum. Using the filter resulted in an average efficiency increase of 3.24% for the solar cell with respect to the solar energy that it receives. The authors found a nearly 2% efficiency increase for the hybrid systems without concentration comparing to PV systems without the filter. However, if solar irradiance concentration is considered, then the hybrid PV-TEG system with the filter will gain more energy and work in higher efficiency than the CPV system at higher concentration levels. The authors concluded that this optical broadband thin film filter for beam splitting is a suitable technology for a hybrid PV-TEG system.

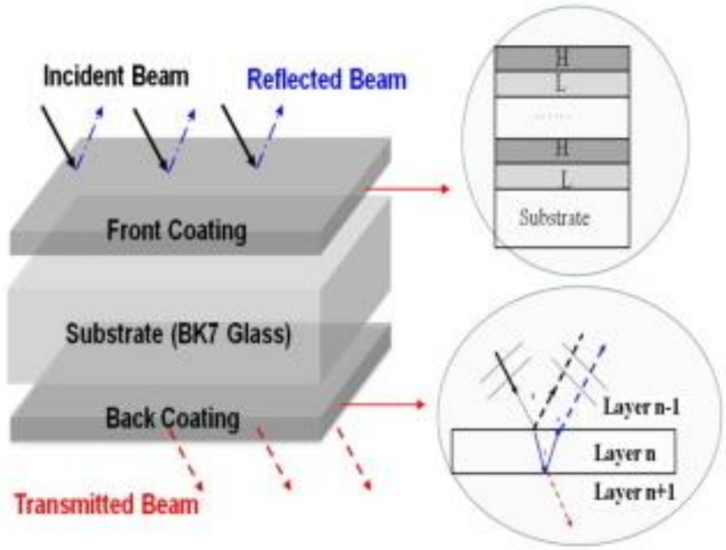

Figure 2.19: *Diagram of the designed thin film filter structure and a simple illustration of the interference of the lights reflected from a random layer's two sides* [98].

Crisostomo et al. [91] designed a beam splitter fabricated based on SiNx/SiO_2 multilayer thin film filters, which were used in a hybrid system of a concentrating photovoltaic thermal (PV/T) solar collector with a linear Fresnel mirror-based concentrator (10 sun). Thin film filters were designed to achieve high reflectance from beams between 713–1067 nm, and a high transmittance outside this window. The results revealed that the PV cells that illuminated with the light reflected by the filters had a 9.2% higher efficiency, on average, than those illuminated without the filter. This happens because the unused part of the spectrum by the cells is removed, which in turn lowers the temperature of the cells under filtered light by 8 ºC. The authors also noted, based on the measured optical properties of the filters, that this system can utilise up to 85.6% of the solar spectrum.

Mojiri et al. [99] developed a novel spectrally splitting hybrid solar receiver by combining a simple dichroic filter and a liquid channel as a selective absorbing medium. A simple dichroic filter made of titanium dioxide and silicon dioxide (five layers) was designed, optimised, and fabricated. The authors indicated that this filter directs 54.5% of the concentrated light to the silicon PV cells, which can convert 26.1% of this energy into electricity. This figure is significantly higher than their 20.6% efficiency under the full spectrum. This is due to the fact that 73.3% of the incident flux on the silicon cell is within the range that falls on the cell’s spectral response, which can be efficiently utilised and hence converted to electricity.

Wei An et al. [100] developed a polypyrrole nanofluid spectral splitting filter for a hybrid PV/T system. The authors found that the maximum overall efficiency of this hybrid PV/T system with polypyrrole nanofluid filter was 25.2%, which was 13.3% higher than that without the filter. This happened because the nanofluid absorbs the solar radiation that cannot be efficiently utilised by a PV cell unit. More importantly, the resulting medium-temperature thermal energy can be harvested in this hybrid system.

Hu et al. [101] detailed a two-stage parabolic trough concentrating (PV/T) system that consists of a concentrator, a SBS filter, an evacuated collector tube and the solar cell components (as shown in Figure 2.20). The authors developed a detailed optical model to predict the optical properties of the hybrid solar system. Their results revealed that the heat load of the overall incident radiation energy on the cell can be reduced by 20.7% by removing photons under the bandgap of the cell. Up to 10.5% of the removed part of the total incident solar energy can be recovered by the receiver. Moreover, the overall optical efficiency is, in theory, about 0.764 when using the optimised splitting coating.

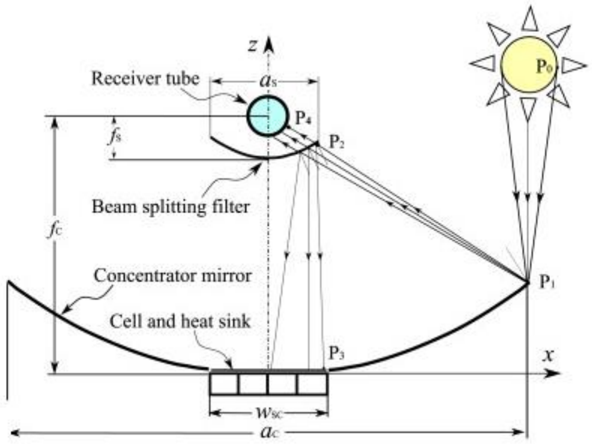

Figure 2.20: *Schematic diagram of the concentrating beam splitting solar system, shown in two dimensions* [101].

2.5 Thermoelectric Technology

Thermoelectric (TE) technology is an environmentally friendly technology for converting heat directly into electrical energy using TEG. It can also be used in reverse as coolers and heaters based on the Peltier effect, which converts electrical energy into heat energy for cooling and heating purposes. One of the most important features of TE technology is its ability to directly convert thermal energy to electrical energy, making it one of the most promising direct power generation techniques to recover waste heat energy. However, these devices suffer from low efficiency, mainly due to the low figure-of-merit (ZT) of the materials [102].

TE devices are semiconductor devices that have the ability to generate a voltage when a temperature difference is applied across it (based on the Seebeck effect) or they can produce a temperature difference when an electric power source is connected (based on the Peltier effect) [103]. TE modules offer an alternative green energy technology and low-cost electricity without the use of moving parts or production of environmentally deleterious wastes [104].

These devices are constructed as arrays of N-type and P-type semiconductors. A basic unit is shown in Figure 2.21, which consists of P-type and N-type semiconductors that are connected electrically in series and thermally in parallel between the ceramics [105]. Electric power is produced by applying a heat source on one side and a cooler heat sink to the other side (see Figure 2.21 (a)); and vice versa, electric power can produce cooling or heating by reversing the current direction (see Figure 2.21 (b)) [107].

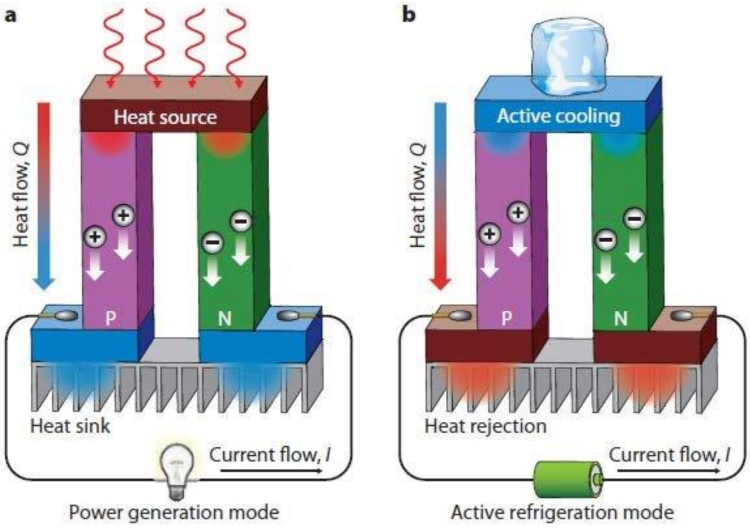

Figure 2.21: *a) Power generation and b) cooling/heating by thermoelectric device* [107].

2.5.1 Thermoelectric Effect

The term "thermoelectric effect" refers to three physical effects, namely: the Seebeck effect, the Peltier effect, and the Thomson effect, which will be described in the following subsections.

2.5.1.1 Seebeck Effect

The Seebeck effect was discovered in 1821 and is named after the Baltic German physicist Thomas Johann Seebeck. This effect happens when two dissimilar materials are joined together, and the junctions are kept at a temperature difference (ΔT). A voltage difference (ΔV) then develops that is proportional to the temperature difference (ΔT). If the two sides are connected through an electrical circuit, then a direct current (DC) flows through that circuit.

The ratio of the developed voltage to the temperature gradient ($\Delta V/\Delta T$) is related to an important property of the material, which is called the Seebeck coefficient, α. The Seebeck coefficient ranges from a few μV/K for metals to a few hundred μV/K for semiconductors [108].

2.5.1.2 Peltier Effect

In 1834, a French physicist called Jean Charles Peltier discovered the phenomenon of the Peltier effect. This effect is the reverse phenomenon of the Seebeck effect. This effect occurs when an electrical current flows through a junction of two dissimilar materials where, depending on the direction of the current, heat is emitted at one junction and absorbed at another, or vice versa. This effect is useful when heat needs to be transferred from one medium to another on a small scale. The Peltier effect is exploited in devices that are used for cooling electronic equipment and computers [109].

2.5.1.3 Thomson Effect

This effect was first discovered by William Thomson in 1851. The Thomson effect is a combination of the two previous effects (i.e., Seebeck effect and Peltier effect). If a current flows across two points of a homogeneous wire with a temperature difference between the two points of that wire, then heat will either be emitted or absorbed [110].

2.5.2 Thermoelectric Figure-of-Merit (ZT)

Thermoelectric materials are evaluated by the figure-of-merit (ZT), where T is the absolute temperature. This figure is defined in terms of intrinsic material properties. Three physical properties determine this quantity, namely the Seebeck coefficient (α), electrical conductivity (σ) and thermal conductivity (K). ZT is defined as:

$$ZT = \alpha^2 \sigma T / K \tag{2.6}$$

It is well-known that for a thermoelectric generator to achieve high efficiency, the ZT of the thermoelectric materials should be as high as possible [111]. The best thermoelectric materials for thermoelectric devices operating at room temperature ($T \approx 300$ K) are Bi_2Te_3-based materials, which possess a value of $ZT \approx 1$. For these devices to be widely-employed commercially, high-performance TE materials of $ZT > 4$ are needed. However, the achievement of this goal has remained a formidable challenge [112].

The history of thermoelectric materials can be characterised by the progress in increasing ZT, as shown in Fig. 2.22.

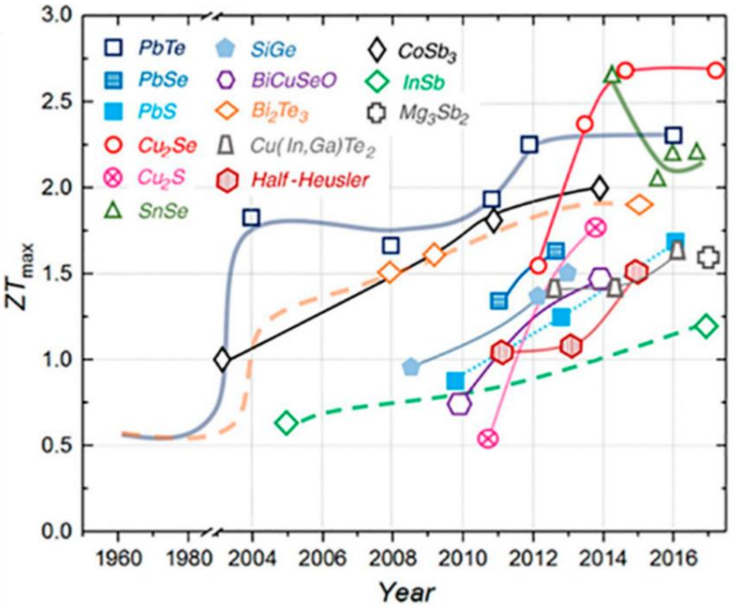

Figure 2.22: *ZT of many typical thermoelectric materials as a function of year [113].*

2.5.3 Advantages of Thermoelectric Devices

Thermoelectric devices have many distinct advantages over other technologies [105], as follows:

- They have no moving parts and hence need significantly less maintenance.
- They can reach to 100,000 hours of steady-state operation.
- They contain no materials that require periodic replenishment.
- Heat pumping in a thermoelectric system can work in both directions, either emitted or absorbed, by changing the direction of the electrical current. In other words, it can be used as a cooler or as a heater.
- They enable a precise temperature control to within ±0.1 °C.
- They can operate under environments that are too severe, too sensitive, or too small compared to conventional refrigeration.
- They are not position-dependent.

The main disadvantage of thermoelectric devices is their relatively low conversion efficiency compared with other technologies. The efficiencies for thermoelectric power generation currently are between 5%-10%. Many are lower depending on temperature differences. However, in the case of waste heat or solar energy, the efficiency of the thermoelectric generation system is not an overriding consideration because it provides a free source of heat [114].

2.6 PV-TE Hybrid Systems

When the temperature increases by 1 ºC, the efficiency of the PV cells decreases by 0.25–0.5% (depending on the material used in the cell) [115, 116]. Therefore, cooling the PV cell will help to maintain its efficiency and lengthen the cell’s lifespan [117]. Meanwhile, the excess heat can be converted into additional power output and thermal energy [39]. A PV-TE hybrid system offers an appealing option to harvest the waste heat from a PV cell and at the same time maintain the cell’s temperature at low levels.

The concept of integrating a thermoelectric generator with a PV cell has attracted the attention of many researchers in the last decade. Most of this research was done by directly connecting the hot side of the thermoelectric generators (TEG) to the backside of the solar cell [118-121]. In this way, the TEG utilises the wasted heat of the PV cell to generate electricity. The major drawback of this approach is that although increasing the temperature at the hot side of the TEG improves the temperature difference across its plates, it also affects the performance of the PV cell by reducing its efficiency [122].

PV-TE hybrid systems that utilise beam splitting technology have recently gained interest as a promising approach to full spectrum energy harvesting. These systems consist of PV, TE, spectral spitting device and a cooling system. The beam splitter is an optical device that splits the solar irradiance into two parts and then directs each part to a suitable device (PV or TE). By thermally decoupling the PV and the TE, each device can work at different temperatures. This will allow the PV cell to operate at low temperatures, which will improve its efficiency [123].

Bjørk and Nielsen [124] investigated an unconcentrated PV-TEG hybrid system for optimal mathematical efficiency. They developed an analytical model and found that an efficiency gain of 1.8% could be achieved using spectrum splitting in the hybrid system.

Mizoshiri et al. [125] designed and tested a PV-TE hybrid system with a hot dichroic mirror as a beam splitter, as shown in Figure 2.23. A cylindrical lens was used to focus the near infrared radiation (NIR) on the hot side of the TEG module. They used a thin film TE module, which uses air cooling to generate a temperature difference. An open circuit voltage of 78 mV was generated by the module, which resulted in an increase of 1.3% of the hybrid system compared to that of the PV module alone.

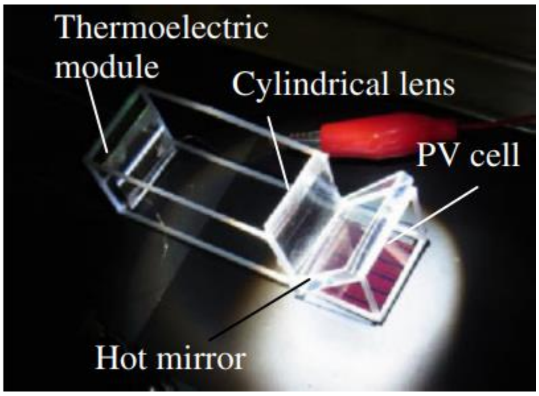

Figure 2.23: *Schematic diagram of CSSPV-TE hybrid system [125].*

Mahmoudinezhad et al. [126] experimentally investigated the performance of a PV-TE hybrid system with spectrum splitting technique, and compared it with the performance of a PV-only system and a TEG-only system under moderate solar concentrations. Their investigations showed that the power generation by the PV in the hybrid system is higher than that of the PV-only system as a result of SBS technique thermal management. However, the power output of the TEG-only system is higher than the share of the TEG in the hybrid system. In general, the hybrid system showed a higher power-conversion efficiency when compared to the PV-only system and TEG-only system under moderate solar concentration.

Yang et al. [127] developed a theoretical model of a PV-TE hybrid system using solar spectrum splitting. The effects of given solar concentration factor on the power output and efficiency of the hybrid system were calculated. The results show that the maximum efficiency of the system can be further improved when the area ratio is optimised. Moreover, they found that the hybrid system can be more efficient compared to PV cell alone, especially at a low concentration factor.

Elsarrag et al. [128] developed a hybrid solar cell made of a standard PV cell and a thermoelectric generator for full spectrum power harvesting. The solar spectrum was split with an optical beam splitting media at 800 nm. The visible and ultraviolet part of the spectrum is transferred to the PV cell, while the infrared part was directed to the TEG module. Their study concluded that PV cell showed a better overall performance with the beam splitting. In addition, the proper selection of selective absorbance materials of the absorber and the alleviation of the convective heat loss from the surface of the absorber results in a substantial positive impact to the TEG power generation.

Yin et al. [92] proposed a concentrated solar spectrum splitting method for a PV-thermoelectric hybrid system (as shown in Figure 2.24). The novel optimal design method aimed at higher utilisation of solar spectrum energy. Their study optimised the operating temperature and the cut-off wavelength of the mirror for maximum efficiency. The findings show an inverse relationship between the optimum cut-off wavelength of the splitter and the thermoelectric ZT.

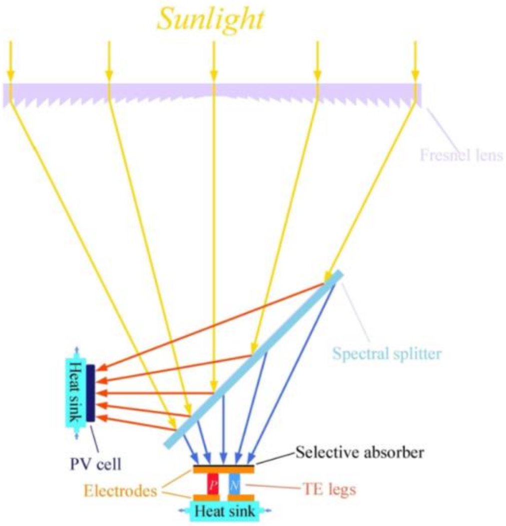

Figure 2.24: *Schematic diagram of CSSPV-TE hybrid system [92].*

Ju et al. [129], developed an energy-based numerical model to optimise a spectrum splitting concentration PV-thermoelectric hybrid system (as shown in Figure 2.25). Their hybrid system was composed of a GaAs solar cell and a skutterudites CoSb3 solar thermoelectric generator. The electrical and thermal performance of the hybrid system was evaluated, and they conclude that the PV-TE hybrid system is more suitable for working under high concentrations.

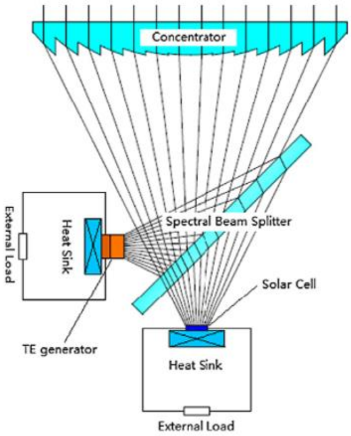

Figure 2.25: *Schematic diagram of the PV-TE hybrid system [129].*

The most important advantage of spectrum splitting in the PV-TE hybrid system is that the two systems—the PV and the TEG—are thermally decoupled, which allows the TEG to operate at higher temperatures. However, the thermalisation energy of the cell is not used, which forces the dissipation of the heat via a heat sink [130].

2.7 Conclusion

From this literature review, it can be concluded that integrating PV cells with TEGs is a promising technique for full solar spectrum power harvesting. Previous research was successful in increasing the efficiencies of hybrid systems compared to bare cells. However, the majority of the research discussed in this review used numerical or analytical methods and concentrated on the influence of solar irradiance on the performance of the PV-TEG hybrid system. Therefore, a reliable experimental study to evaluate the actual performance of these hybrid systems is needed.

Almost all of the efforts that have been reviewed in this chapter were carried out under different levels of solar concentration. Although PV-TE hybrid systems with optical beam splitter are more efficient under solar concentration, light reflected from the concentrator will generate a wide-angle cone of light on the beam splitter surface. The beam splitter (e.g., dichroic mirror) is sensitive to the light incident angle, and hence rays with angles deviated from the mirror design angle will miss the reflection/transmission curve. This results in undesirable rays being directed to the wrong receiver.

Despite the few efforts that have been made to investigate the efficient performance of a PV-TE hybrid system with beam splitting techniques, all of them (to my knowledge) have placed the thermoelectric generator directly under the beam splitter. None of them have tried to transfer split heat to a different location for more fixable utilisation of the heat by a thermal receiver. Therefore, this study aims to bridge this gap by developing a design that allows the transfer of the heat generated by the absorber for more fixable utilisation.

Chapter Three: Research Methodology

3.1 Introduction

In this chapter, the design and construction of experimental setups for investigation of the performance of the proposed PV/TE hybrid system will be described. The design was verified using “TracePro” software for the optical performance and “SolidWorks” software for the thermal characteristics. This chapter will also present the experimental techniques that are employed in this project to determine the optical, electrical, and thermal performance of the photovoltaic cells, thermoelectric generators, concentrators, and beam splitters.

3.2 Research Concept

Beam splitting techniques divide sunlight into different bands according to the wavelength. In this study, as shown in Figure 3.1, sunlight is split into two bands by a cold dichroic mirror (i.e., reflects UV-vis range and transmits IR range). The aim is to direct each band to a suitable receiver (i.e., the PV cell or the TEG). PV cells only use that part of the spectrum which falls above the cell bandgap (i.e., photons with energies higher than the cell bandgap energy). In contrast, the part of the spectrum that is under the bandgap (longer wavelength) does not have enough energy to ionise the electrons of the cell but will heat the cell material and affect its performance. A dichroic mirror is used in beam splitting and is designed to have a cut-off point that matches the bandgap of the cell. This allows the suitable band to be reflected to the cell and then transmits the other band to the second receiver (i.e., the TEG). Given that designing a mirror to have a desired cut-off point is not cost-effective, the strategy in this study is to use an off-the-shelf mirror that matches the bandgap of a PV cell. This will be a much more cost-effective approach. The commercially available mirror that was selected has a cut-off point of

725 nm, and hence a PV cell with a bandgap close to this wavelength should be identified for this hybrid-system design. InGaP cells have a bandgap of 1.88 eV, which corresponds to a cut-off wavelength of 658 nm. This provides the closest match to the cut-off wavelength of the selected mirror and consequently was selected for use as PV cells in the hybrid-system design.

The rays transmitted from the mirror, which is placed in an angle of 45° of incoming light (also transmitted rays, as shown in Figure 3.1), are concentrated onto an absorber (copper rod) that converts infrared radiation into heat for the TEG. The concentrator helps to reduce the absorber's surface area, which minimises the heat losses and maximises the heat delivery to the TEG.

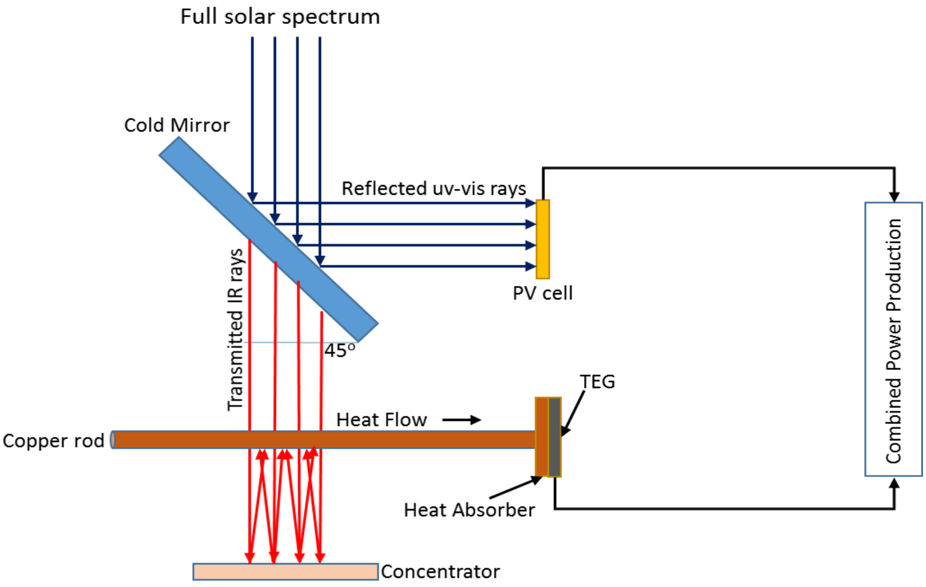

Figure 3.1: *Schematic of the conceptual hybrid PV-TE system.*

3.3 Experimental System

The proposed hybrid system consists of a dichroic mirror, PV solar cell, parabolic concentrator, thermal absorber, and TEG module (as shown in Figure 3.1). The full spectrum solar irradiance is split by the dichroic mirror. The reflected light is directed to the PV cell and the transmitted light is directed onto the parabolic concentrator. In this project, two types of parabolic concentrators were considered. The first setup uses a parabolic trough as a solar concentrator and the second uses a parabolic dish. The parabolic trough is a line focussing concentrator, while the dish is a point focussing concentrator. The intention is to identify the most suitable configuration for the design and construction of a high-performance hybrid PV-TE system through comparative study.

3.3.1 Trough Hybrid System

The first hybrid-system setup utilises a parabolic trough as a solar concentrator, which concentrates the transmitted rays from the dichroic mirror onto a copper rod (thermal absorber) that is placed at the focal line of the trough. The theory of the design of the parabolic trough, simulation studies to support the design, and the fabrication process will be detailed in the following subsections.

3.3.1.1 Parabolic Trough Design

A number of factors need to be considered in trough design, which are listed in Table 3.1 [131-134]:

Table 3.1: *Parabolic troughs structure advantages and disadvantages.*

	Advantages	**Disadvantages**
Larger trough aperture	Increases the concentration ratio.	Increases the wind loads on the structure.
Bigger receiver diameter	Increases the reflected rays' absorption.	Increases the heat lost to surroundings.
Deep troughs	Slower wind speed around the receiver, leading to less heat loss to the environment.	Higher wind forces on the trough itself due to increased curvature.
Shallow troughs	Lower wind forces on the trough.	Higher wind speed around receiver, and hence more heat transfer to environment.

In the trough design, a copper rod is used as a thermal absorber. The design of the parabolic curvature and position of the copper rod is crucial to ensure accurate concentration of light onto the copper rod. The equation that represents the parabola is [85]:

$$x^2 = 4fy \tag{3.1}$$

where f is the focal point of the parabola. Figure 3.2 shows the parameters that control the parabolic reflector.

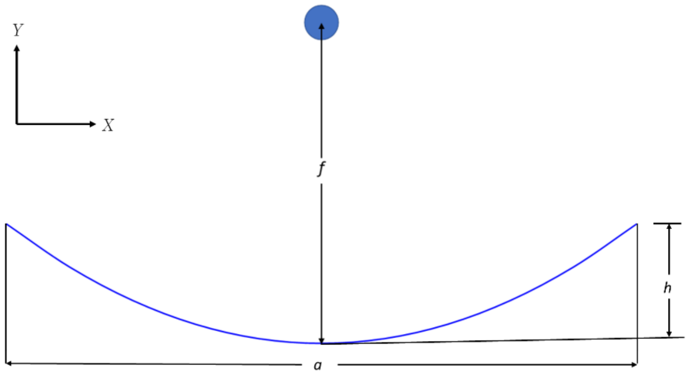

Figure 3.2: *Parameters of parabolic reflector.*

The position of the copper rod relative to the parabolic mirror can be determined from Equation 3.1 [135]:

$$f = \frac{a^2}{16h} \tag{3.2}$$

where, h is the height of reflector, a is the aperture width and f is the focal point where the absorber will be located. A deeper trough has a shorter focal point, as illustrated in Figure 3.3 [85].

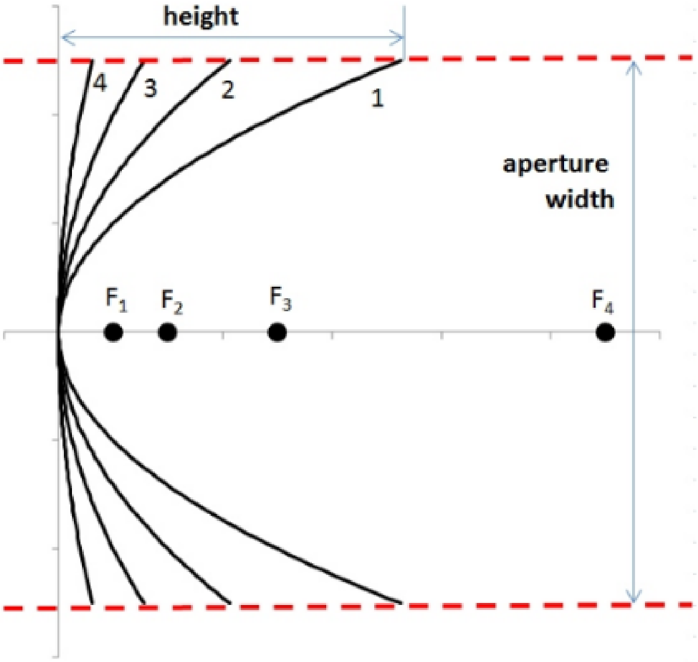

Figure 3.3: *Focal points for different parabolic curves.*

The experimental setup of the trough hybrid system was designed using "SolidWorks" and was then constructed in-house by Cardiff University's workshop. Figure 3.4 shows the design drawing of the experimental setup by the SolidWorks and the corresponding assembly drawing.

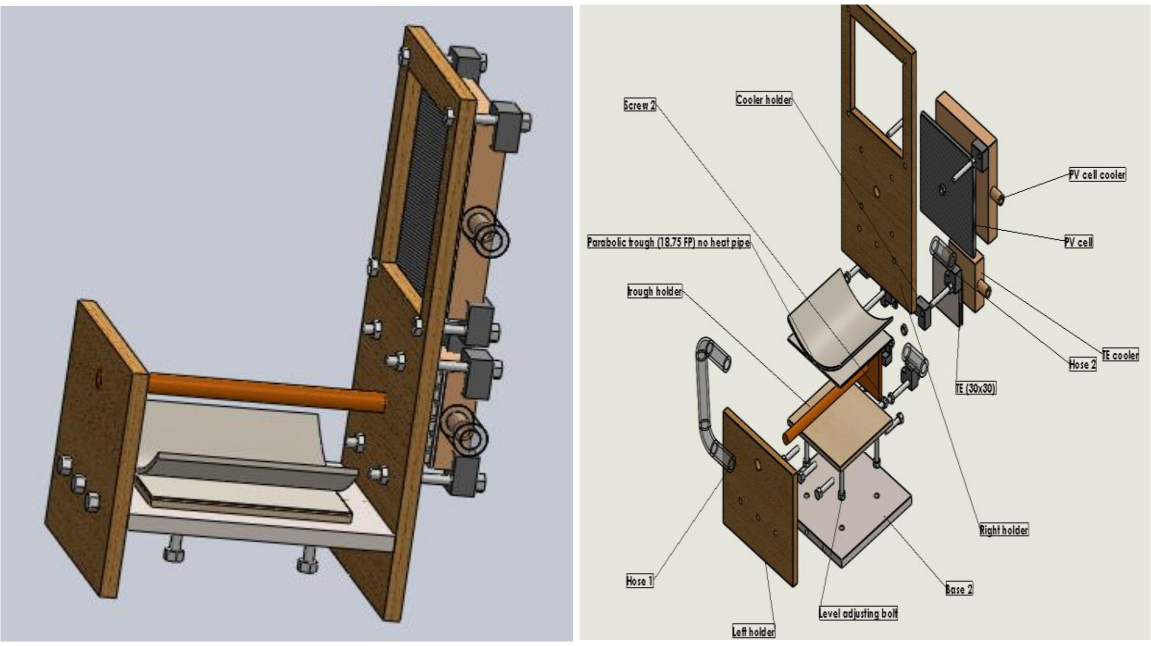
(a) (b)

Figure 3.4: *a) Final design of the trough system and b) assembly drawings.*

The setup was designed to fit into an existing solar simulator testing facility, which has an illumination area of 55 mm x 55 mm. A solid copper rod of 6 mm in diameter and 89 mm long (data sheet in Appendix 3.3) is placed in the focal line of the trough, which receives rays reflected from the parabolic trough and converts light into heat. The copper rod has a square end (30 mm x 30 mm x 3 mm) to mount the TEG. A dichroic mirror (not shown in the Figure) is placed above the parabolic trough mirror at a 45 degree angle, which reflects the visible light (below 725 nm) to a PV cell held vertically behind a window and transmits the infrared radiation onto the parabolic trough concentrator.

3.3.1.2 Simulation Studies

To identify and verify the best design for a trough hybrid system, the thermal performance of the trough systems was investigated using SolidWorks simulation and the optical performance was investigated using TracePro ray tracing software.

3.3.1.2.1 Trough Concentrator

The trough system design aims to reduce the thermal absorber surface area to minimise the heat loss from the thermal absorber to the environment (as shown in Figure 3.4). To demonstrate the advantage of this design, the thermal performance of a simple thermal absorber without optical concentration was simulated using SolidWorks. The simple absorber is a piece of square copper plate (60 mm x 60 mm x 1 mm), as shown in Figure 3.5, which is placed underneath the dichroic mirror with a TEG attached to its back side.

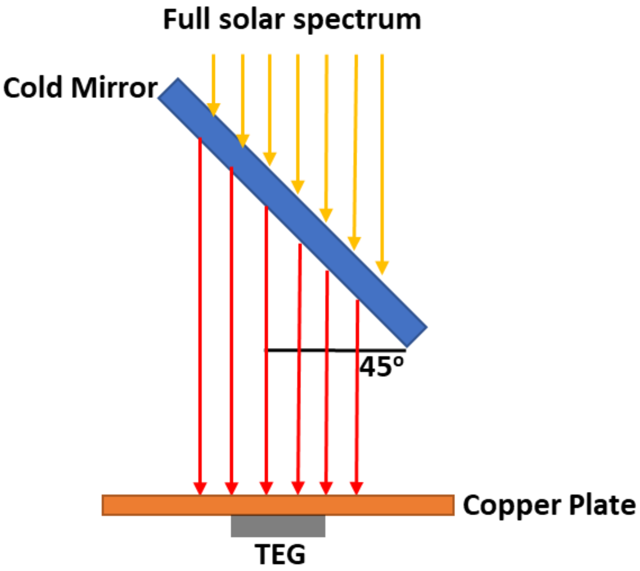

Figure 3.5: *Straight-forward simulated design (copper plate).*

Five TEGs were selected for this study, which are commercially available thermoelectric modules. Their geometries are given in Table 3.2.

Table 3.2: *Dimensions of the commercial thermoelectric modules that were selected for this study.*

Module	Size (mm)	Thickness (mm)
1	30x30	4.0
2	20X20	2.8
3	15X15	3.3
4	9x9	3.8
5	6x6	3.8

The purpose of this simulation is to predict the steady-state temperature of a copper plate that is illuminated by a solar irradiance of 1000 W/m^2. The hot side of the TEG is attached to the copper plate, while the cold side of the TEG is maintained at 12 ^{o}C by a water cooler. Figure 3.6 shows the simulation results for all the TEGs.

6x6

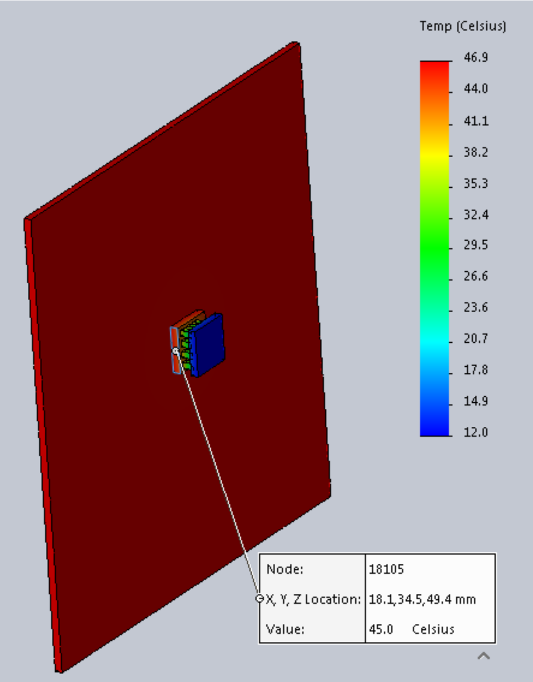

Node: 18105
X, Y, Z Location: 18.1,34.5,49.4 mm
Value: 45.0 Celsius

9x9

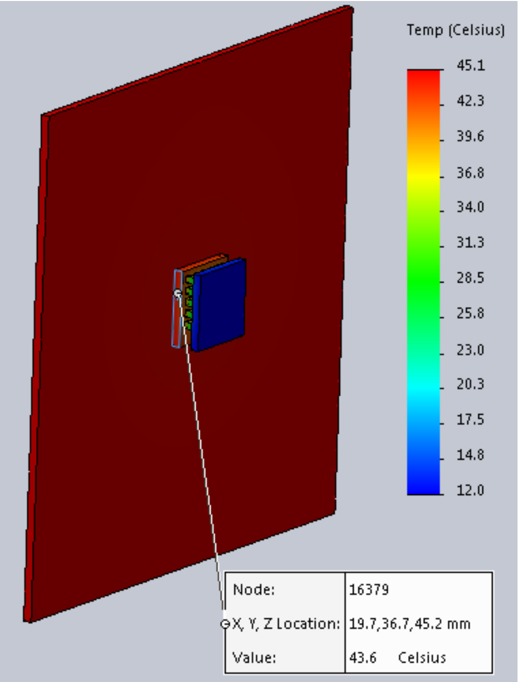

Node: 16379
X, Y, Z Location: 19.7,36.7,45.2 mm
Value: 43.6 Celsius

15x15

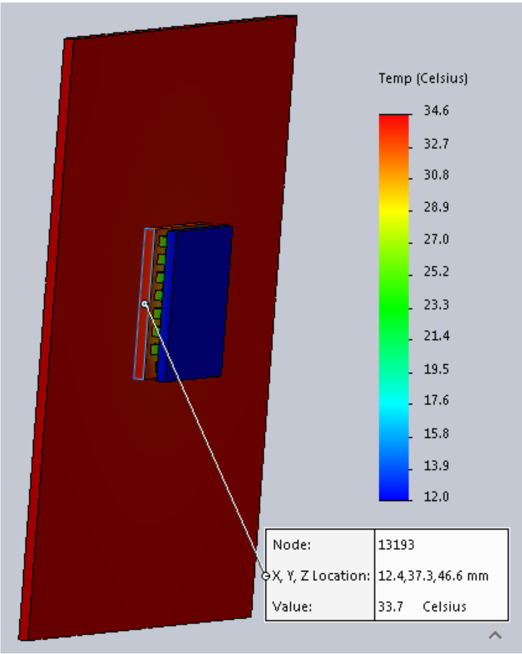

Node: 13193
X, Y, Z Location: 12.4,37.3,46.6 mm
Value: 33.7 Celsius

20x20

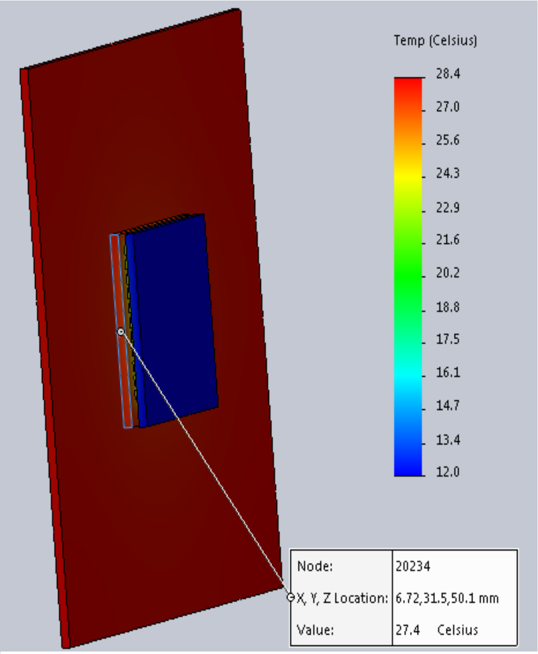

Node: 20234
X, Y, Z Location: 6.72,31.5,50.1 mm
Value: 27.4 Celsius

30x30

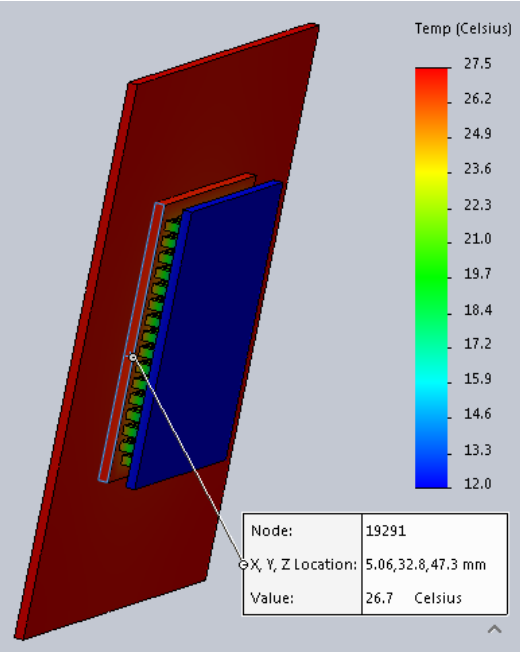

Node: 19291
X, Y, Z Location: 5.06,32.8,47.3 mm
Value: 26.7 Celsius

Figure 3.6: *Steady-state temperature of copper plates simulated with SolidWorks thermal simulation.*

The trough design is also simulated to predict the steady-state temperature of the absorber while the TEG is attached to the absorber and the copper rod is illuminated by 1000 W/m^2. This simulation aimed to find the ΔT across the TEG in both designs for comparison. Figure 3.7 shows the temperature difference (ΔT) across the TEG obtained from SolidWorks simulation for both designs. The simulation results show the trough design ΔT across the TEG is higher by 35%, 29%, 38%, 18% and 18% for module 6x6, 9x9, 15x15, 20x20 and 30x30, respectively. The higher ΔT that was achieved by the trough design can be explained by the difference in the absorber's surface area between the two designs, and hence less heat loss to the environment by convection and radiation. The absorber surface area for the trough design is 53% less when compared to the plate design. This can justify the use of the trough/dish concentrators—even though they add complexity to the design, they will result in heat loss reduction and hence a higher system power output. More details of this study are available in Appendix 3.1.

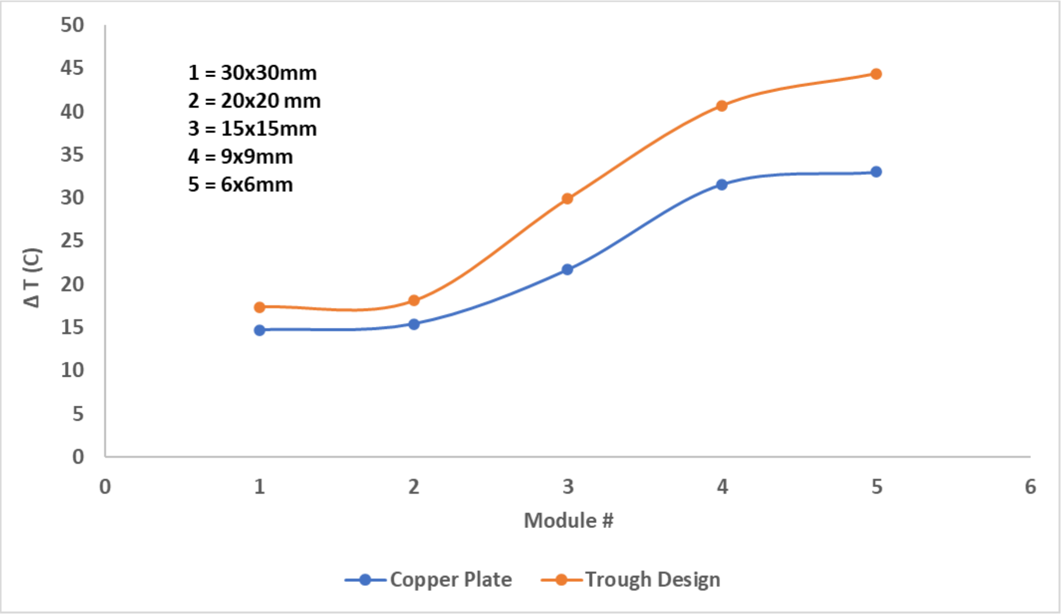

Figure 3.7: *Simulated ΔT obtained by trough design and copper plate design for all modules.*

3.3.1.2.2 Thermal Absorber End Size

Because this study involved the use of different sized TEG modules, changing the size of the square end of the absorber to match the TEG's effective area was studied to verify that fixing the size of the square end will not lead to significant heat loss and reduction in power output. Solidworks thermal simulation was conducted to predict the steady-state temperature of absorbers with different square end sizes. The results obtained were compared with the trough design results that were obtained for all of modules. Figure 3.8 compares the simulation results of a TEG module (15x15mm) for fixed and variable absorber sizes. Figure 3.9 compares the ΔT result for both cases (fixed and variable) for all five modules. It is clear from Figure 3.9 that only the small modules (6x6mm and 9x9mm) have a significant difference in delta temperature across the TEG sides, and therefore the fixed size absorber is incorporated into both hybrid designs.

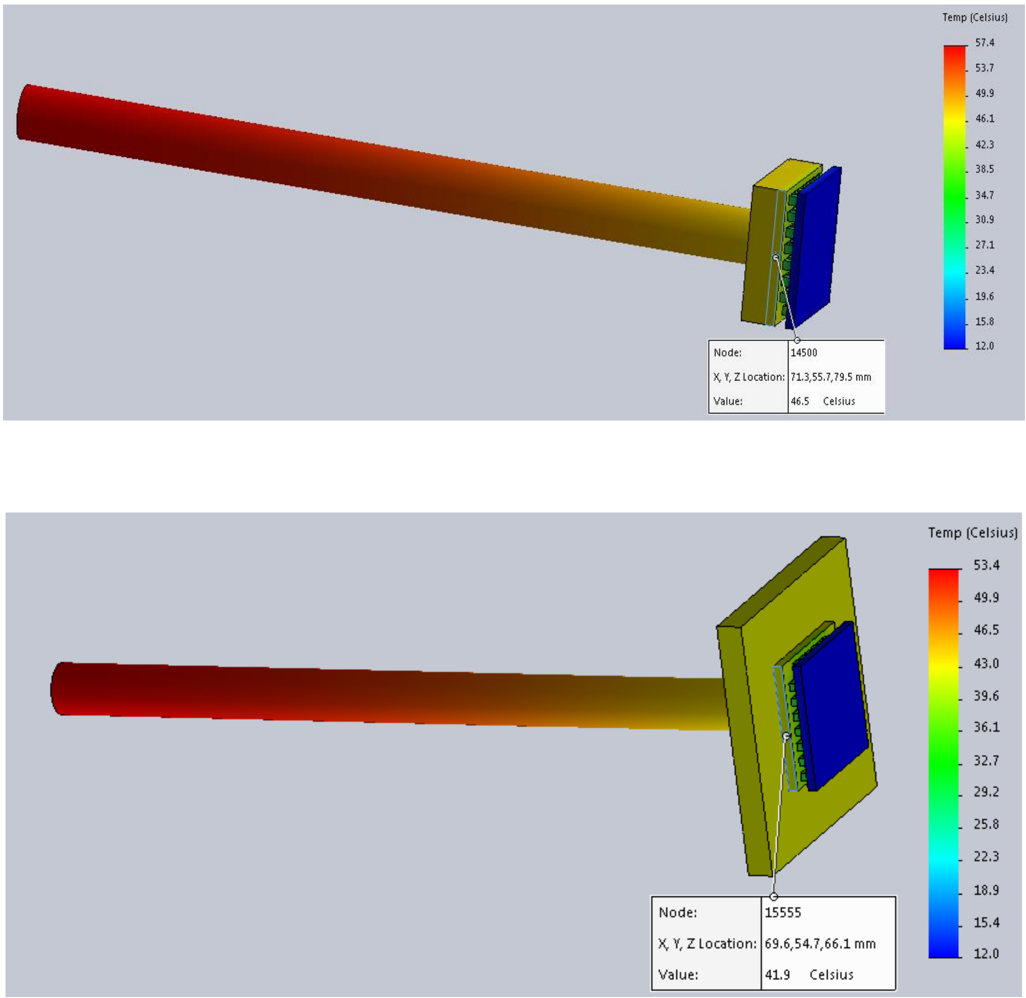

Figure 3.8: *Simulated fixed absorber vs. variable absorber for TEGs (15x15mm).*

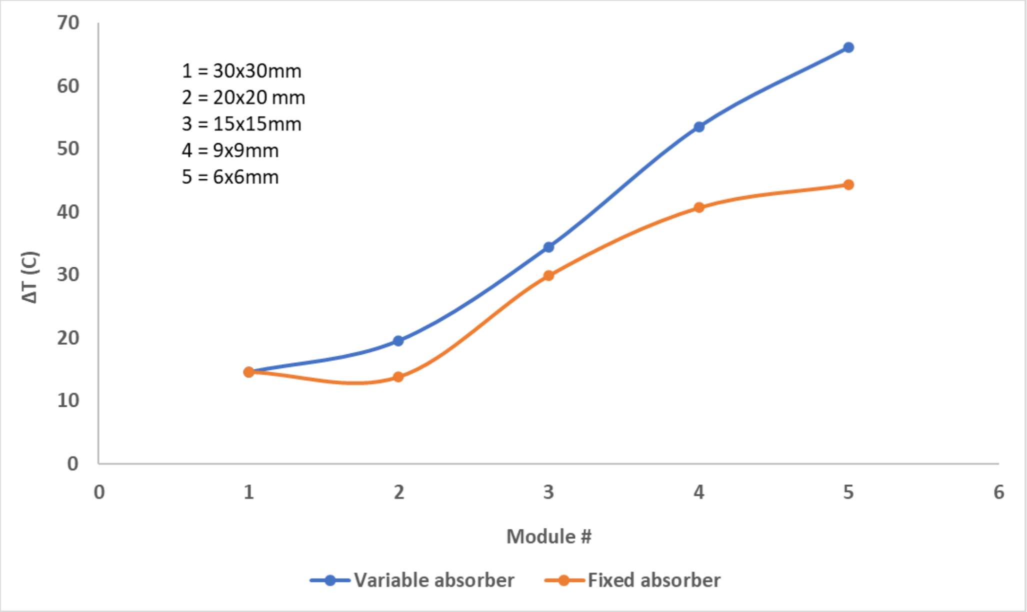

Figure 3.9: *Delta temperature across the five TEGs attached to absorbers with variable and fixed sizes.*

3.3.1.2.3 Optimum Diameter for the Copper Rod

The trough design minimises the copper absorber surface to reduce heat loss to the environment by convection and radiation. Therefore, the copper rod diameter is optimised to find the suitable copper rod diameter that has the minimum surface area and at the same time has the capability of receiving all of the reflected rays. A study was carried out using ray tracing software (TracePro) for copper rods with different diameters (i.e., 3, 4, 5, and 6mm). It was found that a copper rod (6mm in diameter) can receive all of the reflected rays within ± 3mm from theoretical focal line in all four directions. Using a rod thinner than this diameter (6mm) will reduce the copper rod's surface area but will be extremely difficult to align correctly in the focal line of the trough to receive all of the reflected rays from the concentrator. Further details of this study are available in Appendix 3.3.

3.3.1.2.4 TracePro Simulation to Verify the Parabolic Trough Design

Eight different designs for the trough curvature (from almost flat to very deep) were selected to find the most suitable design based on the advantages and disadvantages that are given in Table 3.1 and to suit the model design that was described in Section 3.3.1. The eight designs were simulated using TracePro software and the results are shown in Figure 3.10.

Design 1

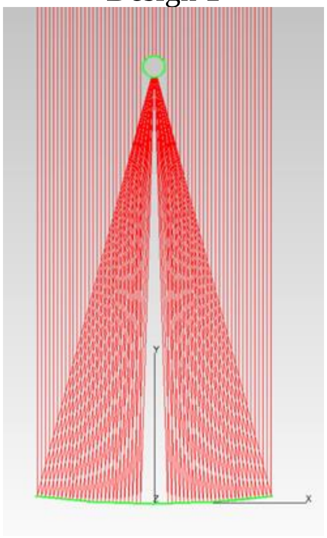

Design 2

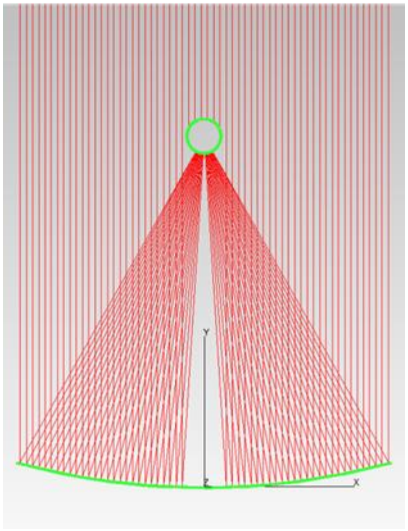

Design3 Design 4

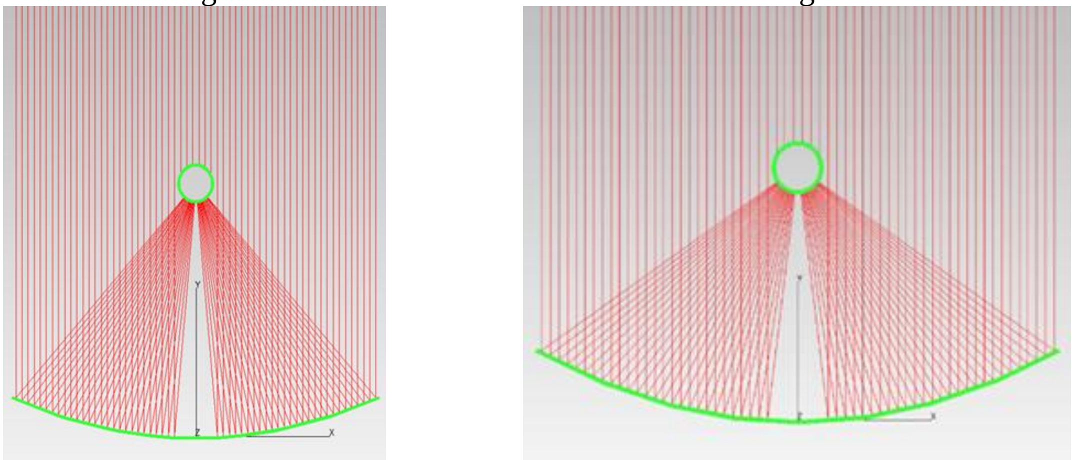

Design 5 Design 6

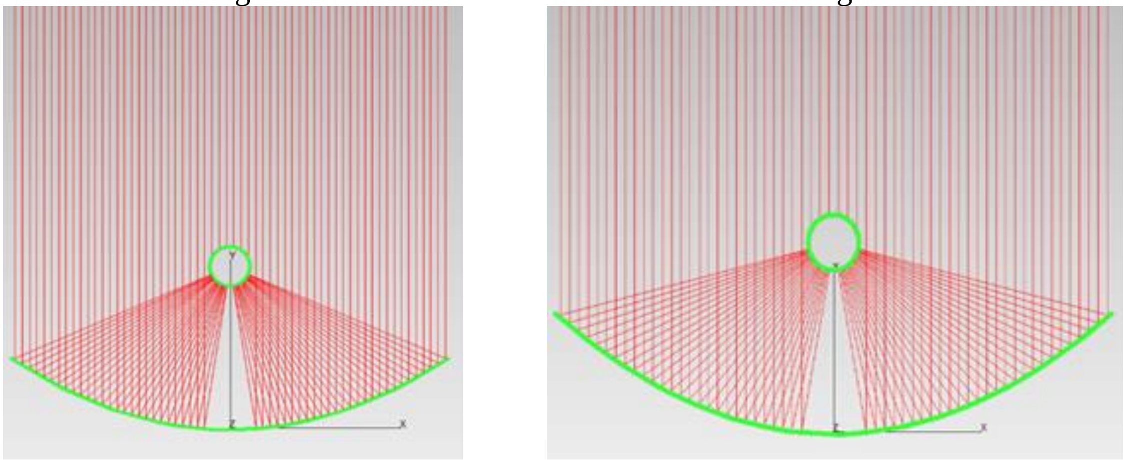

Design 7 Design 8

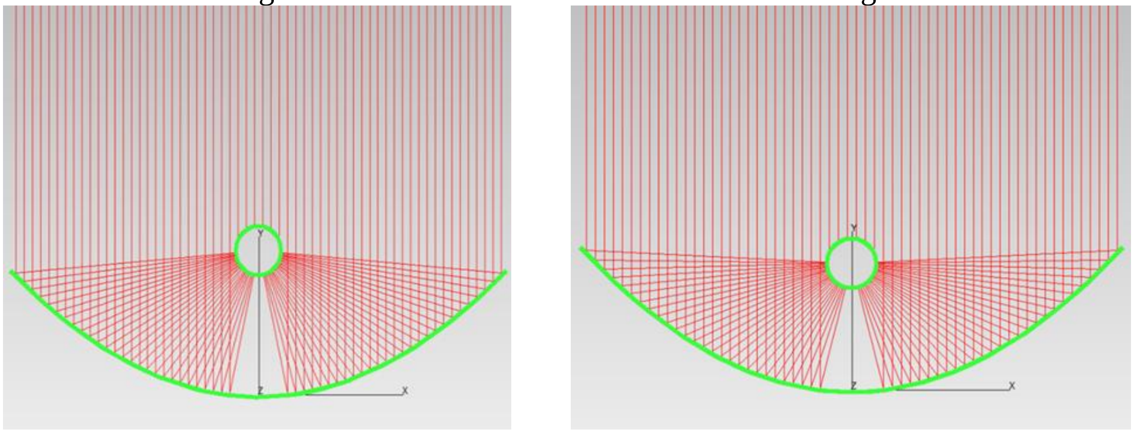

Figure 3.10: *Eight different designs simulated by TracePro.*

The design details of the trough mirror are summarised in Table 3.3.

Table 3.3: *Simulation results for the parabolic trough designs.*

Design		Dimensions (mm)	Trough Depth (mm)	Focal Length (mm)	F/D	Ψ_{rim}	Total Flux (W)	Avg. Flux (W/m^2)	Geometrical Concentration (Cg)	Optical Eff.
Design 1		60 x 60	2	112.5	1.88	15.1	3.0477	8454.8	2.9	0.84576
Design 2		60 x 60	4	56.25	0.94	29.8	3.0477	8454.8	2.9	0.84576
Design 3		60 x 60	6	37.5	0.63	43.3	3.0477	8454.8	2.9	0.84576
Design 4		60 x 60	8	28.13	0.47	56.0	3.0477	8454.8	2.9	0.84576
Design 5		60 x 60	10	22.5	0.38	66.7	3.0477	8454.8	2.9	0.84576
Design 6		60 x 60	12	18.75	0.31	77.8	3.0477	8454.8	2.9	0.84576
Design 7		60 x 60	14	16.07	0.27	85.6	3.0477	8454.8	2.9	0.84576
Design 8	**Upper absorber surface image**	60 x 60	16	14.06	0.23	94.8	0.5821	1616.5	2.9	0.16171
	Lower absorber surface image						2.4656	6838.3		0.68405
	Total						3.0477	8454.8		0.84576

Table 3.1 shows that deeper dishes have the advantage of slower wind speed around the receiver, leading to less heat loss to environment; however, the wind load will be high around its curvature. In contrast, shallow dishes have less load around their curvature but the wind speed around the receiver will be high, and hence there will be more heat loss to the environment. Based on this, Designs 1–4 can be eliminated due to their long focal lengths and Designs 7 and 8 can be eliminated due to their very short focal lengths. Consequently, the comparison will focus on Designs 5 and 6, the latter will eventually be selected because it has a reasonable focal length.

3.3.1.3 Trough System Construction

The trough system setup (see Figure 3.3) was designed to maintain the main components of the hybrid system in place and fixed firmly under the solar simulator to accurately run all of the measurements. The main components of the hybrid system are described in the following subsections.

3.3.1.3.1 Parabolic Trough Concentrator

SolidWorks software was used to design the parabolic trough based on Equation 3.1. The equation was implemented in the equation section of SolidWorks, as shown in Figure 3.11, with f = 18.75 mm specified in Design 6 in Table 3.3. The aperture of the trough is set to 60mm to suit the illumination area of the solar simulator.

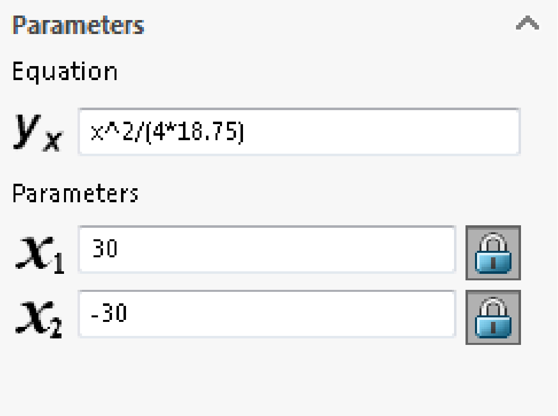

y_x: x^2/(4*18.75)

x_1: 30

x_2: -30

Figure 3.11: *Parabola parameter entry in SolidWorks.*

To make the trough rigid and easy to handle, the parabola was given a thickness of 2mm. The parabola was extruded using “Extruded Boss/Base” feature in SolidWorks. The resulting parabolic trough is shown in Figure 3.12.

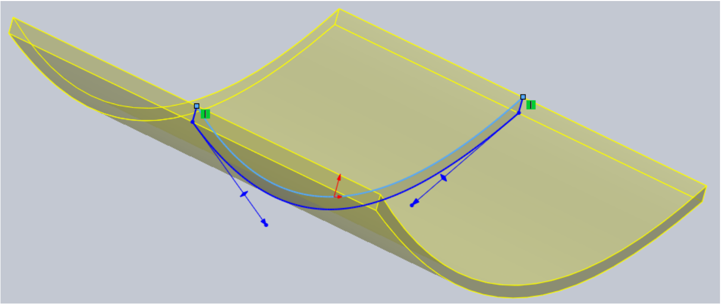

***Figure 3.12**: The trough after extruding to the required trough length using extruding feature in SolidWorks.*

The completed trough design in SolidWorks should be saved in STL format to enable it to be printed on a 3D printer. However, the file should first be sliced by “CURA” software (software used by Ultimaker 3D printers). This software can be downloaded free of charge from the Ultimaker website. After slicing the STL file with the software, a g-code file is generated and saved on an SD card to transfer the g-code file to the 3D printer. Figure 3.13 shows the 3D printer that was used for the parabolic trough printing.

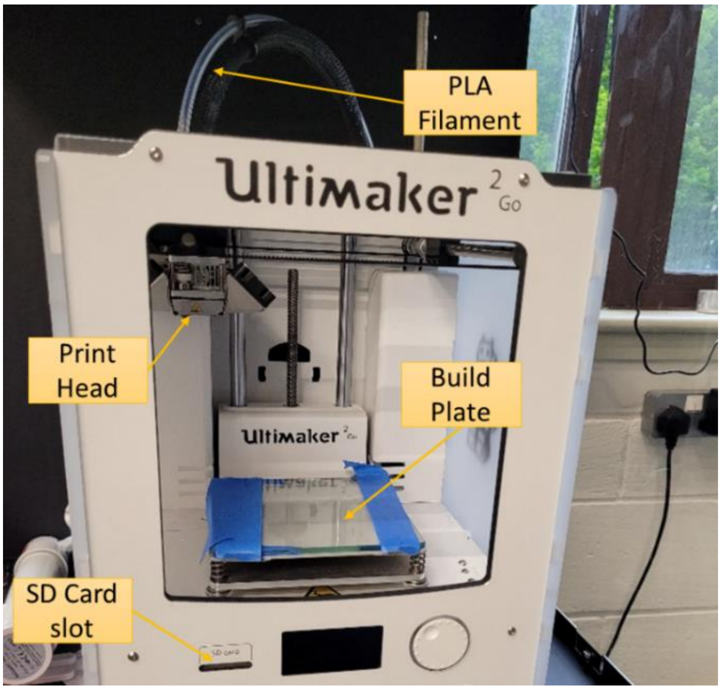

***Figure 3.13:** Ultimaker 2 GO 3D printer that was used to print the parabolic trough.*

This printer uses polylactic acid (PLA) as a filament for printing the desired objects. PLA is a biodegradable polymer that has a good surface quality and prints details with a high resolution [136]. Figure 3.14 shows the printed trough.

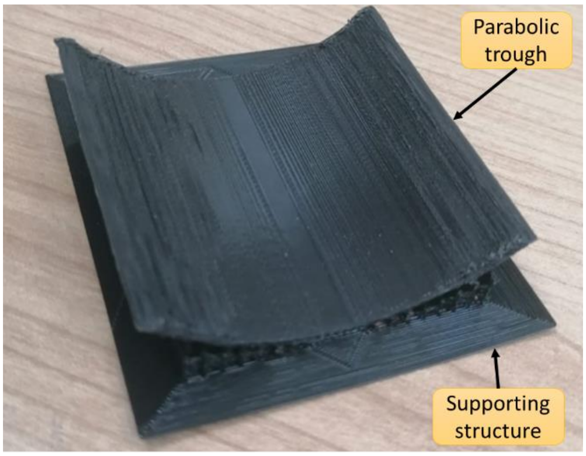

Figure 3.14: *Parabolic trough printed using the Ultimaker 2 3D printer.*

Alanod MIRO high-reflection sheet (reflectivity of 0.95) was used to cover the interior of the trough (data sheet available in Appendix 3.4). Super glue was used to fix the reflector in place, as shown in Figure 3.15.

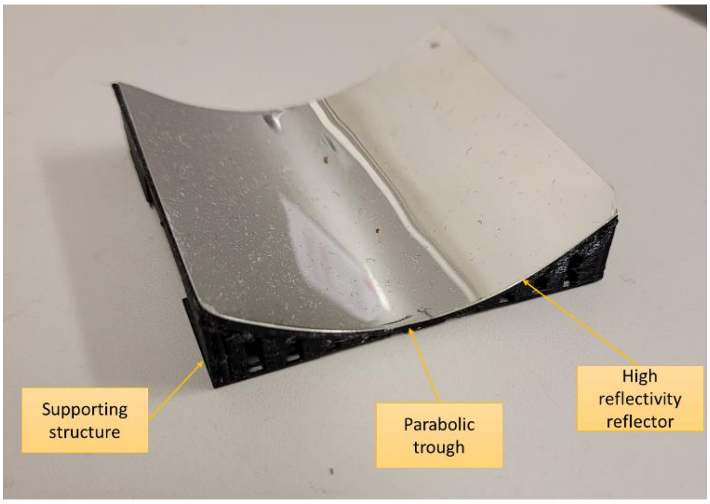

Figure 3.15: *High reflectivity reflector fixed on the inner surface of the parabolic trough.*

All of the components of the trough design (e.g., the copper absorber, left/right holders, the base, and the cooling system) were designed using SolidWorks and handed to the university workshop for manufacturing. The complete trough hybrid system is shown in Figure 3.16.

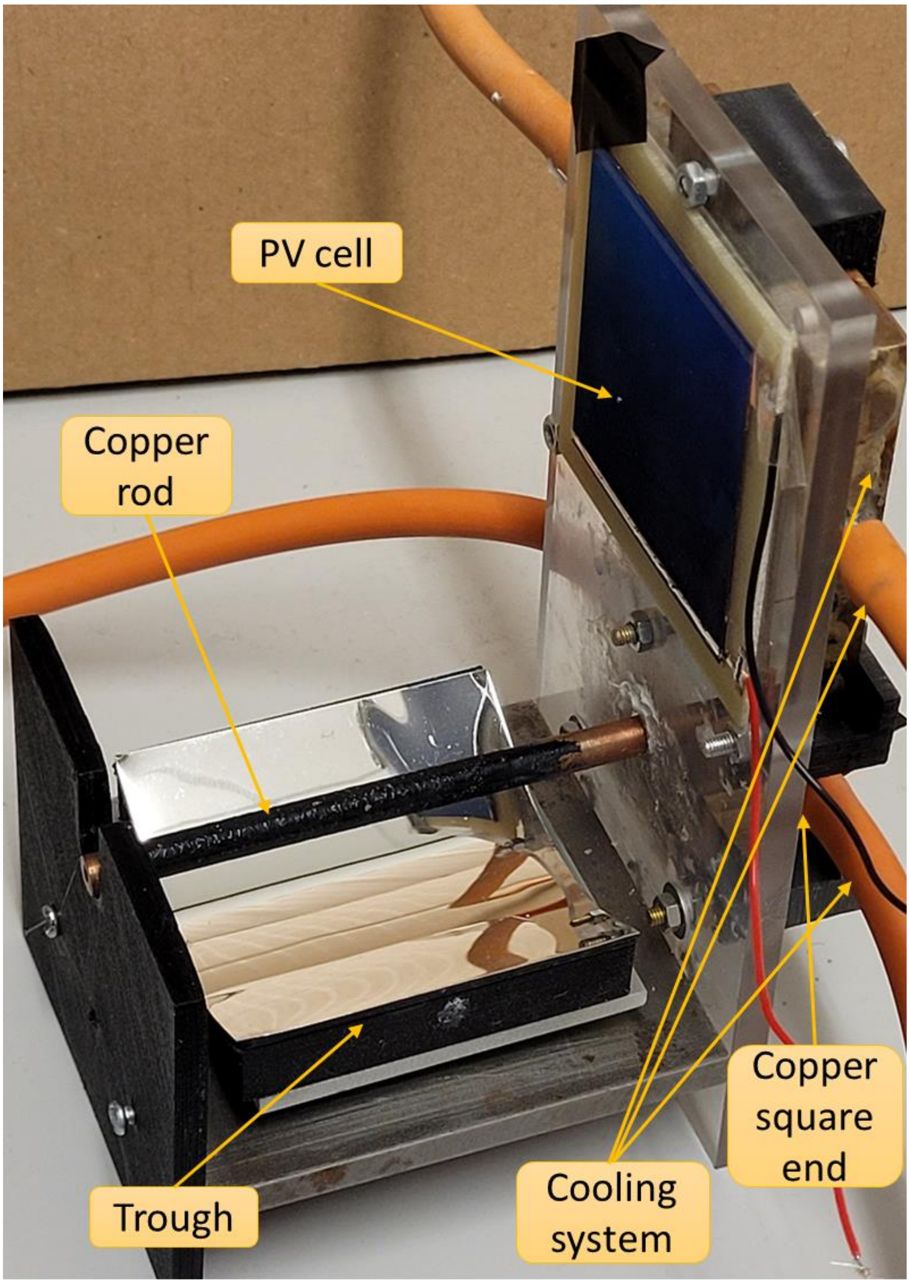

Figure 3.16: *Completed setup of the hybrid trough system.*

3.3.2 Dish Hybrid System

The dish design is very similar to the trough design, except that the mirror is a parabolic dish, and the copper rod is shorter. The parabolic dish is a point focussing concentrator, which implies vertical alignment of the copper rod (as can be seen in Figure 3.17).

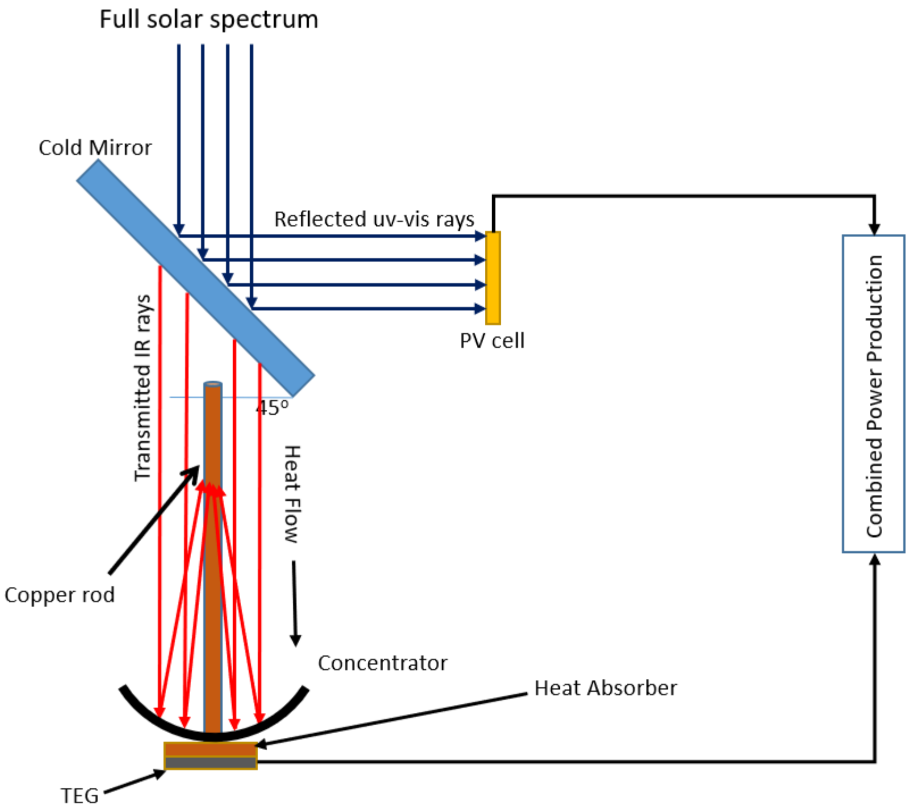

Figure 3.17: *Schematic of the experimental setup of the dish design.*

The dish concentrator in this hybrid system is illuminated under a solar simulator with a square illumination area of 55x55mm. The minimum dish diameter that occupies this illumination area is 85.5mm, and therefore a dish with a diameter of this size was designed in SolidWorks. The second part of the dish setup that is different from the trough setup is the copper rod, which is much shorter (30% shorter). The absorber is placed vertical to the dish concentrator to receive reflected rays at the dish's focal point with minimum length. The copper rod has a diameter of 6 mm, and it is 62 mm long. The squared end of the absorber has the same dimensions as the trough design (30x30x3 mm). A dichroic mirror is placed at an inclination of 45^o and is in the way of falling rays of the solar simulator. As in the trough design, the PV cell receives the suitable band of the spectrum, and the rest of the spectrum (IR) is transmitted by the mirror to the dish concentrator.

A thermoelectric generator (TEG) is sandwiched between the square copper end and a water cooler. The TEG's generated power is combined with the power generated from the solar cell to represent the hybrid system total generated power, as illustrated in Figure 3.17.

3.3.2.1 Parabolic Dish Design

Given that reducing the copper rod's length is preferable to reducing its surface area, and hence provides more heat to the TEG (as will be detailed in Chapter 5), a shorter focal point should be employed (which can also be determined using Equation 3.1). However, it will be difficult to cover a deeper dish with high reflective reflector on the inner surface of the dish. Therefore, a focal point of 18.75 mm was selected in the design of the parabolic dish. The copper rod was designed in the same way as the trough system and a tolerance of 10 mm above the focal point was given to ensure that it received all of the reflected rays. The components of the dish hybrid system were designed using SolidWorks. Detailed drawings with all measurements were prepared for construction by the university's mechanical workshop. Figure 3.18 shows the final design of the dish system and the assembly drawings.

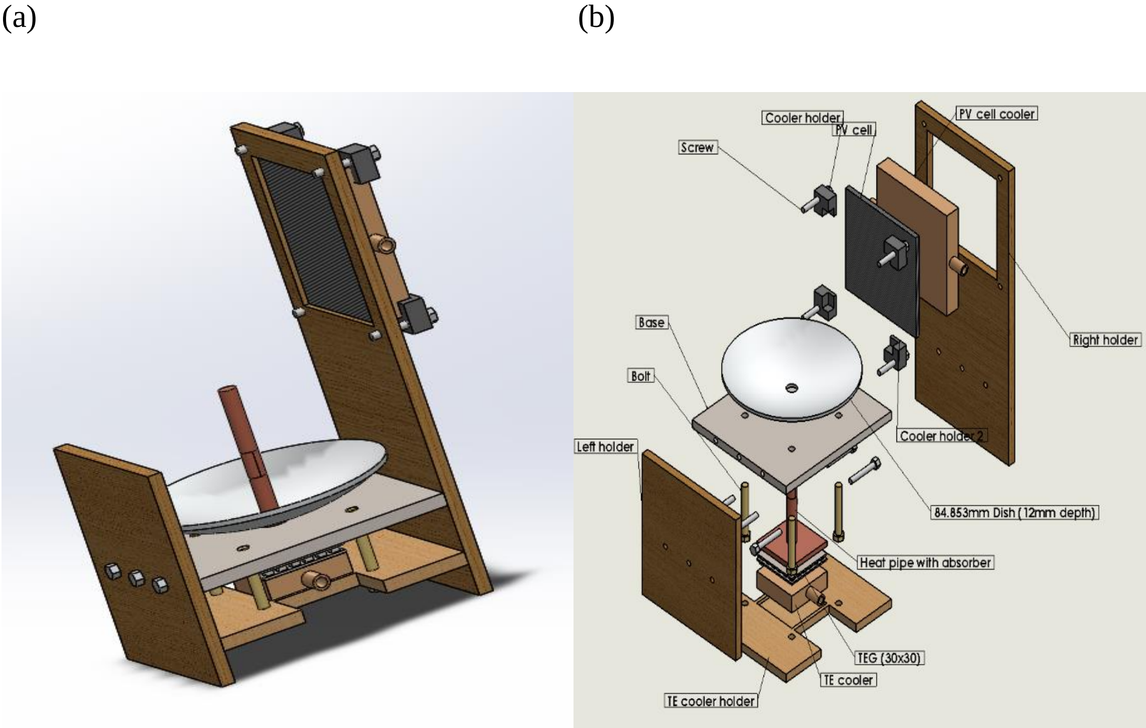

__Figure 3.18:__ a) Final design of the dish system and b) assembly drawings.

3.3.2.2 Parabolic Dish Concentrator

Once the dish concentrator has been designed with a diameter of 85.5mm using SolidWorks software, the design file is imported by CURA software for slicing. The generated g-code file was then transferred to the Ultimaker 3D printer via a SD card for printing. Figure 3.19 shows the parabolic dish that was printed using a 3D printer.

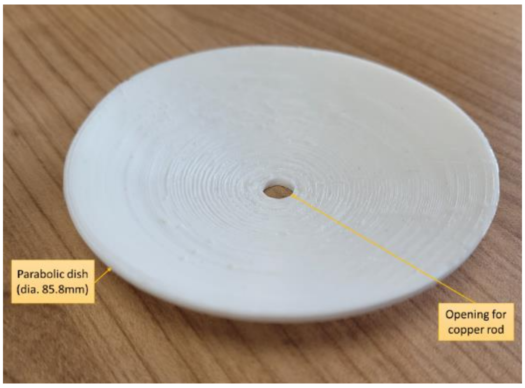

__Figure 3.19:__ Parabolic dish that was printed using a 3D printer.

To cover the inner surface of the dish with Alanod MIRO high-reflection sheet, the sheet had to be cut into several pieces. Unlike the parabolic trough, a smooth dish reflective surface cannot be formed using a single flat piece. A trial to cover the dish with four pieces (pizza shape) was first tested. However, experimental measurement of the copper absorber's steady state temperature using the fabricated dish with four pieces reflector showed unsatisfactory results. This happens because of the inaccuracy of the alignment of reflector pieces due to the lack of sophisticated equipment. Inaccuracy of aligning the reflector pieces will diffuse the incident radiation and some reflected radiation will miss the absorber. Other trails with 6, 8, 12 and 16 pieces were tried, but all the results were unsatisfactory.

Figure 3.20 shows all the dishes covered with different numbers of pieces, which were then used in experimental testing.

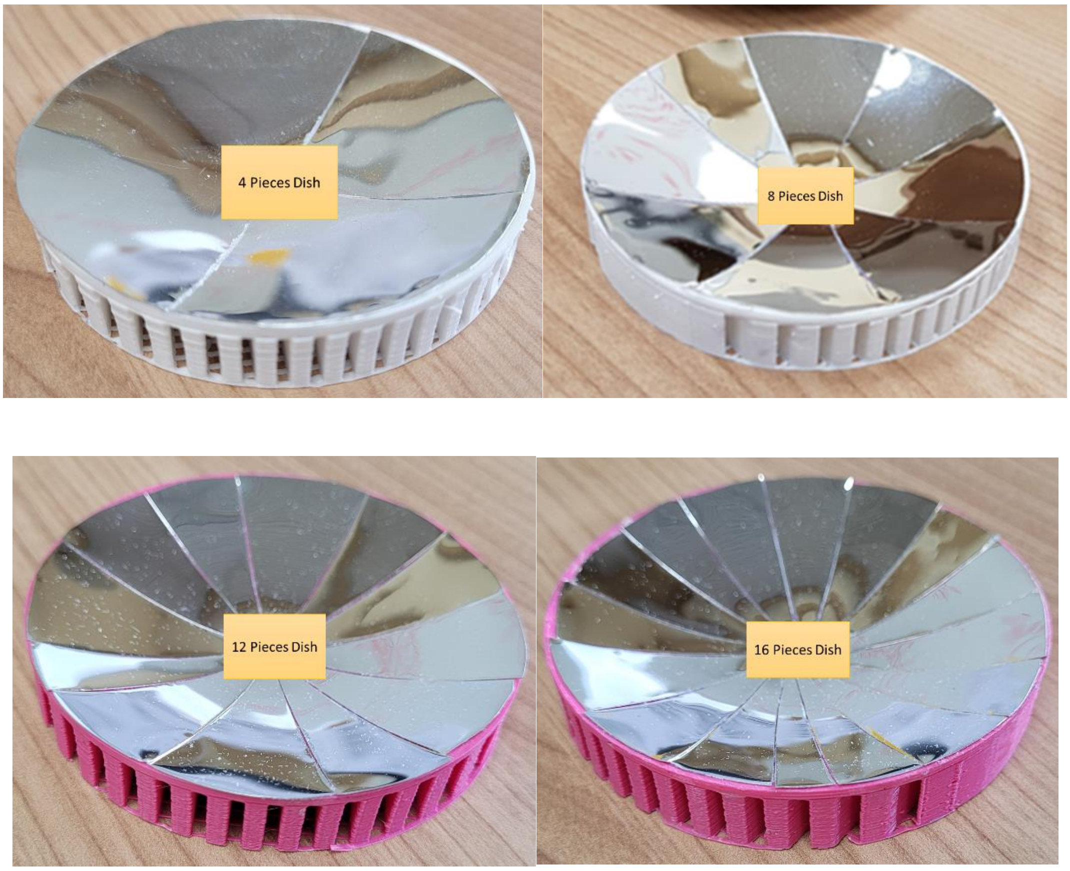

Figure 3.20: *Parabolic dishes covered with different numbers of reflector pieces.*

An alternative approach tried to manufacture the whole dish from a metal material and to mirror polish the inner surface of the dish to give a high reflectivity, which is close to that of the Alanod MIRO high-reflection sheet. This will give a fair comparison with the parabolic trough that was covered with a high reflective sheet.

An aluminium dish was fabricated by Cardiff University's workshop and its inner surface was mirror polished by Almond & Mellor Services Ltd (a specialised company in metal polishing) to increase reflectivity and minimise heat absorption by the dish. Figure 3.21 shows the dish after polishing. The experimental results using the aluminium polished dish were successful and the expected results were obtained, as will be detailed in Chapter 5.

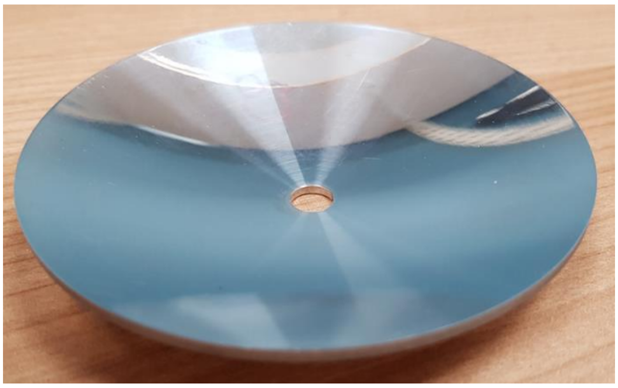

Figure 3.21: *Polished aluminium dish.*

Figure 3.22 shows the complete dish hybrid system after construction by Cardiff University's workshop.

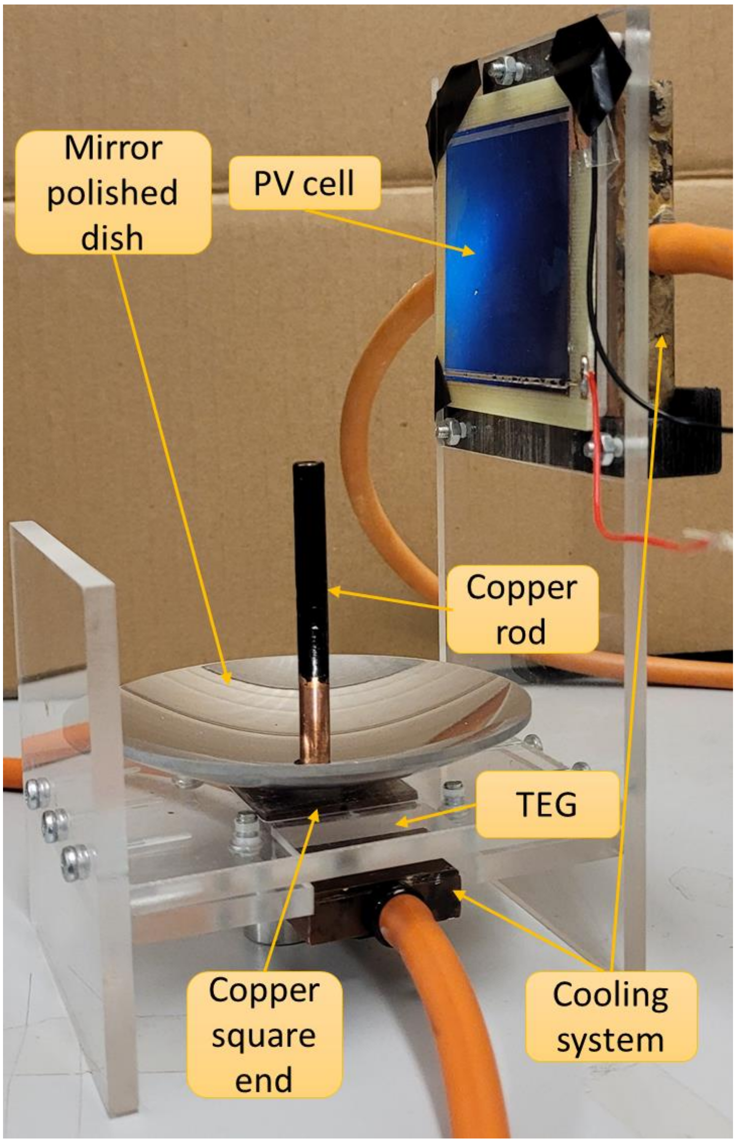

Figure 3.22: *Hybrid dish system complete setup.*

3.4 Experimental Instrumentation

The instrumentation and equipment used in this study are described in this section.

3.4.1 Solar Simulator

The solar simulator at Cardiff University's laboratory was used as a light source to run all the experiments needed for this study. This simulator is manufactured by "Oriel Instruments Newport Corporation (LCS-100 Class ABB)". The solar simulator offers a similar intensity and spectral irradiance to sunlight. The simulator generates 1 sun (1000 W/m^2) irradiance with an AM1.5G filter at a distance of 7.0 inches (178mm). As the lamp ages, the distance needs to be reduced to maintain 1 sun irradiance. The certified illumination area of the simulator is 1.5 inch x 1.5 inch (38mm x 38mm), which meets Class ABB as defined by the ASTM and IEC standards.

The spectral irradiance of LCS-100 Solar Simulator (taken from the simulator manual [137]) is plotted against the ASTM reference spectrum (AM1.5G) [138] in Figure 3.23.

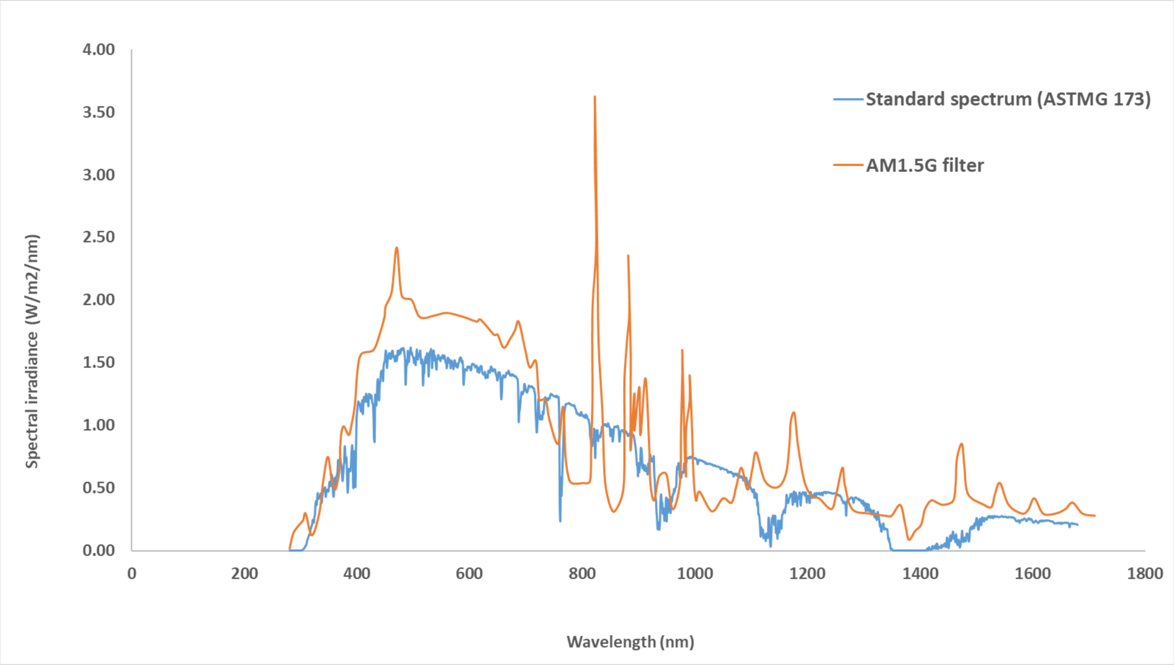

Figure 3.23: *Spectral irradiance of the reference solar spectrum (AM1.5G) and the solar simulator (LCS-100).*

It can be seen from this figure that there is a reasonable match between the spectrum generated by the solar simulator and ASTM AM1.5G standard reference spectrum.

The simulator used in this study is placed in a Faraday cage to eliminate any interference of light or any electromagnetic fields that may affect the accuracy of measurements. Figure 3.24 shows the instrumentation and equipment used in the measurements.

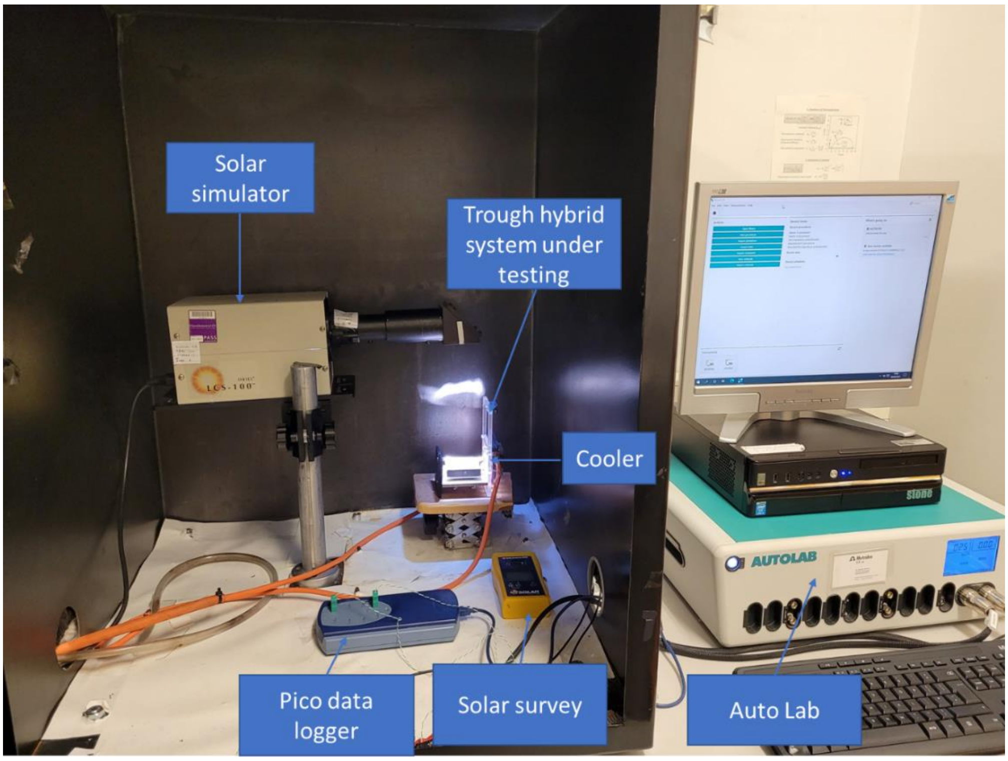

Figure 3.24: *Instrumentation and equipment used for measurements in this study.*

The solar simulator that was used in this study is guaranteed by the manufacturer to have a uniform illumination area of 40 mm x 40 mm. However, the illumination area of both the trough and dish concentrators of this study is 55 mm x 55 mm. Therefore, uniformity of the solar simulator over this area had to be determined. For this purpose, the illuminated area (55x55mm) was divided into nine equal squares (18.3 mm each) and irradiance intensity was measured using the "Solar Survey" (a calibrated portable device for measuring solar irradiance). The Solar Survey was first placed in the central square (Figure 3.25) to ensure that the measured intensity is 1000 W/m^2 and it was then moved to the other eight squares for irradiance measurements.

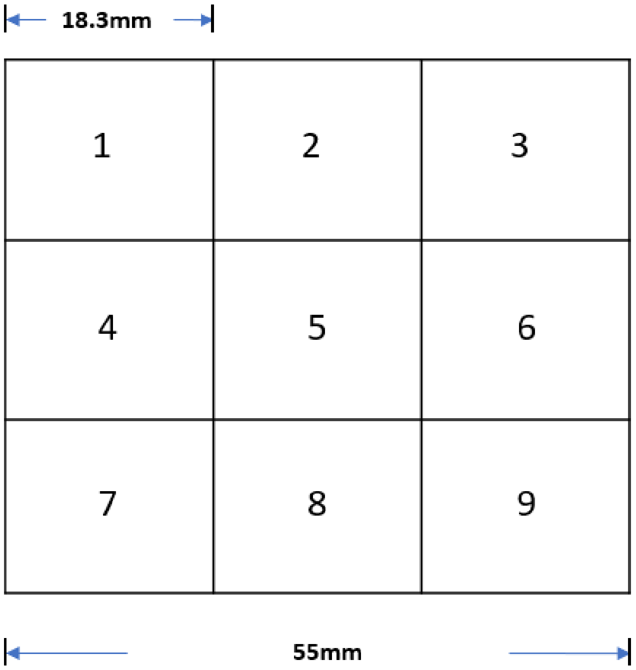

Figure 3.25: *Solar simulator illumination area divided into nine squares for irradiance measurement.*

The measurements were conducted twice. The average values are presented in Figure 3.26.

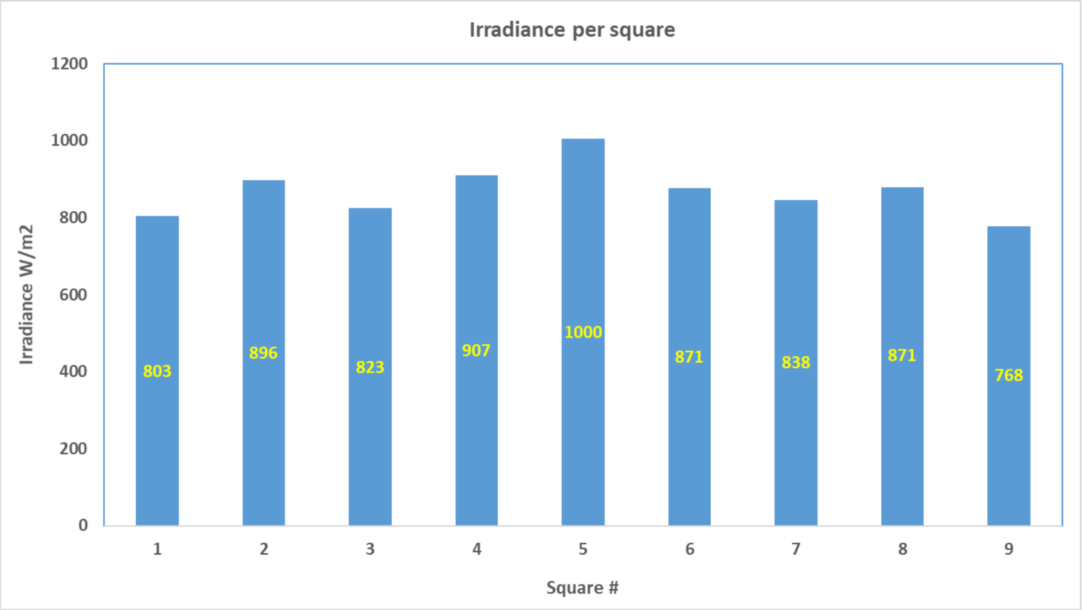

Figure 3.26: *The irradiance measurement results for the nine squares.*

It is clear from Figure 3.26 that the squares relatively far away from the centre (i.e., sq.1,3,7 & 9) have less irradiance power than those relatively close to the centre (i.e., sq. 2,4,6 &8). The average irradiance over the area of 55 mm x 55 mm is 864 W/m^2, which will be considered in the theoretical calculations in this study.

3.4.2 Autolab System

“Autolab” is an electrochemical measurement system manufactured by “Metrohm” (as shown in Figure 3.24). The system is equipped with “NOVA” software to determine the I-V and P-V curves for the PV cells and TEG modules. Combined with the solar simulator, this is an important measurement facility in this research. Many important parameters for characterisation of the devices (i.e., the PV cell and TEG) can be determined from the I-V curves, such as short-circuit current (I_{SC}), open-circuit voltage (V_{OC}), fill factor (FF) and efficiency [139].

3.4.3 Thermocouple Data Logger

The temperature measurements and recording in this study are carried out using thermocouples and a data logger, which are connected and controlled by a computer to monitor and record the temperatures. The components that are used in this study are shown in Figure 3.27. The thermocouples used in temperature measurements are K-type thermocouples supplied by RS Components. The data logger (T-08) for data acquisition is purchased from “Pico technology”, which has eight channels for thermocouples that can be measured simultaneously. The data logger has a measurement range from −270 °C to +1820 °C and it can maintain more than 0.025 °C resolution over a range of −250 °C to +1370 °C. In addition, the data logger has a fast-sampling rate that can take up to 10 measurements per second.

Figure 3.27: *Temperature measurement, monitoring and recording sequence.*

3.5 PV Cell Characterisation and Parameters

PV cells are characterised by measuring their current–voltage (I-V) curves, as shown in Figure 3.28 [140]:

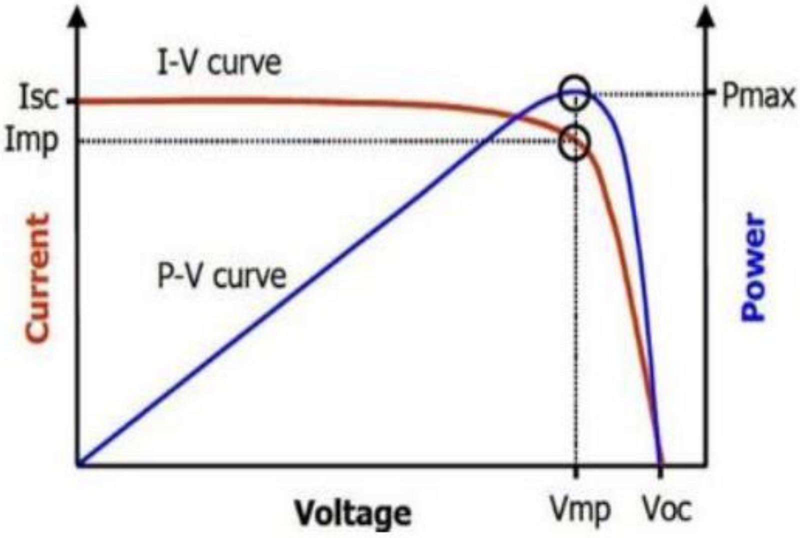

Figure 3.28: *Typical I-V and P-V curves of a solar cell* [140].

The P-V curve is derived from the I-V curve by multiplying the current to the voltage at each point of the curve. The maximum power of the cell is the product of the maximum power point current (**I_{MP}**) and the maximum power output voltage (**V_{MP}**) [141]:

$$P_{max} = I_{mp} V_{mp} \tag{3.3}$$

The power extracted from the solar cell is proportional to the cell's area. The input power to the PV cell is equal to:

$$P_{in} = GA_{pv} \tag{3.4}$$

where **G** is the solar irradiance (W/m^2) and **A_{pv}** is the effective area of the solar cell (m^2). Another important parameter is the filling factor because it is used to evaluate the quality of the cell [142, 143]:

$$FF = \frac{I_{MP} V_{MP}}{I_{sc} V_{oc}} \tag{3.5}$$

where **I_{sc}** is the short-circuit current and **V_{oc}** is the open-circuit voltage. The maximum efficiency of the PV cell can be expressed as [141]:

$$\eta_{pv} = \frac{I_{MP} V_{MP}}{GA_{pv}} \tag{3.6}$$

Three PV cells were tested in this project (i.e., c-Si, GaAs and InGaP). The PV cell that best suits the hybrid system is the InGaP cell (as described earlier). The other two cells were tested for comparison (i.e., c-Si and GaAs). The GaAs cell has a band gap of 1.43 eV, which is equivalent to the energy of a photon with a wavelength of 864 nm, while the Si has a band gap of 1.1 eV, which corresponds to the energy of a photon with a wavelength of 1127nm wavelength.

Monocrystalline silicon (c-Si 10 mm x10 mm) solar cells were procured from “Solar Capture Technologies”. The GaAs and InGaP cells were procured from “Arima Photovoltaic & Optical Corporation” in Taiwan. This company provides a datasheet for single junction GaAs under 1 sun only, as can be seen in Table 3.4. Because no datasheets are available from the manufacturers for the c-Si and InGaP cells, their parameters were obtained from the literature.

Table 3.4: *PV cell parameters from the provider and from the literature.*

	I_{SC} [mA]	V_{OC} [V]	I_{MP} [mA]	V_{MP} [V]	P_{MP} [mW]	FF [%]	Eff. [%]	Ref.
GaAs	27.9	1.0	26.4	0.89	23.5	84.6	23.4	Arima Lab
InGaP	14.4	1.39	13.9	1.249	17.4	86.9	17.4	[144, 145]
C-Si	29.9	0.579	25.1	0.51	13.7	74.0	12.8	[143, 146-149]

These three cells were tested at Cardiff Solar Laboratory under standard test conditions (STCs), where the irradiance is 1000 W/m^2 (one sun), the air mass (AM) is 1.5G, and the temperature is 25 ^{o}C. Prior to testing the solar cells, the solar simulator has to be switched on and warmed up for at least 10 minutes for the lamp to become stable. The Solar Survey instrument is placed in the middle of illumination area to check the light intensity and ensure 1 sun irradiance. The distance between the light source and solar cell testing surface was measured and maintained during testing. Figure 3.29 shows the I-V curves for the three cells tested under STC. The parameters of the solar cells can be obtained from the measured I-V curves. Table 3.5 shows the parameters for the three cells measured at Cardiff Solar Lab. The measurements were conducted 12 times and the values shown in the table are an average of 12 measurements. The results from these two tables show a reasonable agreement considering that both measurements involve different testing conditions, measurement instruments, and soldering of contacts of the solar cells.

Table 3.5: *PV cell parameters from measurements conducted at Cardiff University's laboratory.*

	I_{SC} [mA]	V_{OC} [V]	I_{MP} [mA]	V_{MP} [V]	P_{MP} [mW]	FF [%]	EFF [%]	Ref.
GaAs	25.8	1.0	23.7	0.9	20.3	79.2	20.3	Cardiff Lab
InGaP	12.1	1.4	11.6	1.2	14.1	86.1	14.1	Cardiff Lab
C-Si	29.6	0.58	27.3	0.5	13.1	75.6	13.1	Cardiff Lab

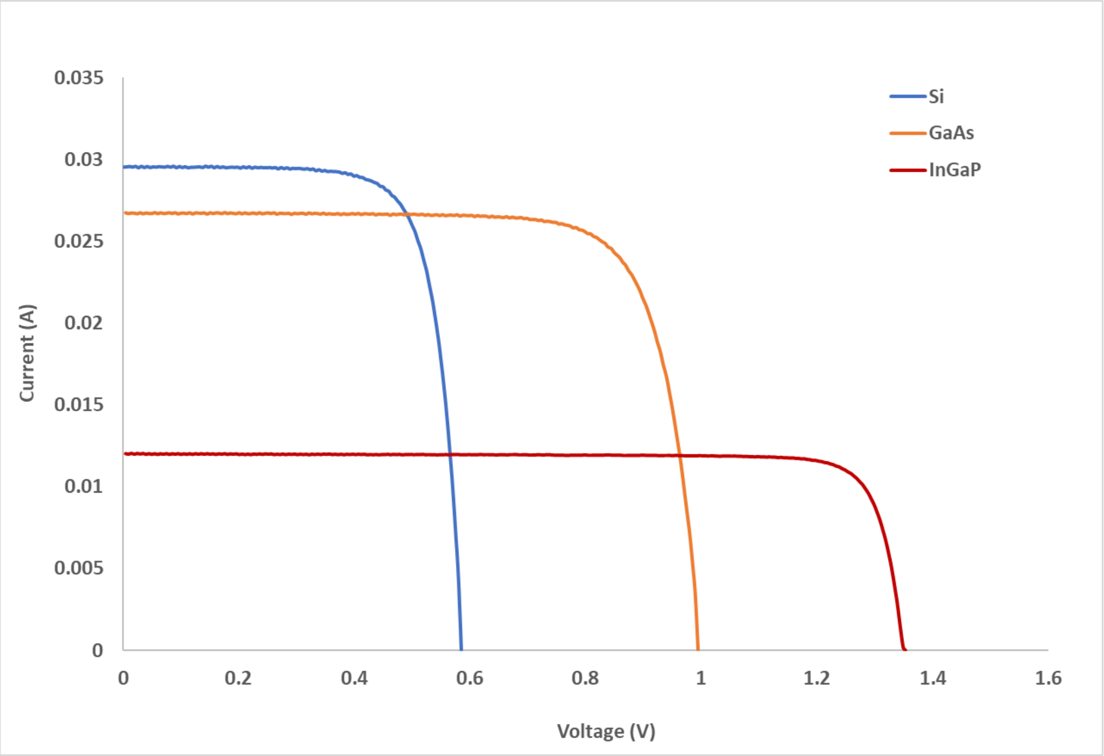

Figure 3.29: *I-V curves for the three PV cells measured under STC.*

3.6 Determining Heat Absorption

This section aims to determine the amount of thermal energy obtained by the thermal absorber from the solar radiation. Figure 3.30 shows a schematic illustration of the energy flow of the system under experiment, where $\mathbf{Q_{in}}$ is the light energy falling onto the surface of the copper rod, $\mathbf{Q_r}$ is the light energy reflected by the copper rod's surface [150, 151], $\mathbf{Q_u}$ is the light energy absorbed (i.e., light energy converted into heat) by the thermal absorber, and $\mathbf{Q_a}$ is the thermal energy retained by the thermal absorber (copper rod).

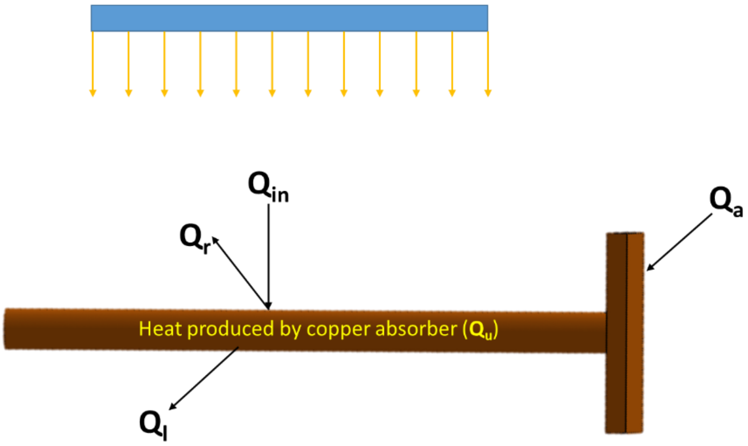

Figure 3.30: Energy flow in the experimental system.

The heat produced ($\mathbf{Q_u}$) is simply the solar irradiance ($\mathbf{Q_{in}}$) minus the heat reflected ($\mathbf{Q_r}$):

$$Q_u = Q_{in} - Q_r \tag{3.7}$$

The heat retained in the absorber (**Q_a**) is the heat produced by the absorber (**Q_u**) minus the heat lost to surroundings (**Q_l**):

$$Q_a = Q_u - Q_l \tag{3.8}$$

The heat lost to the surroundings (**Q_l**) is mainly due to the convection and radiation and depends on the temperature difference between the absorber and ambient temperature. The following equation is used to calculate heat lost by convection and radiation [152]:

$$Q_l = [hA_a(T_h - T_a)] + [\varepsilon\sigma A_a(T_h^4 - T_a^4)] \tag{3.9}$$

where h is the convective heat transfer coefficient, A_a is the area of the absorber, T_h is the temperature of the absorber, T_a is the ambient temperature, ε is the average emissivity of the absorb and σ is a Stefan-Boltzmann constant (5.67 x 10^{-8} W m^{-2} K^{-4}).

At the beginning of the illumination, the increase in the temperature of thermal absorber, and consequently the temperature difference between the thermal absorber and ambient (ΔT), is very small. Hence, **Q_l** can be neglected, and Equation (3.8) can be rewritten as:

$$Q_a \approx Q_u \tag{3.10}$$

The useful heat retained in the copper absorber (**Q_a**) is proportional to the rate of temperature increase according to the following equation:

$$Q_a = m\,C_p\,\frac{\Delta T}{\Delta t} \tag{3.11}$$

where m is the mass of copper and C_p is the specific capacity. By combining Equations (3.10) and (3.11), at the beginning of the illumination, we obtain:

$$Q_u = m\, C_p\, \frac{\Delta T}{\Delta t} \tag{3.12}$$

Given that the mass and specific capacity of the copper are known, and by measuring (Δ T/ Δ t), **Q** can be calculated using Equation (3.12). Figure 3.31 shows the heating curve of the copper absorber after reaching steady state. The inset in the figure shows the curve at the beginning of illumination, where Δ T is quite small, and a linear relationship between Δ T and Δ t is clear. This linearity allows the use of Equation (3.12) to calculate the thermal energy converted from solar radiation in the copper rod by finding the slope of the heating curve at the beginning of illumination (the line in the inset in Figure 3.31). In Chapter 4, this technique will be used to determine the absorbed thermal energy.

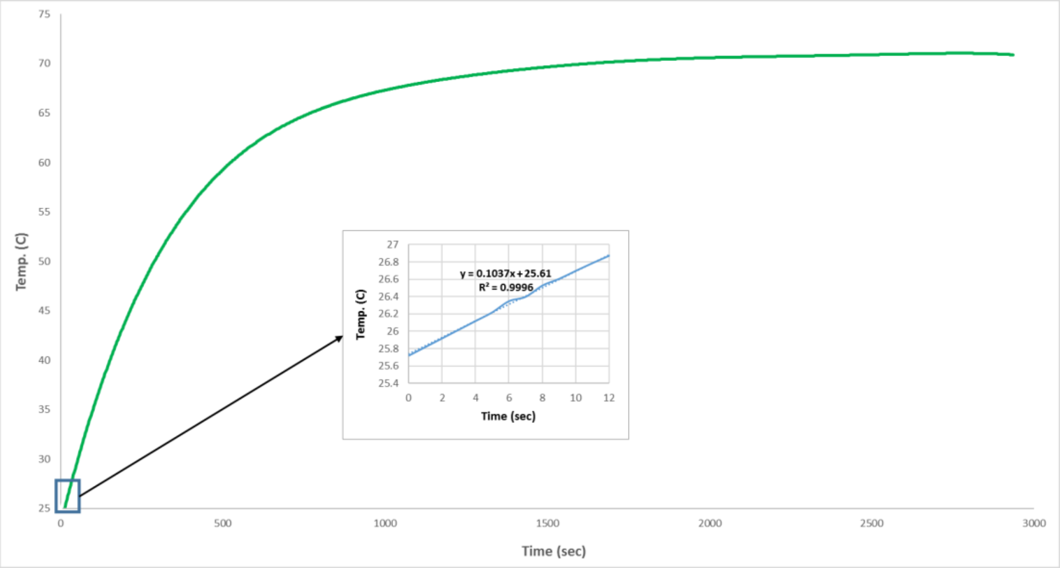

Figure 3.31: *The heating curve of the copper rod and absorber illuminated under solar simulator (1000 W/m^2). The inset shows the slope of the curve at the initial period of illumination.*

The useful heat available for the TEG module (**Q_a**) can be also expressed as (**Q_{TEG}**), which represents the heat used by the TEG to produce electrical power.

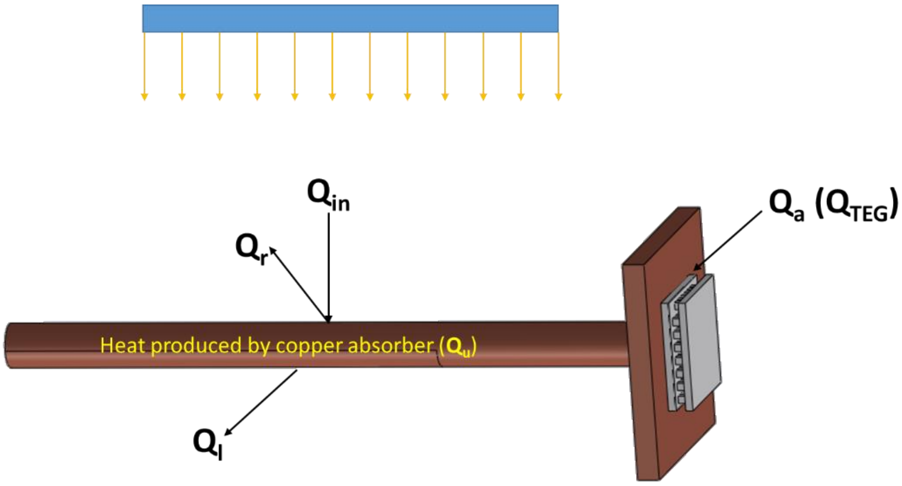

Figure 3.32: *Energy flow in the experimental system with TEG attached*

At the steady state and when a thermoelectric generator is attached to the thermal absorber as shown in Figure 3.32, **Q_u** is balanced with the heat lost to surroundings (**Q_l**). The heat balance equation is given by:

$$Q_u = Q_l + Q_{TEG} \tag{3.13}$$

The heat conducted through the TEG to the cooling water that is in contact with the cold side of the TEG can be expressed as:

$$Q_{TEG} = \frac{kA_{TEG}\,(T_h - T_c)}{L} \tag{3.14}$$

where k is the thermal conductivity of the thermoelectric material, A_{TEG} is the total cross-sectional area of the thermoelements, T_c is the temperature of the cooling water, and L is the length of the thermoelement. Here, the TEG is assumed to be at open circuit because the ΔT of the TEG is different at closed circuit due to the Peltier effect.

Using Equations (3.09) and (3.14), Equation (3.13) can now be expressed as:

$$Q_u = [hA_a(T_h - T_a)] + [\varepsilon\sigma A_a(T_h^4 - T_a^4)] + \frac{kA_{TEG}(T_h - T_c)}{L} \tag{3.15}$$

Because **Q_u** can be determined from the slope technique (which was described earlier), the other parameters are known from the literature, including the convective heat transfer coefficient (h), the emissivity (ε) and the thermal conductivity of thermoelement material (Bi_2Te_3) [153-156]. The ambient temperature and cold side temperature of the TEG are known from experiments. The TEG hot side temperature can be calculated from Equation 3.15. The area of the absorber (A_a) is determined by measurement and the length of the thermoelement of the modules is obtained from the data sheet. This equation will be used in Chapter Four to optimise the geometry of the TEGs that are used in this study.

3.7 Power Generated by TEG Modules

Due to the Seebeck effect, a thermoelectric generator (Figure 3.33) can convert heat into electricity if there is a temperature difference across it. The voltage generated due to the applied temperature difference can be calculated using [157]:

$$V = \alpha\Delta T \tag{3.16}$$

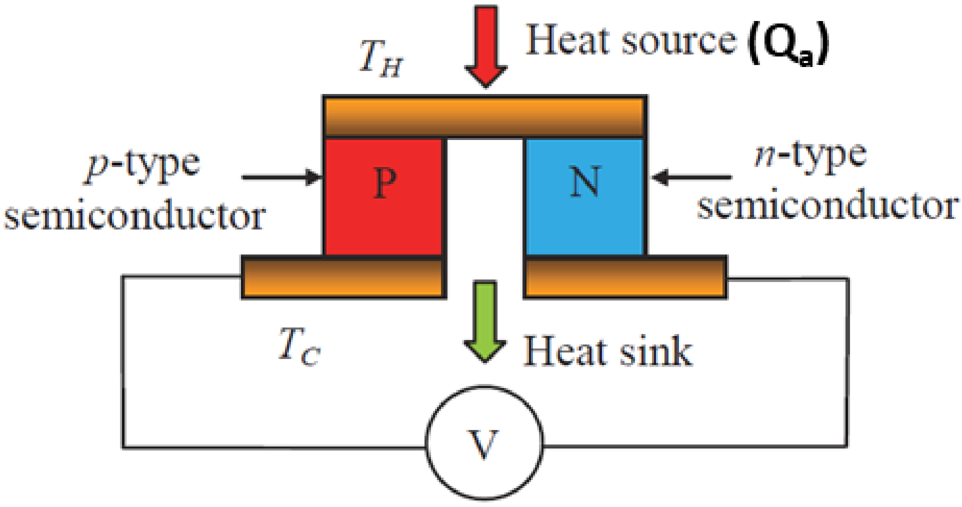

Figure 3.33: *Typical thermoelectric generator.*

where α is Seebeck coefficient and ΔT is the temperature difference between the hot and cold sides of the TE module.

In a steady state, **Q$_a$** is also the heat supplied to the hot side of the TEG, and therefore the conversion efficiency of the TEG can be expressed as:

$$\eta_{TE} = \frac{P_{TE}}{Q_a} \tag{3.17}$$

where P_{TE} is the power output generated by the TEG. Based on the TEG theory [30, 31], the heat flowing into the TEG at its hot side (**Q$_a$**) and the heat dissipated at its cold side (**Q$_C$**) are given, respectively, as:

$$Q_a = \alpha I T_H + k(T_H - T_C) - 0.5RI^2 \tag{3.18}$$

$$Q_C = \alpha I T_C + k(T_H - T_C) + 0.5RI^2 \tag{3.19}$$

where R is the internal resistance of the thermoelectric module and k is the thermal conductivity.

Because the power generated by the TEG is equal to the product of the voltage (**V**) times the current (**I**), which is also equal to the difference between the absorbed heat (**Q_a**) and the dissipated heat (**Q_C**), we have:

$$P = IV = Q_a - Q_C = \alpha I(T_H - T_C) - RI^2 \tag{3.20}$$

In addition, the voltage can be expressed as:

$$V = \alpha(T_H - T_C) - RI \tag{3.21}$$

At open circuit, there is no current (I =0) flowing through the load and the open-circuit voltage (**V_{oc}**) will be:

$$V_{oc} = \alpha(T_H - T_C) \tag{3.22}$$

By replacing $\alpha(T_H - T_C)$ in Equation (3.22) with V_{oc}, Equation (3.21) can be written as:

$$V = V_{oc} - RI \tag{3.23}$$

The current generated by the TEG can be expressed as follows:

$$I_{TEG} = \frac{\alpha \Delta T}{R_{TEG} + R_{Load}} \tag{3.24}$$

where R_{TEG} is the internal resistance of TEG and R_{LOAD} is the resistance of external load. Because V = IR, we then have:

$$V_{TEG} = \frac{\alpha \Delta T}{R_{TEG} + R_{Load}} R_{Load} \tag{3.25}$$

And,

$$P_{TEG} = V_{TEG} I_{TEG} \tag{3.26}$$

Or,

$$P_{TEG} = \frac{(\alpha \Delta T)^2}{(R_{TEG} + R_{Load})^2} R_{Load} \tag{3.27}$$

Because the maximum power is achieved when the internal resistance (R_{TEG}) of the TEG equals the load resistance (R_{Load}), the maximum power output of the TEG can be calculated by:

$$P = \frac{(V_{OC})^2}{4R_{TEG}} \tag{3.28}$$

In practice, the power output of TEG is also affected by the contact thermal and electrical resistance. Equation (3.29) can be used to calculate the power output of a TEG, while taking into account the electrical and thermal contact resistances [158]:

$$P_{TEG} = \frac{\alpha^2 \, A_{TEG} \, N \, (\Delta T_C)^2}{2 \, \rho \, (n + L_{TEG}) \left(1 + \frac{2 \, r \, L_C}{L_{TEG}}\right)^2} \tag{3.29}$$

where A_{TEG} is the cross-sectional area of a thermoelement, N is the number of thermocouples, ΔT_c is the temperature difference across the TEG, ρ is the electrical resistivity, n is the electrical contact parameter, *r* is the thermal contact parameter, L_{TEG} is the length of thermoelement, L_c is the thickness of the ceramic contacts layers in the TEG.

The conversion efficiency of the TEG can be calculated by:

$$\eta_{TEG} = \frac{V_{TEG}\, I_{TEG}}{Q_a} \tag{3.30}$$

3.8 Energy Distribution by Beam Splitter

The interference filter (in this study, a dichroic mirror) is used to split the light into two bands, over which the energy distribution is determined by the cut-off wavelength of the filter. The cut-off wavelength should be selected based on the bandgap of the PV cells, so that the light beams contributing to the photovoltaic effect are directed to the PV cells and the rest is directed to the thermal absorber. As mentioned earlier, the strategy that is used in this study selects a commercial dichroic mirror with a cut-off wavelength that closely matches the bandgap of commercially available PV cells. Therefore, InGaP is selected for this study because it has a bandgap of 1.88 eV [159-161] that corresponds to a cut-off wavelength of 658 nm [162], which closely matches a commercial dichroic mirror with a cut-off wavelength of 725nm.

One of the characteristics of dichroic mirrors is their sensitivity to the angle of incidence [163]. In this study, the mirror is placed at 45^{o} of incident rays, which is used in the manufacturer's design. A spectroradiometer measuring a wavelength range of 200 nm–1700 nm was used to find the energy distribution of each band after splitting. This consists of two separate instruments: a Blue Wave Spectrometer (UV-VIS) covering a wavelength range of 200 nm–1050 nm, and a Red Dwarf Star Spectrometer (NIR) covering a wavelength range of 900 nm–1700 nm. A schematic of the spectrometer that was used to measure the performance of the dichroic mirror is given in Figure 3.34. Two spectrometers (blue wave and dwarf star) are connected together via a Y-Fibre Optic Cable SMA 905 to a receptor, which was placed directly under the solar simulator irradiance to measure the power from the whole spectrum without a dichroic mirror. The receptor was then placed directly under the dichroic mirror, which is tilted at an angle of 45^{o}, to measure the power of the transmitted spectrum (as shown in Figure 3.34). The characteristics of reflected spectrum can also be measured by turning the receptor 90 degrees to face the reflected irradiance. The outputs of the spectrometers are connected to a PC that uses SpectraWiz software to acquire, store and analyse the spectral data.

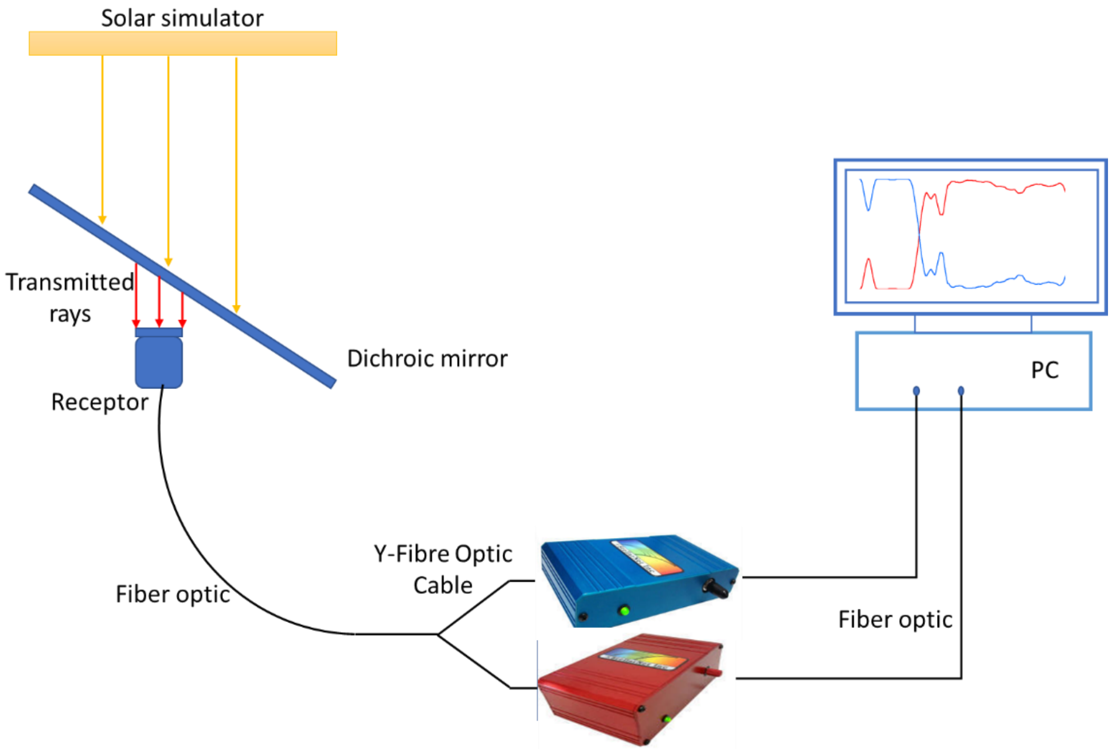

Figure 3.34: *Schematic of the experimental setup for characterising the performance of a dichroic mirror using a spectroradiometer.*

Figure 3.35 shows the light reflection (blue) and transmission (red) measured using the spectroradiometer over a range of 300 nm–1700 nm. The results show that 95.6% of the photon energy in the range of 300–725 nm (i.e., below the mirror's cut-off point) is reflected and 4.4% is transmitted, while the reflected rays over the range of 725 nm–1700 nm is13.5% and transmission is 86.5%. Clearly, this mirror can provide the required spectral splitting for the proposed hybrid systems.

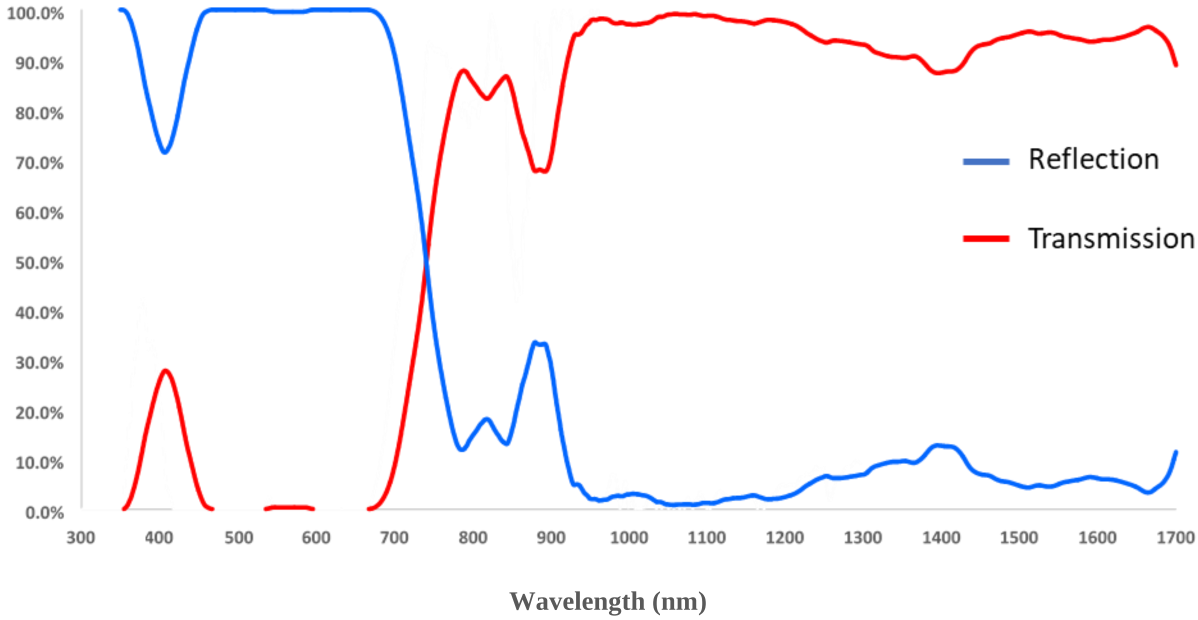

Figure 3.35: Transmission and reflection characteristics of the dichroic mirror measured using spectroradiometer.

R 300 – 716 nm = 95.6%
T 300 – 716 nm = 4.4%

R 725 – 1700 nm = 13.5%
T 725 – 1700 nm = 86.5%

Total Energy Transmitted = 46.8%
Total Energy Reflected = 53.2%

Reflection, 300-725 nm is 95.6%
Transmission, 725-1700 nm is 86.5%

3.9 Conclusion

The experimental techniques that are used to investigate the performance of the proposed hybrid systems were described in this chapter. The design and construction of the two concentrators that were employed in the hybrid systems has also been described. The concentrator’s fabrication techniques were detailed, which yield a high-quality concentrator that fits in the proposed hybrid systems for accurate measurements.

Solidworks thermal simulation and TracePro raytracing were used to justify the proposed designs. The simulation results reveal the adequacy of the proposed designs for the best hybrid system for thermal and electrical power generation.

The three PV cells (i.e., Si, GaAs and InGaP) that are used in this study were benchmark tested. The results show a good agreement with those in the literature. This ensures that the reliability and accuracy of the system are able to meet the requirements of this study.

The energy distribution light split by a beam splitter (e.g., dichroic mirror) utilising a spectrometer was measured. The results show a total energy transmittance of 47% and reflectance of 53%. These results will be used in theoretical calculations in the following chapters.

Chapter Four: PV-TE Hybrid System Using a Dichroic Mirror and a Parabolic Trough Concentrator

4.1 Introduction

A laboratory-scale hybrid system utilising a parabolic trough was designed and constructed. This system uses a dichroic mirror for spectrum splitting to direct visible light spectrum to the PV cell and infrared spectrum to the TEG. Three solar cells were investigated to evaluate the system performance, electrical performance, and the splitting effect. The temperature coefficient of the InGaP cell was determined. The heat generated on the copper absorber was determined by the slope technique described in Chapter Three. The thermoelectric modules were characterised and compared to theoretical calculations to identify the optimum length and width in ambient and vacuum environments. Finally, the power production of the hybrid system was evaluated in comparison to a bare cell.

4.2 Electrical Power Output of the PV Cell

As mentioned in Chapter Three, the PV cell, and the thermal receiver (the TEG) are decoupled using a beam splitter (the cold dichroic mirror). Decoupling the two receivers allows the second receiver (i.e., the TEG) to work at much higher temperature without affecting the PV cell. In addition, sending suitable band of the light spectrum to the PV cell can reduce the operating temperature of the PV cell (as will be discuss later on) and improve the durability of the PV cell.

4.2.1 Splitting Effect

Splitting the full spectrum solar irradiance into appropriate bands has a positive effect on the PV cell by removing unwanted rays (i.e., the part of the spectrum in which the energy of the photons is smaller than the bandgap of the PV cell). However, these rays cannot ionise the semiconductor and create electron-hole pairs. Instead, they are absorbed by the PV cell material to produce heat and increase the PV cell's temperature, which reduces efficiency.

To investigate the splitting effect on the PV cells' performance, I-V and P-V curves were obtained for the three types of PV cells (i.e., c-Si, GaAs and InGaP). In addition, the effect of splitting on the cell temperature was investigated.

4.2.1.1 Power and I-V Curves

Three types of PV cells (i.e., c-Si, GaAs and InGaP) were characterised by measuring their I-V curves with and without splitting to investigate the effect of spectral splitting on their power output. The InGaP cell is used in this hybrid system, as mentioned in Chapter Three because of its bandgap energy, which matches the cut-off point of the cold dichroic mirror that is used to split the light. Using a commercially available splitting mirror is much cheaper than designing one to match the bandgap energy of commercially available PV cells (c-Si for example). Another reason for selecting InGaP cell for this study is that it leaves a wider spectrum, and consequently more thermal energy, for the TEG than using other types of PV cells because it has a greater bandgap energy (1.9 eV) [144].

The c-Si and GaAs cells, which have smaller energy bandgaps than InGaP, were also investigated in this study to show why the InGaP cell was selected for the hybrid system. These three PV cells were tested under the standard test condition (STC) using the solar simulator that was described in Section 3.6. First, their performance characteristics were tested without beam splitting by placing them directly under the solar simulator. Then, a cold dichroic mirror was used as a beam splitter and reflect the rays from the solar simulator, at an angle of 45^o, to the PV cell placed perpendicularly to the reflected rays. Figure 4.1 presents the I-V and P-V curves with and without light splitting for c-Si, GaAs and InGaP solar cells. The c-Si cell has a bandgap of 1.1 eV, which can harness the light energy over a spectrum range up to 1127 nm. The GaAs cell has a bandgap of 1.4 eV, which corresponds to a spectrum range up to 864 nm. Finally, the InGaP has a bandgap of 1.9 eV, which corresponds to a spectrum range up to 700 nm. Because the cut-off wavelength of the dichroic mirror employed in this study is approximately 700 nm, a significant portion of useful light energy for c-Si cell and a noticeable portion of useful light energy for GaAs were not reflected onto both PV cells. Meanwhile, due to the spectrum match between the InGaP cell and the dichroic mirror, all of the useful light energy for InGaP cell has been reflected onto the cell.

(A)

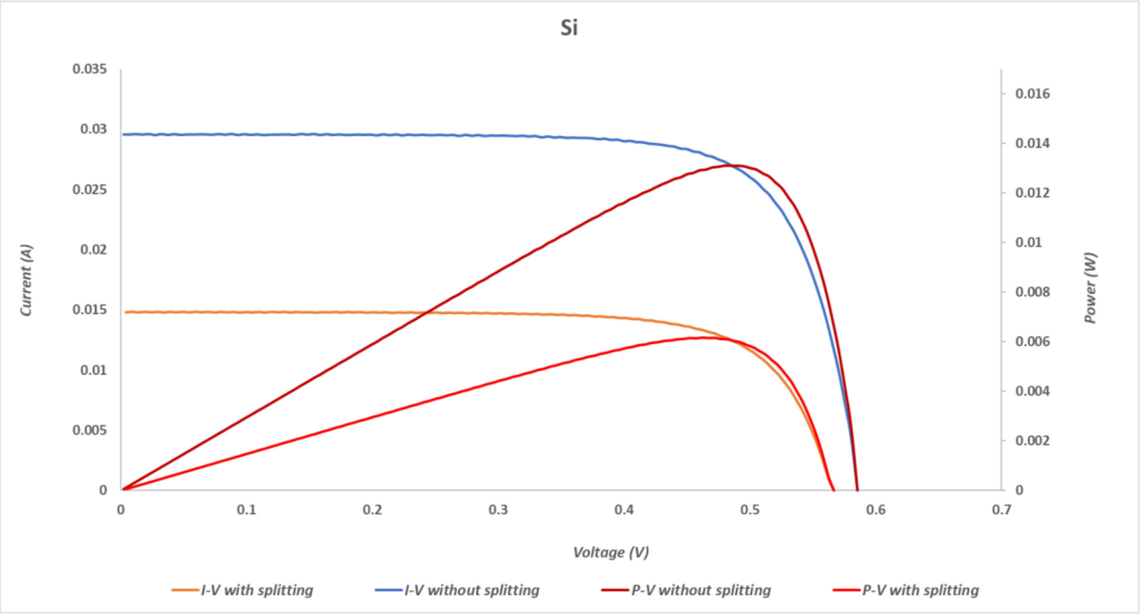

(B)

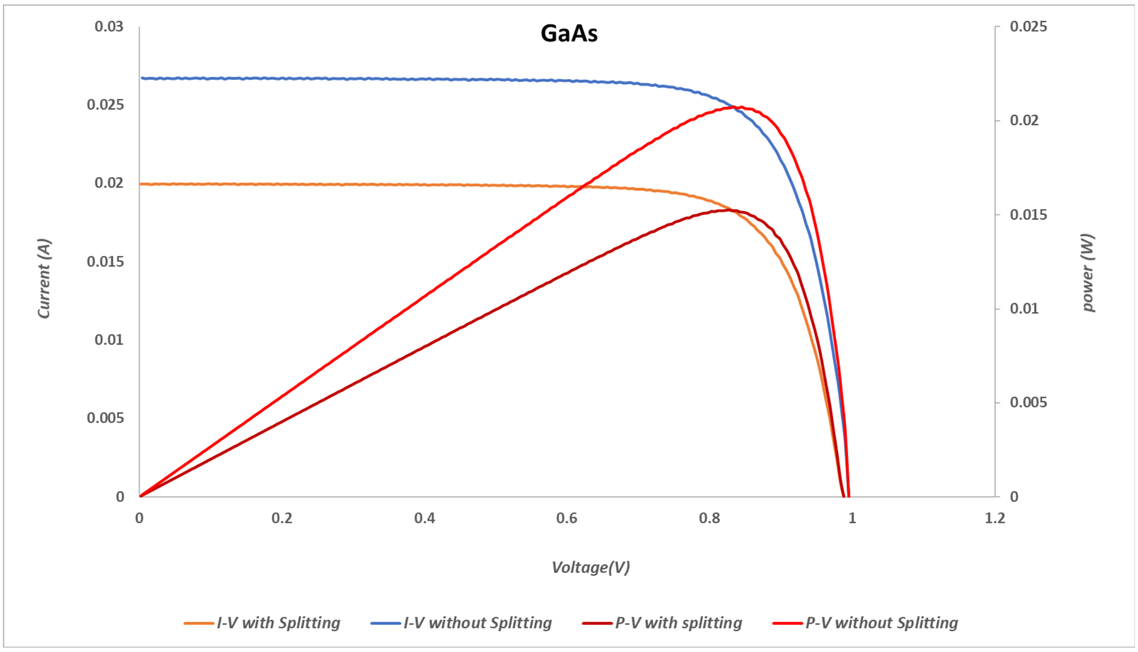

(C)

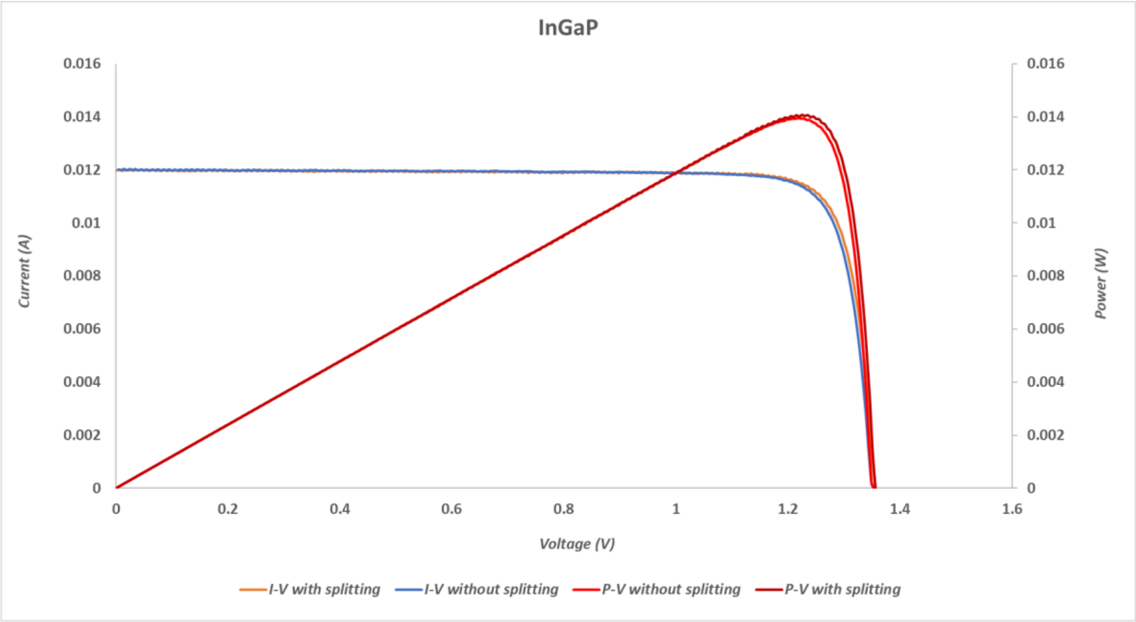

Figure 4.1: *I-V and P-V curves for the three solar cells: (A) Si cell, (B) GaAs cell, and (C) InGaP cell with/without splitting.*

It can be seen from Figure 4.1(A) that the I-V curve for c-Si cell showed a significant decrease in the current and the power output after light splitting, due to a loss of part of useful spectrum.

For the GaAs cell, a noticeable decrease in current and power output can be seen in Figure 4.1 (B), which is due to a less significant mismatch in the light spectrum after light splitting. However, for the InGaP cell, the I-V curves for testing before and after splitting are almost identical, as shown in Figure 4.1(C). This indicates that a perfect match between the InGaP cell and the selected dichroic mirror. In this case, all of the useful light energy has been reflected by the mirror onto the InGaP cell, while all of the useless energy for the InGaP cell was passed through for thermal production.

Table 4.1 shows the experimental results of the performance parameters for the three solar cells without splitting (A) and with splitting (B). The adverse splitting effect is clear for the silicon cell due to a significant decrease in the short-circuit current (I_{SC}) and the maximum power output (P_{max}), and hence the conversion efficiency. The decrease in I_{sc}, P_{max} and η_{PV} is less for the GaAs cell because the spectrum mismatch is less significant in GaAs than in c-Si cells. It is interesting to note that the experimental results of InGaP cell demonstrate that spectrum splitting has no effect for the performance parameters of a solar cell if the spectrum match is ensured.

Table 4.1: *PV cell (Si, GaAs & InGaP) results: (a) without splitting, and (b) with splitting.*

(a)

Cell Type	Active area (mm2)	ISC (mA)	VOC (mV)	IMP (mA)	VMP (mV)	PMax (mW)	FF (%)	ηPV (%)
InGaP	10x10	12.0	1353.1	11.5	1218.1	14.0	85.7%	14.0%
GaAs	10x10	25.8	995.5	23.9	834.0	20.0	77.8%	20.0%
Si	10x10	29.6	585.6	27.3	480.2	13.1	75.6%	13.1%

(b)

Cell Type	Active area (mm2)	ISC (mA)	VOC (mV)	IMP (mA)	VMP (mV)	PMax (mW)	FF (%)	ηPV (%)
InGaP	10x10	12.0	1356.0	11.5	1225.1	14.1	86.4%	14.1%
GaAs	10x10	19.7	987.5	18.6	822.8	15.3	78.7%	15.3%
Si	10x10	14.8	566.9	13.4	462.2	6.2	73.3%	6.2%

4.2.1.2 Temperature Effect

Another advantage of spectral beam splitting is to remove the irradiation that does not participate in charge generation but contributes to heat production. Without spectral splitting, this part of irradiation can be absorbed and turned into heat inside the solar cell. This results in an increase in its temperature and consequently a reduction in the conversion efficiency. An experiment was conducted to investigate the effect of spectral splitting on the temperature and the power output of the solar cell. The InGaP cell was placed on a piece of wood to eliminate any source of cooling. To measure its temperature, a thermocouple was attached to the back of the cell through a grove on the wood (as shown in Figure 4.2).

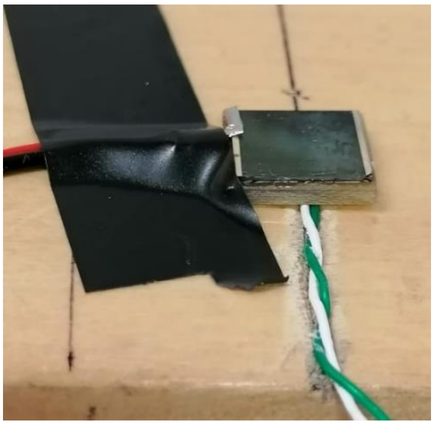

Figure 4.2: *The setup for testing the spectral splitting effect on the temperature of the PV cell. A dichroic mirror (not shown in the photograph) was placed between the solar cell and the solar simulator (not shown in the photograph).*

An irradiance of 1000 W/m^2 from a solar simulator was shined on the InGaP cell for 15 minutes with and without splitting. The temperature of the solar cell was recorded using the Pico logger every minute and the corresponding power output was measured using the Autolab, as described in Chapter Three. The results are shown in Figure 4.3. It can be seen that the temperature of the InGaP cell increases with time to reach a steady-state value of 55.0 ºC when tested without spectral splitting, while it increased only slightly to about 38 ºC when tested with spectral splitting. A reduction of 17 ºC in the cell temperature is achieved using the spectral splitting, which led to beneficial effect on the power output. As shown in Figure 4.3, the power output of the InGaP remains almost unchanged with spectral splitting. However, the power output of the InGaP cell decreased significantly (up to about 5%) without spectral splitting. This happens because the power output of the solar cell decreases as the cell temperature increases.

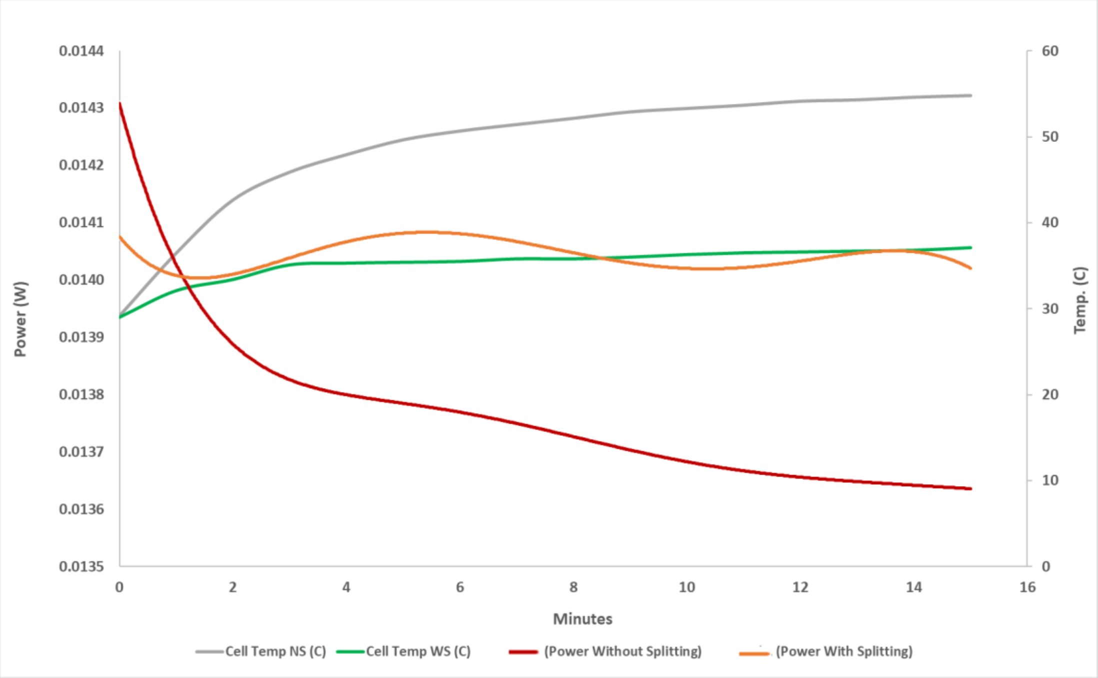

Figure 4.3: *The effect of spectral splitting on the temperature and power output of the InGaP cell.*

Preventing a temperature increase in the solar cell has another positive effect in that, it can slow the degradation and increase the lifetime of the solar cell [164].

The experiment was repeated using the c-Si and GaAs cells to examine the spectral splitting effect on their performance. Because the dichroic mirror is selected to provide spectral match with the InGaP cell, the effect of spectral splitting is less effective for GaAs cell and much less effective for c-Si cell. From Figure 4.4, it can be seen that the spectrum range reflected by the dichroic mirror matches exactly the response range of the InGaP cell, and hence there is no power loss after spectral splitting. However, the part of response range of the GaAs (i.e., 725nm - 865nm) was lost through transmission and this resulted in power reduction. The loss of the response range for the c-Si cell (i.e., 725nm–1117nm) was even higher, resulting in more significant power reduction.

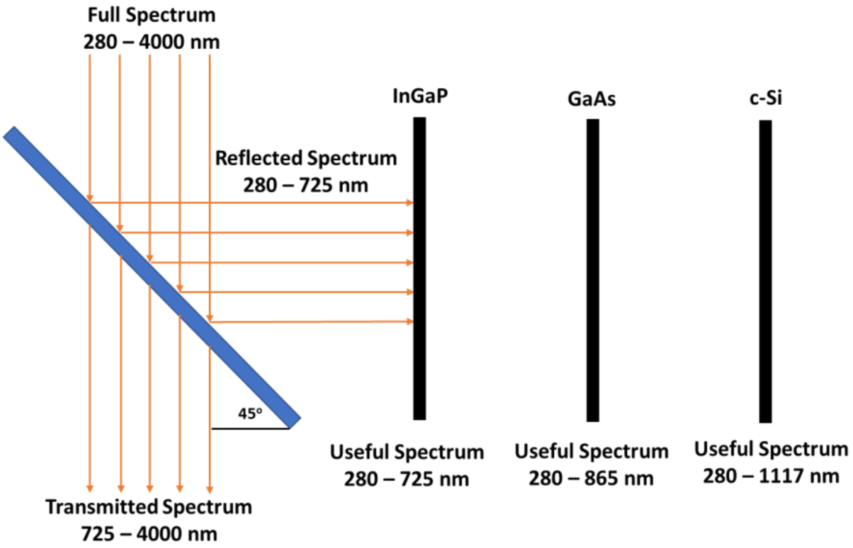

Figure 4.4: *Splitter reflected rays for the three PV cells (InGaP, GaAs & c-Si).*

Figures 4.5 and 4.6 show the spectral splitting effect on the temperature and power output of the GaAs and c-Si cells.

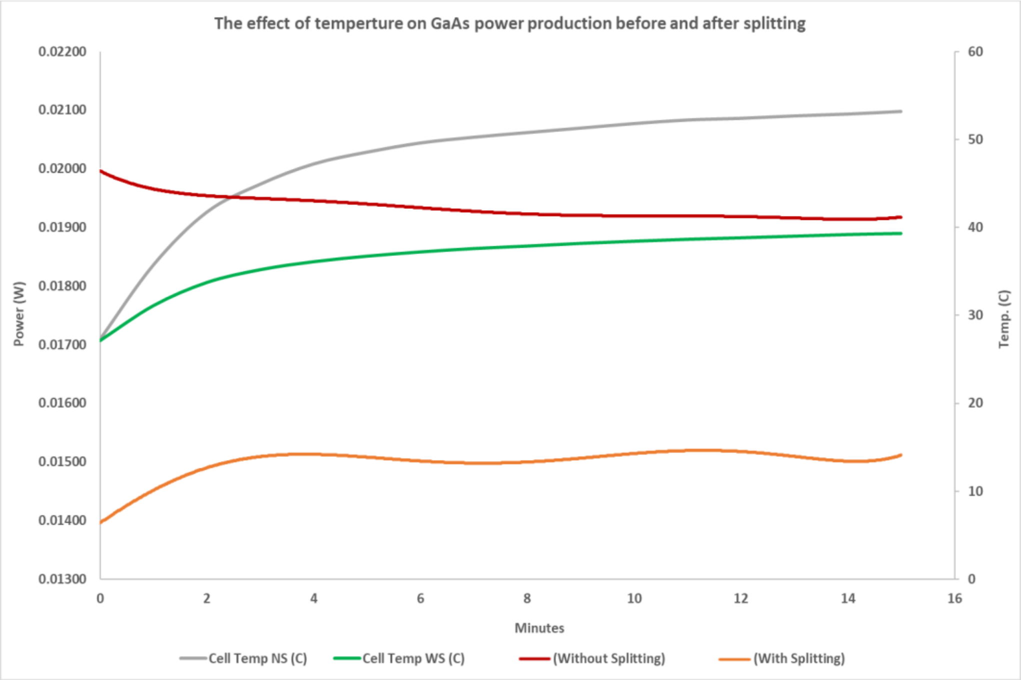

Figure 4.5: *The effect of spectral splitting on the temperature and power output of the GaAs cell.*

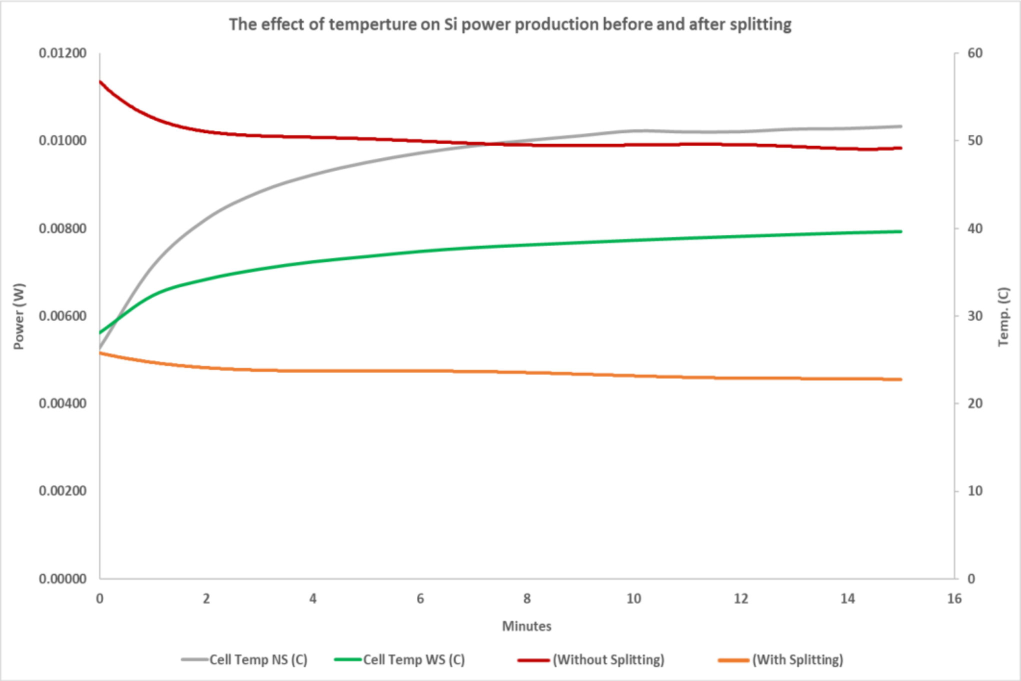

Figure 4.6: *The effect of spectral splitting on the temperature and power output of the Si cell.*

The temperature coefficients for InGaP cell can be derived from the experimental data of I_{SC}, V_{OC} and Pmax as function of temperatures obtained from measured I-V curves without spectral splitting. Figure 4.7 shows the short circuit current (I_{SC}), open circuit voltage (V_{OC}) and maximum power output (P_{MAX}) as a function of the temperature for InGaP cell. The temperature coefficients for the three parameters are calculated from the slopes of the fitted lines [165].

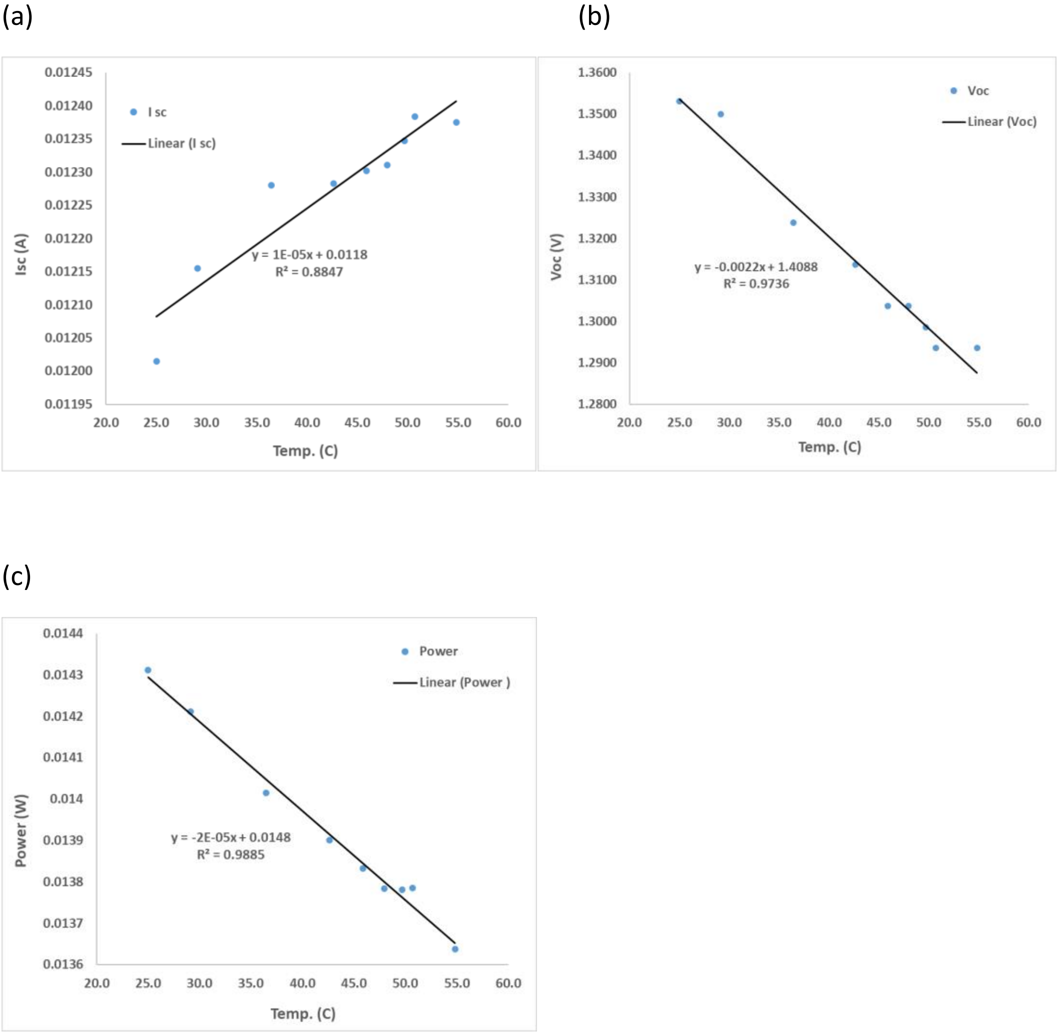

Figure 4.7: *InGaP cell temperature coefficient of: (a) short circuit current, (b) open circuit voltage, and (c) power.*

Table 4.2 lists the calculated coefficients compered to published values for the three parameters of the InGaP cell. They are in reasonable agreement with the published data.

Table 4.2: InGaP calculated temperature coefficients versus the literature.

Cell Type	Calculated			Published		
	Temperature coefficient (%/°C)			Temperature coefficient (%/°C)		
	Isc	Voc	Pmax	Isc	Voc	Pmax
InGaP	0.083	-0.163	-0.140	0.070 [166-168]	-0.210 [166, 168, 169]	-0.170 [170]

4.3 Thermal Output of the Parabolic Trough Concentrator

As elaborated in Section 3.2.2, the infrared spectrum will pass through a dichroic mirror to reach a parabolic trough concentrator, which concentrates the light onto a copper absorber to produce heat. The slope technique was employed to determine the heat production by the copper rod illuminated under the solar simulator of standard illumination power of 1000 W/m^2. This technique was also used to determine the heat lost to the surrounding (as described later on).

4.3.1 Heat Produced by the Copper Absorber

The following four cases were investigated to determine the heat generation by the copper absorber:

- No concentration and no splitting (NCNS)
- With concentration and no splitting (WCNS)
- No concentration and with splitting (NCWS)
- With concentration and with splitting (WCWS)

This comparative study is intended to provide useful information and deep understanding of heat generation from the sunlight under different intensity and spectrum range. The temperature raising profiles for the four cases were measured until the corresponding steady state had been reached, as shown in Figure 4.8. The four curves show a sharp increase in temperature during the initial few minutes of illumination because the heat loss to surroundings during this period is negligible. However, the increase becomes slower over time, until they are completely flat at the steady state. At the steady state, the heat loss to surroundings is equal to the heat produced by the absorber, and hence there is no further increase in temperature. The graph also shows a rapid increase in the case of concentration without splitting compared to the other cases because more heat is received by the copper absorber.

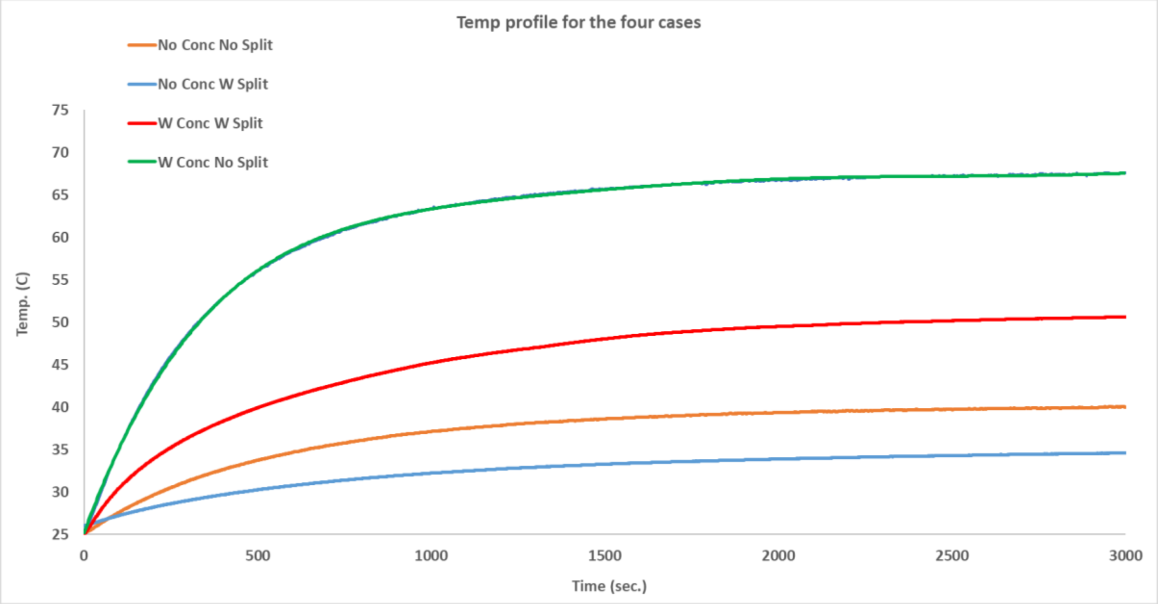

Figure 4.8: *Temperature profiles for four cases of light irradiance.*

The slope technique is a procedure that determines the heat retained in the absorber from the slope of the temperature profile at different points. For a given absorber with known mass and specific heat capacity, the heat retained in the absorber at a given time can be calculated using Equation 3.11 and the slope of $\Delta T/\Delta t$ determined from the measured temperature profiles. The slopes of the temperature profiles at intervals of 1 minute along the curves were determined for all four cases. Using a mass (m) of 46.6 g for the copper absorber and the specific heat capacity

(C_p) of 0.385 (J/g.C) for copper, the heat retained in the absorber for four cases at different time are shown in Figure 4.9.

To determine the heat absorbed by the absorber (i.e., the thermal energy produced by the light before the part of it lost to the surroundings), it is necessary to determine the heat absorption without heat loss, which corresponds to point of x=0 on Figure 4.9. Because the curves start at x = 1 minute, it is necessary to extrapolate the curves to the intercept with the y-axis. The extrapolation is obtained by curve fitting (solid lines) based on the experimental data (solid dots), as shown in Figure 4.9, and the corresponding heat absorption (Qa) was obtained from the incepts on the y-axis.

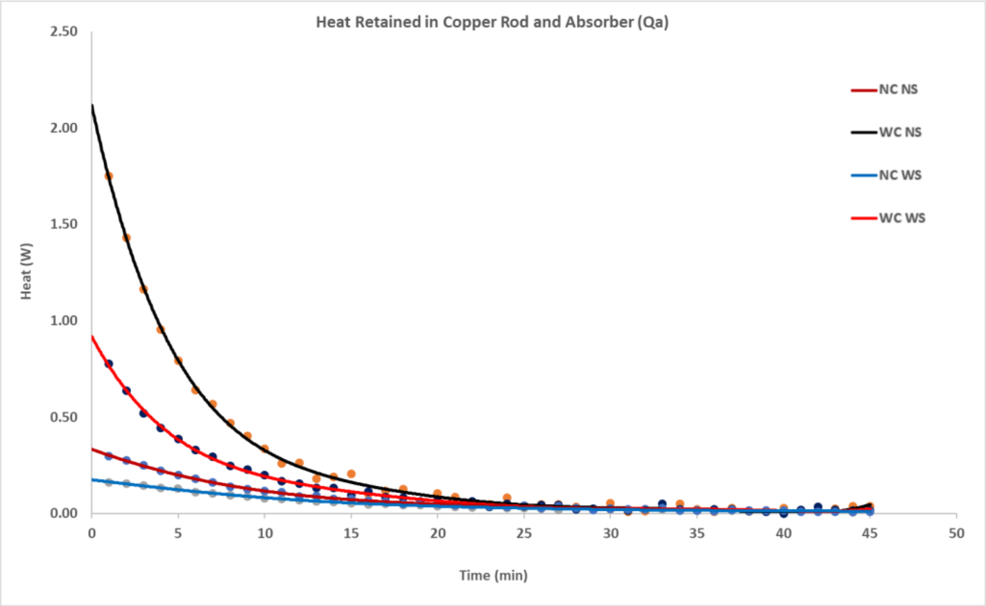

Figure 4.9: *Heat retained by the copper absorber (Qa) determined using the slope technique for four cases. The curves are extrapolated to the y-axis to find the heat absorbed by the copper absorber.*

The values of the heat generated by the copper absorber (Qu) for the four cases, determined from Figure 4.9 (at y-intercept) are listed in Table 4.3, together with the light power available from the simulator and concentrator. Because the conversion efficiency of light energy into thermal energy using black paint on copper is over 90% [171], the results obtained by the slope technique are close to the measured figures. Table 4.3 shows a good agreement between values from slope technique and the solar simulator irradiance reading by the solar survey.

Table 4.3: *Comparing heat generated by the copper absorber (Qu) with solar simulator irradiance for all cases.*

	Qu (W)	Simulator Irr. (W)	Drop (%)
Without concentration and without splitting	0.333	0.358	6.9%
With concentration and without splitting	2.117	2.235	5.3%
Without concentration and with splitting	0.175	0.167	-4.6%
With concentration and with splitting	0.945	1.046	9.6%

4.3.2 Convective Heat Transfer Coefficient

The convective heat transfer coefficient surrounding the copper absorber is an important parameter in the design and optimisation of the hybrid system. Using the data obtained from this experiment, the convective heat transfer coefficient of the system can be determined through data fitting based on Equation 3.09. An Excel sheet (see Appendix 4.2) was created based on Equation 3.09 to determine the convective heat transfer coefficient surrounding the copper absorber at the steady state. It can be seen from Equation 3.09 that, except for the convective heat transfer coefficient, all of the other parameters can be known, either as a constant (i.e., Stefan-Boltzmann constant, 5.67 x 10^{-8} W m^{-2} K^{-4}) or measured quantities (e.g., temperatures).

At steady state, the heat lost to surroundings (**Q_l**) is equal to the heat produced by the copper absorber (**Q_u**), whose values were determined from the slope technique, together with the corresponding final temperature. Using the theoretical model developed in Excel (Appendix

4.2), the convective heat transfer coefficient (h) of the copper absorber can be determined from the values that produce a good agreement between the theory and experiments. Table 4.4 shows the experimental and calculated heat absorption and steady state temperature for the four cases, together with the corresponding convective heat transfer coefficient. It can be seen that the convective heat transfer coefficient of this investigated system is between 12 W/m^{2}K to 16 W/m^{2}K, which is within the range of free convection. A significant deviation between the experimental and theoretical values of the absorbed heat for the third case (without concentration & with splitting) is likely because of low illumination on the copper absorber, which is anticipated to introduce more uncertainty into the measurements.

Table 4.4: *Convective heat coefficient predicted based on theoretical model built to match experimental heat generated (Qu) with theoretical calculated.*

	Exp. (Q_u)	**Exp. T_{final} (C)**	**Conv. Heat Coff. (h) to match experiments (W/(m^{2}K))**	**Theo. (Q_u)**	**Theo. T_{final} (C)**	**(Q_u) Diff. (%)**	**(T_{final}) Diff. (%)**
Without concentration and without splitting	0.33	41.2	16.0	0.36	40.6	6.9	1.4
With concentration and without splitting	2.1	67.0	14.0	2.24	68.6	5.3	-2.4
Without concentration and with splitting	0.18	39.1	12.0	0.17	38.2	-4.6	2.3
With concentration and with splitting	0.95	51.7	12.0	1.05	53.1	9.6	-2.7

4.4 Thermoelectric Module Characterisation

The performance of the thermoelectric power generation system depends on the operating conditions and dimensions of the thermoelectric modules. A wide range of thermoelectric modules with different geometries are commercially available. Selecting a suitable thermoelectric module for the proposed hybrid system requires a good knowledge of the factors that affect the performance of the thermoelectric power generation. In this section, experimental characterisation and theoretical simulation were carried out to gain a detailed understanding and useful knowledge of thermoelectric modules for proper design and optimisation of the hybrid system.

4.4.1 Power Output and Matched Load

Five commercial TEGs of different aspect ratios (2NA/L) were selected for this investigation because their sizes are broadly suited for the hybrid system. As discussed in Section 3.7, the maximum power output of a TEG is obtained when the load resistance is equal to the internal resistance of the TEG. Therefore, it is necessary to determine the internal resistance of these TEGs experimentally.

The module internal resistance (R_{TEG}) was connected in series with a variable external resistance (R_{Load}) in a circuit. The voltage drop is then measured with different load resistances (R_{Load}) by Autolab. The P_{max} occurs when the external load matched the internal resistance of the TEG module. The electrical power (P) can be calculated by measuring the closed circuit voltage (V_c) and the load resistance (R_{Load}) as follows:

$$P = \frac{(V_C)^2}{R_{Load}} \tag{4.1}$$

The curves for the electrical power for the five modules as a function of the load resistance are depicted in Figure 4.10.

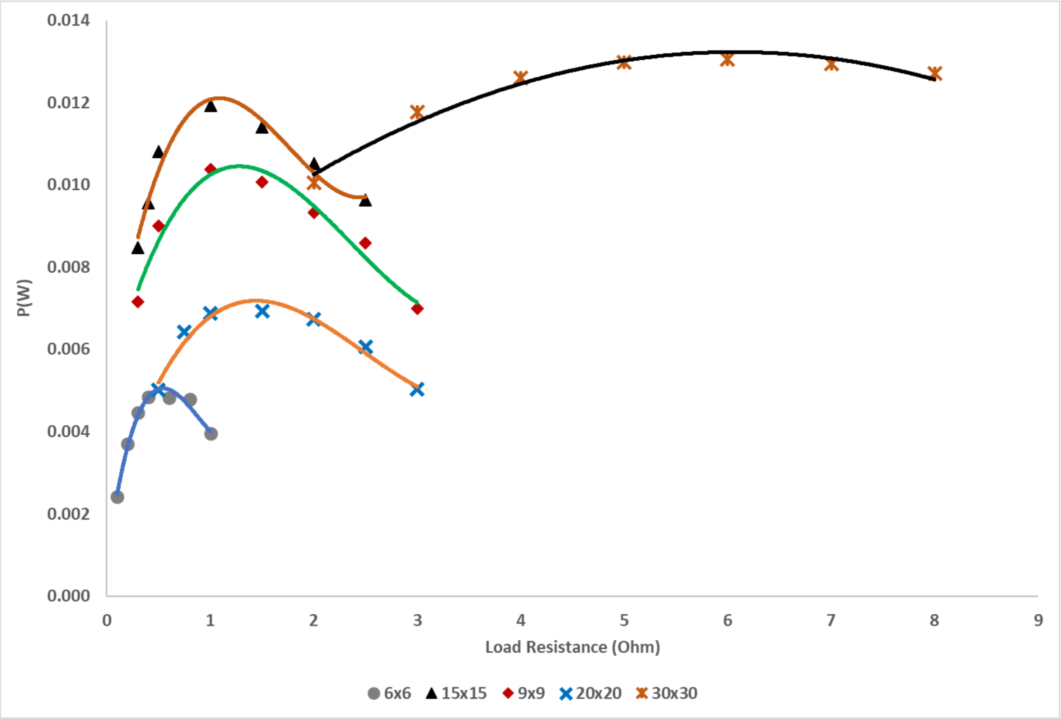

Figure 4.10: *TEG module power output as a function of load resistance.*

The experimental results obtained for the matched load resistance for the five TEG modules are shown in Table 4.5.

Table 4.5: *TEG module geometry with internal resistance measured by matched load experiments.*

Module	N	A (mm^2)	L (mm)	2N*A/L (mm)	R_{TEG} (Ω)
6x6	7	0.64	1.5	6	0.53
9x9	17	0.64	1.5	15	1.10
15x15	31	1.0	1.3	48	0.99
20x20	71	1.0	0.8	178	1.25
30x30	127	1.0	2.0	127	5.9

Note that N is the number of thermocouples, A is the cross-sectional area of thermoelement, L is the length of thermoelement and R_{TEG} is the module internal resistance.

Equations (3.28) and (3.29) (see Chapter Three) will be used for calculation to validate the experimental results. The open circuit voltages from the output terminals of the TEGs were recorded as a function of time from the moment when the light source was switched on to the period when the system reached the steady state. Because the internal resistances of each TEG were determined by match load experiments, the electrical power generated by the TEGs were calculated using Equation (3.28) (experimental). Meanwhile, Equation (3.29) was used to calculate the TEG's power output (theoretical). The results for the five TEG modules without/with splitting are shown in Figure 4.11.

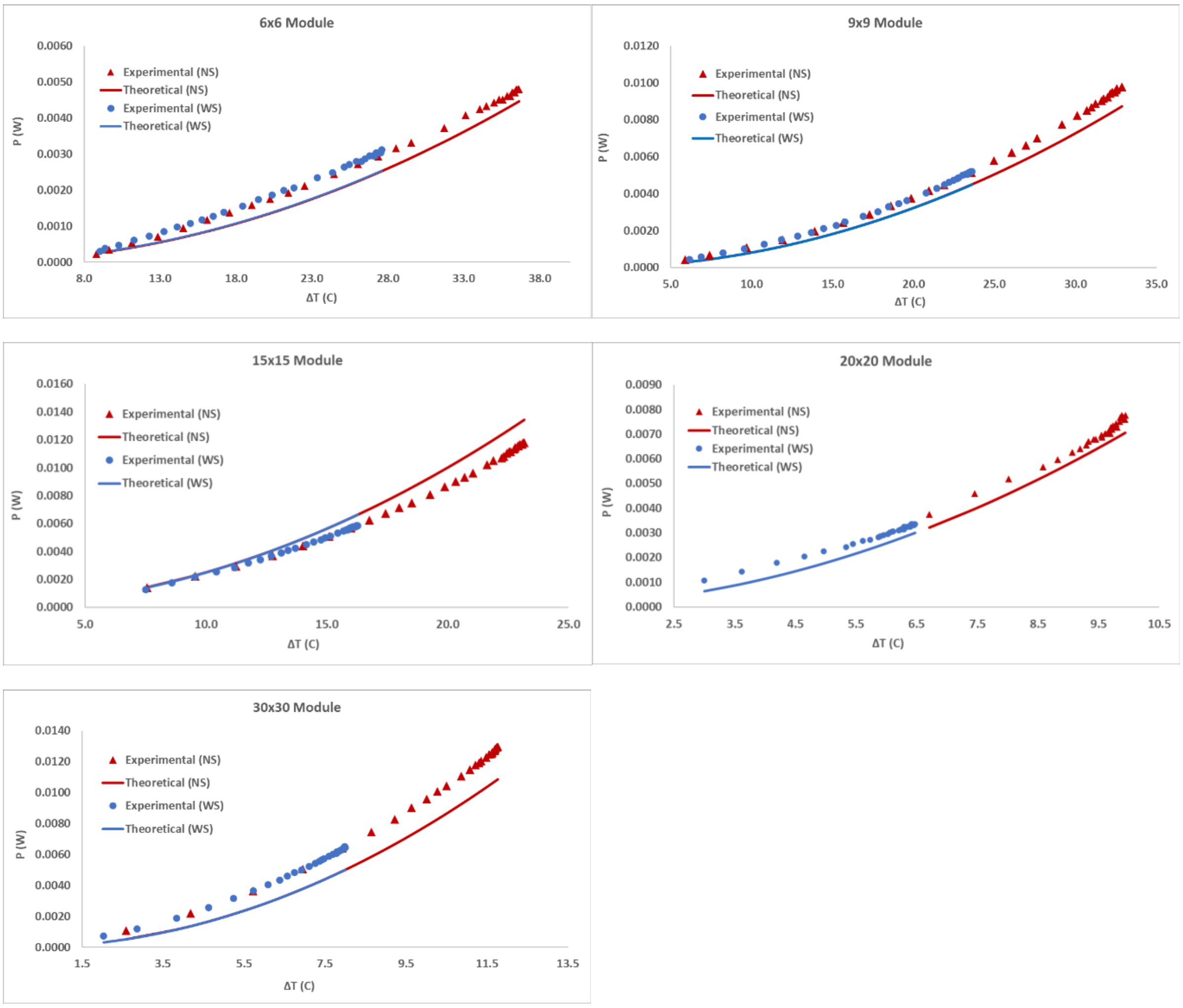

Figure 4.11: *Theoretical and experimental power output for the 5 TEG modules as a function of ΔT with/without splitting.*

In Figure 4.11, a reasonably good agreement between experimental and theoretical results is evident. The parabolic curves for theoretical and experimental results are expected from the TEG theory [172].

Figures 4.12 illustrates the steady state temperature of the absorber, after illuminating it under 1 sun (1000 W/m^2), when the hot sides of the five TEGs are attached to the copper absorber without connecting the modules to any load.

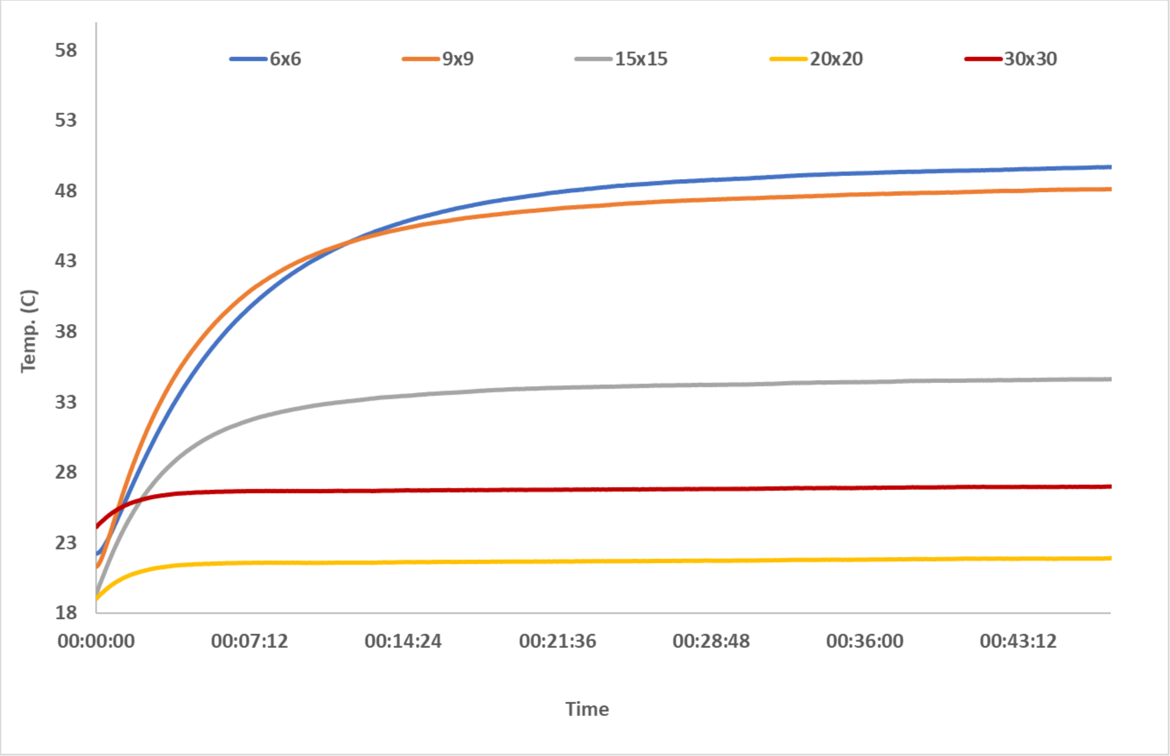

Figure 4.12: *Absorber temperature of TEG modules classified by its aspect ratio.*

Because the modules' cold side temperature was around 12 ºC, it is clear from Figure 4.13 that the absorber temperature is inversely proportional to the aspect ratio of the modules. Because the heat conducted through a module is less for small modules (with small aspect ratios), due to smaller cross-sectional area and fewer thermocouples, the hot side temperature of the small modules is higher than the big modules, based on Fourier's law.

Because the surface area of the copper, and the ambient and TEG cold side temperatures are known from measurements, and ε, σ and k are known materials properties, the temperature difference (ΔT) across each thermoelectric module can be calculated using Equation 3.15. The results are shown in Figure 4.13 for all of the modules that were investigated.

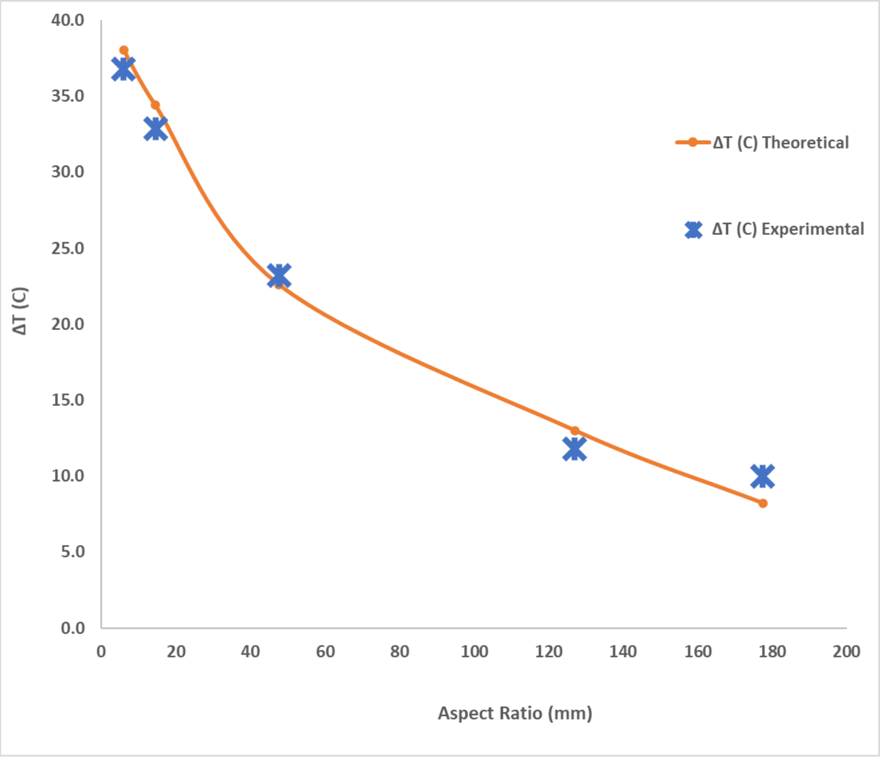

Figure 4.13: *Temperature difference across the five TEG modules vs. their aspect ratio.*

The good agreement between theoretical and experimental results is clear from Figure 4.13, which validates the use of theoretical model in optimising the module geometry in the following sections. The trend of the temperature difference across a module decreasing as the aspect ratio increases is expected from Fourier's law because the module with a large aspect ratio conducts more heat into the water cooler. The aspect ratio takes into account the length of the thermoelement. This is the reason why module (20x20) has a larger aspect ratio than module (30x30), even though the latter has more thermocouples (127). Module (20x20), with a thermoelement length of 0.8 mm, exhibits a smaller ΔT than module (30x30), which has a thermoelement length of 2.0 mm, because longer thermoelements have larger thermal resistance, and hence less heat to be dissipated by the water cooler.

Figure 4.14 compares the calculated TEG power output based on ΔT from Figure 4.13 using Equation 3.29 and the experimental TEG power measurements. This figure shows that the maximum power output is obtained from module (30x30) that has an aspect ratio of 127.

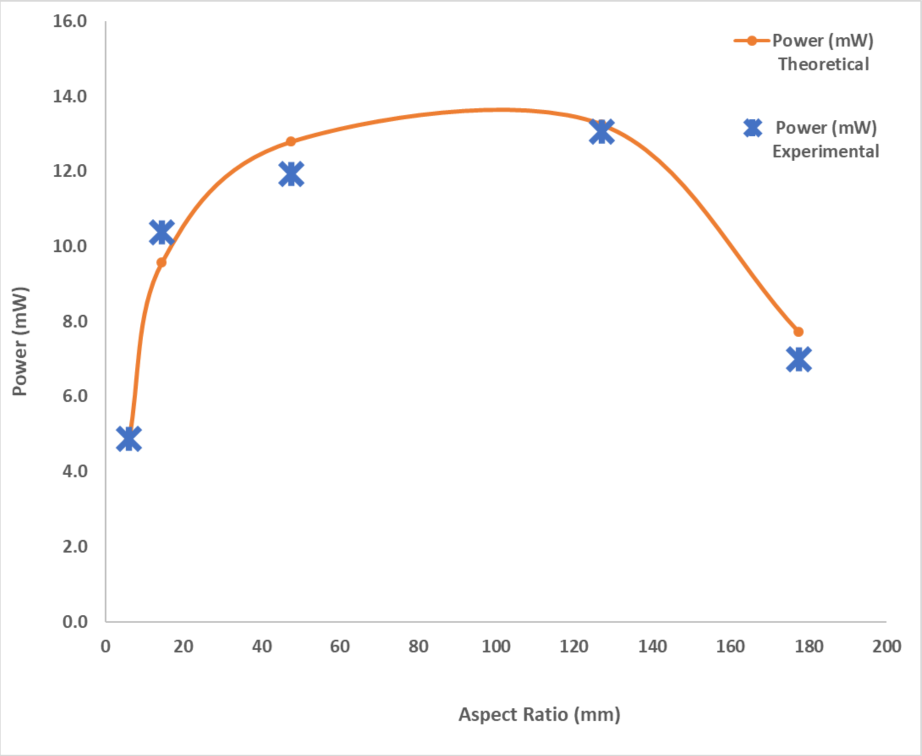

Figure 4.14: *TEG modules power output as a function of aspect ratio.*

The measured voltage with respect to the load resistance of the five modules is depicted in Figure 4.15.

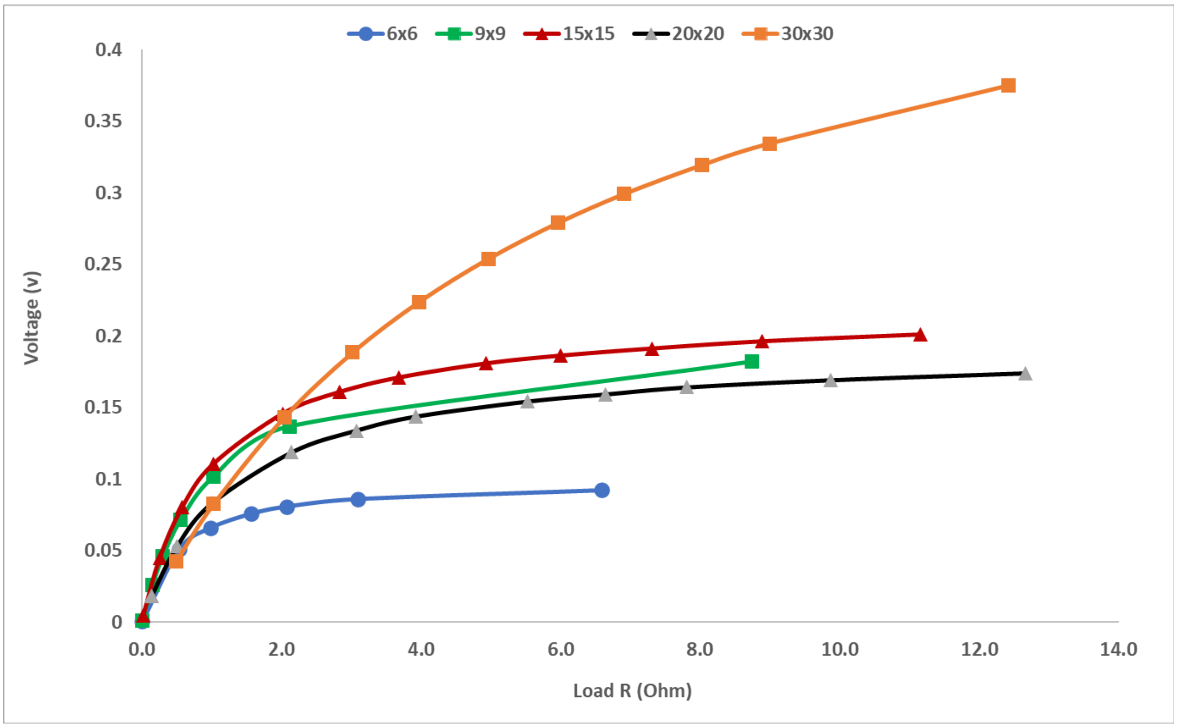

Figure 4.15: *Voltage vs. load resistance for the five TEG modules.*

Figure 4.15 shows that at zero load (i.e., when the output terminals of the TEG are short circuited), the output voltages for all modules are also have zero values. The voltage increases rapidly as the load resistance rises then it presents slower increase at higher load resistance. Not only the load resistance affects that increase of the output voltage but also the temperature gradient, which differ greatly among all modules depending on the aspect ratio, as shown in Figure 4.12. These two parameters (i.e., load resistance and ΔT) explain the different behaviours of the TEG curves in Figure 4.15. Module 30x30 shows the highest output voltage as a result of reasonable ΔT it has and its high aspect ratio. In contrast, module 6x6 shows the lowest voltage output due to its very low aspect ratio, although it maintained high ΔT across its two sides.

Figure 4.16 shows the power output and current as a function of the voltage for the five modules investigated with and without splitting. The largest module (30x30) shows the highest power output among the five TEG modules. However, the medium size module (15x15) shows a slightly smaller power output than that of the largest module (30x30), but its volume is about 2.6 times less (0.127/0.048 = 2.64). Clearly, a trade-off between achieving a large power output and using minimal thermoelectric material should be considered in specific applications.

As indicated by Equation 3.29, both large ΔT and aspect ratio are required to achieve a large power output. Although it has a large aspect ratio, module (20x20) exhibits a small power output because it has a small ΔT across the module. The reason for the small ΔT is because of the very short thermoelement length (0.8mm) of the module. Meanwhile, the smallest module (6x6) has a large ΔT, but still produce a small power output due to its small aspect ratio. Clearly, the power output of TEG module is a trade-off between ΔT and aspect ratio.

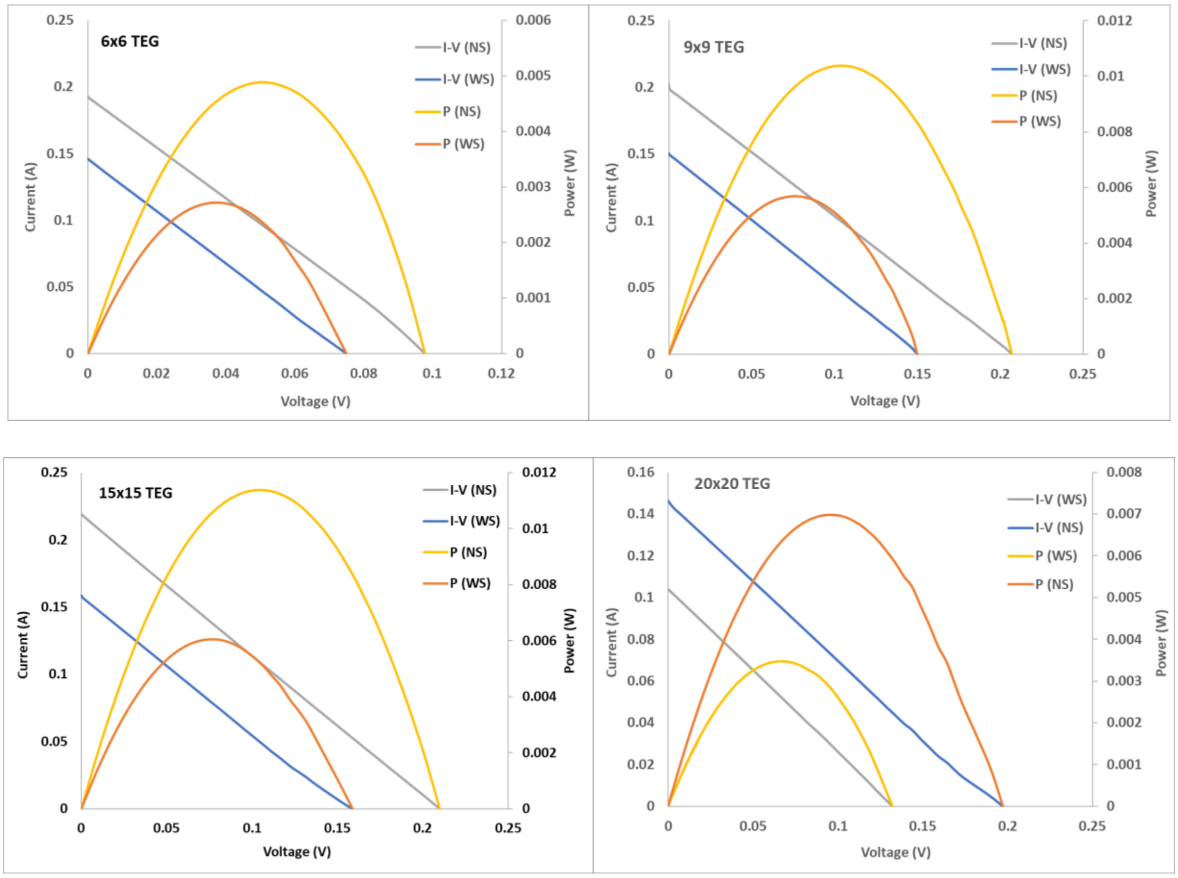

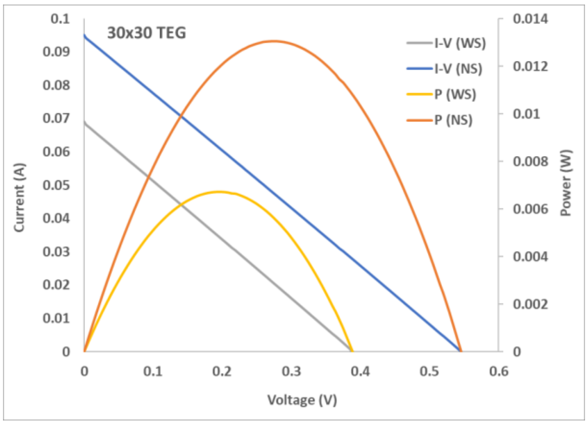

Figure 4.16: *I-V curves and P-V curves for the five TEG modules.*

4.4.2 Simulation and Theoretical Calculation

“SolidWorks” thermal simulation was used to find the hot side temperature of the TEG modules after reaching the steady state upon illuminating the copper absorber with the 1 sun (i.e., 1000 W/m^2). The SolidWorks thermal simulation allows the study of temperature distribution and heat flow with taking into consideration of conduction, convection, and radiation effects. This software uses the methods of finite element analysis to solve thermal problems by meshing models prepared in SolidWorks into finite elements.

The heat transfer by conduction is modelled directly [11]. However, convection and radiation are applied as boundary conditions by defining convection and radiation coefficient to the surfaces participating in heat exchange with environment. When specifying convection, the convective heat transfer coefficient and the ambient temperature need to be entered. Similarly, for radiation, the emissivity and the surrounding temperature need to be specified, while the Stefan-Boltzmann constant is automatically defined. Figure 4.17 shows the thermal loads that need to be entered into SolidWorks for thermal analysis, which should be assigned to each face of the model designed in the SolidWorks software. The model's material (copper in this case) is also defined.

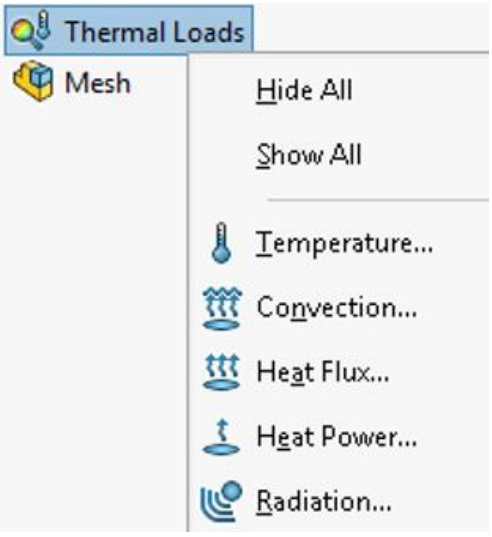

Figure 4.17: *Thermal load addition in SolidWorks.*

The thermoelectric generators modelled in SolidWorks are designed based on the actual dimensions of module plates and thermoelements. Because the material (Bi_2Te_3) for the thermoelements of the TEGs is not available in SolidWorks, ceramic porcelain that has a thermal conductivity of 1.495 (W/m.K) was selected because it is very similar to the thermal conductivity of Bi_2Te_3. All of the thermal analysis in this study is performed based on steady state condition only.

The simulation was based on the following parameters:

Convective heat coefficient (h) = 17 W/(m^2K)

Emissivity of the absorber, $\varepsilon = 0.90$ (for black painted part), 0.18 (for unpolished part)

Irradiance = 864 W/m^2 (light uniformity applied)

Trough reflectivity = 0.95

Copper absorber absorptivity = 0.9

TEG cold side temperature = Experimental measured temperatures (≈12.0 °C)

The copper emissivity is calculated from the emissivity of polished copper (0.18) and black coated area (0.90), while the parabolic trough reflectivity was taken from the Alanod MIRO reflector, which has light reflection of 95% [12].

The heat power entered to the copper absorber facing the trough concentrator is calculated based on the surface area of the absorber that receives the reflected rays from the concentrator, as well as the direct simulator irradiance falling on the top side of the copper rod. The copper rod is divided into faces so that only those faces which receive the simulator irradiance, either direct or reflected from the trough, will have heat power entered. When simulating without splitting, the irradiance will be 864 W/m^2; however, when simulating with splitting, only transmitted irradiance is considered.

Figure 4.18 shows the temperature reading at both sides of the thermoelectric module (6x6) with and without splitting. The results of the other modules are available in the appendix 4.5.

(a)

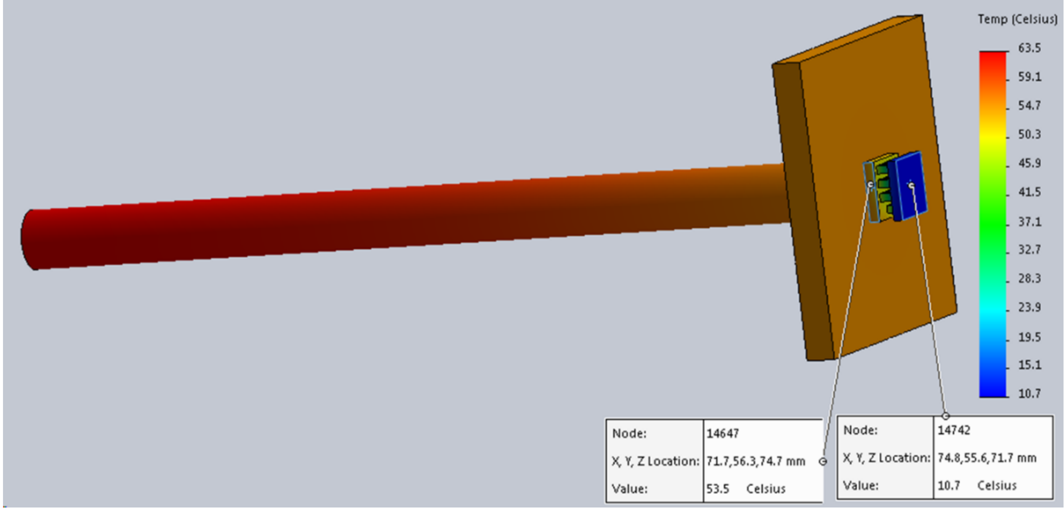

Node: 14647
X, Y, Z Location: 71.7,56.3,74.7 mm
Value: 53.5 Celsius

Node: 14742
X, Y, Z Location: 74.8,55.6,71.7 mm
Value: 10.7 Celsius

(b)

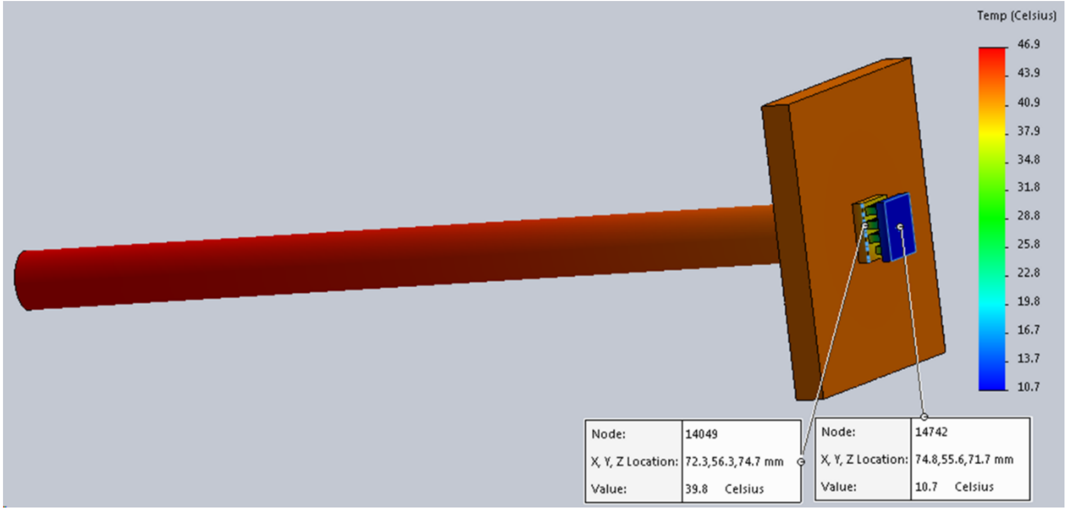

Figure 4.18: *TEG module 6x6 hot side simulation under concentration (a) without splitting, (b) with splitting.*

Table 4.6 summarises the simulated temperature at both sides of the five TEG modules with and without splitting, together with the aspect ratio of each module.

Table 4.6: *The simulation results of the hot and cold side temperatures and temperature difference across the TEG modules with and without splitting.*

					NS			WS		
Module	**A (mm^2)**	**L (mm)**	**N**	**2N.A/L (mm)**	**T_h (C)**	**T_C (C)**	**ΔT**	**T_h (C)**	**T_C (C)**	**ΔT**
6x6	**0.64**	**1.5**	**7**	**6**	53.5	10.7	42.8	39.8	10.8	29
9x9	**0.64**	**1.5**	**17**	**15**	51.1	11.7	39.4	36.8	11.5	25.3
15x15	**1.00**	**1.3**	**31**	**48**	39.4	11.7	27.7	30.7	11.7	19.0
20x20	**1.00**	**0.8**	**71**	**178**	24.8	12.0	12.8	19.6	12.1	7.5
30x30	**1.00**	**2.0**	**127**	**127**	24.5	10.8	13.7	20.0	10.9	9.1

As mentioned earlier, the hot side temperature of the TEG module can be calculated theoretically using Equation 3.15. Figure 4.19 compares ΔT obtained by simulation, experiments, and theoretical calculation without and with splitting for all modules.

(a)

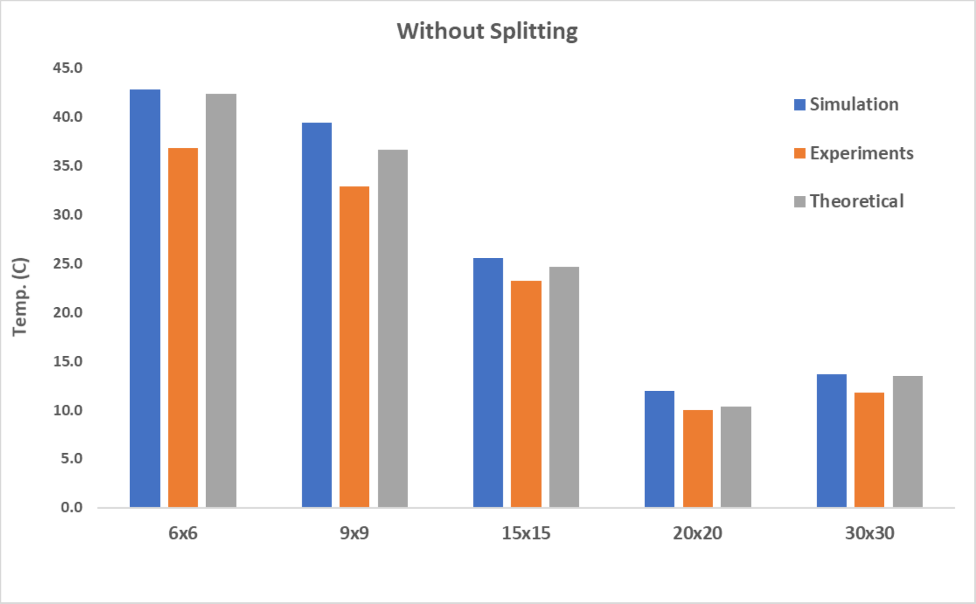

(b)

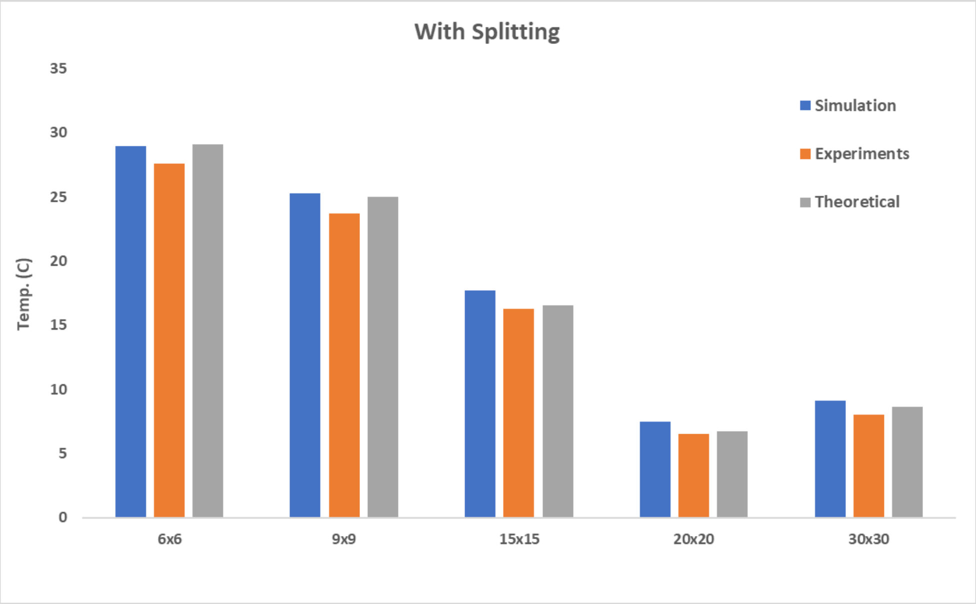

Figure 4.19: *ΔT across TEG modules obtained from simulation, experiments, and theoretical calculations: (a) without splitting, (b) with splitting.*

Figure 4.19 show a reasonably good agreement among the three methods for the results both with and without splitting. The theoretical results are higher than experimental results on average by 10% and 5% for without splitting and with splitting, respectively. This deviation is expected because theoretical calculation assumes ideal conditions. The simulation results are slightly higher than the theoretical results, which is unexpected because the simulation should be closer to the experimental results. Nevertheless, the deviations are fairly small, and the results are acceptable.

4.5 Power Production of the Hybrid System

Based on the spectral splitting arrangement, the total power output of the hybrid system is simply the sum of the power output of the solar cell and the power output of the TEG. As described in Section 3.3.1, the area illuminated by the reflected beam of the hybrid system is 55mm x 55mm. Due to the limited availability of an InGaP cell of the correct size and number, the strategy is instead to measure the power output from a small cell (10mm x10mm) and scale-up to the whole illuminated area (i.e., 55mm x 55mm). However, the uniform illumination area of the solar simulator that was employed is only guaranteed within 40mm x 40mm, in accordance to manufacturer specifications of Class ABB solar simulators [137]. To obtain a realistic scaling factor of the constructed hybrid system, a monocrystalline cell (c-Si) with an area of 55mm x 55mm was placed on the reflected beam illuminated area to measure the power output under irradiance of 1 sun (1000 W/m^2) with and without splitting. A small c-Si cell, which has the same size as the InGaP cell (i.e., 10mm x 10mm) was prepared from the same batch as the larger cell and tested under the same conditions. The results are shown in Table 4.7.

Table 4.7: *Power output of large PV cell compared to small PV cell with and without splitting.*

	Small Cell	Big Cell Test 1	Big Cell Test 2	Big Cell Test 3	Ave.	$P_{big\ cell}/P_{small\ cell}$
c-Si cell without splitting Power (mW)	13.1	284.9	282.4	280.8	282.7	21.6
c-Si cell with splitting Power (mW)	6.2	147.5	145.9	145.9	146.4	23.6

It can be seen from Table 4.7 that the large cell produces a power output that is 22.6 times (on average) of the small cell. This indicates that the power output of a InGaP cell with the size of the illumination area (55mm x 55mm) can be estimated from the power output measured from the small InGaP cell by multiplying the derived scaling factor of 22.6. It should also be noted that the geometrical scaling factor based on the ratio of large cell area to the small cell area is 30.25, which is about 30% higher than the realistic scaling factor determined from this experiment. The possible influence of ununiform light distribution near the edge of illumination area is usually more significant for a large cell compared to a small cell.

The InGaP cell that was used in this research produced 14.1 mW under illumination by the reflected beam from the dichroic mirror (see appendix 4.6). Because the PV cell is decoupled from the thermoelectric generator, the size and the geometry of the TEG module has no effect on PV cell's power production. The TEG module (15x15) that was used in the experiments produced 6.0 mW after the copper rod attached to it was illuminated by the transmitted beam through the dichroic mirror (see Appendix 4.7). The efficiency of the hybrid system (η_{PV-TE}) can be calculated by the following equation:

$$\eta_{PV-TE} = \frac{P_{PV-TE}}{G_{in}} \tag{4.2}$$

where $P_{PV\text{-}TE}$ is the total hybrid system output power and G_{in} is the solar irradiance on the dichroic mirror. Table 4.8 summarises the results that were obtained.

Table 4.8: *Bare PV cell, TEG module (15x15) and hybrid system power production.*

	PV (10x10mm) Experimental	PV (55x55mm) Calculated	Power Increase	η_{PV}	η_{TE}	η_{PV-TE}
Bare (InGaP) cell power (mW)	14.1	318.7				
TEG (15x15) Power (mW)	6.0	6.0				
Hybrid system Power (mW)		324.7	1.9%			
Efficiency (η)				12.2%	0.6%	12.4%

The hybrid system results in an increase of the total power output by 1.9% when using a thermoelectric module of 15x15 mm (for further detail of the geometry, see Chapter Three (section 3.3)). However, an increase of 3.3% in the power production can be achieved if an optimised TEG geometry for maximum power output is used, as will be detailed in Section 4.6. The efficiency of the hybrid system is 12.4%, which is an increase of about 2% in efficiency compared to the bare cell. This clearly demonstrates the advantage of the hybrid system.

4.6 Further Optimisation

The power output from the TEG of the hybrid system may be further increased through geometry optimisation of the TEG. Five commercially available thermoelectric modules (TEGs) of different geometries were selected for this study. The aim was to find the optimum thermoelement length and width of the thermoelectric module to achieve the maximum power output. The optimisation procedure was performed based on the theory outlined in Chapter Three.

An Excel sheet was developed (see Appendix 4.4 for details) based on Equation 3.15 to solve for the thermoelectric hot side temperature (T_h) iteratively. Once the (T_h) is determined, the power output of the thermoelectric generator was calculated using Equation 3.29 and the corresponding plots were generated for each TEG to determine the optimum thermoelement length/width from the peak of the plots.

The optimisation study makes the following assumptions:

- The cold side temperature of the TEG and the ambient temperature are the actual temperatures at the steady state that were obtained experimentally.
- The irradiance shone on the hybrid system is 1000 W/m^2 (1 sun).
- For simplicity, the temperatures across thermoelectric modules were calculated under the open-circuit condition rather than the closed-circuit condition.

The parameters that were used in calculations are listed in Table 4.9.

Table 4.9: *Parameters used in geometrical optimisation of TEG modules [173-176].*

Parameter		Value	Unit
h	**Convective heat transfer coefficient**	**17.0**	**Wm^{-2}K^{-1}**
ε	**Emissivity**	**0.7**	
σ	**Stefan-Boltzmann constant**	**5.7E-08**	**W/m^{2}K^4**
k	**Thermal conductivity**	**1.5**	**W.m^{-1}K^{-1}**
α	**Seebeck coefficient**	**185.0**	**μV/K**
ρ	**Electrical resistivity**	**1.0E-05**	**Ω.m**
n	**Electrical contact parameter**	**0.0001**	**m**
r	**Thermal contact parameter**	**0.2**	
Lc	**Ceramic thickness**	**0.00075**	**m**

This work will first investigate the length optimisation while keeping the width unchanged and it will then investigate the width optimisation while keeping the length unchanged, and it will finally determine the optimal value from the outcomes of both optimisation processes.

4.6.1 Optimising Thermoelement Length for Maximum Power Output

Using the parameters listed in Table 4.9, the model built in the Excel performs an iterative procedure to solve the steady-state absorber temperature (also the hot side temperature of thermoelectric module) that satisfies Equation 3.15. Figure 4.20 shows the calculated temperature difference across thermoelectric module as a function of thermoelement length for the five modules without spectral splitting. The results show that the temperature difference across the thermoelectric module increases as the thermoelement length of the module is increased. This figure also shows that the hot side temperature increases more quickly for small modules compared to large modules for thermoelement lengths less than 1.5 mm. This happens because the thermal resistance of small modules increases quickly as the thermoelement length increases, which results a quick increase in the temperature difference until their reach the state-state. The thermal resistance of large modules increases slowly as the thermoelement length increases, and there is consequently a slow increase towards the steady state temperature difference.

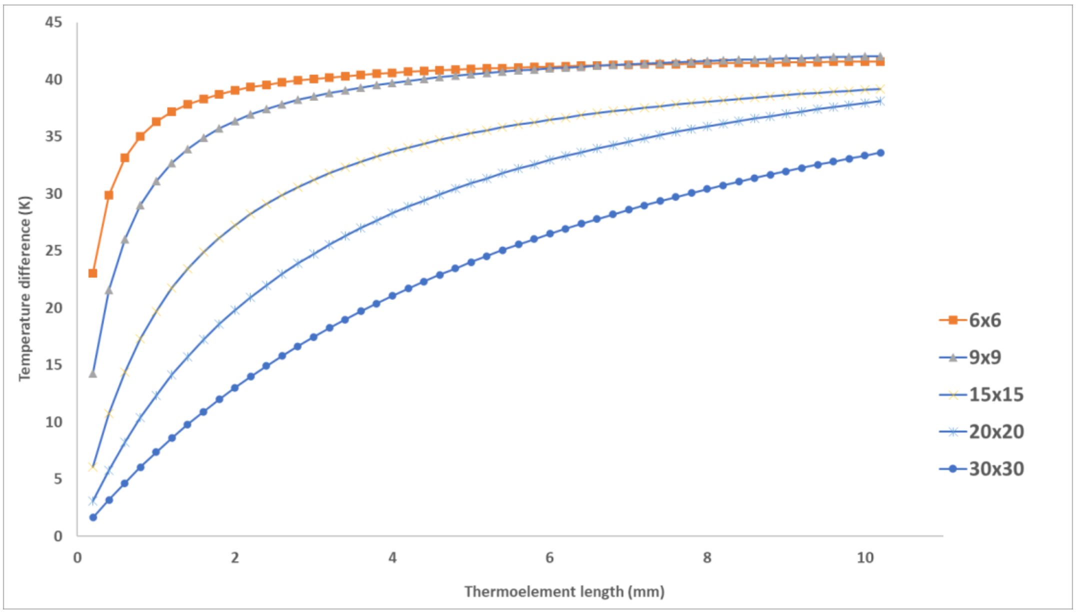

Figure 4.20: *The temperature difference across thermoelectric module as a function of thermoelement length for all 5 TEG modules without spectral splitting.*

The Excel model can also calculate the power output of the TEG for the corresponding temperature difference at each value of the thermoelement length by solving Equation 3.29. The maximum power output and corresponding optimum thermoelement length determined from Excel model calculation for all five modules are listed in Table 4.10.

Table 4.10: *The optimum thermoelement length for all modules. Note that power is based on the full spectrum illumination (without splitting).*

Module	N	W (mm)	L (mm)	A*2N/L (mm)	Theo. Power @ actual L (mW)	Theo. Power @ opt. L (mW)	Optimum L_{TE} (mm)
6x6	7	0.8	1.5	**6**	**4.8**	**5.5**	**0.8**
9x9	17	0.8	1.5	**15**	**9.6**	**9.8**	**1.2**
15x15	31	1.0	1.3	**48**	**12.8**	**14.2**	**2.2**
20x20	71	1.0	0.8	**178**	**7.7**	**20.5**	**4.2**
30x30	127	1.0	2.0	**127**	**13.2**	**23.1**	**7.6**

Figure 4.21 shows the power output as a function of the thermoelement length for five different modules without spectral splitting. The results show that the power output of small modules (e.g., 6x6 and 9x9) increases quickly as the thermoelement length increases, until it reaches the

peak at an optimal length, it then starts to decrease gradually. However, the power output of the large modules (e.g., 20x20 and 30x30) increases gradually with increasing length and then starts to decrease gradually after passing the peak value at a longer length (> 3.0 mm). Therefore, the optimum length for the biggest module (30x30) is 7.6 mm. For medium size thermoelectric module (15x15), the maximum power output is achieved at a reasonable length of 2.2 mm. Compared to the actual (15x15) module that has a thermoelement length of 1.3 mm, an 11% increase in the power output can be achieved if the thermoelement length is increased from 1.3 mm to 2.2 mm. This can be seen from the data presented in Table 4.10. In general, the optimal thermoelement length is proportional to the number of thermocouples (N) in a module. N is larger when the optimal thermoelement length is longer, which is due to the fact that the temperature difference across a module is related to the ratio of thermoelement length to the product of thermocouple number and cross-sectional area of the thermoelement.

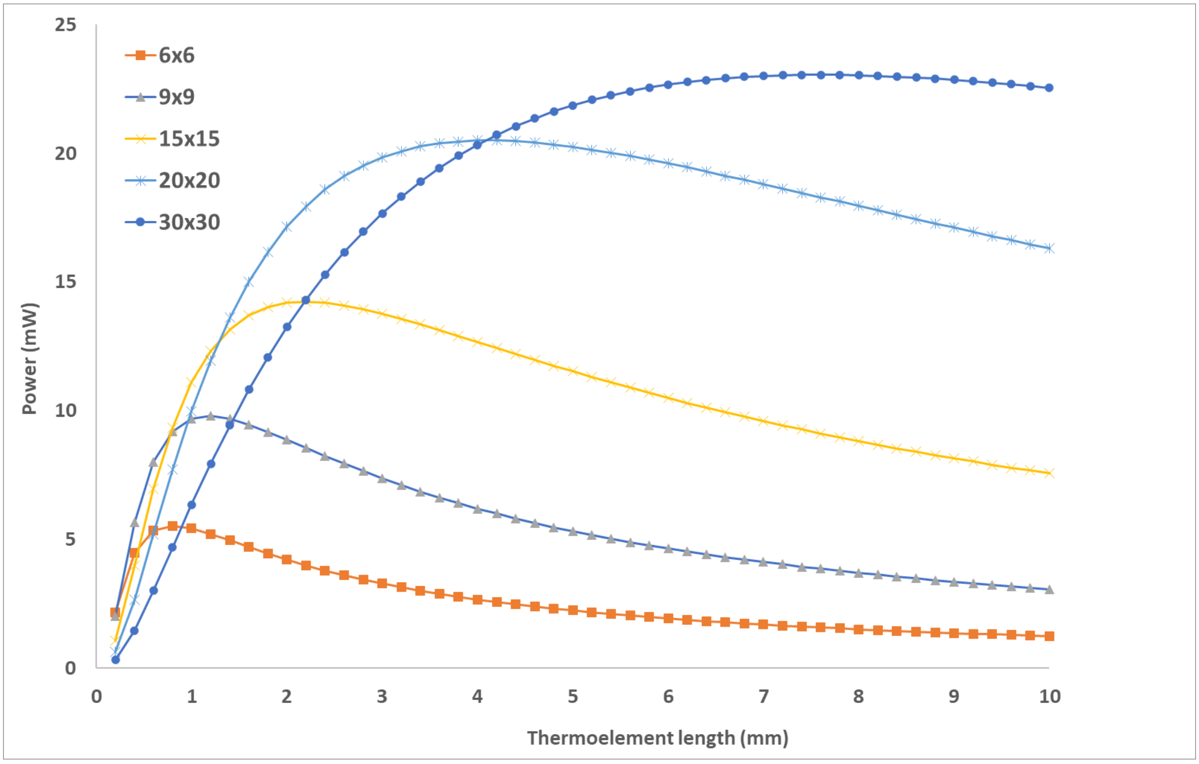

Figure 4.21: *Power output as a function of thermoelement length for all TEG modules without splitting.*

4.6.2 Optimising Thermoelement Width for Maximum Power Output

Similar to determining the optimal thermoelement length to obtain the maximum power output for given thermoelement width (the actual width of commercial modules), it is also possible to determine the optimal thermoelement width for a given thermoelement length (i.e., the actual length of commercial modules). The optimised widths that were obtained are listed in Table 4.11.

Table 4.11: *Optimum thermoelement width for the selected modules.*

Module	N	Actual Width (mm)	L (mm)	A*2N/L (mm)	Theo. Power @ actual W (mW)	Theo. Power @ opt. W (mW)	Optimum W_{TE} (mm)
6x6	7	0.8	1.5	**6**	**4.8**	**13.3**	**2.35**
9x9	17	0.8	1.5	**15**	**9.6**	**14.5**	**1.50**
15x15	31	1.0	1.3	**48**	**12.8**	**12.8**	**1.00**
20x20	71	1.0	0.8	**178**	**7.7**	**11.9**	**0.50**
30x30	127	1.0	2.0	**127**	**13.2**	**19.0**	**0.55**

Figure 4.22 shows the power output of each module compared with the thermoelement width without splitting. It can be seen that modules with a small aspect ratio (e.g., 6x6) have a wider optimal thermoelement width. A 55% and 44% increase in the power output can be obtained for modules 20x20 and 30x30, respectively, if the thermoelement is optimised to their respective optimal width. The power output cannot be further increased for the medium-sized module (15x15) because the actual width is coincidently the same as the optimal value. Because the sizes for the smaller modules (6x6 & 9x9) do not allow for wider thermoelement widths due to the limitation of ceramic size, the maximum width of the thermoelements for both modules cannot exceed 1.0 mm. At this width, the power outputs for both modules are 6.8 mW and 12.5 mW, respectively. This is an increase by 42% and 30% for module 6x6 and module 9x9 compared with the power obtained with their actual widths, respectively.

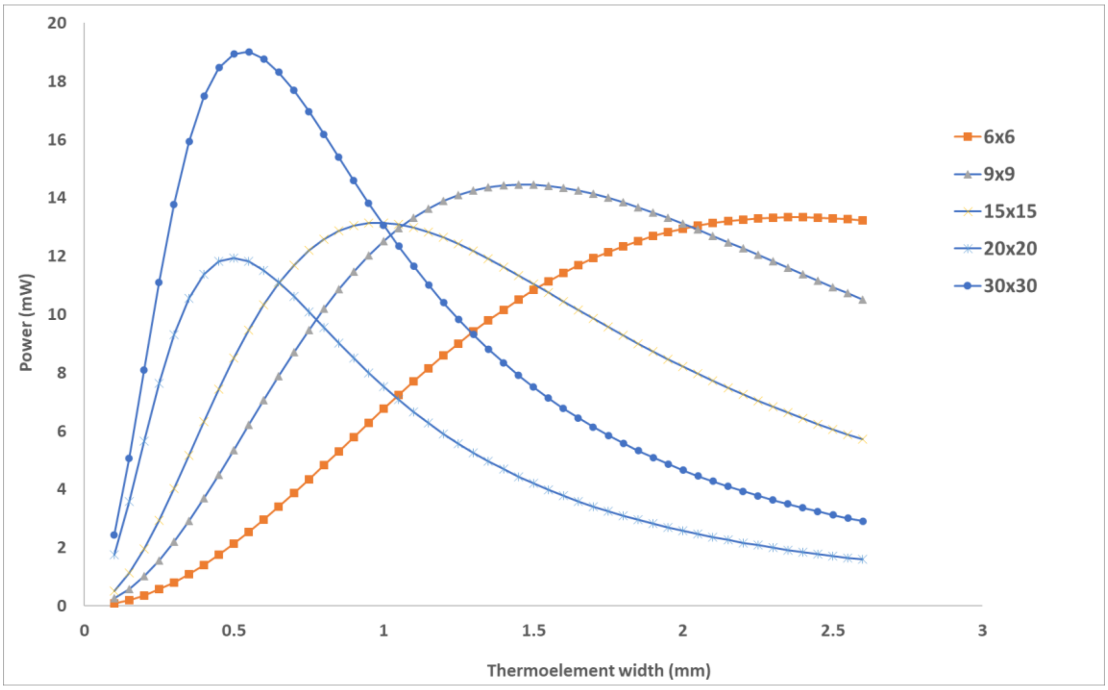

Figure 4.22: *Power production as a function of thermoelement width for all TEG modules without splitting.*

4.6.3 Optimisation Considering Thermoelement Length and Width

The work in this section considers simplistic optimisation for the five selected modules, in which the module geometry is kept broadly unchanged (e.g., the thermocouple numbers, module surface area, as well as the material properties, and input thermal energy, etc). The only changes are associated with thermoelement length and width to ensure that the suggested changed can easily be implemented by the manufacturers. For example, the optimal thermoelement widths calculated above for modules 6x6 and 9x9 are 2.35mm and 1.5mm, respectively. However, due to restriction of the module total area, the maximum width that can be practically set for these two modules is 1.0mm. Therefore, the width is selected to approach the ideal theoretical value as far as possible but is restricted by the practical limit. Following this strategy, the new optimal thermoelement lengths for the five modules were calculated after the appropriate width of thermoelements had been chosen. The results show that a further increase in power production is achieved at the new optimised thermoelement length for modules (6x6 and 9x9). Compared to the first optimised lengths, an increase in the power output by 31% and 22% were achieved for modules 6x6 and 9x9, respectively. For the medium size module (15x15), there was no increase in power production because the new thermoelement length is the same as the one in the first optimisation. However, the results show a sharp decrease in power output of 42% and 18% for the larger modules (20x20 and 30x30) at the new optimised length, respectively. This happens because at a given thermoelement length, reducing the width (cross-sectional area) of the thermoelement will increase the thermal resistance and will simultaneously increase the electrical resistance. Given that increasing the thermal resistance will have a positive effect on power output by increasing ΔT, increasing electrical resistance will have a negative effect because it will limit the current flow through the leg. Both modules (20x20 and 30x30) have very long optimal thermoelement length, where the increase in ΔT as a result of high thermal resistance is limited if compared with electrical resistance, and hence there is a reduction in the power output. Therefore, the original optimised thermoelement lengths will be kept. Table 4.12 summarises the optimised thermoelement lengths with the percent increase in power production.

Table 4.12: *The optimum thermoelement length for all modules and the percent increase in power production.*

Module	W (mm)	Optimised L (mm)	Thermoelement Volume increase Opt. vs Actual (%)	Power (mW) Theoretical Actual L	Power (mW) Theoretical Opt. Length	% Increase	Power (mW) Experimental
6x6	1.0	1.0	4	4.8	7.3	51%	4.9
9x9	1.0	1.4	56	9.6	11.9	24%	10.4
15x15	1.0	2.2	69	12.8	14.2	11%	11.9
20x20	1.0	4.2	425	7.7	20.5	166%	7.0
30x30	1.0	7.6	280	13.2	23.1	74%	13.1

There is a significant increase in the power output for module (20x20) because this module has a very short thermoelement length (0.8 mm), which is significantly shorter than the optimal value (4.2 mm). Figure 4.23 shows the increase in the volume of the thermoelement material and power production at optimum length compared to the actual lengths.

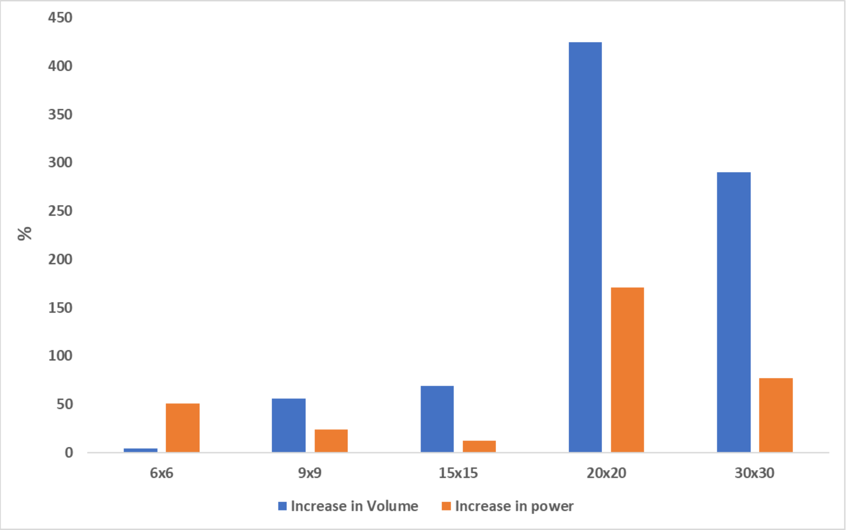

Figure 4.23: *Thermoelement volume increase compared to power increase at optimum length for all modules.*

Figure 4.23 clearly shows a high increase in material volume for bigger modules compared to small modules. The increase in material volume for the smallest module (6x6) is very minor if compared to the increase in its power output. In general, the increase in power output for all modules should be a trade-off between achieving a higher power production and using a less expensive thermoelectric material.

4.6.4 TEG Power Output in Ambient and Vacuum Environments

Operating the hybrid system in a vacuum can reduce the heat loss to the surroundings by convection and result in a higher temperature at the hot side of thermoelectric generators, and hence a higher power output. This section studies the effect of operating the TEG in vacuum on its power output and optimal thermoelement length.

4.6.4.1 Effect of a Vacuum on Power Output for Commercial TEGs

The power output of five commercial TEGs with actual thermoelement length was calculated at ambient and in vacuum. In the ideal case it is assumed that the convective heat loss is completely eliminated by operating the hybrid system in vacuum. Figure 4.24 shows the power outputs of five TEGs as a function of the aspect ratio for operation in ambient and vacuum. It can be seen that the modules with a low aspect ratio exhibit a significant increase in their power output when operated in vacuum, which is 80% and 34% for module (6x6) and (9x9), respectively. Meanwhile, those with high aspect ratio show less increase, which is 13%, 10% and 7% for module (15x15), (30x30) and (20x20), respectively. Because the large size modules (15x15, 20x20 and 30x30) have large aspect ratios that resulted in a smaller temperature difference across the modules, the increase in the temperature difference due to eliminating the convective heat is relatively small and there is consequently less improvement when compared to the modules with a small aspect ratio.

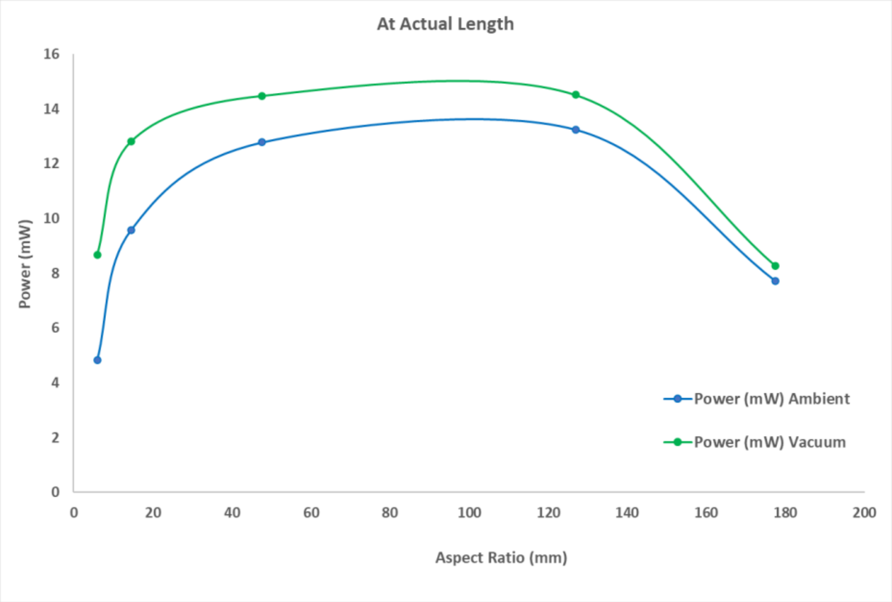

Figure 4.24: *Power output vs. aspect ratio in ambient and vacuum for 5 modules with actual thermoelement length.*

4.6.4.2 TEG Modules Optimised for Thermoelement Length

The effect of vacuum operation on the power output was also investigated for five conceptual modules that have the optimised length and cross-sectional area that is specified in Table 4.13. The power output of those modules was calculated in vacuum by neglecting all of the convective heat losses. The results are shown in Figure 4.25, together with the power outputs of the modules operated at ambient for comparison. Increases of 66%, 28%, 30%, 54% and 48% were obtained for modules 6x6, 9x9, 15x15, 20x20 and 30x30, respectively. A major difference between Figure 4.25 and Figure 4.24 is that the power outputs of the conceptual modules with large aspect ratios also increased significantly when operated in vacuum. This happens because the thermoelement length of the conceptual modules is chosen to be at the optimal value, which is much longer than those of the actual modules. For those modules with optimal thermoelement length, the convective heat loss becomes significant because of the large temperature difference across the modules, which corresponds to a longer thermoelement length.

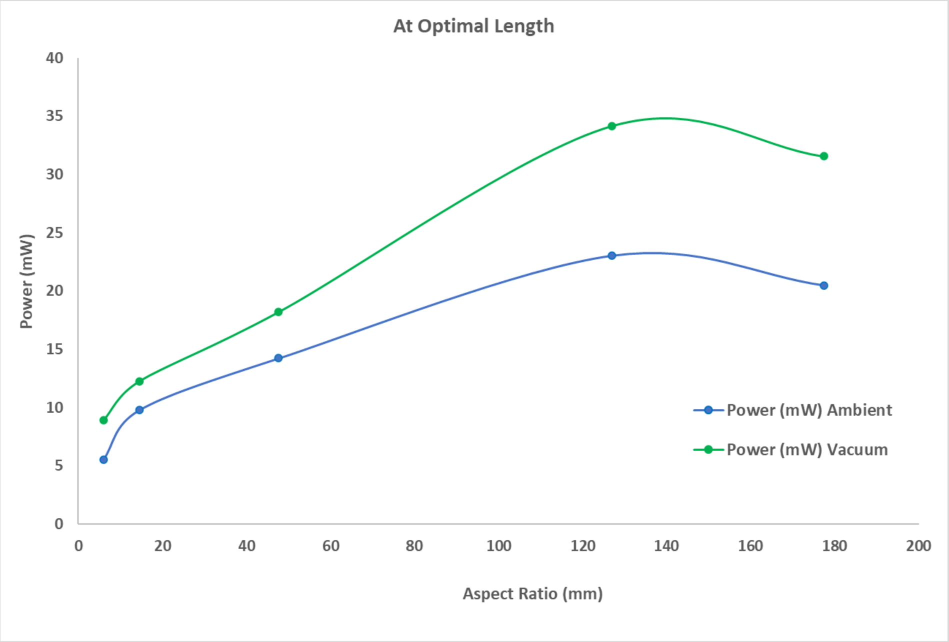

Figure 4.25: *TEG modules theoretical power output vs. the aspect ratio in ambient and vacuum environment at optimum thermoelement length.*

In general, operating the hybrid system under vacuum can improve the power output of the TEGs.

4.7 Advantage of an InGaP Cell for the Hybrid System

InGaP cells were used in this study because they match the cut-off wavelength of commercially available dichroic mirrors. However, an InGaP cell also proved to be a good choice for hybrid system, even if the matching dichroic mirrors are available for other types of solar cells. This happens because an InGaP cell can achieve a power conversion efficiency that is similar to other types of solar cells, but they only use a narrow spectrum range, which leaves more energy in the rest of spectrum for use by the TEG. This is associated with the energy band gap of semiconductor materials. Table 4.13 shows the available solar energy in the visible spectrum and infrared spectrum for different semiconductor materials after spectral splitting using the matched dichroic mirrors. GaP and Ge are not good solar cell materials but are included here to demonstrate spectrum splitting because they have different energy band gaps. It can be seen that InGaP has an energy band gap of 1.9 eV, which corresponds a cut-off wavelength of 652 nm. Consequently, it provides more energy over the infrared spectrum than other good solar cell materials (e.g., Si, GaAs and CdTe). This enables it to produce more heat for the TEG, which will then generate more power output.

Table 4.13: *Solar energy in PV and TE spectrums after spectral splitting for different semiconductor materials.*

Material		Band Gap Energy (eV)	Band Gap wavelength (nm)	Energy directed to PV (W)	Energy directed to TE (W)	Total Energy (W)	Compare to InGaP	
							Diff.	%
GaP	Gallium phosphide	2.26	548	259.0	738.6	997.6	152.1	25.9%
InGaP	Indium gallium phosphide	1.9	652	411.1	586.5	997.6	0.0	0.0%
CdTe	Cadmium telluride	1.5	826	613.3	384.3	997.6	-202.3	-34.5%
GaAs	Gallium arsenide	1.43	867	652.8	344.8	997.6	-241.7	-41.2%
Si	Silicon	1.11	1117	809.0	188.6	997.6	-397.9	-67.8%
Ge	Germanium	0.67	1850	957.7	39.9	997.6	-546.6	-93.2%

4.8 Conclusion

The parabolic trough PV-TE hybrid system has been investigated in this chapter. Light splitting was achieved using a dichroic mirror that has a cut-off point matches the bandgap of the PV cell under investigation (i.e., InGaP). This chapter started by testing the splitting effect on the investigated PV cells (i.e., c-Si, GaAs, and InGaP). The results show that the InGaP cell has a better performance compared to silicon and GaAs cells because its bandgap matches the mirror cut-off point. Moreover, the splitting effect on PV cell operating temperature was examined and the results revealed that light splitting has very minor effect on InGaP cell for power output and cell operating temperature. However, a considerable increase in c-Si and GaAs operating temperature, and a significant and remarkable reduction in power output were observed for the two cells. The integration of a TEG module (15x15) with the InGaP in PV-TE hybrid system was investigated experimentally and the results show an increase of power output and efficiency by 1.9% and 2.0%, respectively.

The validation of the theoretical work by experimental study showed good agreement between the theoretical and experimental results, with an average deviation of 10% and 5% for without splitting and with splitting, respectively. A model was developed to optimise the TEG's geometry for maximum power output based on the equations detailed in Chapter Three. The results demonstrate a remarkable increase in TEG power output if geometry is optimised. The improvement for power production, for module 30x30 for example, can be increased by 74% if module thermoelement length increased to 7.6mm. However, in practice an optimised geometry has to be a trade-off between achieving a large power output and using minimal thermoelectric material. Operating the hybrid system under vacuum was also investigated to examine eliminating the convective heat loss to surroundings on the TEG power output. The results show that a significant increase in power output under vacuum can be achieved. If conceptual TEG modules are considered—the increase of power output may reach 66%.

Chapter Five: PV-TE Hybrid System using Dichroic Mirror and Parabolic-Dish Concentrator

5.1 Introduction

A laboratory-scale hybrid system that uses a parabolic dish was designed and constructed. A dichroic mirror splits the spectrum to direct the visible light spectrum to the PV cell and the infrared spectrum to thermoelectric generator. The system's performance was evaluated in comparison to the hybrid-trough system. The evaluation was based on the thermal part of the system (i.e., TEG power output) because the PV cell is decoupled from the thermal part and its electrical performance is common between both systems. Different dish designs were evaluated using SolidWorks thermal simulation for maximum heat generation optimisation. The thinner copper rod's performance was also evaluated using simulation. Finally, the power production of the hybrid-dish system was evaluated in comparison to the hybrid-trough system and their economic performance was compared.

5.2 Performance of the dish-hybrid system

In the same way as the trough-hybrid system was evaluated, the dish-hybrid system was assessed based on its PV cell's electrical performance, the thermal output of heating the copper absorber and the TEG's power output. The slope technique that was described in Chapter 3 is employed to determine the heat absorbed by the copper absorber and the heat lost to the surroundings. The total power output of the dish-hybrid system is then calculated and compared with the bare cell.

5.2.1 First receiver (PV cell)

Figure 3.17 shows a schematic of the dish design experimental setup, where the dichroic mirror splits light before it reaches the concentration, making the thermal part (TEG) and photovoltaic part (PV) two separate systems. Because the two systems are decoupled from each other, the power output produced by the PV cell of this dish system will be the same as that of the trough system obtained in Section 4.2.

5.2.2 Second receiver (TEG module)

The copper absorber in the dish-hybrid system is aligned vertically, as shown in Figure 3.17, to receive the reflected rays from the parabolic dish. The heated copper rod, which is shorter in the dish design (as elaborated in Chapter 3), will deliver the heat to the TEG attached at the bottom of the copper absorber. The thermal output, power output and total hybrid system will be discussed in the following sections.

5.2.2.1 Thermal output of the parabolic-dish concentrator

The slope technique that was described in Section 4.3 was employed to determine the heat generated by the copper absorber to heat the hot side of the TEG. This technique was explained in Chapter 3 and verified in Chapter 4, where the heat generated by the copper in the trough-hybrid system was assessed. In this section, the same technique was employed to find the heat generated by the copper in the dish-hybrid system.

The following four cases were investigated to determine the heat generation by the copper absorber:

- No concentration and no splitting (NCNS),

- With concentration and no splitting (WCNS),
- No concentration and with splitting (NCWS),
- With concentration and with splitting (WCWS).

These four cases have different intensity and spectrum ranges, which were analysed using the slope technique to determine the heat generated by the absorber from irradiance. Figure 5.1 shows the temperature raising profiles for the four cases, which were measured until they had reached the corresponding steady state. A sharp increase in temperature during the initial few minutes of illumination is apparent for all four curves. However, its rate of increase depends on the intensity of the irradiance received by each case. The cases without concentration exhibit curves that are less steep than those with concentration. It can also be seen that spectral splitting by the dichroic mirror reflected about 53% of irradiance power to the PV cell, leaving about 47% of irradiance power to reach the absorber, and hence flatter curves compared to without spectral splitting.

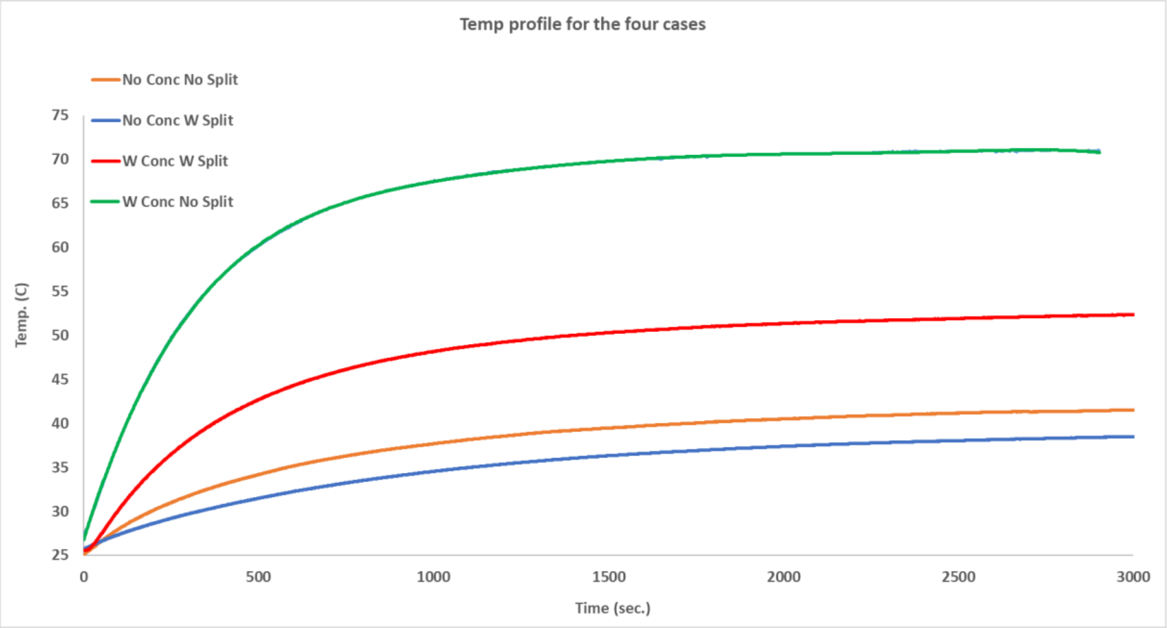

Figure 5.1:*Temperature profiles of the dish system for all cases without attaching the TEG.*

By determining the slope ΔT/Δt from curves in Figure 5.1, Equation 3.11 was used to calculate the heat retained in the absorber at a given time. Using a mass (m) of 39.9 g for the copper absorber (i.e., shorter copper rod for the dish system and hence less mass) and a specific heat capacity (Cp) of 0.385 (J/g.°C) for the copper, the heat retained in the absorber for the four cases at different time are shown in Figure 5.2. By extrapolating the curves (solid lines) to intercept with the y-axis based on the experimental data (solid dots), the heat absorbed by the copper absorber (Qa) can be determined at the y-intercept (or x= 0), where the losses to the surroundings are negligible.

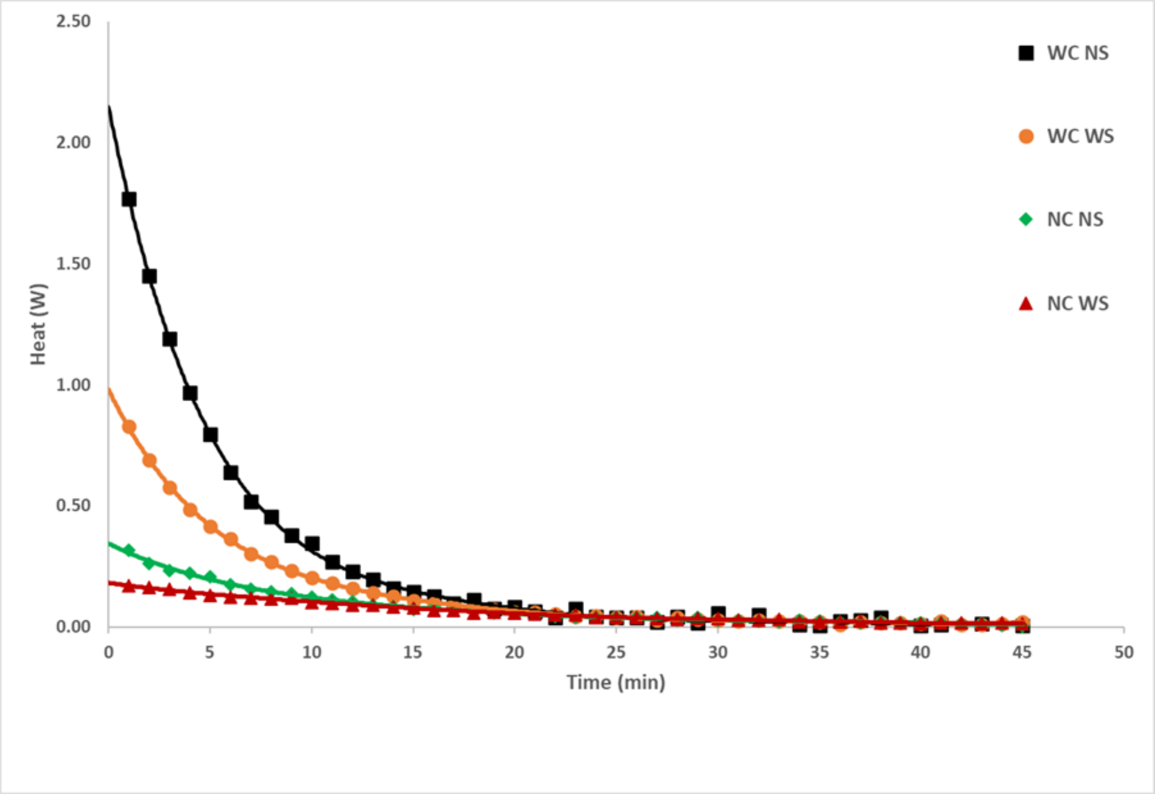

Figure 5.2: *Heat retained by the copper absorber (Qa) extrapolated to hit the y-axis for all cases.*

Table 5.1 shows the values of the heat generated by the copper absorber (Qu) for the four cases, as determined from Figure 5.2 (at y-intercept), compared with the light power available from the simulator and concentrator. Table 5.1 shows a good agreement between the values from the slope technique and the solar simulator irradiance reading by the solar survey, taking into account the uniformity of the solar simulator mentioned in Chapter 3 of (0.864). Low illumination on the copper absorber for the third case (without concentration and with splitting) is most likely to be the reason behind the high deviation between the experimental and theoretical results.

Table 5.1: *Comparing the heat generated by the copper absorber (Qu) with solar simulator irradiance for all cases.*

	Qu (W)	**Simulator Irr. (W)**	**Drop (%)**
Without concentration and without splitting	0.344	0.358	3.8%
With concentration and without splitting	2.145	2.235	4.0%
Without concentration and with splitting	0.182	0.167	-8.8%
With concentration and with splitting	1.0	1.046	4.4%

5.2.2.2 Convective heat transfer coefficient

The convective heat transfer coefficient surrounding the copper absorber of the dish system can be determined in the same way as the calculations done in Section 4.3.2. The convective heat transfer coefficients for the four cases were calculated at the steady state using the Excel sheet (Appendix 4.2) that was created based on Equation 3.09 and based on the data obtained from the above experiment.

At the steady state, the heat produced in the copper absorber **(Q_u)** is equal to the heat lost to the surroundings **(Q_l)**. The convective heat transfer coefficient (h) was determined from the best fitting of the calculated value to the experimental data using the calculation procedure that was developed in Excel (see Appendix 4.2). Table 5.2 shows the experimental and calculated values of the heat absorption and steady state temperatures of the copper absorber for the four cases, together with the corresponding convective heat transfer coefficient. The convective heat transfer coefficient obtained is between 12.5 W/m^{2}K to 16.5 W/m^{2}K, which is within the range of free convection and is in agreement with the results obtained from the trough system.

Table 5.2: *Convective heat coefficients determined from the best fitting between the calculated and experimental values of absorbed heat (Qu) by the copper absorber.*

	Exp. (Q_u) (W)	Exp. T_{final} (C)	Conv. Heat Coff. (h) to match experiments (W/(m^{2}K))	Theo. (Q_u) (W)	Theo. T_{final} (C)	(Q_u) Diff. (%)	(T_{final}) Diff. (%)
Without concentration and without splitting	0.34	42.3	16.5	0.36	42.0	3.8	0.7
With concentration and without splitting	2.15	71.0	15.5	2.24	71.8	4.0	-1.1
Without concentration and with splitting	0.18	39.9	12.5	0.17	38.7	-8.8	3.0
With concentration and with splitting	1.0	52.1	15.0	1.05	53.0	4.4	-1.7

5.2.2.3 Power output of the TEG module during transit state

The measurements for the dish-hybrid system were undertaken using the medium sized thermoelectric module (15x15). First, the open circuit voltages from the output terminals of the module were recorded as a function of time, from the moment when the light source was switched on to the period when the system reached the steady state. Because the internal resistance of the module was determined by the match load experiment in Chapter 4, the electrical power generated by the TEG was calculated experimentally using Equation (3.28) and theoretically using Equation (3.29). The results for the measurements with and without splitting are shown in Figure 5.3.

(a)

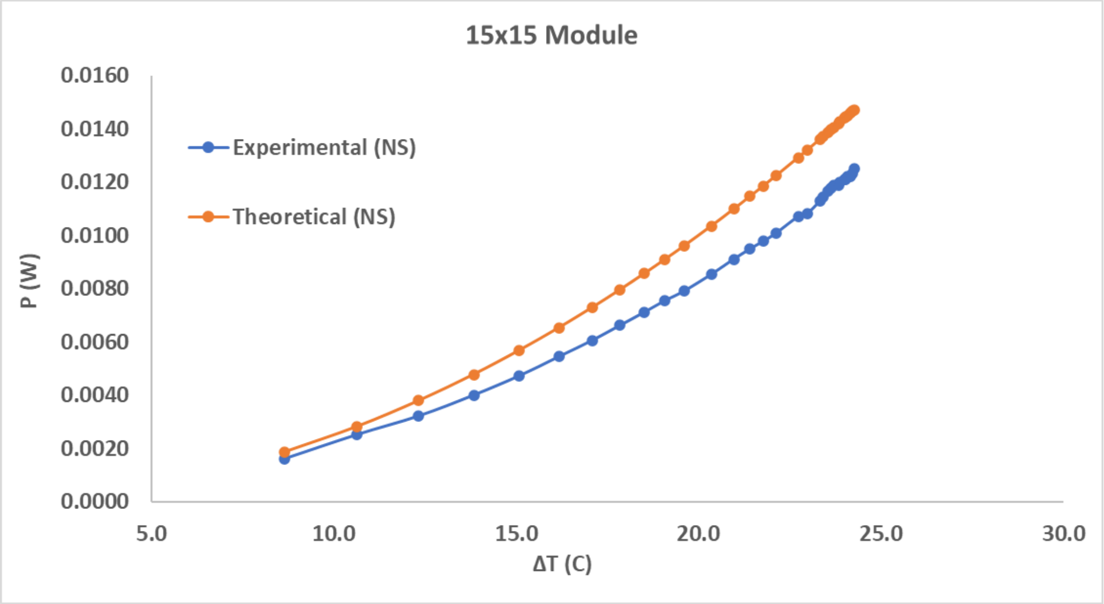

(b)

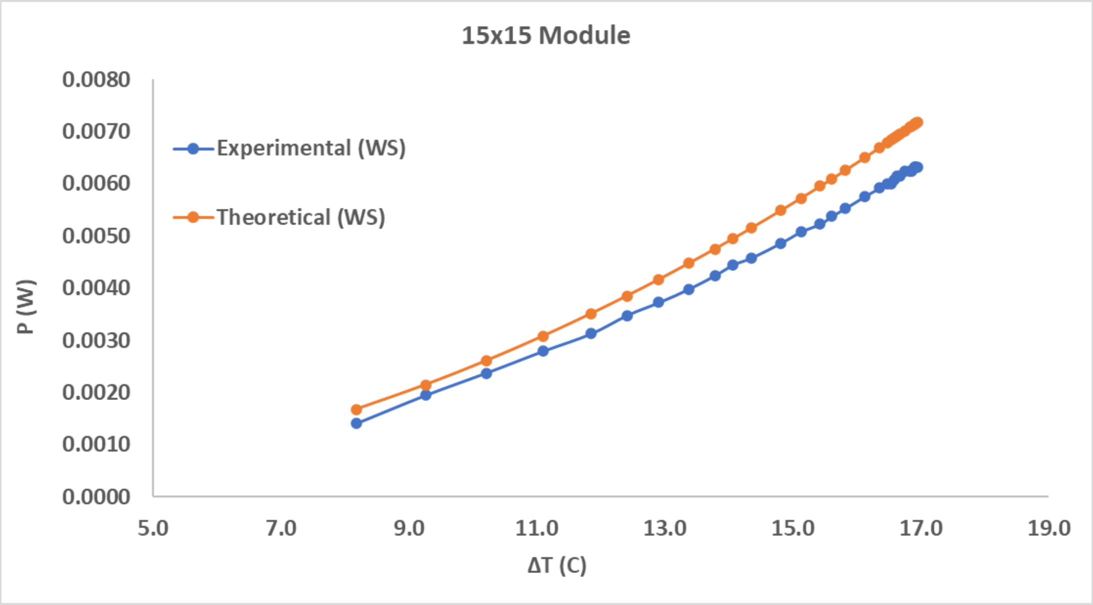

Figure 5.3: *Theoretical and experimental power output of the TEG module (15x15) as a function of ΔT: (a) without splitting, (b) with splitting.*

A reasonably good agreement between experimental and theoretical results can be seen in Figure 5.3. The experimental results are broadly in line with the theoretical calculations—the difference is less than 15% for (a) and 12% for (b). It can be also seen that the difference between the two values (experimental and theoretical) increases with the increase of ΔT.

5.2.2.4 Power output of the TEG module at steady state

The I-V curve and P-V curve of the TEG module investigated in the dish-hybrid system with and without splitting were measured using the characterisation facility described in Section 3.4.2 after reaching the steady state. The results are presented in Figure 5.4.

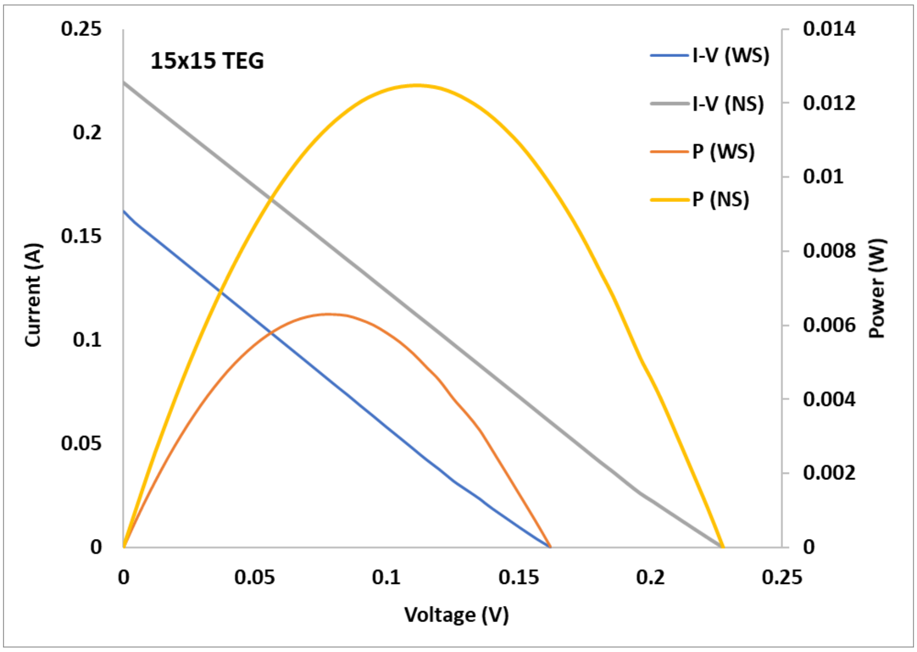

Figure 5.4: *Power and current curves vs. voltage for the TEG module (15x15) with and without splitting.*

In similar way as the trough-hybrid system, the splitting of the light source affects greatly the current, voltage and power output of the thermoelectric generator because 53% of the power of the light spectrum is reflected by the dichroic mirror. However, the power output for the dish system is slightly more than the trough system because of the different geometries of the two systems (which will be elaborated in the following sections).

The power outputs were obtained after the system had reached the steady state, as shown by Figure 5.5. The absorber temperature, which is also the hot side temperature of the TEG, is reduced significantly when the TEG is attached to the absorber. Because the cold side of the

TEG is attached to a water cooler (Figure 3.22), the heat at the cold side of the thermoelectric module was dissipated into the water. Figure 5.5 shows the steady state temperature of the absorber without connecting the module to any load after illuminating the system under 1 sun (1000 W/m^2) with and without splitting.

Figure 5.5: *The temperature profile of the copper absorber attached to a TEG module with and without splitting.*

5.2.2.4.1 The power output of the hybrid system

As mentioned in Section 5.2.1, because the two receivers in the hybrid system (i.e., PV cell and TEG) are decoupled, using different concentrators (i.e., the dish) has no effect on the PV cell's power output. Therefore, the PV cell results obtained with the trough-hybrid system will be employed here.

As can be seen from Figure 5.4, the TEG module 15x15 produces 6.3 mW when it is heated by the transmitted irradiance from the dichroic mirror. Table 5.3 shows the total output of the hybrid system together with the efficiencies of the components and the total hybrid system.

Table 5.3: *Dish system bare PV cell, TEG module (15x15) and hybrid system power production.*

	PV ($10x10mm^2$) experimental	**PV ($55x55mm^2$) scale-up**	**TEG ($15x15mm^2$)**	**Hybrid system**
Power (mW)	14.1	318.7	6.3	325.0
Efficiency (η)		12.2%	0.6%	12.43%

An increase of 2.0% in the total power output of the dish-hybrid system is achieved by using the 15x15 mm thermoelectric module. However, if an optimised TEG geometry for maximum power production is used (as discussed in Section 4.6), a 3.5% increase in the power production can be achieved. The efficiency of the hybrid system is 12.43%, which is an increase of about 2% in efficiency compared to the bare cell.

5.3 Comparison of the two hybrid systems (trough and dish)

This section will compare the two hybrid systems (i.e., trough and dish) in respect to their performance, design, and economic assessment. Because the experiments of the dish-hybrid system use the middle size TEG module (15x15), the results of the trough system employing the same module are used for comparison.

5.3.1 Performance comparison

The performance comparison between the two systems compares the final temperature of the absorbers with and without splitting after reaching the steady state, the power output of the TEG (15x15) attached to the absorber, and the total power output of the hybrid system.

5.3.1.1 The final temperature of the absorber with and without splitting

Figure 5.6 shows the temperature profiles of the absorbers with and without splitting for the trough and dish-hybrid systems, respectively. The temperature profiles were obtained before a TEG module was mounted onto the absorbers.

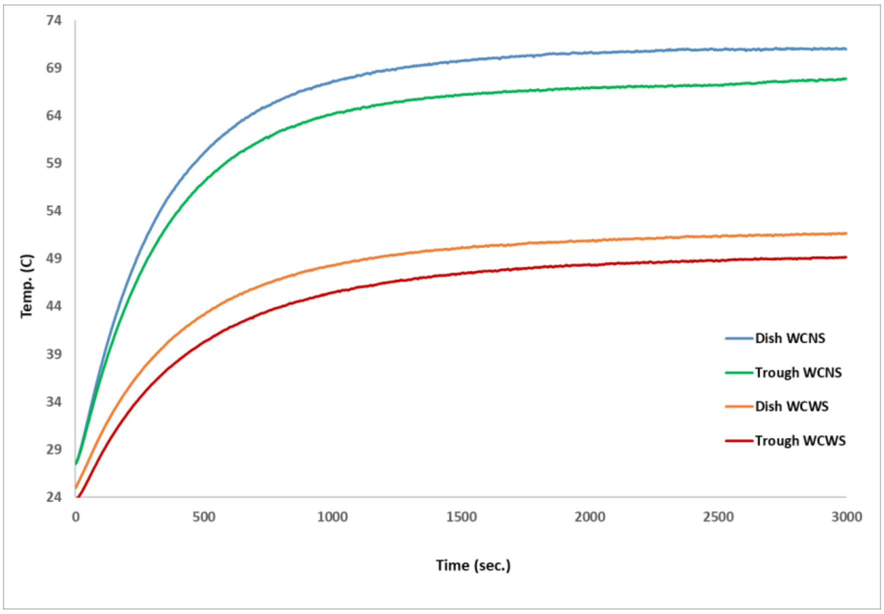

Figure 5.6: *Comparing the absorber steady state temperature for illumination with concentration without and with splitting for the trough and dish concentrators.*

The dish system exhibited a higher steady state temperature for both with and without splitting than the trough system. Because both concentrators have the same reflectivity (95%) and are illuminated with the same light intensity, it is likely that a similar reflected flux will be absorbed by the copper rod. The copper absorbers in both systems have the same dimensions except for the length of the copper rod, which resulted in different absorber surface areas (i.e., 3866 mm^2

for the trough system vs. 3357 mm^2 for the dish system). The steady state temperature is reached when the heat lost to surroundings by convection and radiation is balanced with the heat generated by the absorber **(Q_u)**. Because the heat lost to the surroundings depends on the surface area of the absorber (as known from Equation 3.15), absorber with a smaller surface area will reach higher steady state temperatures.

5.3.1.2 TEG power output

Figure 5.7 compares the power output of the TEG module (15x15) when it is attached to the absorber for both systems with and without splitting.

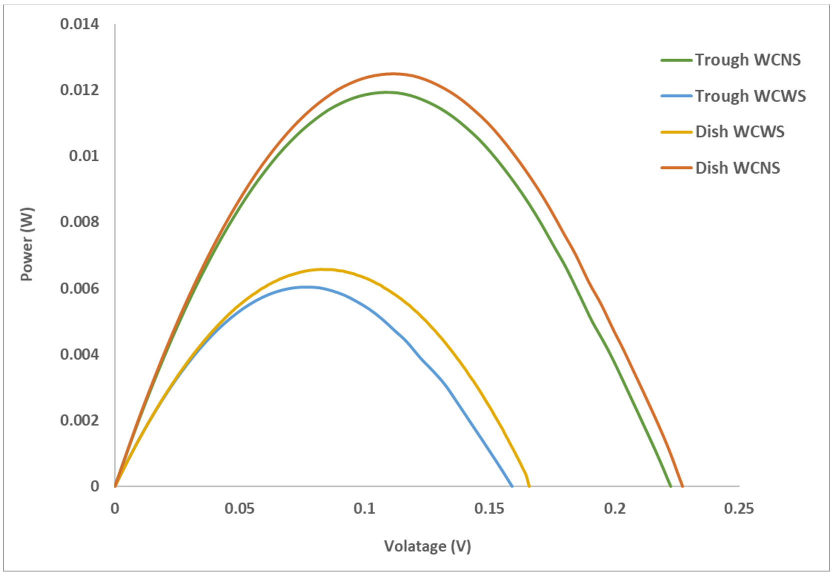

Figure 5.7: *The power output of module (15x15) for both trough and dish systems with and without splitting.*

It is clear from Figure 5.7 that the performance of the dish system is slightly better than that of the trough system, due to the fact that the absorber of the dish system can reach higher steady state temperature than the trough system (as detailed earlier). A higher temperature difference established across the TEG module will result in a higher power output.

5.3.1.3 Total power output of the hybrid system

Because the PV cell is completely decoupled from the TEG (as mentioned earlier), the results obtained for the PV cell in the trough system experiments will be the same as that for the dish system. In other words, the only advantage of one system over the other is the thermal part of the hybrid system. Table 5.4 compares the two hybrid systems, together with the efficiency improvement for both systems compared to the bare cell.

Table 5.4: *A power and efficiency comparison of the trough and dish-hybrid systems.*

	PV (55x55mm) Calculated (mW)	TEG power output (mW)	Hybrid total power output (mW)	Hybrid power increase (%)	η_{PV} (%)	η_{TE} (%)	η_{PV-TE} (%)	Efficiency increase (%)
Trough-hybrid system	319	6.0	325.0	1.9	12.2	0.60	12.44	1.9
Dish-hybrid system	319	6.3	325.3	2.0	12.2	0.63	12.45	2.0

Table 5.4 compares the experimental results between the two hybrid systems (i.e., trough and dish) in terms of power output and systems efficiencies. The two systems have a very similar performance because the only effective difference is the length of the copper rod that receives the reflected rays from both concentrators. Hence, optimising the length of the copper rod of the dish system (as will be detailed in the following sections) can effectively improve the power output of the hybrid system. However, the length of the copper rod of the trough system cannot be optimised because the trough is a line focusing connector, unlike the dish which is a point focusing concentrator.

5.3.2 Design comparison

The two hybrid systems have different concentrators and absorber designs. Therefore, this section will compare their performance using the experimental results based on their design. It will also examine the advantages and disadvantages of each concentrator.

5.3.2.1 Trough design vs. dish design

The advantage of the dish system over the trough system is the surface area of the absorber (as discussed earlier), assuming the same reflectivity of both concentrators and the equal light flux received by the absorbers in each hybrid system. A smaller surface area means that less heat is lost to surroundings and more heat will be available to the thermoelectric generator for power production. Figure 5.8 shows the dimensions of the two absorbers for both hybrid systems.

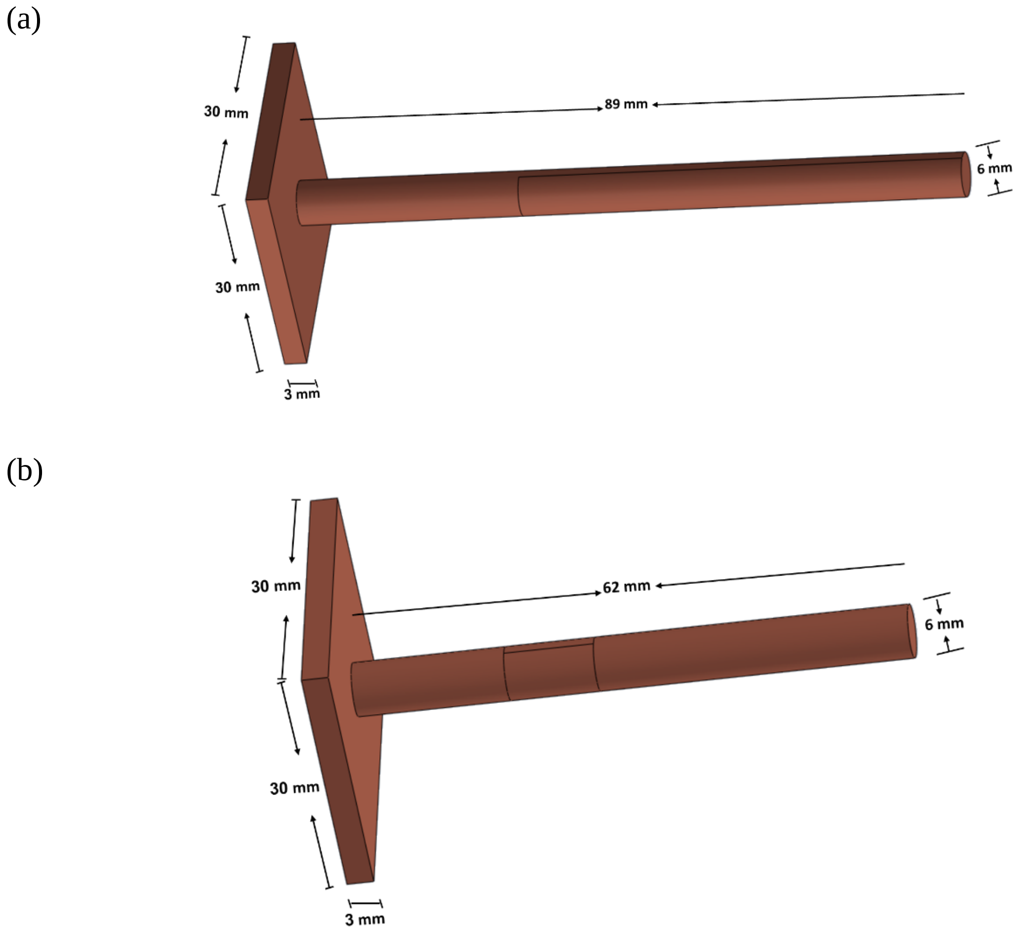

Figure 5.8: *Dimensions of the copper absorber: (a) trough design and (b) dish design.*

Figure 5.8 shows that in the trough design the copper rod has an area of 1706 mm^2 and in the dish design the area is 1197 mm^2 (i.e., the copper rod in the trough design is 42.5% larger). Table 5.5 compares the experimental results for both designs.

Table 5.5: *Comparison of the hot side temperature and TEG power output for trough and dish-hybrid systems.*

	Experimental							
	Without splitting				**With splitting**			
	Hot side temp. (C)	**Cold side temp. (C)**	**ΔT**	**Power (mW)**	**Hot side temp. (C)**	**Cold side temp. I**	**ΔT**	**Power (mW)**
Trough	34.9	11.7	23.2	**11.9**	28	11.7	16.3	**6.0**
Dish	36.1	11.8	24.3	**12.5**	28.6	11.7	16.9	**6.30**

A comparison of the experimental results between both designs indicates the preference of the dish design over the trough design because the latter has more copper rod surface area and hence more heat loss to the environment. Heat saved in the dish design, compared to the trough design, resulted in an increase of the power output by 5% for both cases (with and without splitting).

It is anticipated that the dish-hybrid system will generate more heat and produce more power if the manufacturing of the dish is more accurate. As was detailed in Chapter 3, the manufacturing of the parabolic dish was much difficult than the parabolic trough because covering the inner surface of the dish with high reflective reflector (unlike the trough) requires more sophisticated equipment, which was not available in the university’s workshop. Meanwhile, if the polishing of the aluminium dish that was used in this study is not perfect, then it can diffuse incident radiation to a greater extent than shiny reflectors [177].

The dish requires an accurate manufacturing process because mechanically or thermally induced distortions in one region of the parabola tend to affect the entire paraboloid shape [177]. Another disadvantage of polished aluminium metal is its moderate reflectance of about 90% [178, 179]. In comparison, the Alanod reflector that is used to cover the interior of the trough concentrator (95% reflectivity) gives an advantage to the dish system when the parabolic dish is covered with the same reflector.

5.3.3 Economic comparison: trough vs. dish

Given that the two designs are identical in all parts except the copper absorber’s dimensions and the shape of the concentrators (i.e., trough or dish), the economic comparison will focus on these two parts.

The parabolic concentrators were printed in house by a 3D printer using a filament that costs £36.0 per roll (91 m/roll). The dish concentrator used in this study was fabricated by the university’s workshop and made of aluminium material. However, to be consistent in comparison with the trough design, the original dish (which was printed in the same way as the trough) is given in comparison. The other printing costs for both concentrators were neglected.

The inner surface of both concentrators was covered by a 95% reflective sheet (Alanod) which costs £13.8 per A4 size sheet (297x210mm) [180]. The costs of the copper absorbers are based on the latest copper market prices [181].

The items compared for both systems are those of laboratory scale which are purchased in small quantities and their costs are much more expensive than they would be for mass purchase. Furthermore, other costs such as labour, energy, and design costs, were neglected because the intention is to evaluate the systems in comparison.

Table 5.6 shows the costs of each component in the trough and dish systems and the overall cost of each system.

Table 5.6: *Cost evaluation of the trough and dish-hybrid system components.*

		Filament used mass (g)	Reflector area used (mm^2)	Used copper mass (g)	Filament (£/g)	£/sheet	Copper (£/g)	£
Trough	**Filament**	12.0			0.048			0.58
	Reflector		3954.0			13.80		0.87
	Copper			46.7			0.010	0.45
	Total							**1.91**
Dish	**Filament**	13.2			0.048			0.63
	Reflector		4342.8			13.80		0.96
	Copper			39.9			0.010	0.39
	Total							**1.98**

It can be seen from Table 5.6 that the dish-hybrid system costs more than the trough-hybrid system. Although the dish system uses less copper, it uses a more expensive reflector and more printing filament because the dish concentrator has more surface area. However, the dish-hybrid system produces more power than the trough system (as seen earlier). Table 5.7 compares the two systems in terms of cost per power produced.

Table 5.7: *Cost per watt for two hybrid systems.*

Design	Concentrator cost (£)	Reflector cost (£)	Copper cost (£)	Total cost (£)	Power output (mW)	Cost per output (£/mW)*
Trough	0.58	0.87	0.45	1.91	6.00	**0.32**
Dish	0.63	0.96	0.39	1.98	6.30	**0.31**

The dish system cost 3% less than the trough system in terms of cost per watt. However, it should be noted that these costs are based on laboratory scale and are likely to be different when it comes to utility scale. Furthermore, the dish produces just a small increase of power production as a result of imperfect fabrication of the dish concentrator. In other words, if the simulated power output of the dish is used in the calculations, the cost per power output will be further reduced from 3% less to 37% less.

5.4 Further dish geometry optimisation

The geometry of the dish system can be further optimised for better performance. The copper rod is a major part of the hybrid system for both trough and dish-hybrid systems. However, because the trough is a line focusing concentrator, adjusting the dimensions of the copper rod is very limited and has a minor effect on the trough-hybrid system power output. In contrast, the dish is a point focusing concentrator that can be adjusted to optimise the length and diameter of the copper rod. In the following sections, the dimensions of the copper rod will be optimised in respect to its length and diameter.

5.4.1 Actual dish design vs. different dish geometries

The copper rod for each system that receives all reflected rays from the concentrator was designed with a minimum length to reduce its surface area and thus reduce the heat lost to surroundings. The copper rod for the dish system was designed with a length correspond to the dish focal point length and a tolerance of 10mm. As illustrated in Figure 3.3, the focal length of a parabola depends on how flat the parabola’s curve is. In other words, to have a shorter focal point, the curvature of the dish should be deeper. Meanwhile, a shorter focal point will lead to a shorter copper rod length. To examine the effect of a shorter copper rod on the steady state temperature of the absorber, a “SolidWorks” thermal simulation was carried out with four different geometry dishes (i.e., the actual dish geometry and three deeper dishes). However, the “SolidWorks” model should be validated by actual experimental results first before examining the three proposed geometries. Table 5.8 compares the experimental results of the actual dish geometry with simulated results of the same geometry.

Table 5.8: *Comparison of dish experimental results with simulated results.*

	Experimental						Simulated						ΔT (NS) increase (%)	ΔT (WS) increase (%)
	Without splitting			With splitting			Without splitting			With splitting				
	Th	Tc	ΔT	Th	Tc	ΔT	Th	Tc	ΔT	Th	Tc	ΔT		
Dish	36.1	11.8	24.3	28.6	11.7	16.9	37.0	11.8	25.2	29.5	11.7	17.8	**3.7%**	**5.3%**

Table 5.8 shows a good agreement between the actual and simulated results, with a small deviation of 3.7% and 5.3% for the illumination without splitting and with splitting, respectively. This validates the use of the simulation model to predict the absorber steady state temperature for the three proposed dish geometries and corresponding copper rods. Figure 5.9 shows the four different geometries after simulation without splitting and without attaching the TEG to the absorber.

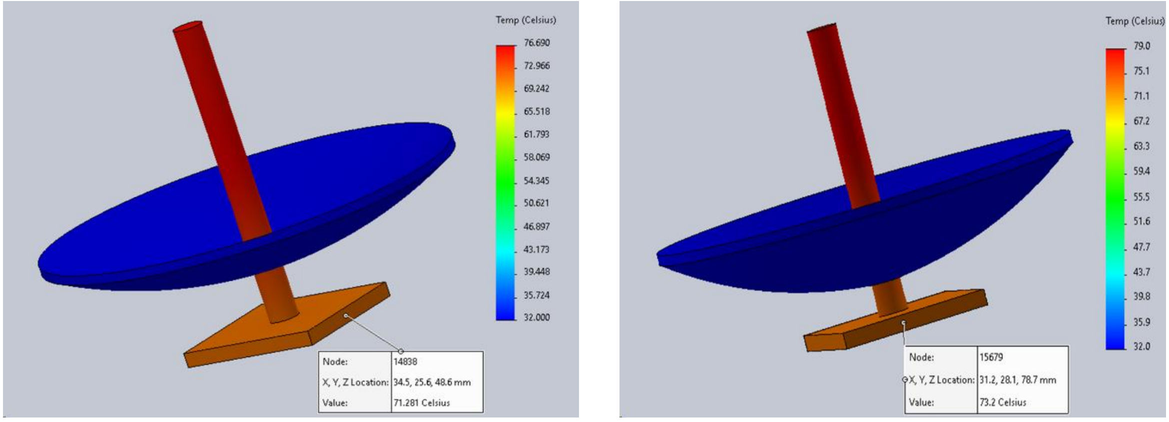

Actual Dish (12mm deep)

Dish 1 (15mm deep)

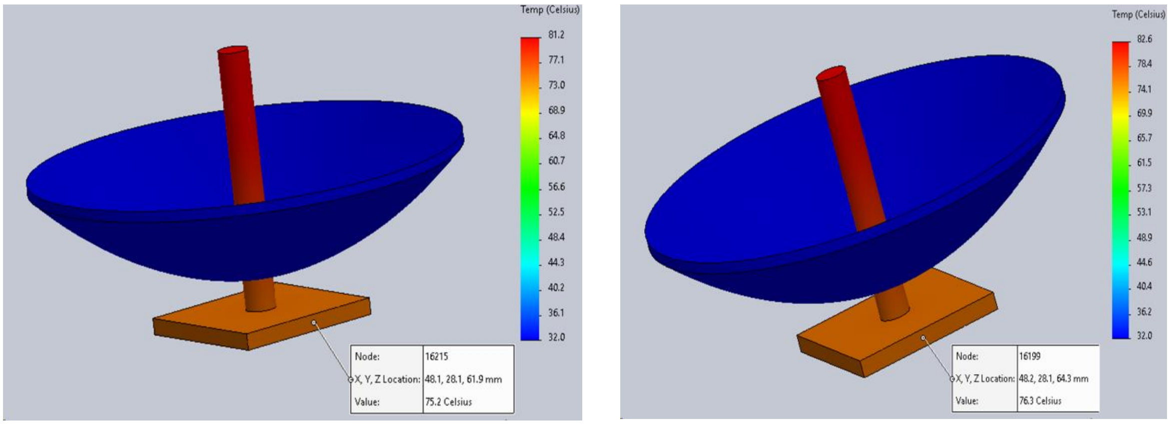

Dish 2 (20mm deep)

Dish 3 (25mm deep)

Figure 5.9: *Simulation results of the four dish geometries.*

The simulation was run without attaching the TEG to the absorber to reduce the complexity and to achieve more accurate results because the intention is to determine the effect of deeper dishes and hence shorter copper rods in delivering more heat to the hot side of the TEG. Figure 5.10 shows the increase in the absorber's final temperature for the four geometries.

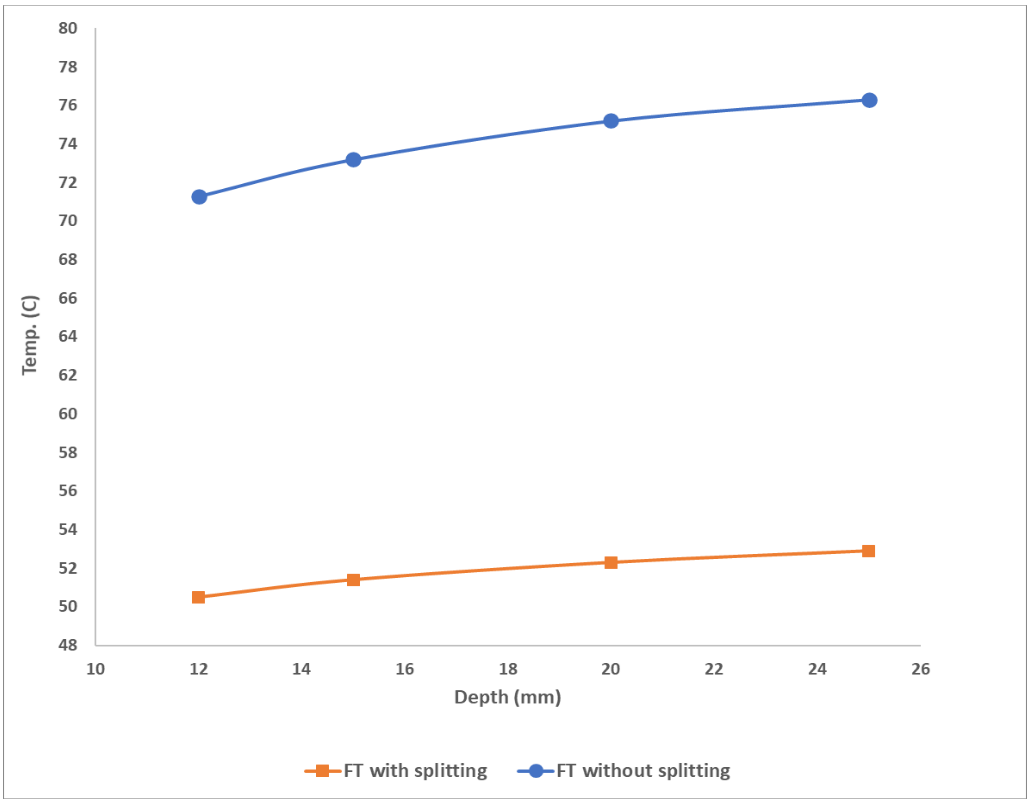

Figure 5.10: Absorber steady state temperature for the four dish geometries with and without splitting.

Figure 5.10 shows the steady state temperature plotted as a function of dish depth. The steady state temperature increases with the increase of the dish depth as a result of the shorter focal point of the deeper dishes. Accordingly, the copper rod's surface area will be less for deeper dishes, which will result in an increase of the steady state temperature. Table 5.9 shows the geometry details of the actual dish and the three proposed dishes with the absorber final temperature obtained by simulation with and without splitting and the percent increase for each case.

Table 5.9: *Actual and proposed dish geometry details and absorber steady state temperature obtained by simulation.*

	Dish diameter	Depth	Focal point	ψ	Copper rod length	Copper rod diameter	Copper rod mass	Without splitting		With splitting	
	(mm)	(mm)	(mm)		(mm)	(mm)	(g)	SS Temp.	%	SS Temp.	%
Actual Dish	84.85	12	37.5	59	62.0	6.0	39.8	71.3		50.5	
Dish 1	84.85	15	30.0	70.5	54.0	6.0	37.8	73.2	2.7%	51.4	1.8%
Dish 2	84.85	20	22.5	86.6	47.0	6.0	36.0	75.2	5.5%	52.3	3.6%
Dish 3	84.85	25	18.0	99.9	43.0	6.0	35.0	76.3	7.0%	52.9	4.8%

These results show the effect of varying the geometry of the dish to achieve a higher steady state temperature. An increase of steady state temperature of 7% and 5% can be achieved through dish geometry optimisation for the cases without and with splitting, respectively. Table 5.9 also shows a reduction in the copper rod length of up to 30%. The diameter of the cylindrical receiver that intercepts the entire reflected rays from the reflector is determined by the rim angle of the concentrator, which decreases with an increasing rim angle. It is worth mentioning that even deeper dishes show better thermal performance, even though their rim angle is not at the optimum. Although many papers have concluded that the optimal rim angle for solar dishes is around 45°, their conclusions are based on flat receivers [182-184].

The simulation was also carried out after attaching the TEG to the absorber to predict its power output after changing the geometry of the dish. Table 5.10 show the simulation output for the four dishes under consideration.

Table 5.10: *Actual and proposed dish geometry details and absorber steady state temperature obtained by simulation.*

	Without splitting			With splitting		
	ΔT (C)	Power (mW)	Power increase (%)	ΔT (C)	Power (mW)	Power increase (%)
Actual Dish	25.2	14.1		17.8	7.0	
Dish 1	26.2	15.2	8.1%	18.3	7.4	6.0%
Dish 2	27.2	16.4	16.5%	18.9	7.9	13.1%
Dish 3	27.8	17.1	21.7%	19.2	8.2	16.7%

Table 5.10 shows that the power output of the TEG can be increased by 22% and 17% through dish geometry optimisation for the cases of without and with splitting, respectively. Equation 3.29 was used to calculate the TEG power output from the ΔT obtained by simulation based on the material parameters of the thermoelectric generator in Table 4.9.

5.4.2 Actual dish copper rod diameter vs. thinner copper rod diameter

It is clear from these results that the copper rod’s surface area has a considerable effect on the heat generated by the absorber and the power output of the TEG. Therefore, reducing the diameter of the copper rod from its actual size (6mm) to a thinner diameter of 3mm to reduce the rod’s surface area was also simulated to examine its impact on the absorber’s steady state temperature and the TEG’s power output. The simulation was carried out for the four dish geometries mentioned earlier. Figure 5.11 shows a comparison between the steady state temperature of the actual copper diameter and the thinner diameter for the four dishes with the TEG attached.

(a)

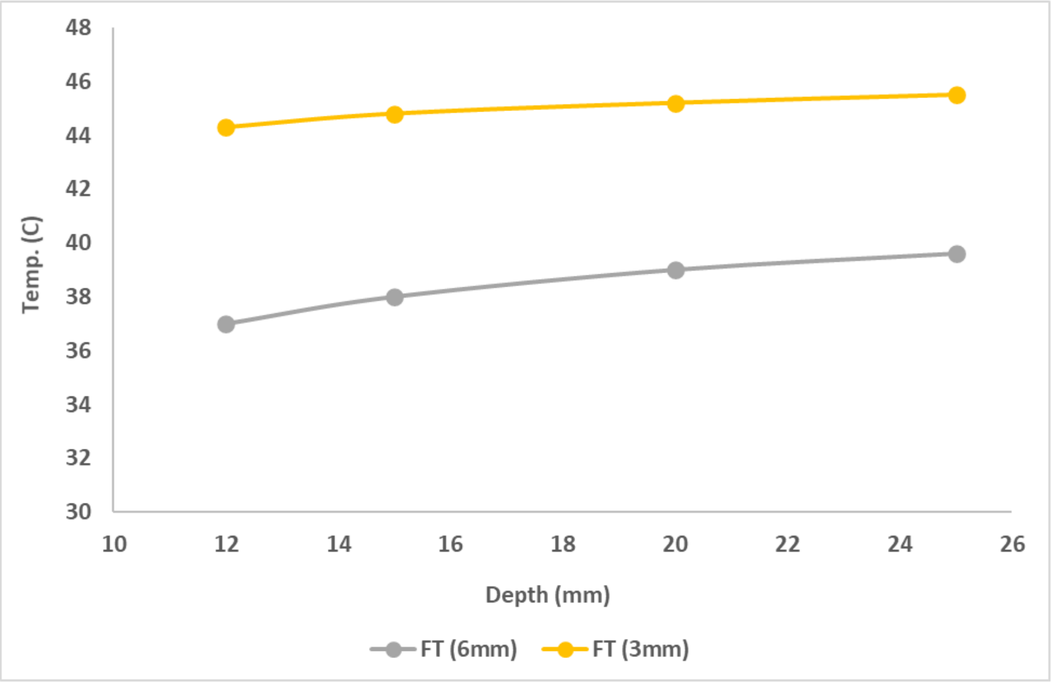

(b)

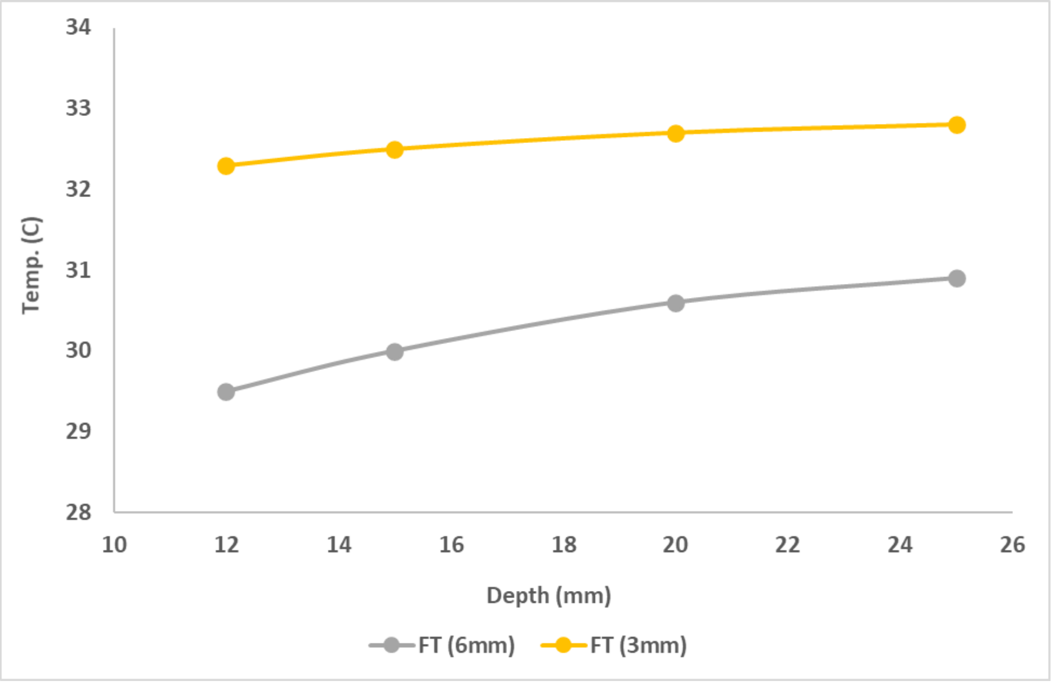

Figure 5.11: *Thinner copper rod diameter simulated absorber steady state temperature vs. actual copper rod diameter: (a) without splitting, (b) with splitting.*

It can be seen from Figure 5.11 that there was a further increase in the absorber’s steady state temperature for a thinner copper rod of up to 20% and 9% for illumination without splitting and with splitting, respectively, compared to the actual copper rod. The improvement of thermoelectric power output is up to 66% and 36% for illumination without splitting and with splitting, respectively, as shown in Table 5.11.

Table 5.11: *Thinner copper rod simulation results.*

	Without splitting			**With splitting**		
	ΔT (C)	**Power (mW)**	**Power increase (%)**	**ΔT (C)**	**Power (mW)**	**Power increase (%)**
Actual Dish	32.5	23.4	66%	20.7	9.5	36%
Dish 1	33.0	24.1	59%	20.8	9.6	29%
Dish 2	33.4	24.7	51%	21.0	9.8	23%
Dish 3	33.7	25.2	47%	21.1	9.9	21%

Although deeper dishes will have shorter copper rods, the high cost of their fabrication will overwhelm the saving in the copper material cost. It is to be concluded that even though deeper dishes are much difficult than flat dishes to fabricate, and hence more expensive, the high cost can be offset by the higher power that they produce.

5.5 Conclusion

The thermal and electrical performance of a parabolic dish-hybrid system was investigated in this chapter. The heat absorbed by the copper absorber, determined by slope technique, and the electric power measured for the TEGs under investigation show a reasonably good agreement between the experimental and theoretical results. The dish system investigated in this chapter was compared with the trough system investigated in Chapter 4 with respect to their performance, design, and economic assessment. The results show the dish system is potentially better than the trough system. The dish system will require a smaller absorber area which will have considerable reduction in heat loss to surroundings and hence a higher power output produced by the TEG. The economic evaluation shows that dish system costs 3% less than the trough system in terms of cost per watt. This cost can be reduced further to 37% less if the optimised dish geometry is employed. The curvature of the dish and the copper rod's diameter were investigated for further improvement in heat loss saving and power production enhancement. The results reveal that there is an increase of TEG power output of up to 66%.

Chapter Six: Minimising Convective Heat Loss in the Copper Rod by Insulation

6.1 Introduction

The simulation results in Chapter Five show that reducing the absorber's surface area, which reduces the heat loss to the surroundings, will increase the TEG's power output. To further increase the power output from the TEG, the copper rod that absorbs and delivers heat to the TEG should be insulated to reduce heat loss to the surroundings by convection. Although minimising radiative heat loss should also be considered, this would require a selective optical coating to be used, which is outside the scope of this study. This chapter will study the effectiveness of insulation to reduce convective heat loss from the copper rod to the environment. The copper rod will be covered by a glass tube that allows the sunlight to reach the copper rod and at the same time minimises convective heat loss to the surroundings.

6.2 Insulation for the Trough Hybrid System

Commercial parabolic trough concentrators (PTCs) use evacuated receivers by reducing the air pressure in the annular gap to a very low pressure. Because evacuating the annular gap around the receiver will eliminate the heat loss by conduction and convection, the receiver should be coated with a solar selective coating, with high absorbance for the solar spectrum and low emittance for the infra-red region, to minimise the heat loss by radiation. The thick glass envelope together with the glass-metal seal that is needed to maintain a high vacuum and the solar selective coating of the receiver contribute to about 12% of the total cost of PTC installations [185]. Meanwhile, stagnant air, with a thermal conductivity of 0.026 W/m·K, is a good thermal insulating material, which makes it a good candidate for low temperature insulation. In air filled PTCs, the total heat loss from the copper absorber is mainly due to conduction and radiation because the convection is mostly suppressed if the temperature of the absorber is much higher than the surrounding temperature [186].

In this study, using the resources available at Cardiff University's laboratory, the trough hybrid system that was described in Chapter 4 was modified using a cylindrical glass tube to cover the copper rod and a 3D printed acrylic cover to cover the square copper end. The effects of this insulation will be investigated in the following subsections.

6.2.1 Insulation: Experimental Setup

Figure 6.1 shows a schematic diagram of the insulation setup for the copper absorber of the trough system. The same copper absorber that was used in the trough system described in Chapter Four was used here, the modification was made to cover it with a glass tube and a square cover (as shown in the figure).

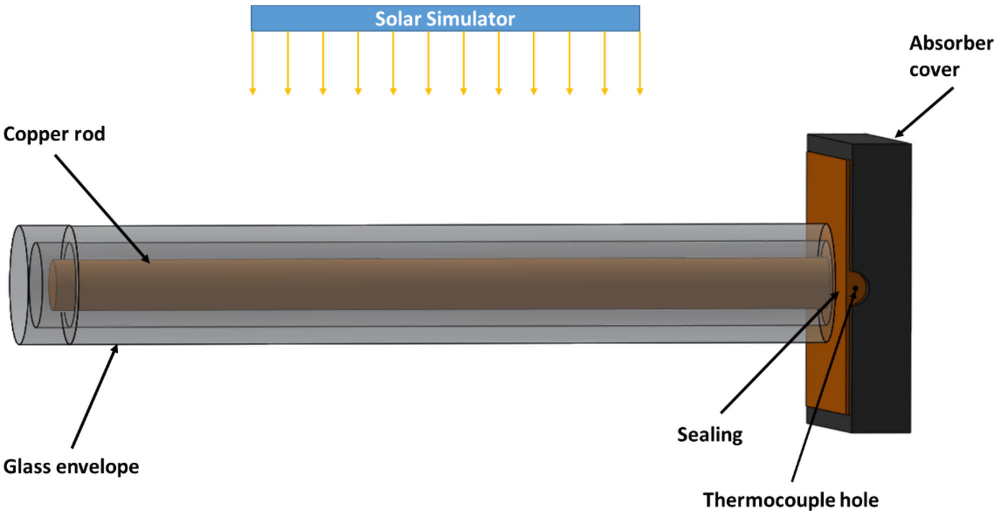

Figure 6.1: *Schematic diagram of the insulation setup.*

6.2.1.1 Glass Cover for the Copper Rod

Because the copper rod used in the trough setup has a diameter of 6.0mm, the inner diameter of the glass tube used for insulation should be as small as possible. Reducing the space between the glass cover and the copper rod will significantly reduce heat loss by convection [187]. Therefore, an 8mm (inner dia.) thin glass (1mm thick) was used to insulate the copper rod in this study. Figure 6.2 shows the glass tube that was used.

Figure 6.2: *borosilicate glass tube that was used to cover the copper rod.*

The glass material used to cover the copper rod is borosilicate glass, which is used widely in industry. This glass consists of substantial amounts of silica (SiO_2) and boric oxide (B_2O_3). The B_2O_3 content is 12–13% and the SiO_2 content is over 80%, which has good chemical durability and low thermal expansion (3.3×10^{-6}/K). The solar transmittance for borosilicate glasses is from 0.91 to 0.93, with a good thermal shock resistance [188]. The glass envelope has an absorptance of $\alpha = 0.023$, while the emissivity has an average value of $\varepsilon = 0.90$ [189]. If the glass tube is coated with an anti-reflective coating, then the glass will have a higher solar transmittance. Borosilicate glass has a high light transmissivity in the wavelength range 380–2100 nm, but it drops significantly beyond that. The light transmissivity of borosilicate glass is available, and the data shown in Figure 6.3 was obtained from Ref. [190].

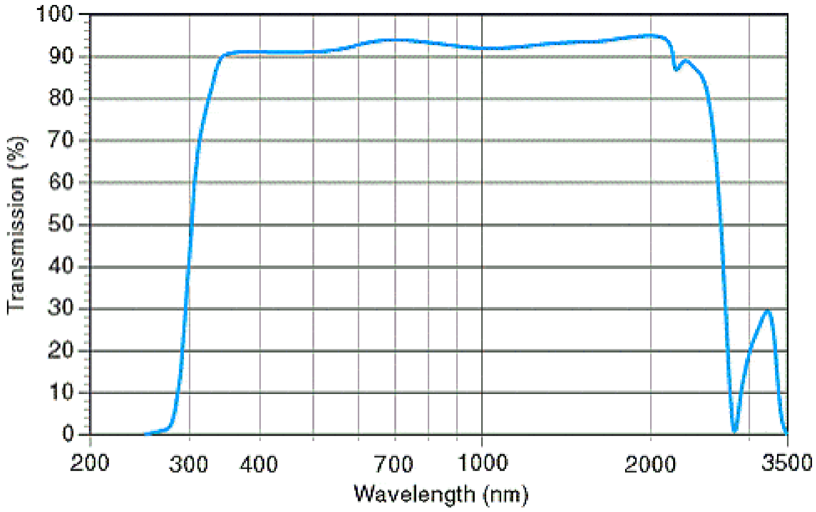

Figure 6.3: *Optical transmission of borosilicate glass in visible and near-infrared ranges (the data shown above is obtained from https://asgs-glass.org/optical-transmission/, [190]).*

Another factor that affects the heat loss from the copper rod is the quality of the sealing between the copper rod insulation tube and the holder of the copper rod at the open end of the tube. Heat loss from a setup without sealing can be at a factor of four higher than that with good sealing [191, 192]. Consequently, the open end of the glass tube was sealed to the right-hand side holder of the trough system setup using a silicone sealant, which will prevent air to go through the open end of the glass tube to increase convection.

Silicone sealant was applied around the open end of the glass tube attaching to the holder to ensure that the gaps between the glass and the holder was filled by the sealant to prevent any air flow through the opening. Figure 6.4 shows the sealing of the glass tube and the absorber cover to the holder.

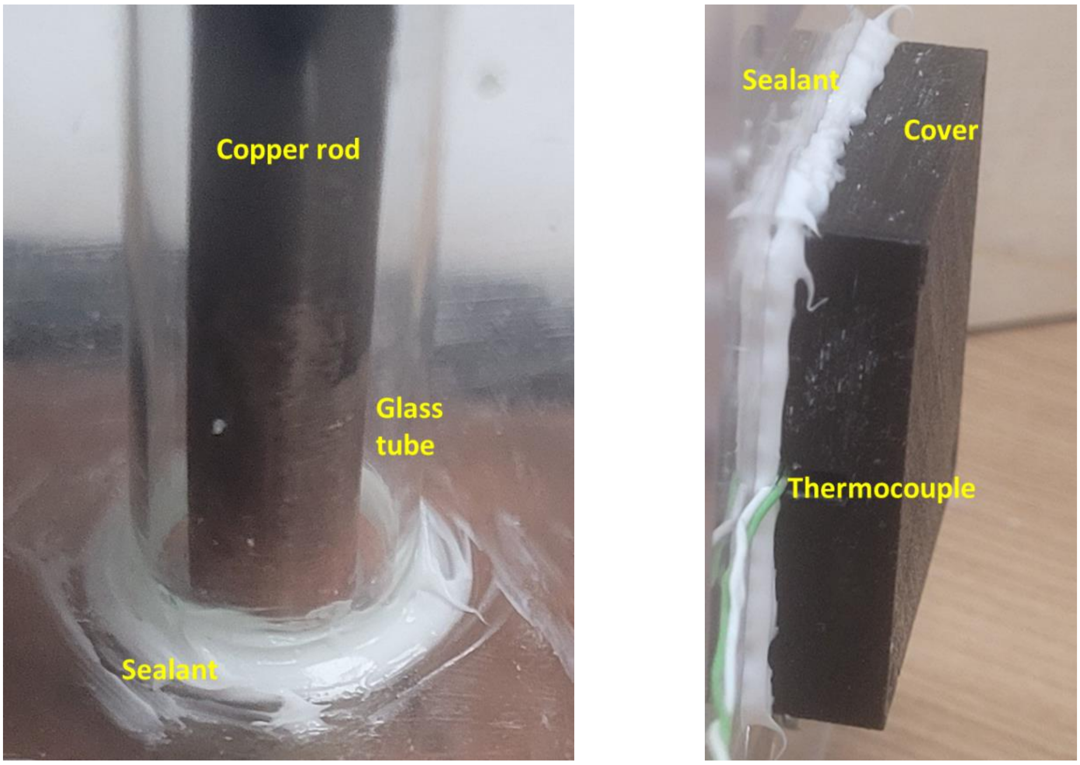

Glass envelope sealing

Copper squared end cover sealing

Figure 6.4: *Photograph of the glass tube and square absorber cover sealed to the holder using silicone sealant.*

6.2.1.2 Absorber Cover

To eliminate heat loss to the surroundings by convection and radiation from the squared copper absorber end, it should also be covered to prevent the air flow around the absorber end to reduce convective heat loss. The cover was designed using “SolidWorks” software according to the dimensions of the absorber end, with minimum space between the absorber and the cover. It was intended to minimise the air flow around the absorber, and hence reduce the convective heat loss. The cover was made by a 3D printer using the design file in STL format, the printed cover is shown in Figure 6.5.

Figure 6.5: *The 3D printed cover for the copper absorber end for insulation experiments.*

Figure 6.6 shows the final experimental setup of the thermally insulated the trough hybrid system. Figure 6.6 (a) shows the front view of the insulation setup, showing the copper rod inside a glass tube and sealed to the holder. Figure 6.6 (b) shows the back view of the setup to show the end cover with a K-type thermocouple attached to the copper absorber to measure the absorber’s temperature. Another thermocouple was used to measure the ambient temperature inside the Faraday cage where this experiment was taking place.

(a)

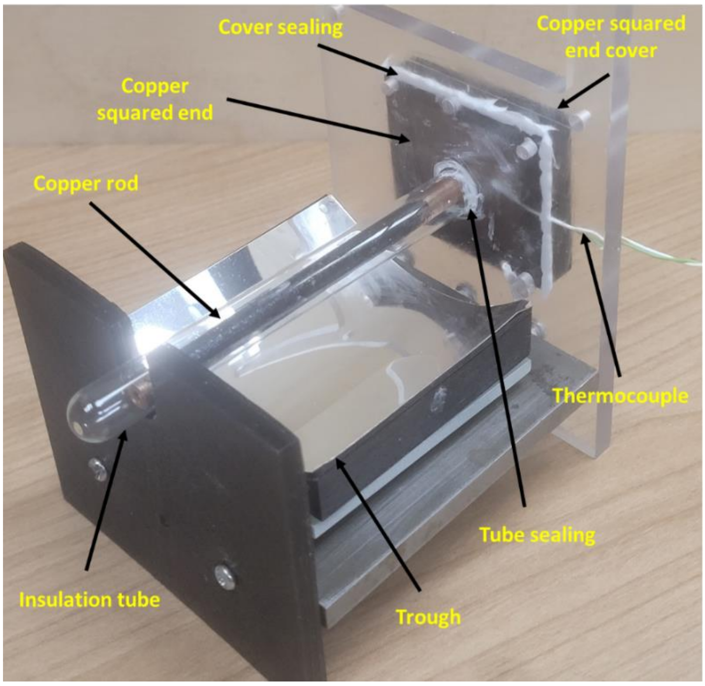

(b)

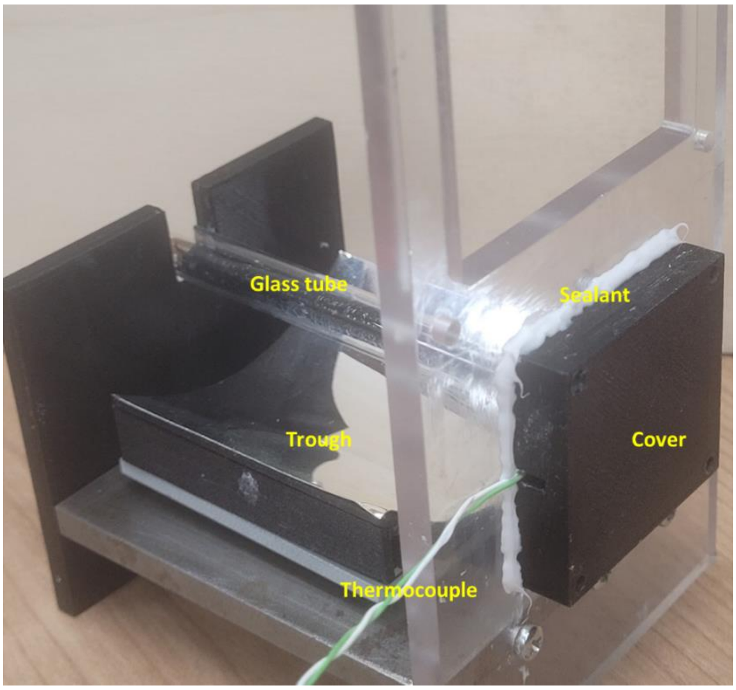

Figure 6.6: *Copper insulation experiment setup: (a) front side, (b) back side.*

6.2.2 Absorber Temperature Measurements

The setup that is illustrated in Figure 6.6 was used to investigate the absorber's temperature for four cases: without splitting and without insulation (NSNI), with splitting and without insulation (WSNI), without splitting and with insulation (NSWI), and with splitting and with insulation (WSWI). The intention was to determine the effectiveness of insulation to improve the heat production with and without splitting. The measurements were carried out with and without attaching the TEG to the absorber, as detailed in the following subsections.

6.2.2.1 Improvement Without Attaching the TEG

Bare and insulated copper rod was illuminated under solar simulator by 1000 W/m^2 illumination (1 sun) without attaching the thermoelectric generator to the copper absorber. The intention was to study the insulation's effect on the copper absorber only. Figure 6.7 shows the measured temperature of the copper absorber as a function of time for the four cases that were described earlier.

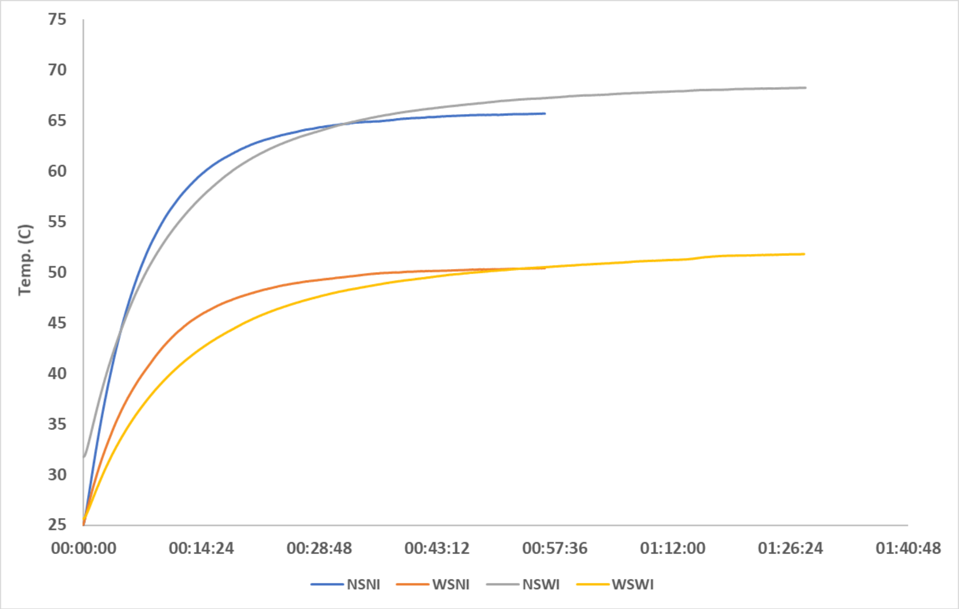

Figure 6.7: *The temperature profiles of the copper absorber for the four cases (No TEG attached).*

Figure 6.7 shows that at the start of the heating curves, the absorber temperatures with insulation increase at a lower rate than the temperatures without insulation and it took longer to reach the steady state temperature. In contrast, the temperatures of the absorber without insulation increase rapidly and reach steady state faster. The reason for this is that the illumination which reaches the insulated copper absorber is reduced by about 8% due to the reflection and absorption of light by the glass cover. Meanwhile, the bare copper rod receives full irradiation, and its temperature increase is faster. Although the insulated copper absorber received slightly low light irradiation, its steady state temperature is higher than the absorber without insulation because the convective heat loss to the surroundings is reduced after insulation. Table 6.2 lists the steady state temperatures for the four cases, showing an increase in the temperature of the copper absorber after insulation. It can be seen from Table 6.1 that the steady state temperature of the copper absorber without splitting increases by 2.5 ºC (3.8%) after adding insulation to the system, while the increase is 1.4 ºC (2.8%) for the case after spectral splitting.

Table 6.1: *The steady state temperatures of copper absorber for the four cases.*

	Case	**SS Temp. (^{o}C)**	**Increase (^{o}C)**	**%**
Insulation effect without splitting	NSNI	65.7	**2.5**	**3.8%**
	NSWI	68.2		
Insulation effect with splitting	WSNI	50.4	**1.4**	**2.8%**
	WSWI	51.8		

6.2.2.2 Improvement After Attaching the TEG

Attaching the hot side of the TEG to the copper absorber will reduce the temperature of the absorber thanks to heat conduction through the thermoelectric generator to the water cooler attached to the cold side of the TEG. In addition, part of the heat will be converted to electrical power by the TEG. Therefore, a significant decrease in the absorber's temperature is anticipated. The objective of this experiment is to examine if the insulation can improve the hot side temperature of the TEG, and consequently its power output. The medium size thermoelectric module (15x15) was employed in this investigation. Figure 6.8 shows the heating curves of the absorber with the TEG attached for the four cases. It can be seen that the hot side temperatures of the TEG at steady state are slightly higher with insulation than those without insulation.

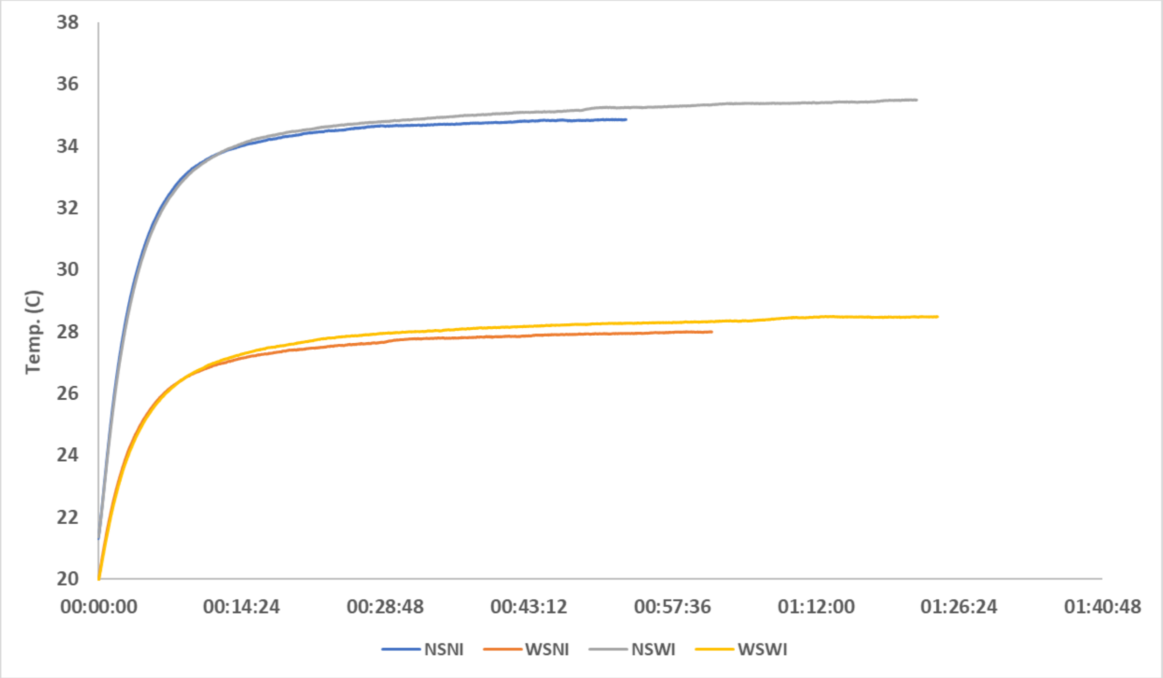

Figure 6.8: *Copper absorber steady state temperature for the four cases after attaching the TEG.*

Table 6.2 lists the steady state temperatures of the copper absorber attached to a TEG for the four cases. It can be seen from Table 6.2 that the steady state temperature of the copper absorber with insulation is increased by 0.6 ºC (1.8%) without spectral splitting, while the increase is 0.5 ºC (1.7%) for the case after spectral splitting. The data sheet of the Pico data logger utilised in the temperature measurements of this study, specified a measurement accuracy of ±0.2% [193]. Using this value to calculate the upper and lower limits for measurement uncertainty will result in ±0.07 ºC for uninsulated steady state temperature or 34.97 ºC and 34.83 ºC for upper and lower limit, respectively. It is clear that the insulated steady state temperature that is measured is far from the upper limit of measurement uncertainty. Although the increase is very small, it proves the positive effect of insulation on increasing the steady state temperature of the copper absorber, and hence power output from the thermoelectric generator.

Table 6.2: *Insulation effect on the copper steady state temperature for the four cases (TEG attached).*

	Case	**SS Temp. (^{o}C)**	**Increase (^{o}C)**	**%**
Insulation effect without splitting	NSNI	34.9	**0.6**	**1.7%**
	NSWI	35.5		
Insulation effect with splitting	WSNI	28	**0.5**	**1.8%**
	WSWI	28.5		

6.2.2.3 The Effect of Insulation on the TEG's Power Output

The power output of the module was measured for the four cases when the hot side of a thermoelectric generator (15x15) was attached to the absorber and a cooler with an average temperature of 11.7 ºC was attached to the cold side. Table 6.3 shows that the insulation led to a 1.6 mW (13.4%) increase of the TEG's power output without spectral splitting. Meanwhile, the insulation led to a 0.8 mW (13.3%) increase of the TEG's power output with spectral splitting.

Table 6.3: *TEG (15x15) power output for the four cases.*

	Case	**Power (mW)**	**Increase (mW)**	**%**
Insulation effect without splitting	NSNI	11.9	**1.6**	**13.4%**
	NSWI	13.5		
Insulation effect with splitting	WSNI	6.0	**0.8**	**13.3%**
	WSWI	6.8		

Yu et al [194] found in their study that about 70–90% of heat loss to environment is due to radiation and 10–30% is due to convection. However, because the radiation heat loss is dependent on the hot side temperature, which is very low in this experiment, the radiation loss can be neglected, and only convective heat loss can be considered.

The absorber is a key component of the parabolic trough solar plant because it plays an important role in the energy conversion of concentrated sunlight into thermal energy [195]. The copper rod that was used in this study was coated with a black coating with a solar absorptance of 90%. Its thermal emittance was also high. A good spectrally selective coating is characterised by high absorptance and a low emittance [196]. Using a spectrally selective coating to coat the copper rod will greatly reduce the radiative losses and increase the heat in the absorber.

6.3 Investigating the Insulation Effect by Thermal Simulation

To investigate the insulation effect further, the "SolidWorks" simulation model that was used in Chapter Four was adapted to include the insulation cover (glass tube and the absorber cover) that was described earlier to find the absorber's final temperature (after reaching the steady state). The simulation was performed with and without a TEG attached to the copper absorber.

6.3.1 Simulation Procedure

To examine the insulation effect on the absorber temperature, the copper absorber was first simulated without insulation and without a TEG attached to it. The simulation was carried out by assuming:

- Perfect insulation, which means that there is no loss of heat by convection. (Simulation with insulation).
- Glass tube solar transmittance of 0.92.
- Trough reflectivity of 0.95.
- Copper rod black paint absorptivity of 0.90.
- Copper un-painted emissivity of 0.18.
- Ambient temperature = 32.0 ºC.

- Convective heat transfer coefficient = 17.0 (W/m^2. ºC) (simulation without insulation).

Figure 6.9 presents the results of the "SolidWorks" simulation, which shows the temperature distribution on the copper absorber at steady state without insulation. The results obtained from the simulation shown in Figure 6.9 are very close to the steady state temperatures measured from the experiments (table 6.1), with deviations of 1.1% and 0.6% for the cases without spectral splitting and with spectral splitting, respectively. This validates the simulation model, which will later be used in the evaluation of the insulated systems.

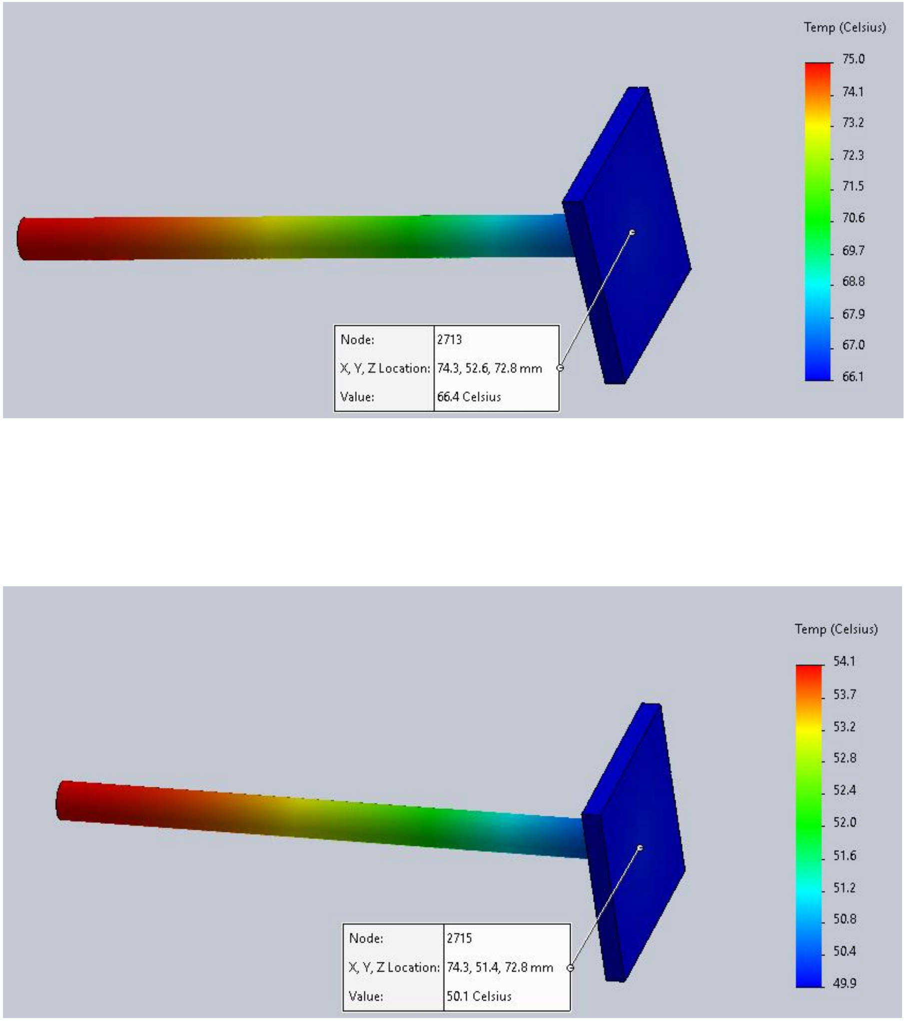

(a)

Node: 2713
X, Y, Z Location: 74.3, 52.6, 72.8 mm
Value: 66.4 Celsius

(b)

Node: 2715
X, Y, Z Location: 74.3, 51.4, 72.8 mm
Value: 50.1 Celsius

Figure 6.9: *The steady state temperature distribution of the copper absorber without insulation: (a) without splitting, (b) with splitting.*

A glass tube and an absorber end cover were designed in “SolidWorks”, which were then wrapped around the entire copper absorber as the insulation. The thermal inputs were entered by assuming 92% glass solar transmittance of covering tube, while other inputs were similar to the input for the simulation without insulation. Figure 6.10 shows the simulation results of the temperature distribution on the insulated copper absorber at steady state.

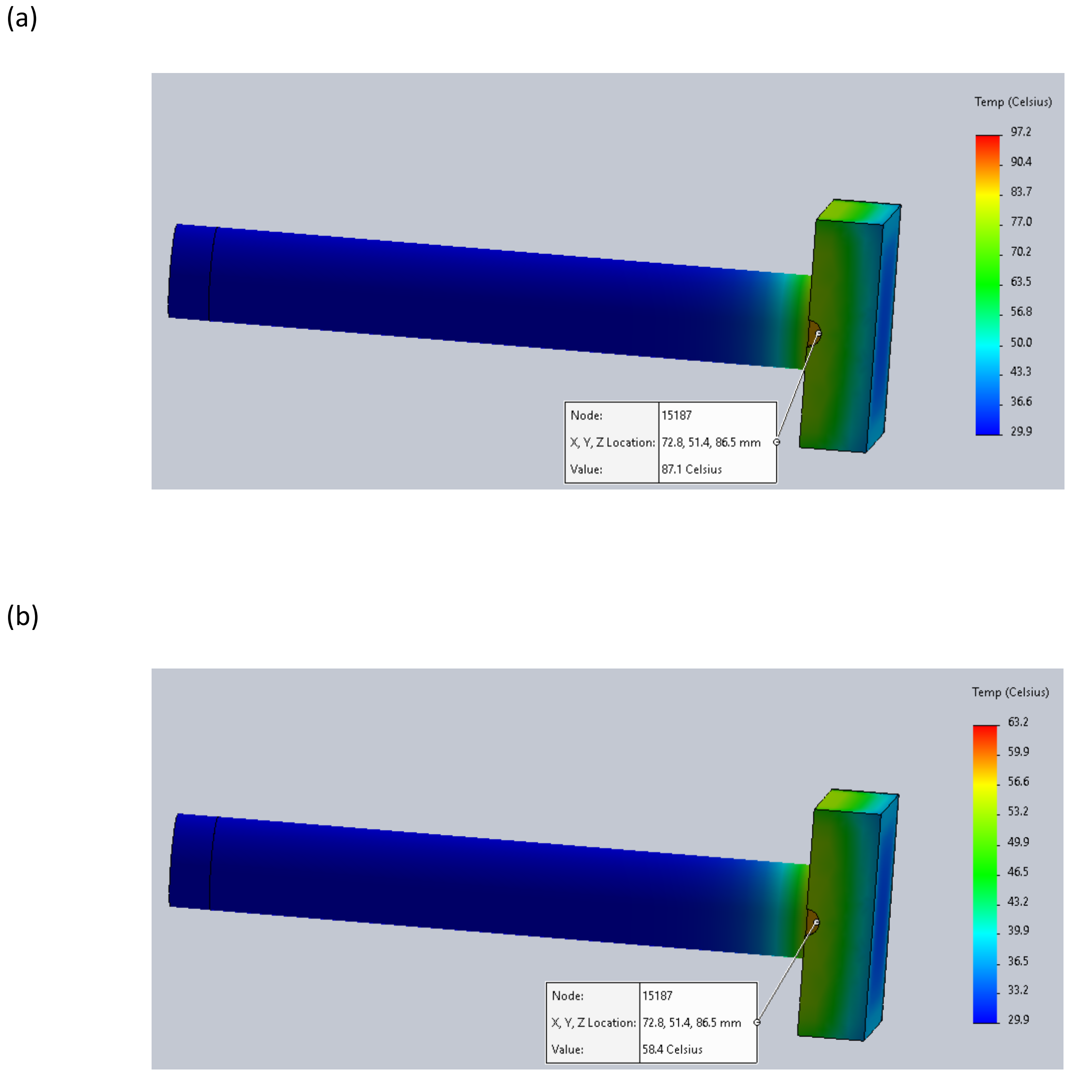

Figure 6.10: *The steady state temperature distribution on the insulated copper absorber covered by a glass tube and an absorber end cover: a) without splitting, b) with splitting.*

The simulation was carried out again after attaching the TEG to the absorber using the same thermal inputs for both with and without spectral splitting. The results were found to be in agreement with the experimental results without insulation. However, the results of the simulation of the insulated absorber for both cases with and without the TEG differ significantly from the experimental results. Table 6.4 compares the simulation and experimental results for the four cases.

Table 6.4: *Measured and simulated results of the steady state temperature of the copper absorber, both with and without TEG.*

	Case	**Measured SS Temp. (°C)**	**Simulated SS Temp. (°C)**	**Diff. (°C)**	**%**
No TEG attached	NSNI	65.7	**66.4**	**0.7**	**1.1%**
	WSNI	50.4	**50.1**	**-0.3**	**-0.6%**
	NSWI	68.2	**87.1**	**18.9**	**27.7%**
	WSWI	51.8	**58.4**	**6.6**	**12.7%**
TEG attached	NSNI	34.9	**36.5**	**1.6**	**4.6%**
	WSNI	28	**28.8**	**0.8**	**2.9%**
	NSWI	35.5	**41**	**5.5**	**15.5%**
	WSWI	28.8	**32.6**	**3.8**	**13.2%**

The measured steady state temperatures of the absorber are considerably lower than those of the simulated results because the simulation assumes perfect insulation in the space between the absorber and glass tube. Therefore, the convective heat loss from the absorber was zero in this simulation. In reality, the gap between the copper rod and the inner surface of the glass tube is filled with air. Heat transfer by convection will still take place between the absorber surface and the inner surface of the glass tube. This results in convective heat loss from the absorber and a lower temperature compared to the simulated results. To achieve the improvement predicted by the simulation, the glass tube needs to be tightly sealed and the gaps in-between need to be evacuated.

6.3.2 Further Investigations Using the Simulation Model

Given that the simulation model has been verified by experimental results, it can be used for further investigation of the insulation effect on the TEG power output. The convective heat transfer coefficient that matches the experimental results was obtained, which was found to be 9.5 W/m^2.K and 6.8 W/m^2.K without spectral splitting and with spectral splitting, respectively. To demonstrate the effect of evacuation of air in the gaps, different vacuum levels were assumed by multiplying the convective heat transfer coefficient by the percentage of vacuum level. In other words, no vacuum is assumed by multiplying the coefficient by 1 (i.e., all of the convective heat loss will be considered) and complete vacuum by multiplying the coefficient by 0 (i.e., no convective heat loss will be considered). Figure 6.11 depicts the simulation results before and after attaching the TEG to the absorber for illumination without splitting and with splitting.

(a)

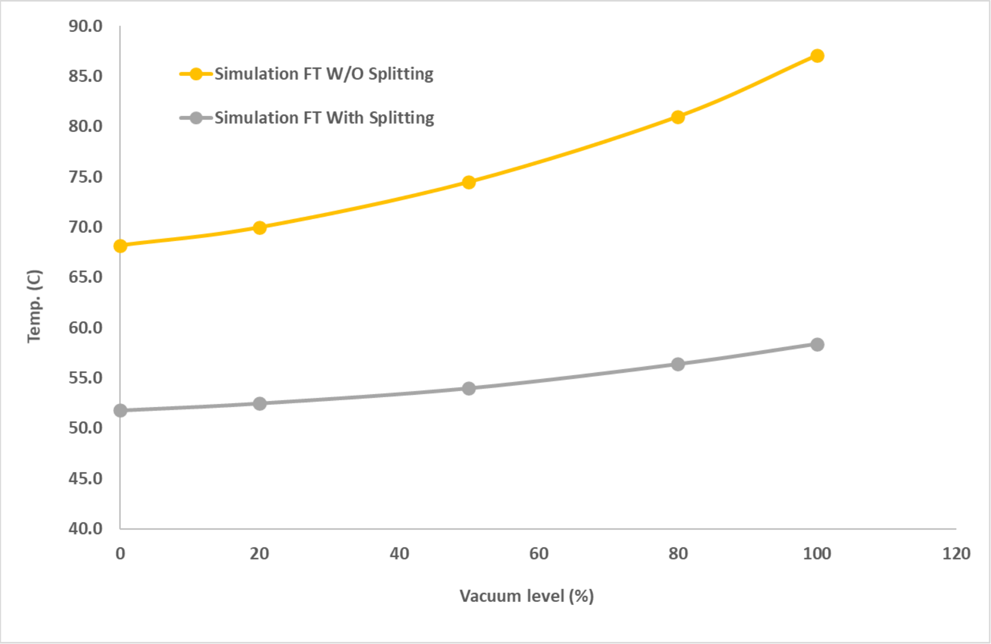

(b)

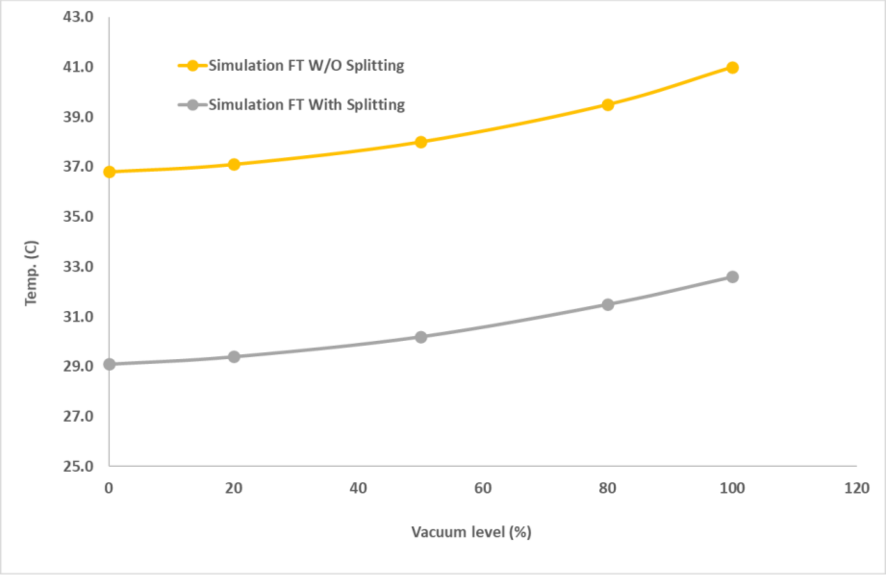

Figure 6.11: *Simulated temperature of the absorber at steady state for different vacuum levels: (a) without the TEG, (b) with the TEG.*

Figure 6.11 shows the positive effect of vacuum on the temperature of the absorber in the four cases. However, after attaching the TEG to the absorber, the temperature increase with the vacuum level becomes flatter. This is expected given that most of the heat will be conducted through TEG to the cooling system. The power output with and without spectral splitting can be calculated using Equation 3.29 and the results are shown in Figure 6.12.

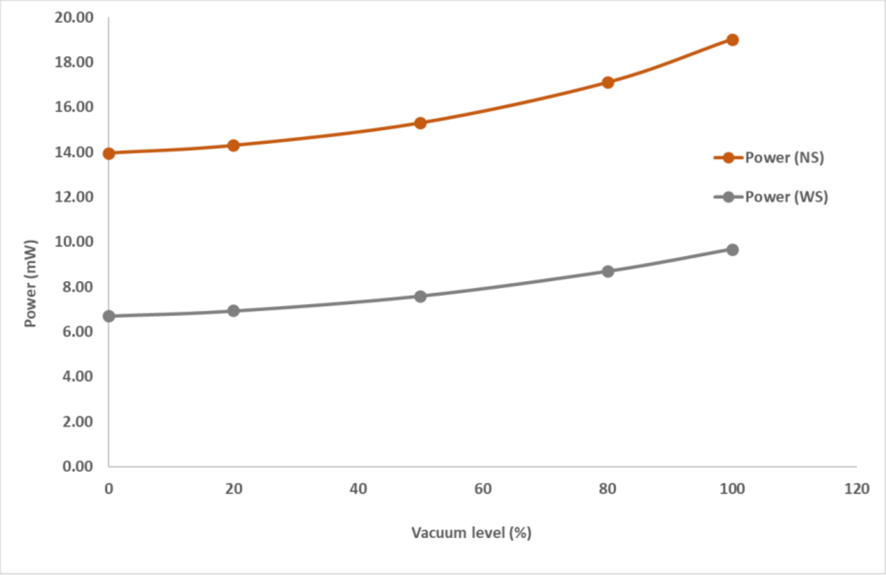

Figure 6.12: *TEG power output for different vacuum levels with and without splitting.*

As can be seen in Figure 6.12, a significant increase in the power output can be achieved by evacuating the gaps between the glass tube and the copper absorber. An improvement of 36% and 44% can be obtained for illumination without and with spectral splitting, respectively.

It is anticipated that the TEG's power output can be further improved by increasing the concentration ratio of the trough system and by increasing the mirror's surface area. Therefore, the simulation model was used to examine the effect of increasing the mirror's surface area on the TEG's power output, assuming that the copper absorber is perfectly insulated (100% vacuum).

Figure 6.13 shows the TEG power output as a function of the intensity of illumination for the cases with and without splitting, respectively. It can be seen that by doubling the concentration ratio, the TEG's power output can be increased by 224% and 150% without spectral splitting and with spectral splitting, respectively. The huge increase of the TEG's power output is due to a significant increase in the temperature difference across the module. Doubling the concentration ratio results in a significant increase in ΔT, and hence the power output.

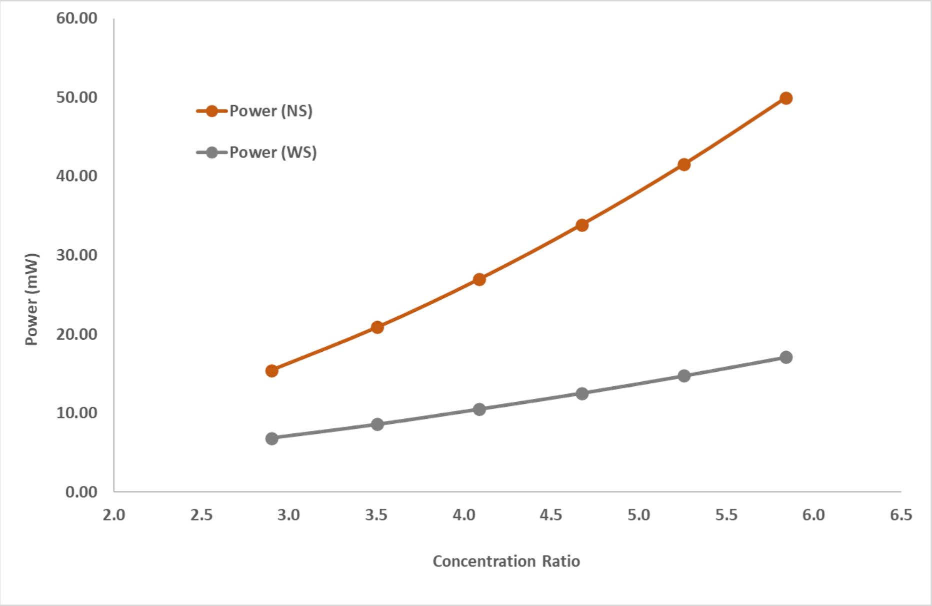

Figure 6.13: *TEG power output as a function of different irradiance with and without splitting.*

6.4 Conclusion

The copper rod that receives the reflected rays from the parabolic trough was insulated using borosilicate glass tube to reduce thermal losses to the environment and increase the heat delivered to the thermoelectric generator. The experimental results show that insulation resulted in an increase of the steady state temperature of the absorber by 3.8% and 2.8% without splitting and with splitting, respectively. When the hot side of the thermoelectric generator (15x15) was attached to the copper absorber, the insulation resulted in an increase of the power output by 13.4% and 13.3% without splitting and with splitting, respectively.

“SolidWorks” thermal simulation was used to investigate the effect of different levels of vacuum in the evacuated copper absorber on the TEG power output. The simulation results show that a significant increase of the TEG power output can be achieved if a good vacuum can be ensured in the glass envelope. In addition, a considerable improvement can be obtained if the trough system concentration ratio is doubled.

Chapter Seven: Conclusion and Future Work

7.1 Conclusion

This study aimed to investigate the feasibility of full solar spectrum harvesting using a PV-TE hybrid system that is based on beam splitting. The laboratory-scale prototype systems were designed and constructed, consisting of a dichroic mirror for spectral beam splitting and solar concentrator to focus the irradiance onto a thermal absorber. Systematic experiments were carried out to investigate the feasibility of the proposed systems. The investigation also involves theoretical aspects, such as SolidWorks thermal simulations, TracePro ray tracing, and a theoretical model for TEG geometry optimisation. The possibility of insulating the copper absorber was also investigated experimentally and theoretically. The main outcomes of this study are as follows:

1) Two hybrid systems were developed to investigate the feasibility of employing spectral beam splitting in a concentrating PV-TE hybrid system, which consist of solar concentrators (trough and dish), a dichroic mirror for beam splitting and an InGaP cell. The performance of the two systems was evaluated in terms of their thermal and electrical productivity. The results show that the hybrid system increases power output and efficiency by 2% compared to the bare cell. The successful demonstration was achieved due to the spectral splitting, the use of an InGaP solar cell and optimised thermoelectric module, and appropriate design of the solar concentrator and thermal absorber.
2) Spectral splitting experiments were performed using a cold dichroic mirror (which reflects UV-Vis and transmits IR) and three PV cells (i.e., c-Si, GaAs and InGaP). The results of the experiments confirms that the visible spectrum was successfully directed to the solar cell and the infrared spectrum can be separated and directed to the thermal receiver. A

careful selection of the solar cell (InGaP in this case) to match a given dichroic mirror enables generation of the same power output for operation under partial spectrum as that operating under full spectrum. In addition, the temperature of the solar cell is lower when operating under partial spectrum than that under full spectrum. This work provides important experimental evidence for the feasibility and benefits of spectral splitting and has laid the foundation for the proposed PV-TE hybrid systems.

3) A comparative study between the two developed hybrid systems were performed in terms of their performance, design, and economic viability. The results of this study show that the dish system is potentially better than the trough system because it has a smaller absorber. Using a smaller absorber, the heat loss to the surroundings can be significantly reduced and thus produce more power output.
4) Five commercial TEG modules were tested to investigate the influence of the TEG's geometry—aspect ratio (A.N/L)—on the power output of the hybrid system. The results show that the temperature difference across the TEG module decreases with increasing the aspect ratio and the aspect ratio has significant influence on the power output of TEG module. The experimental results from these five modules indicate that the power output of TEG module can be improved by optimising the geometry of the TEG modules.
5) A theoretical model was established and validated to enable optimisation of thermoelectric geometry. The results of theoretical calculation indicate that the power output of the TEG module can be improved by 74% by increasing the length of thermoelements to 7.6 mm for module 30 x 30. Furthermore, it is predicted that the power output of the same TEG module can be improved by 48% by operating in a vacuum.
6) Experimental investigation on insulating the thermal absorber of the trough hybrid system was performed to examine the effect of the convective heat loss on the power output of the TEG module. The insulation was attempted by covering the copper rod with a borosilicate

glass and the copper squared end by an acrylic box. The experimental results show that an increase in the power output of the TEG by 13.3% and 13.4% was obtained for illumination with and without splitting, respectively. The thermal simulation by Solidworks was carried out to predict the hybrid system's performance under different vacuum levels. The results indicate that an improvement in TEG power output 44% and 36% can be obtained for illumination with and without splitting, respectively. The simulation was also carried out to investigate the possible improvement by increasing the trough concentration ratio. The results show that by doubling the concentration ratio (i.e., by doubling the size of concentrator mirror), the power output of the TEG can be increased by 224% and 150% for irradiance without and with splitting, respectively.

7) The Solidworks thermal simulation model was validated using the experimental results and then used to optimise the dish geometry for maximum power production. The results indicate that the power output can be increased by 17% and 22% by optimizing the dish geometry with and without splitting, respectively. The improvement is achieved by reducing the length of the thermal absorber. The simulation was also carried out with a thinner copper rod diameter. The simulation indicates that an increase in the power output by 36% and 66% for illumination with and without splitting, respectively, can be obtained by using a thinner copper rod.

7.2 Future Work

This work was conducted with the time and resources that were available. However, if less time constraints and more sophisticated resources were available, the following work may be investigated further:

1) To increase its power output, a large temperature difference across the TEG should be established. This requires more heat, and hence higher light concentration. Due to the small

area of the solar simulator available at the university laboratory, the prototype hybrid systems developed for this study has a limited concentrator size. This led to a lower concentration ratio and therefore limited heat flux input. If a large area solar simulator is available, a hybrid system with large concentration ratio can be developed, which is anticipated to produce a larger power output from the TEG module due to more heat available, compared to the hybrid system developed in this work.

2) Some significant improvements in the performance of the hybrid systems have been predicted by the simulation studies in this work. However, they are not yet demonstrated experimentally. Further experimental demonstration is crucial to evaluate realistic feasibility of such hybrid systems.
3) In this study, a copper rod was used to transfer the heat from the absorber section to the hot side of the TEG. The heat pipe that is more efficient for heat transfer should be used and tested in the hybrid system. It is more efficient, and it also facilitates more flexible design.
4) The dichroic mirror used in the hybrid systems is an expensive component of the system. Less expensive solar spectrum splitting techniques should be investigated to reduce the cost of beam splitting parts, which will make the PV-TE hybrid system more economically viable and can be implemented in utility scale.
5) The copper absorber that was used in this study was painted with a black high temperature PNM paint that has solar absorptance of 90%. However, its thermal emittance is also as high. If a spectrally selective coating was used to coat the copper rod, then a significant reduction of the radiative losses to the environment is anticipated and hence more heat will be delivered to the thermoelectric for power generation.
6) The design of the hybrid systems that were developed in this project demonstrated their feasibility to achieve higher power output compared to a bare cell. However, for practical applications, further research should be performed to assess the economic viability of the

hybrid system and explore the possibility of low-cost options. In addition, outdoor testing should be considered to evaluate their performance in real world operation.

References:

1. NOW, R.R. *Why is renewable energy important?* 2021; Available from: https://www.ren21.net/why-is-renewable-energy-important/.
2. (EIA), T.U.S.E.I.A., *TODAY IN ENERGY*. 2021.
3. Daneshazarian, R., et al., *Concentrating photovoltaic thermal (CPVT) collectors and systems: Theory, performance assessment and applications.* Renewable and Sustainable Energy Reviews, 2018. **81**: p. 473-492.
4. Cuce, E. and T. Bali. *Variation of cell parameters of a p-Si PV cell with different solar irradiances and cell temperatures in humid climates*. in *Fourth international exergy, energy and environment symposium*. 2009.
5. De Brito, M.A.G., et al., *Evaluation of the main MPPT techniques for photovoltaic applications.* IEEE transactions on industrial electronics, 2012. **60**(3): p. 1156-1167.
6. Al-Waeli, A.H., et al., *A review of photovoltaic thermal systems: Achievements and applications.* International Journal of Energy Research, 2021. **45**(2): p. 1269-1308.
7. Price, H., et al., *Advances in Parabolic Trough Solar Power Technology.* Journal of Solar Energy Engineering, 2002. **124**(2): p. 109-125.
8. Bijarniya, J.P., K. Sudhakar, and P. Baredar, *Concentrated solar power technology in India: A review.* Renewable and Sustainable Energy Reviews, 2016. **63**: p. 593-603.
9. Zhang, Z., et al., *Effectiveness of amino acid salt solutions in capturing CO2: A review.* Renewable and Sustainable Energy Reviews, 2018. **98**: p. 179-188.
10. Shuba, Eyasu S. and D. Kifle, *Microalgae to biofuels: 'Promising' alternative and renewable energy, review.* Renewable and Sustainable Energy Reviews, 2018. **81**: p. 743-755.
11. Medipally, S.R., et al., *Microalgae as sustainable renewable energy feedstock for biofuel production.* BioMed research international, 2015. **2015**.
12. Graus, W., E. Blomen, and E. Worrell, *Global energy efficiency improvement in the long term: a demand-and supply-side perspective.* Energy efficiency, 2011. **4**(3): p. 435-463.
13. Hasanuzzaman, M., et al., *Global electricity demand, generation, grid system, and renewable energy polices: a review.* Wiley Interdisciplinary Reviews: Energy and Environment, 2017. **6**(3): p. e222.
14. Ellabban, O., H. Abu-Rub, and F. Blaabjerg, *Renewable energy resources: Current status, future prospects and their enabling technology.* Renewable and Sustainable Energy Reviews, 2014. **39**: p. 748-764.
15. Klugmann-Radziemska, E. *Environmental impacts of renewable energy technologies*. in *Int Conf Environ Sci Technol. IPCBEE, Singapore*. 2014.
16. Secretariat, R., *Renewables 2020 global status report.* Rep. Paris: REN12, 2020.
17. Magazine, W.E.a.E.V. *Renewables now*. 2021 [cited 11/03/2021]; Available from: https://www.evwind.es/2019/06/18/renewables-now-supply-more-than-a-quarter-26-of-global-electricity/67622.
18. International, P.E. *Global renewables installations totalled 260GW in 2020 – IRENA*. 2022 [cited 2022 25/01/2022]; Available from: https://www.powerengineeringint.com/renewables/global-renewable-energy-capacity-installations-totalled-260gw-in-2020/#:~:text=The%20world%20installed%20more%20than,estimates%20and%20all%20previous%20records.

19. Kusch-Brandt, S., *Urban Renewable Energy on the Upswing: A Spotlight on Renewable Energy in Cities in REN21's "Renewables 2019 Global Status Report".* Resources, 2019. **8**(3): p. 139.
20. Guo, C., et al., *Introducing optical fiber as internal light source into direct absorption solar collector for enhancing photo-thermal conversion performance of MWCNT-H2O nanofluids.* Applied Thermal Engineering, 2020. **173**: p. 115207.
21. Kumar Moluguri, N., C. Rama Murthy, and V. Harshavardhan, *Solar Energy System and Design - Review.* Materials Today: Proceedings, 2016. **3**(10, Part B): p. 3637-3645.
22. Sakthivadivel, D., et al., *Chapter 1 - Solar energy technologies: principles and applications*, in *Renewable-Energy-Driven Future*, J. Ren, Editor. 2021, Academic Press. p. 3-42.
23. Hu, E., et al., *Solar thermal aided power generation.* Applied Energy, 2010. **87**(9): p. 2881-2885.
24. Malik, N.K., et al., *A Review on Solar PV Cell'.* International Journal of Innovative Technology Exploring Engineering, 2013. **3**: p. 116-19.
25. Nelson, D.B., M.H. Nehrir, and C. Wang, *Unit sizing and cost analysis of stand-alone hybrid wind/PV/fuel cell power generation systems.* Renewable Energy, 2006. **31**(10): p. 1641-1656.
26. World, R.E. *Advantages and disadvantages of Solar Photovoltaic*. 2021 [cited 12/03/2021]; Available from: https://www.renewableenergyworld.com/storage/advantages-and-disadvantages-of-solar-photovoltaic-quick-pros-and-cons-of-solar-pv/#gref.
27. Aprà, F.M., et al., *Overview of the Enablers and Barriers for a Wider Deployment of CSP Tower Technology in Europe.* Clean Technologies, 2021. **3**(2): p. 377-394.
28. Singh, G.K., *Solar power generation by PV (photovoltaic) technology: A review.* Energy, 2013. **53**: p. 1-13.
29. Cho, E.-C., et al., *Silicon quantum dots in a dielectric matrix for all-silicon tandem solar cells.* Advances in OptoElectronics, 2007. **2007**.
30. Bhaskar, M.A., et al. *A simple PV array modeling using MATLAB*. in *2011 International Conference on Emerging Trends in Electrical and Computer Technology*. 2011. IEEE.
31. Bhuvaneswari, G. and R. Annamalai. *Development of a solar cell model in MATLAB for PV based generation system*. in *2011 Annual IEEE India Conference*. 2011. IEEE.
32. Chen, J., Y. Hu, and H. Guo, *First-principles analysis of photocurrent in graphene P N junctions.* Physical Review B, 2012. **85**(15): p. 155441.
33. Globe, C. *Photovoltaic or Solar Cel*. 2021 [cited 13/03/2021]; Available from: https://circuitglobe.com/photovoltaic-or-solar-cell.html.
34. Modeling, P.P. *Single Diode Equivalent Circuit Models*. 2018 [cited 14/03/2021]; Available from: https://pvpmc.sandia.gov/modeling-steps/2-dc-module-iv/diode-equivalent-circuit-models/.
35. Potscavage Jr, W.J., A. Sharma, and B. Kippelen, *Critical interfaces in organic solar cells and their influence on the open-circuit voltage.* Accounts of chemical research, 2009. **42**(11): p. 1758-1767.
36. Mohanty, P., et al., *Solar radiation fundamentals and PV system components*, in *Solar Photovoltaic System Applications*. 2016, Springer. p. 7-47.
37. Hassan, S. *Design and performance analysis of an efficient GaAs/AlGaAs heterojunction bipolar transistor solar cell*. 2017.
38. Sampaio, P.G.V. and M.O.A. González, *Photovoltaic solar energy: Conceptual framework.* Renewable and Sustainable Energy Reviews, 2017. **74**: p. 590-601.

39. Tyagi, V.V., et al., *Progress in solar PV technology: Research and achievement.* Renewable and Sustainable Energy Reviews, 2013. **20**: p. 443-461.
40. El Chaar, L., L.A. lamont, and N. El Zein, *Review of photovoltaic technologies.* Renewable and Sustainable Energy Reviews, 2011. **15**(5): p. 2165-2175.
41. Kim, D.S., et al. *String ribbon silicon solar cells with 17.8% efficiency*. in *3rd World Conference onPhotovoltaic Energy Conversion, 2003. Proceedings of*. 2003.
42. Hahn, G., et al. *Review on Ribbon Silicon Techniques for Cost Reduction in PV*. in *2006 IEEE 4th World Conference on Photovoltaic Energy Conference*. 2006.
43. NREL, N., *Best research-cell efficiency chart.* US Department of Energy, 2019.
44. Raj, V., et al., *Topical Review: Pathways toward cost-effective single-junction III-V solar cells.* Journal of Physics D: Applied Physics, 2021.
45. Ibn-Mohammed, T., et al., *Perovskite solar cells: An integrated hybrid lifecycle assessment and review in comparison with other photovoltaic technologies.* Renewable and Sustainable Energy Reviews, 2017. **80**: p. 1321-1344.
46. Mehdi, H., et al., *Investigation of N2 plasma GaAs surface passivation efficiency against air exposure: Towards an enhanced diode.* Applied Surface Science, 2022. **579**: p. 152191.
47. Schubert, M., et al., *Optical constants of Ga x In1− x P lattice matched to GaAs.* Journal of Applied Physics, 1995. **77**(7): p. 3416-3419.
48. Shoji, Y., et al., *InGaP/GaAs dual-junction solar cells with AlInGaP passivation layer grown by hydride vapor phase epitaxy.* Progress in Photovoltaics: Research and Applications, 2021. **29**(12): p. 1285-1293.
49. Kalkman, J., et al., *Emerging technologies in Solar PV: identifying and cultivating potential winners.* Arthur D Little Dubai, 2015.
50. Yamaguchi, M., *III–V compound multi-junction solar cells: present and future.* Solar Energy Materials and Solar Cells, 2003. **75**(1): p. 261-269.
51. Yamaguchi, M., et al., *Multi-junction solar cells paving the way for super high-efficiency.* Journal of Applied Physics, 2021. **129**(24): p. 240901.
52. Hong, L., et al., *Eco-compatible solvent-processed organic photovoltaic cells with over 16% efficiency.* Advanced materials, 2019. **31**(39): p. 1903441.
53. Jain, A. and A. Kapoor, *A new approach to study organic solar cell using Lambert W-function.* Solar Energy Materials and Solar Cells, 2005. **86**(2): p. 197-205.
54. Swami, R., *Solar cell.* International Journal of Scientific and Research Publications, 2012. **2**(7): p. 1-5.
55. Arora Abrol, S., C. Bhargava, and P.K. Sharma, *Material and its selection attributes for improved DSSC.* Materials Today: Proceedings, 2021.
56. Hu, L. and A. Mandelis, *Advanced characterization methods of carrier transport in quantum dot photovoltaic solar cells.* Journal of Applied Physics, 2021. **129**(9): p. 091101.
57. Niu, G., X. Guo, and L. Wang, *Review of recent progress in chemical stability of perovskite solar cells.* Journal of Materials Chemistry A, 2015. **3**(17): p. 8970-8980.
58. Ding, X., et al., *Passivation functionalized phenothiazine-based hole transport material for highly efficient perovskite solar cell with efficiency exceeding 22%.* Chemical Engineering Journal, 2021. **410**: p. 128328.
59. Almonacid, F., et al., *Review of techniques based on artificial neural networks for the electrical characterization of concentrator photovoltaic technology.* Renewable and Sustainable Energy Reviews, 2017. **75**: p. 938-953.
60. Pérez-Higueras, P., et al., *High Concentrator PhotoVoltaics efficiencies: Present status and forecast.* Renewable and Sustainable Energy Reviews, 2011. **15**(4): p. 1810-1815.

61. Barlev, D., R. Vidu, and P. Stroeve, *Innovation in concentrated solar power.* Solar Energy Materials and Solar Cells, 2011. **95**(10): p. 2703-2725.
62. Khlief, A.K., et al., *Concentrated solar tower hybrid evacuated tube–photovoltaic/thermal receiver with a non-imaging optic reflector: A case study.* Journal of Cleaner Production, 2021: p. 126683.
63. Corona, B., G.S. Miguel, and E. Cerrajero, *Life cycle assessment of concentrated solar power (CSP) and the influence of hybridising with natural gas.* The International Journal of Life Cycle Assessment, 2014. **19**(6): p. 1264-1275.
64. Fuqiang, W., et al., *Progress in concentrated solar power technology with parabolic trough collector system: A comprehensive review.* Renewable and Sustainable Energy Reviews, 2017. **79**: p. 1314-1328.
65. Al-Mohamad, A., *Global, direct and diffuse solar-radiation in Syria.* Applied Energy, 2004. **79**(2): p. 191-200.
66. Page, J., *Chapter IIA-1 - The Role of Solar-Radiation Climatology in the Design of Photovoltaic Systems*, in *Practical Handbook of Photovoltaics (Second Edition)*, A. McEvoy, T. Markvart, and L. Castañer, Editors. 2012, Academic Press: Boston. p. 573-643.
67. Lovegrove, K. and W. Stein, *Concentrating solar power technology: principles, developments and applications*. 2012: Elsevier.
68. Machinda, G., et al. *Concentrating solar thermal power technologies: a review*. in *India Conference (INDICON), 2011 Annual IEEE*. 2011. IEEE.
69. DSW), C.S.P.D.S.W.C.-. *Technology and Requirements*. 2021 [cited 24/03/2021]; Available from: https://sites.google.com/site/jgmcspdsw1/concentrating-solar-power-csp/technology-and-requirements.
70. Ahmadi, M.H., et al., *Solar power technology for electricity generation: A critical review.* Energy Science & Engineering, 2018. **6**(5): p. 340-361.
71. Silva, R., M. Pérez, and A. Fernández-Garcia, *Modeling and co-simulation of a parabolic trough solar plant for industrial process heat.* Applied energy, 2013. **106**: p. 287-300.
72. Sandeep, H.M. and U.C. Arunachala, *Solar parabolic trough collectors: A review on heat transfer augmentation techniques.* Renewable and Sustainable Energy Reviews, 2017. **69**: p. 1218-1231.
73. Liang, H., S. You, and H. Zhang, *Comparison of different heat transfer models for parabolic trough solar collectors.* Applied Energy, 2015. **148**: p. 105-114.
74. Mohamad, K. and P. Ferrer, *Thermal performance and design parameters investigation of a novel cavity receiver unit for parabolic trough concentrator.* Renewable Energy, 2021. **168**: p. 692-704.
75. Grena, R., *Efficiency gain of a solar trough collector due to an IR-reflective film on the non-irradiated part of the receiver.* International journal of green energy, 2011. **8**(7): p. 715-733.
76. Behar, O., A. Khellaf, and K. Mohammedi, *A review of studies on central receiver solar thermal power plants.* Renewable and sustainable energy reviews, 2013. **23**: p. 12-39.
77. Nixon, J.D. and P.A. Davies, *Cost-exergy optimisation of linear Fresnel reflectors.* Solar Energy, 2012. **86**(1): p. 147-156.
78. Zhang, H.L., et al., *Concentrated solar power plants: Review and design methodology.* Renewable and Sustainable Energy Reviews, 2013. **22**: p. 466-481.
79. Abbas, R., et al., *High concentration linear Fresnel reflectors.* Energy conversion and management, 2013. **72**: p. 60-68.

80. Sirimanna, M. and J. Nixon, *Effects of Mirror Geometry on the Optical Efficiency of a Linear Fresnel Reflector (LFR)*, in *Renewable Energy and Sustainable Buildings*. 2020, Springer. p. 337-347.
81. Bellos, E., C. Tzivanidis, and A. Papadopoulos, *Daily, monthly and yearly performance of a linear Fresnel reflector.* Solar Energy, 2018. **173**: p. 517-529.
82. Kalogirou, S.A., *Solar thermal collectors and applications.* Progress in energy and combustion science, 2004. **30**(3): p. 231-295.
83. Alaphilippe, M., S. Bonnet, and P. Stouffs, *Low power thermodynamic solar energy conversion: coupling of a parabolic trough concentrator and an Ericsson engine.* International Journal of Thermodynamics, 2007. **10**(1): p. 37-45.
84. Uzair, M., T.N. Anderson, and R.J. Nates, *The impact of the parabolic dish concentrator on the wind induced heat loss from its receiver.* Solar Energy, 2017. **151**: p. 95-101.
85. Günther, M., et al., *Parabolic trough technology.* Advanced CSP teaching materials, 2011: p. 1-106.
86. Gunther, M. and R. Shahbazfar, *Solar dish technology.* Advanced CSP teaching materials, 2011. **1**: p. 1-63.
87. Rodriguez-Sanchez, D. and G. Rosengarten, *Improving the concentration ratio of parabolic troughs using a second-stage flat mirror.* Applied Energy, 2015. **159**: p. 620-632.
88. Feuermann, D. and J.M. Gordon, *SOLAR FIBER-OPTIC MINI-DISHES: A NEW APPROACH TO THE EFFICIENT COLLECTION OF SUNLIGHT.* Solar Energy, 1999. **65**(3): p. 159-170.
89. Imenes, A.G. and D.R. Mills, *Spectral beam splitting technology for increased conversion efficiency in solar concentrating systems: a review.* Solar Energy Materials and Solar Cells, 2004. **84**(1): p. 19-69.
90. Li, G., et al., *A review of solar photovoltaic-thermoelectric hybrid system for electricity generation.* Energy, 2018. **158**: p. 41-58.
91. Crisostomo, F., et al., *Experimental testing of SiNx/SiO2 thin film filters for a concentrating solar hybrid PV/T collector.* Renewable Energy, 2014. **72**: p. 79-87.
92. Yin, E., Q. Li, and Y. Xuan, *A novel optimal design method for concentration spectrum splitting photovoltaic–thermoelectric hybrid system.* Energy, 2018. **163**: p. 519-532.
93. Ju, X., et al., *A review of the concentrated photovoltaic/thermal (CPVT) hybrid solar systems based on the spectral beam splitting technology.* Applied Energy, 2017. **187**: p. 534-563.
94. Jackson, E. *Areas for improvement of the semiconductor solar energy converter*. in *Transactions of the Conference on the Use of Solar Energy*. 1955.
95. Moon, R., et al. *Multigap solar cell requirements and the performance of AlGaAs and Si cells in concentrated sunlight*. in *13th Photovoltaic specialists conference*. 1978.
96. Kandilli, C. and G. Külahlı, *Performance analysis of a concentrated solar energy for lighting-power generation combined system based on spectral beam splitting.* Renewable Energy, 2017. **101**(Supplement C): p. 713-727.
97. Chun-Hui, S., et al., *A dielectric multilayer filter for combining photovoltaics with a Stirling engine for improvement of the efficiency of solar electricity generation.* Chinese Physics Letters, 2011. **28**(12): p. 128402.
98. Shou, C., et al., *Investigation of a broadband TiO2/SiO2 optical thin-film filter for hybrid solar power systems.* Applied Energy, 2012. **92**: p. 298-306.
99. Mojiri, A., et al., *A spectrally splitting photovoltaic-thermal hybrid receiver utilising direct absorption and wave interference light filtering.* Solar Energy Materials and Solar Cells, 2015. **139**: p. 71-80.

100. An, W., et al., *Investigation on a spectral splitting photovoltaic/thermal hybrid system based on polypyrrole nanofluid: preliminary test.* Renewable Energy, 2016. **86**: p. 633-642.
101. Jiang, S., et al., *Optical modeling for a two-stage parabolic trough concentrating photovoltaic/thermal system using spectral beam splitting technology.* Solar Energy Materials and Solar Cells, 2010. **94**(10): p. 1686-1696.
102. Twaha, S., et al., *A comprehensive review of thermoelectric technology: Materials, applications, modelling and performance improvement.* Renewable and Sustainable Energy Reviews, 2016. **65**: p. 698-726.
103. Montecucco, A., J.R. Buckle, and A.R. Knox, *Solution to the 1-D unsteady heat conduction equation with internal Joule heat generation for thermoelectric devices.* Applied Thermal Engineering, 2012. **35**: p. 177-184.
104. Seetawan, T., et al., *Thermoelectric Energy Conversion of p–Ca3Co4O9/n–CaMnO3 Module.* Energy Procedia, 2014. **61**: p. 1067-1070.
105. Riffat, S.B. and X. Ma, *Thermoelectrics: a review of present and potential applications.* Applied Thermal Engineering, 2003. **23**(8): p. 913-935.
106. Zheng, X.F., et al., *A review of thermoelectrics research – Recent developments and potentials for sustainable and renewable energy applications.* Renewable and Sustainable Energy Reviews, 2014. **32**: p. 486-503.
107. Srinivasan, B., *Novel chalcogenide based glasses, ceramics and polycrystalline materials for thermoelectric application*. 2018, Université Rennes 1.
108. Tritt, T.M.a.S., M. A., *Thermoelectric Materials, Phenomena, and Applications: A Bird's Eye View,.* MRS Bulletin, Cambridge University Press, (2006). **31(3)**: p. 88–198.
109. Sharma, S., V. Dwivedi, and S. Pandit, *A review of thermoelectric devices for cooling applications.* International journal of green energy, 2014. **11**(9): p. 899-909.
110. Bulusu, A. and D.G. Walker, *Review of electronic transport models for thermoelectric materials.* Superlattices and Microstructures, 2008. **44**(1): p. 1-36.
111. Li, P., et al., *Design of a Concentration Solar Thermoelectric Generator.* Journal of Electronic Materials, 2010. **39**(9): p. 1522-1530.
112. Hamid Elsheikh, M., et al., *A review on thermoelectric renewable energy: Principle parameters that affect their performance.* Renewable and Sustainable Energy Reviews, 2014. **30**: p. 337-355.
113. Dong, Z., et al., *Raman characterization on two-dimensional materials-based thermoelectricity.* Molecules, 2019. **24**(1): p. 88.
114. Gould, C.A., et al. *A comprehensive review of thermoelectric technology, micro-electrical and power generation properties*. in *2008 26th International Conference on Microelectronics*. 2008.
115. Grubišić-Čabo, F., S. Nižetić, and T. Giuseppe Marco, *Photovoltaic panels: A review of the cooling techniques.* Transactions of FAMENA, 2016. **40**(SI-1): p. 63-74.
116. Peng, J., et al., *Study on the overall energy performance of a novel c-Si based semitransparent solar photovoltaic window.* Applied Energy, 2019. **242**: p. 854-872.
117. Siecker, J., K. Kusakana, and B.P. Numbi, *A review of solar photovoltaic systems cooling technologies.* Renewable and Sustainable Energy Reviews, 2017. **79**: p. 192-203.
118. Fisac, M., F.X. Villasevil, and A.M. López, *High-efficiency photovoltaic technology including thermoelectric generation.* Journal of power sources, 2014. **252**: p. 264-269.
119. Park, K.-T., et al., *Lossless hybridization between photovoltaic and thermoelectric devices.* Scientific reports, 2013. **3**(1): p. 1-6.
120. Zhu, W., et al., *High-performance photovoltaic-thermoelectric hybrid power generation system with optimized thermal management.* Energy, 2016. **100**: p. 91-101.

121. Mahmoudinezhad, S., A. Rezaniakolaei, and L.A. Rosendahl, *Numerical parametric study on the performance of CPV-TEG hybrid system.* Energy Procedia, 2019. **158**: p. 453-458.
122. Mahmoudinezhad, S., et al., *Experimental investigation on spectrum beam splitting photovoltaic–thermoelectric generator under moderate solar concentrations.* Energy, 2022. **238**: p. 121988.
123. Mojiri, A., C. Stanley, and G. Rosengarten, *Spectrally Splitting Hybrid Photovoltaic/thermal Receiver Design for a Linear Concentrator.* Energy Procedia, 2014. **48**: p. 618-627.
124. Bjørk, R. and K.K. Nielsen, *The maximum theoretical performance of unconcentrated solar photovoltaic and thermoelectric generator systems.* Energy Conversion and Management, 2018. **156**: p. 264-268.
125. Mizoshiri, M., M. Mikami, and K. Ozaki, *Thermal–photovoltaic hybrid solar generator using thin-film thermoelectric modules.* Japanese Journal of Applied Physics, 2012. **51**(6S): p. 06FL07.
126. Mahmoudinezhad, S., et al., *Experimental investigation on spectrum beam splitting photovoltaic–thermoelectric generator under moderate solar concentrations.* Energy, 2022. **238**: p. 121988.
127. Yang, Z., et al., *Maximum efficiency and parametric optimum selection of a concentrated solar spectrum splitting photovoltaic cell-thermoelectric generator system.* Energy Conversion and Management, 2018. **174**: p. 65-71.
128. Elsarrag, E., et al., *Spectrum splitting for efficient utilization of solar radiation: a novel photovoltaic–thermoelectric power generation system.* Renewables: Wind, Water, and Solar, 2015. **2**(1): p. 1-11.
129. Ju, X., et al., *Numerical analysis and optimization of a spectrum splitting concentration photovoltaic–thermoelectric hybrid system.* Solar energy, 2012. **86**(6): p. 1941-1954.
130. Zhou, Y.-P., et al., *Design and experimental investigation of a novel full solar spectrum utilization system.* Applied Energy, 2020. **260**: p. 114258.
131. Paetzold, J., et al., *Wind engineering analysis of parabolic trough solar collectors: the effects of varying the trough depth.* Journal of Wind engineering and industrial Aerodynamics, 2014. **135**: p. 118-128.
132. Akbarzadeh, S. and M.S. Valipour, *Heat transfer enhancement in parabolic trough collectors: A comprehensive review.* Renewable and Sustainable Energy Reviews, 2018. **92**: p. 198-218.
133. Yılmaz, İ.H. and A. Mwesigye, *Modeling, simulation and performance analysis of parabolic trough solar collectors: A comprehensive review.* Applied Energy, 2018. **225**: p. 135-174.
134. Cheng, Z.-D., et al., *A detailed parameter study on the comprehensive characteristics and performance of a parabolic trough solar collector system.* Applied thermal engineering, 2014. **63**(1): p. 278-289.
135. Hafez, A., et al., *Solar parabolic dish Stirling engine system design, simulation, and thermal analysis.* Energy conversion and management, 2016. **126**: p. 60-75.
136. Support, U. *Which Ultimaker material should I use?* 2021 [cited 2021 13/06/2021]; Available from: https://support.ultimaker.com/hc/en-us/articles/360011940320-Which-Ultimaker-material-should-I-use-.
137. Corporation, N. *Class ABB Small Area Solar Simulators*. 2021 [cited 05/03/2021]; Available from: https://www.newport.com/f/small-area-solar-simulators.
138. Laboratory, N.R.E. *Reference Air Mass 1.5 Spectra*. [cited 2021 18/08/2021]; Available from: https://www.nrel.gov/grid/solar-resource/spectra-am1.5.html.

139. Khunchan, S. and B. Wiengmoon. *Method to determine the single curve IV characteristic parameter of solar cell*. in *Journal of Physics: Conference Series*. 2018. IOP Publishing.
140. Tips, P.E. *Solar cells and power, Part 2 – power extraction*. 04/03/2021]; Available from: https://www.powerelectronictips.com/solar-cells-power-part-2-power-extraction/.
141. Kalogirou, S.A., *Solar Energy Engineering: Processes and Systems*. 2014: Elsevier.
142. Masters, G.M., *Renewable and Efficient Electric Power Systems*. 2004: A JOHN WILEY & SONS, INC., PUBLICATION.
143. Luque, A. and S. Hegedus, *Photovoltaic science and engineering*. 2003: Wiley Online Library.
144. Aihara, T., et al., *Analysis of subcell open-circuit voltages of InGaP/GaAs dual-junction solar cells fabricated using hydride vapor phase epitaxy.* Japanese Journal of Applied Physics, 2020. **59**(SG): p. SGGF02.
145. Takamoto, T., et al., *Structural optimization for single junction InGaP solar cells.* Solar energy materials and solar cells, 1994. **35**: p. 25-31.
146. Chen, H.-C., et al., *Enhanced efficiency for c-Si solar cell with nanopillar array via quantum dots layers.* Optics Express, 2011. **19**(S5): p. A1141-A1147.
147. Lopez-Delgado, R., et al., *Enhanced conversion efficiency in Si solar cells employing photoluminescent down-shifting CdSe/CdS core/shell quantum dots.* Scientific Reports, 2017. **7**(1): p. 14104.
148. Yamamoto, H., et al., *High-efficiency μc-Si/c-Si heterojunction solar cells.* Solar Energy Materials and Solar Cells, 2002. **74**(1): p. 525-531.
149. Archer, M.D. and M.A. Green, *Clean electricity from photovoltaics*. Vol. 4. 2014: World Scientific.
150. Kennedy, C.E., *Review of mid-to high-temperature solar selective absorber materials*. 2002, National Renewable Energy Lab., Golden, CO.(US).
151. Dury, M.R., et al., *Common black coatings–reflectance and ageing characteristics in the 0.32–14.3 μm wavelength range.* Optics communications, 2007. **270**(2): p. 262-272.
152. Rohsenow, W.M., J.P. Hartnett, and Y.I. Cho, *Handbook of heat transfer*. Vol. 3. 1998: McGraw-Hill New York.
153. Kreith, F. and R.M. Manglik, *Principles of heat transfer*. 2016: Cengage learning.
154. YENER, T., Ş.Ç. YENER, and R. MUTLU, *Convection Coefficient Estimation of Still Air Using an Infrared Thermometer and Curve-Fitting.* Journal of Engineering Technology and Applied Sciences. **4**(2): p. 95-103.
155. Ando, M., et al. *Emissivity of black plated open honeycomb and black coatings at cryogenic temperatures*. in *IOP Conference Series: Materials Science and Engineering*. 2019. IOP Publishing.
156. Park, D., et al., *Thermal and electrical conduction of single-crystal Bi 2 Te 3 nanostructures grown using a one step process.* Scientific reports, 2016. **6**(1): p. 1-9.
157. Kanimba, E. and Z. Tian, *Modeling of a thermoelectric generator device.* Thermoelectrics for Power Generation—A Look at Trends in the Technology, 2016: p. 461-479.
158. Rowe, D. and G. Min, *Design theory of thermoelectric modules for electrical power generation.* IEE Proceedings-Science, Measurement and Technology, 1996. **143**(6): p. 351-356.
159. Dong, Y., et al., *Band offsets of In Ga P/ Ga As heterojunctions by scanning tunneling spectroscopy.* Journal of applied physics, 2008. **103**(7): p. 073704.

160. Keener, D., et al. *Progress toward technology transition of GaInP/sub 2//GaAs/Ge multijunction solar cells*. in *Conference Record of the Twenty Sixth IEEE Photovoltaic Specialists Conference-1997*. 1997. IEEE.
161. McMahon, W., et al. *Criteria for the design of GaInP/GaAs/Ge triple-junction cells to optimize their performance outdoors*. in *Conference Record of the Twenty-Ninth IEEE Photovoltaic Specialists Conference, 2002*. 2002. IEEE.
162. Liang, H., et al., *Progress in full spectrum solar energy utilization by spectral beam splitting hybrid PV/T system.* Renewable and Sustainable Energy Reviews, 2021. **141**: p. 110785.
163. Optics, E. *Optical Filters*. 2021 [cited 2021 05/03/2021]; Available from: https://www.edmundoptics.co.uk/knowledge-center/application-notes/optics/optical-filters/#0.
164. Sharma, R., et al., *Life span and overall performance enhancement of Solar Photovoltaic cell using water as coolant: A recent review.* Materials Today: Proceedings, 2018. **5**(9, Part 3): p. 18202-18210.
165. Dash, P. and N. Gupta, *Effect of temperature on power output from different commercially available photovoltaic modules.* International Journal of Engineering Research and Applications, 2015. **5**(1): p. 148-151.
166. Helmers, H., M. Schachtner, and A.W. Bett, *Influence of temperature and irradiance on triple-junction solar subcells.* Solar Energy Materials and Solar Cells, 2013. **116**: p. 144-152.
167. Aiken, D., et al. *Temperature dependent spectral response measurements for III-V multi-junction solar cells*. Conference Record of the Twenty-Ninth IEEE Photovoltaic Specialists Conference, 2002. 2002; 828-831].
168. Steiner, M.A., et al. *Temperature-dependent measurements of an inverted metamorphic multijunction (IMM) solar cell*. in *2011 37th IEEE Photovoltaic Specialists Conference*. 2011. IEEE.
169. Friedman, D. *Modelling of tandem cell temperature coefficients*. in *Conference Record of the Twenty Fifth IEEE Photovoltaic Specialists Conference-1996*. 1996. IEEE.
170. Landis, G.A., et al. *High temperature solar cell development*. in *18th Space Photovoltaic Research and Technology Conference*. 2005.
171. Hu, M., et al., *Experimental study on a hybrid photo-thermal and radiative cooling collector using black acrylic paint as the panel coating.* Renewable Energy, 2019. **139**: p. 1217-1226.
172. Bijukumar, B., et al., *MPPT algorithm for thermoelectric generators based on parabolic extrapolation.* IET Generation, Transmission & Distribution, 2018. **13**(6): p. 821-828.
173. García-Cañadas, J. and G. Min, *Impedance spectroscopy models for the complete characterization of thermoelectric materials.* Journal of Applied Physics, 2014. **116**(17): p. 174510.
174. Jaegle, M. *Multiphysics simulation of thermoelectric systems-modeling of Peltier-cooling and thermoelectric generation*. in *COMSOL Conference 2008 Hannover*. 2008.
175. Enescu, D. and E.O. Virjoghe, *A review on thermoelectric cooling parameters and performance.* Renewable and Sustainable Energy Reviews, 2014. **38**: p. 903-916.
176. Min, G. and D. Rowe, *Improved model for calculating the coefficient of performance of a Peltier module.* Energy conversion and management, 2000. **41**(2): p. 163-171.
177. Stine, W.B., *Progress in parabolic dish technology*. 1989, Solar Energy Research Inst.(SERI), Golden, CO (United States).

178. Adelkhani, H., S. Nasoodi, and A. Jafari, *A study of the morphology and optical properties of electropolished aluminum in the Vis-IR region.* Int. J. Electrochem. Sci, 2009. **4**(9).
179. Ayieko, C.O., et al., *Controlled texturing of aluminum sheet for solar energy applications.* 2015.
180. Alanod. *Alanod Products*. 2021 [cited 07/03/2021]; Available from: https://alanod-westlake.com/products.
181. *The LONDON METAL EXCHANGE*. [cited 2021 15/11/2021]; Available from: https://www.lme.com/.
182. Idlimam, R., et al. *Impact of the parabolic solar concentrator's rim angle on the quantity of reflected rays and concentrated flux on the receiver*. in *2018 6th International Renewable and Sustainable Energy Conference (IRSEC)*. 2018. IEEE.
183. Zayed, M.E., et al., *Optimal design parameters and performance optimization of thermodynamically balanced dish/Stirling concentrated solar power system using multi-objective particle swarm optimization.* Applied Thermal Engineering, 2020. **178**: p. 115539.
184. Hernández, N., et al., *Conical receiver for a paraboloidal concentrator with large rim angle.* Solar energy, 2012. **86**(4): p. 1053-1062.
185. Patil, R.G., et al., *Alternative designs of evacuated receiver for parabolic trough collector.* Energy, 2018. **155**: p. 66-76.
186. Al-Ansary, H. and O. Zeitoun, *Numerical study of conduction and convection heat losses from a half-insulated air-filled annulus of the receiver of a parabolic trough collector.* Solar Energy, 2011. **85**(11): p. 3036-3045.
187. Abbas, M.S., et al., *A Review Study on the Effect of Glass Envelope, Working Fluid and Geometry Contributions for the Receiver on Performance of Parabolic Trough Collector (PTC).* vol, 2006. **13**: p. 8199-8210.
188. Blanco, M. and L.R. Santigosa, *Advances in concentrating solar thermal research and technology*. 2016: Woodhead Publishing.
189. Özişik, M.N., et al., *Finite difference methods in heat transfer*. 2017: CRC press.
190. Society, A.S.G. *Optical Transmission*. 2021 [cited 2021 23/05/2021]; Available from: https://asgs-glass.org/optical-transmission/.
191. Liu, J., D. Lei, and Q. Li, *Vacuum lifetime and residual gas analysis of parabolic trough receiver.* Renewable energy, 2016. **86**: p. 949-954.
192. Wu, Z., et al., *Structural reliability analysis of parabolic trough receivers.* Applied energy, 2014. **123**: p. 232-241.
193. Technology, P. *TC-08 Data Logger*. 2022 [cited 2022 08/02/2022]; Available from: https://www.picotech.com/data-logger/tc-08/usb-tc-08-manuals.
194. Yu, Q., et al., *Thermal properties of high temperature vacuum receivers used for parabolic trough solar thermal power system.* Progress in Natural Science: Materials International, 2017. **27**(4): p. 410-415.
195. Lei, D., et al., *An experimental study of thermal characterization of parabolic trough receivers.* Energy Conversion and Management, 2013. **69**: p. 107-115.
196. Vinetsky, Y., et al., *CNT-Based Solar Thermal Coatings: Absorptance vs. Emittance.* Coatings, 2020. **10**(11): p. 1101.

Appendices:

Appendix 3.1:

To justify the use of the trough/dish compact design in this study, a copper plate (60x60x1mm) was designed and simulated in Solidworks that replaces the trough/dish concentrators and the copper rod absorber, the copper plate will be the absorber instead. The simulated results were compared with simulated results obtained from trough compact design. The aim of the comparison is to validate the use of the concentrator (trough/dish) in the design which will increase the cost and complexity of the system, however, it will be justified by the increase in power production.

First, the copper plate was manufactured in the university workshop and painted with black paint (High Temp. Paints: PNM/PAM) on one side to maximize the heat absorption. The plate was tested by placing it under a radiation of 1000 W/m^2 to measure its final temperature after reaching steady state. The steady state temperature measured was (52.8 C).

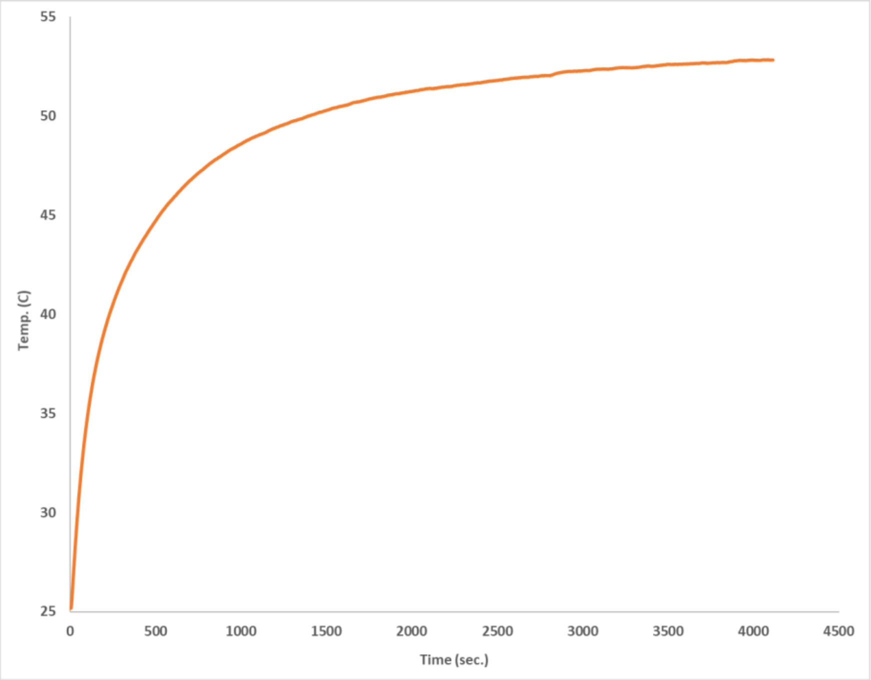

Figure 1: *Experimental copper plate steady state temperature*

The copper plate design in Solidworks was illuminated under (1000 W/m^2) to compare result with actual measured temperature. Figure 2 below shows result obtained.

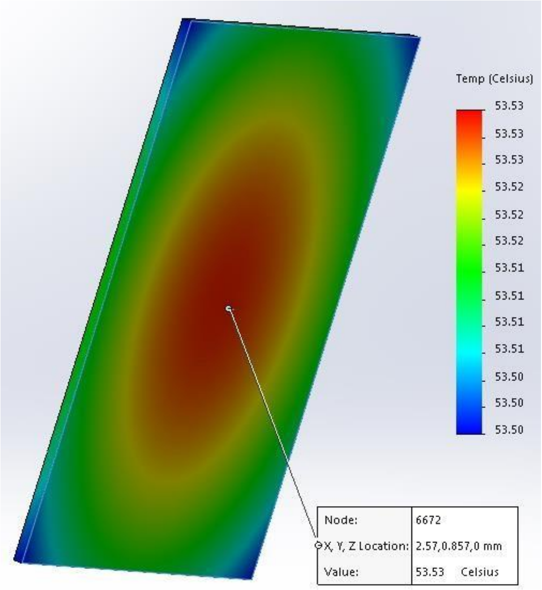

Figure 2: *Simulated copper plate steady state temperature*

The two results were in full agreement which add confidence on simulated results.

The simulation study was run by using five different sizes thermoelectric generators, TEGs (mentioned in chapter 3).

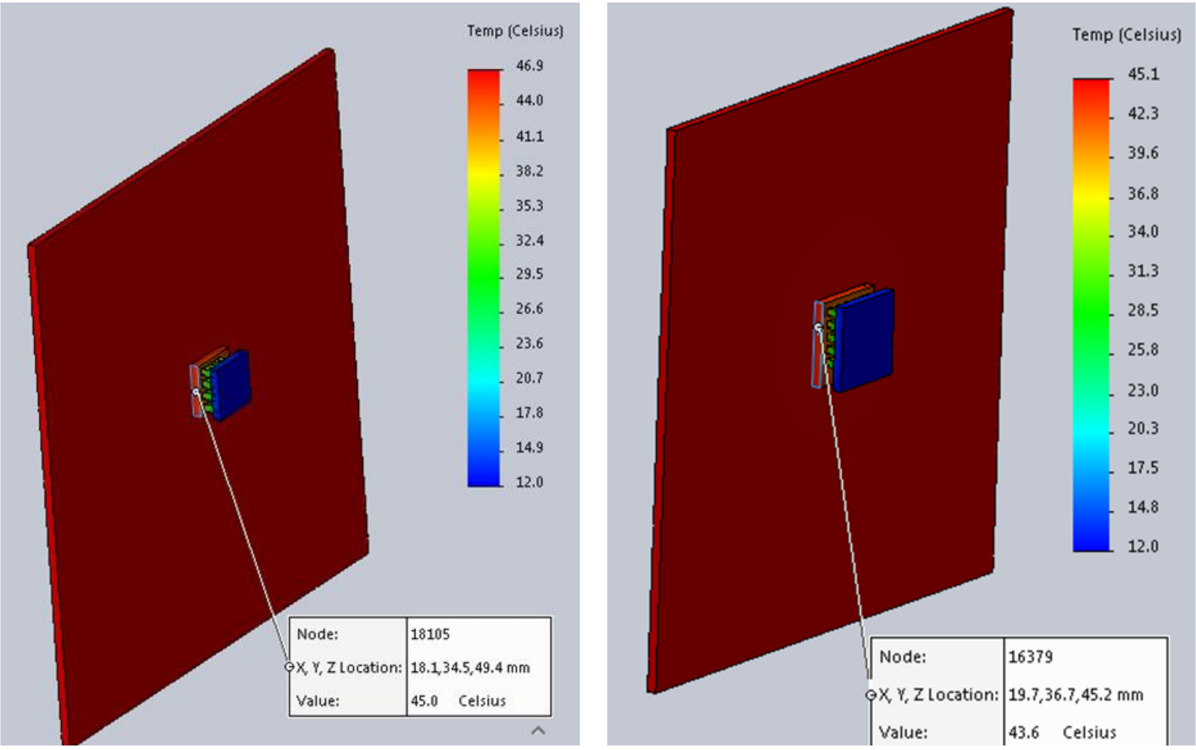

6x6mm TEG **9x9mm TEG**

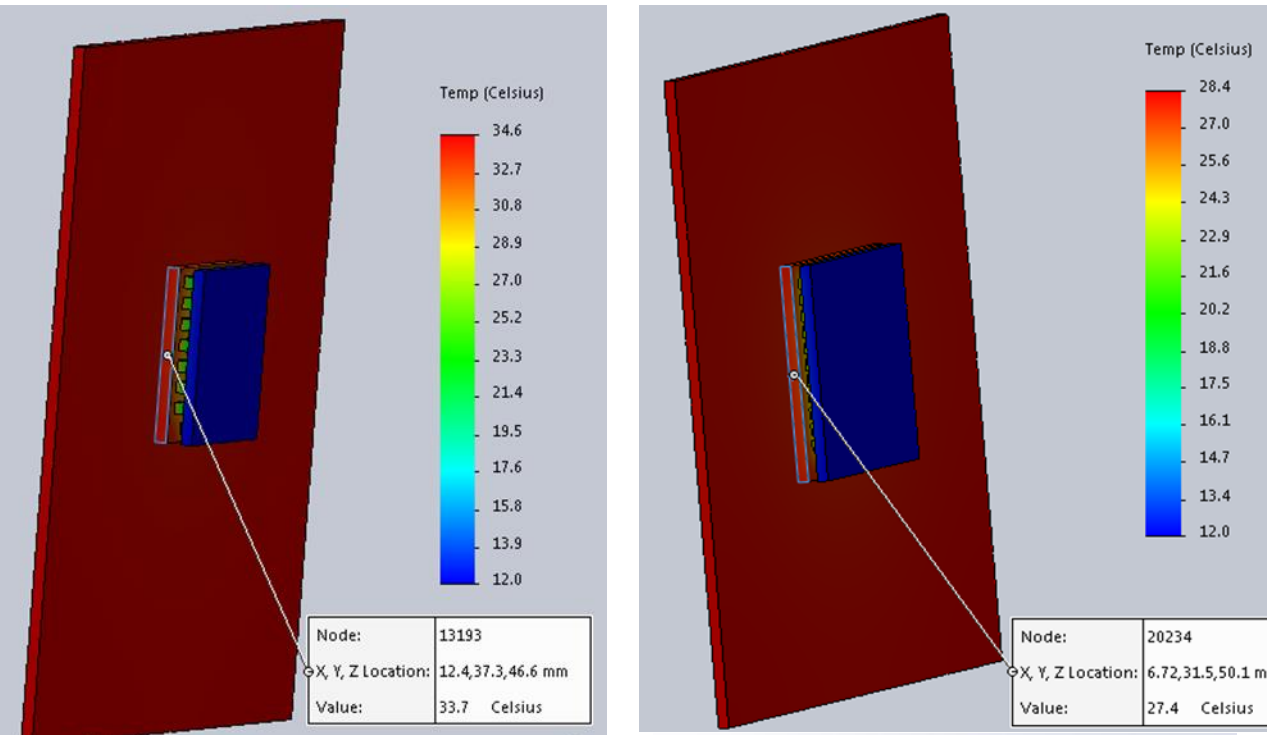

Node:	13193
X, Y, Z Location:	12.4,37.3,46.6 mm
Value:	33.7 Celsius

Node:	20234
X, Y, Z Location:	6.72,31.5,50.1 m
Value:	27.4 Celsius

15x15mm TEG **20x20mm TEG**

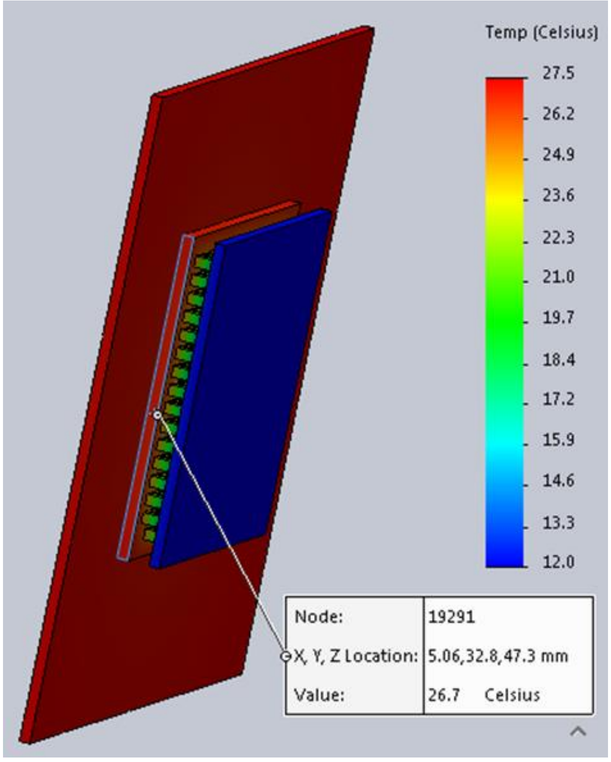

Node:	19291
X, Y, Z Location:	5.06,32.8,47.3 mm
Value:	26.7 Celsius

30x30mm TEG

Figure 2: *Copper plates simulation for all TEGs.*

Table 1 below summarises the results of simulation (cold side of the TEG was kept at 12 C).

Table 1: *Copper plate simulated results for all five TEGs.*

Module	**TEG Size (mm)**	**T_{hot} (C)**	**T_{cold} (C)**	**ΔT (C)**
1	30x30	26.7	12	14.7
2	20x20	27.4	12	15.4
3	15x15	33.7	12	21.7
4	9x9	43.6	12	31.6
5	6x6	45.0	12	33.0

All five TEGs are also simulated with fixed heat absorber (30x30mm). TEG (30x30m) size simulation is shown in figure 3 below.

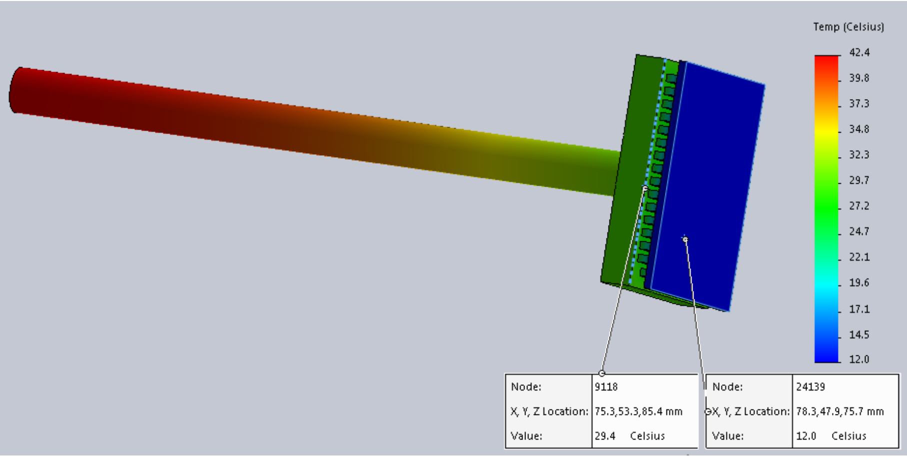

Node:	9118
X, Y, Z Location:	75.3,53.3,85.4 mm
Value:	29.4 Celsius

Node:	24139
X, Y, Z Location:	78.3,47.9,75.7 mm
Value:	12.0 Celsius

Figure 3: *Simulated fixed absorber for TEG (30x30mm) steady state temperature*

Comparing the results of copper plate simulation for all TEGs with that of the compact design revealed the advantage of the compact design as higher delta temperature will result in more power production. Figure 4 below shows the comparison for all five modules.

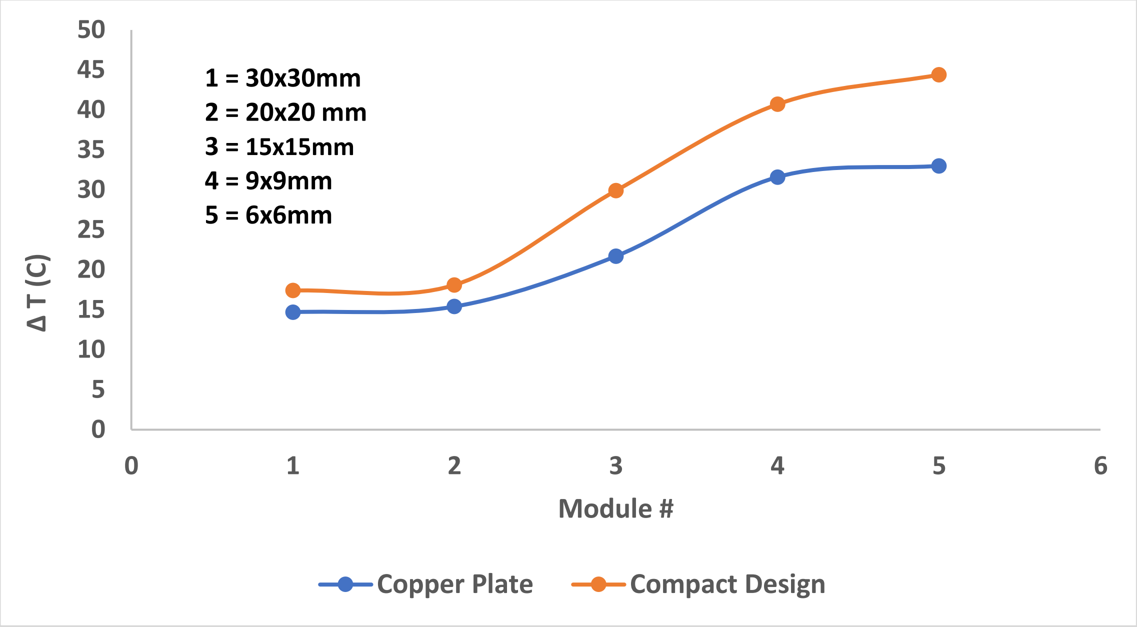

Figure 4: *Simulated compact design vs. copper plate for all five TEGs.*

The results above showed that the compact design resulted in higher delta temperature for all modules compared to that for copper plate which clearly justify the use of compact design in this study.

Appendix 3.2:

Copper rod optimum diameter:

To optimize the copper rod diameter that has a minimum surface area and in the same time, it can practically be used in the compact trough design, a study was done using ray tracing software (TracePro) to find out the tolerance of mis-alignment of the rod from theoretical focal line and yet receiving all reflected rays from the trough.

Vertical alignment:

The placement of the copper rod on the focal point of the parabolic trough have been tested using TracePro. First, the copper rod was placed exactly on the focal point of the trough and simulated using TracePro to find out if the reflected rays fall completely on the rod or not. In addition, the total flux on the copper rod was reflected in the irradiance map.

After that, the copper rod was raised and lowered (up and down) one millimetre in each simulation to find out at which level the reflected rays will miss the copper rod. Results showed that up to 3 mm up/down the reflected rays would be collected by the rod completely.

Below rays, reflection for each simulation is illustrated:

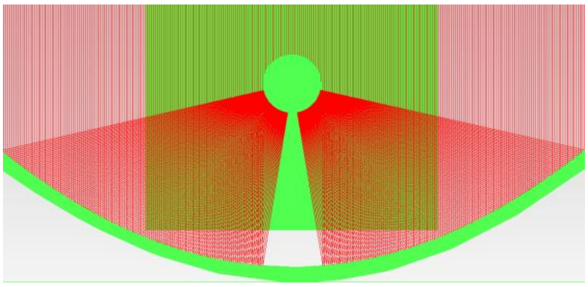

At focal point

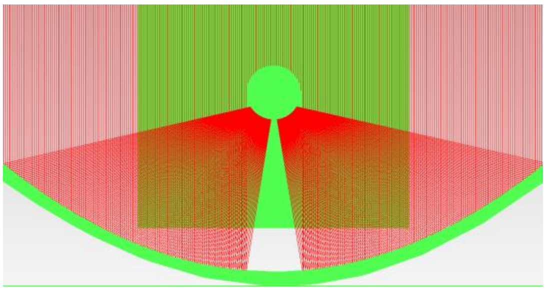

1 mm up

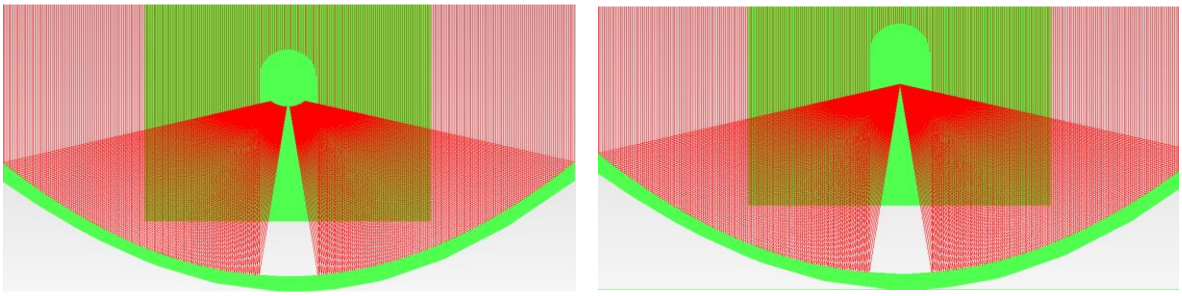

2 mm up

3 mm up

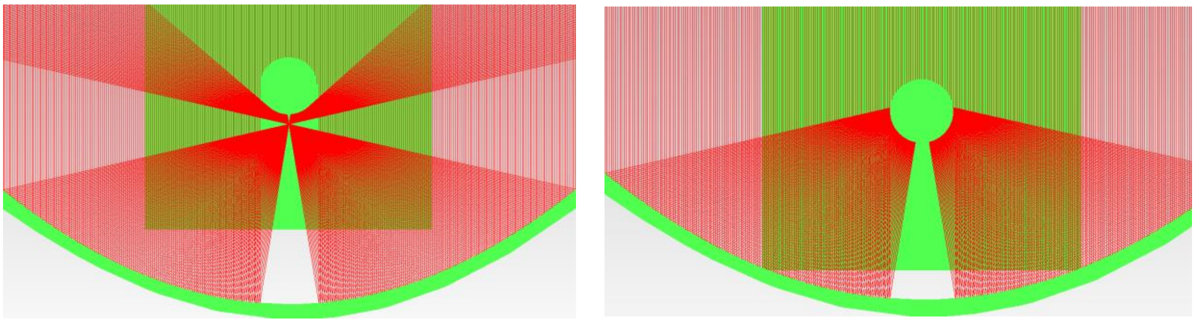

4 mm up

1 mm down

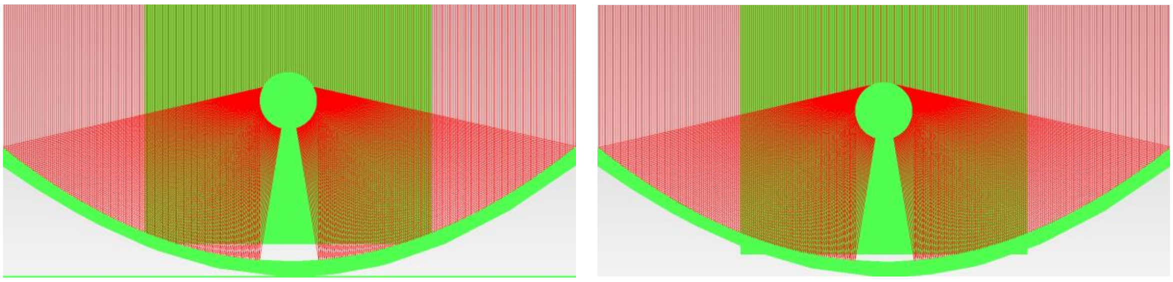

2 mm down

3 mm down

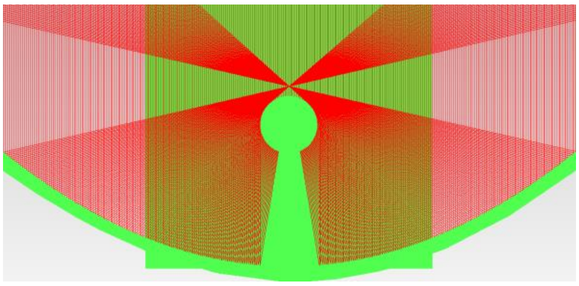

4 mm down

Figure 7: *TracePro simulation for different copper rod positions changed vertically.*

Horizontal alignment:

The same was done but horizontally, in other words, the copper rod was shifted from focal point right and left to see at what position the rays will miss the rod. Simulation was done four times to the right and four time to the left and results revealed the up to 3 mm right the reflected rays will fall completely on the copper rod, however, only 2 mm to the left will secure the receipt of all reflected rays on the copper rod.

Below rays, reflection for each simulation is illustrated:

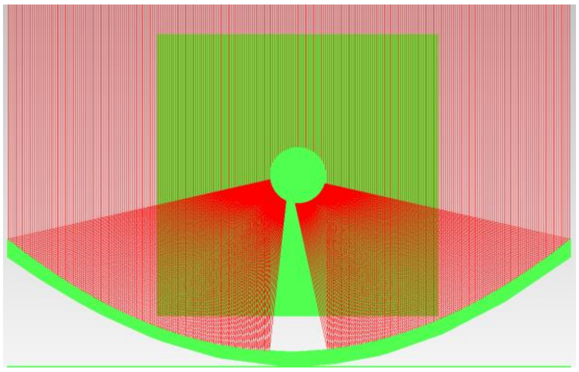

1 mm to the right

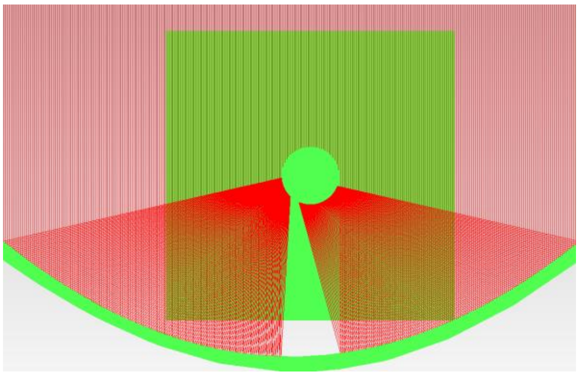

2 mm to the right

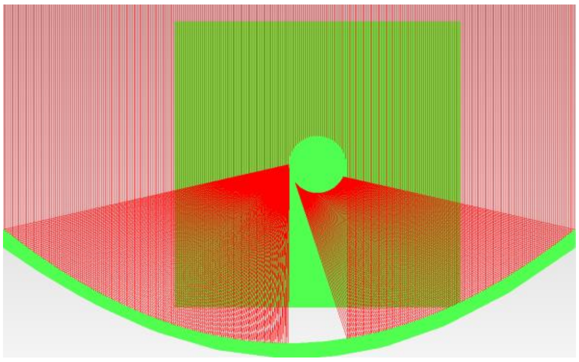

3 mm to the right

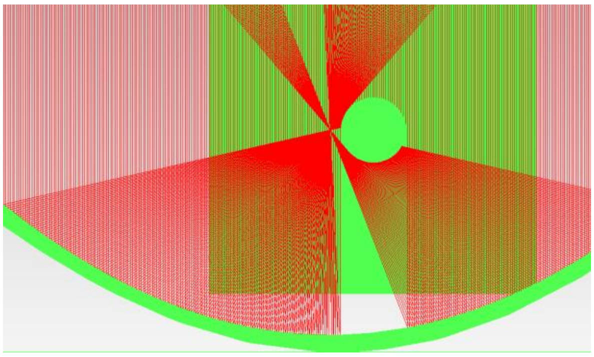

4 mm to the right

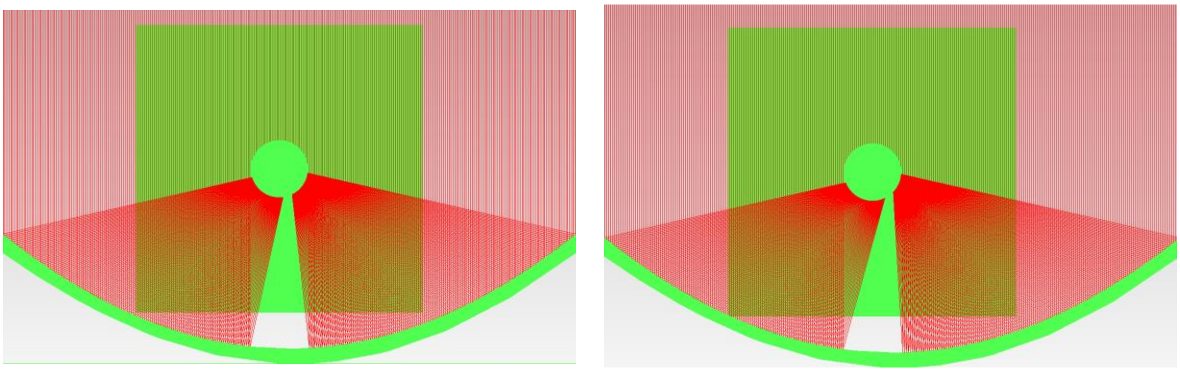

1 mm to the left

2 mm to the left

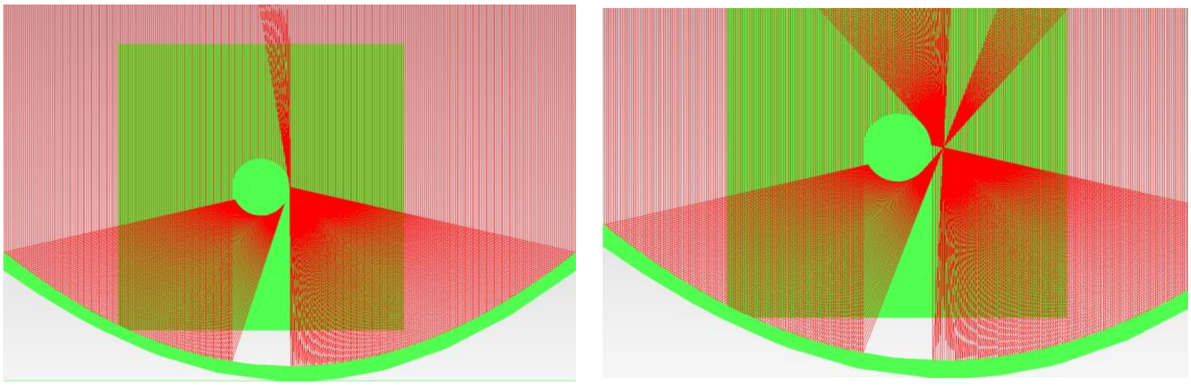

3 mm to the left

4 mm to the left

Figure 8: *TracePro simulation for different copper rod positions changed horizontally.*

The below tables summarize the total flux (W) on both surfaces of the copper rod (up & down):

Table 2: *Total flux received by copper rod at different positions changed vertically and horizontally simulated by TracePro.*

Vertical Alignment

Flux (W)	At Focal point	+ 1mm	+ 2mm	+ 3mm	+ 4mm	- 1mm	- 2mm	- 3mm	- 4mm
Upper Face	0.358	0.358	0.358	0.358	0.358	0.6967	1.488	1.986	0.86624
Lower Face	3.044	3.044	3.044	3.044	1.579	2.706	1.917	1.421	1.060
Total Flux	3.402	3.402	3.402	3.402	**1.936**	3.403	3.405	3.406	**1.926**

Horizontal Alignment

Flux (W)	At Focal point	+ 1mm	+ 2mm	+ 3mm	+ 4mm	- 1mm	- 2mm	- 3mm	- 4mm
Upper Face	0.358	0.358	0.358	0.358	1.273	0.358	0.358	1.872	1.239
Lower Face	3.044	3.044	3.044	3.044	0.9133	3.044	3.044	1.353	0.880
Total Flux	3.402	3.402	3.402	3.402	**2.186**	3.402	3.402	**3.225**	**2.119**

Appendix 3.3:

Copper data sheet

PRO

ENGLISH

Datasheet

Stock No: 684-254

RS Pro Copper Rod, 1000mm x 6mm Diameter

Product Details:

Copper HDHC Rod, Bar & Sheet

A high conductivity, corrosion resistant, malleable copper in rod, bar and sheet form.

Chemical analysis:	
Copper	99.90
Lead	0.005
Bismuth	0.001
Tensile Strength:	
Sheet	240N/mm^2
Half Hard	240N/mm^2

Standards

BS2874/C101 (1986), BS EN 12164 CW 004A

Specifications:

Material:	Copper
Form:	Rod
Length:	1000mm
Rod Diameter:	6mm
Tensile Strength:	240 N/mm^2

Appendix 3.4:

Alanod reflector data sheet

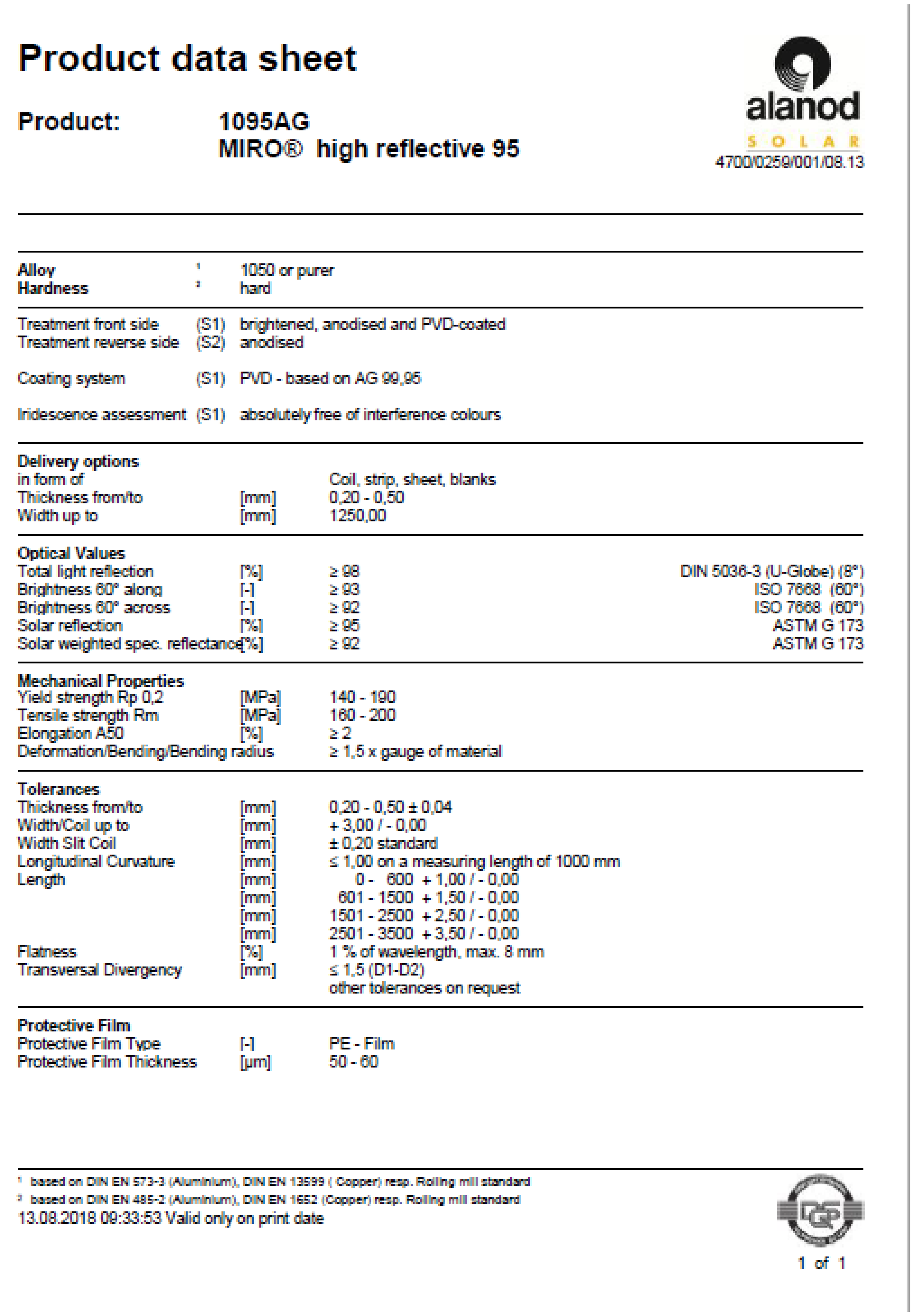

Product data sheet

Product: **1095AG**
MIRO® high reflective 95

alanod SOLAR
4700/0259/001/08.13

Alloy	[1]	1050 or purer
Hardness	[2]	hard

Treatment front side	(S1)	brightened, anodised and PVD-coated
Treatment reverse side	(S2)	anodised
Coating system	(S1)	PVD - based on AG 99,95
Iridescence assessment	(S1)	absolutely free of interference colours

Delivery options		
in form of		Coil, strip, sheet, blanks
Thickness from/to	[mm]	0,20 - 0,50
Width up to	[mm]	1250,00

Optical Values			
Total light reflection	[%]	≥ 98	DIN 5036-3 (U-Globe) (8°)
Brightness 60° along	[-]	≥ 93	ISO 7668 (60°)
Brightness 60° across	[-]	≥ 92	ISO 7668 (60°)
Solar reflection	[%]	≥ 95	ASTM G 173
Solar weighted spec. reflectance	[%]	≥ 92	ASTM G 173

Mechanical Properties		
Yield strength Rp 0,2	[MPa]	140 - 190
Tensile strength Rm	[MPa]	160 - 200
Elongation A50	[%]	≥ 2
Deformation/Bending/Bending radius		≥ 1,5 x gauge of material

Tolerances		
Thickness from/to	[mm]	0,20 - 0,50 ± 0,04
Width/Coil up to	[mm]	+ 3,00 / - 0,00
Width Slit Coil	[mm]	± 0,20 standard
Longitudinal Curvature	[mm]	≤ 1,00 on a measuring length of 1000 mm
Length	[mm]	0 - 600 + 1,00 / - 0,00
	[mm]	601 - 1500 + 1,50 / - 0,00
	[mm]	1501 - 2500 + 2,50 / - 0,00
	[mm]	2501 - 3500 + 3,50 / - 0,00
Flatness	[%]	1 % of wavelength, max. 8 mm
Transversal Divergency	[mm]	≤ 1,5 (D1-D2)
		other tolerances on request

Protective Film		
Protective Film Type	[-]	PE - Film
Protective Film Thickness	[µm]	50 - 60

---

[1] based on DIN EN 573-3 (Aluminium), DIN EN 13599 (Copper) resp. Rolling mill standard

[2] based on DIN EN 485-2 (Aluminium), DIN EN 1652 (Copper) resp. Rolling mill standard

13.08.2018 09:33:53 Valid only on print date

1 of 1

Appendix 4.1:

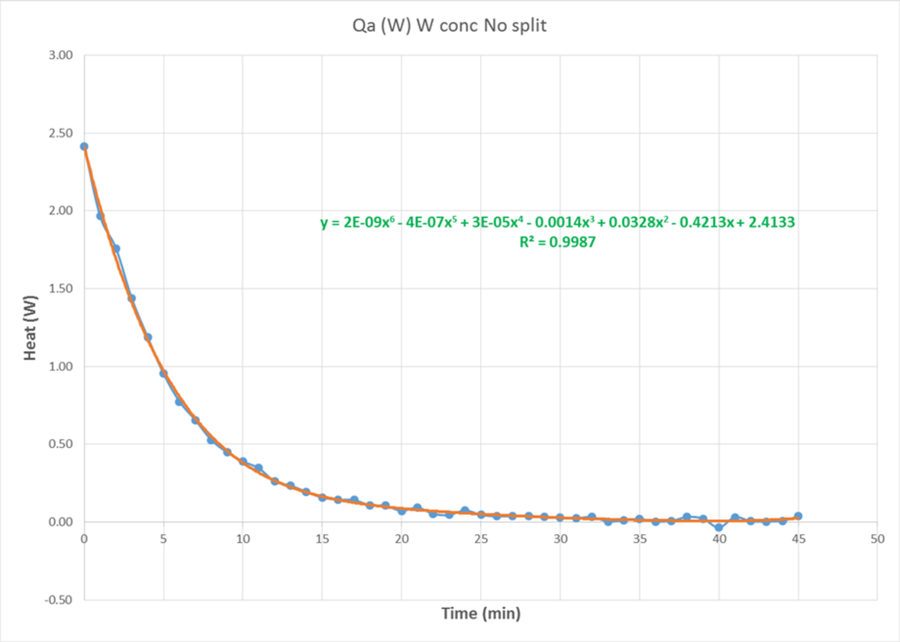

Figure 1: *Heat retained in the copper rod and the absorber (Q_a) versus time extrapolated to find (Q_u) at the beginning of illumination.*

Appendix 4.2:

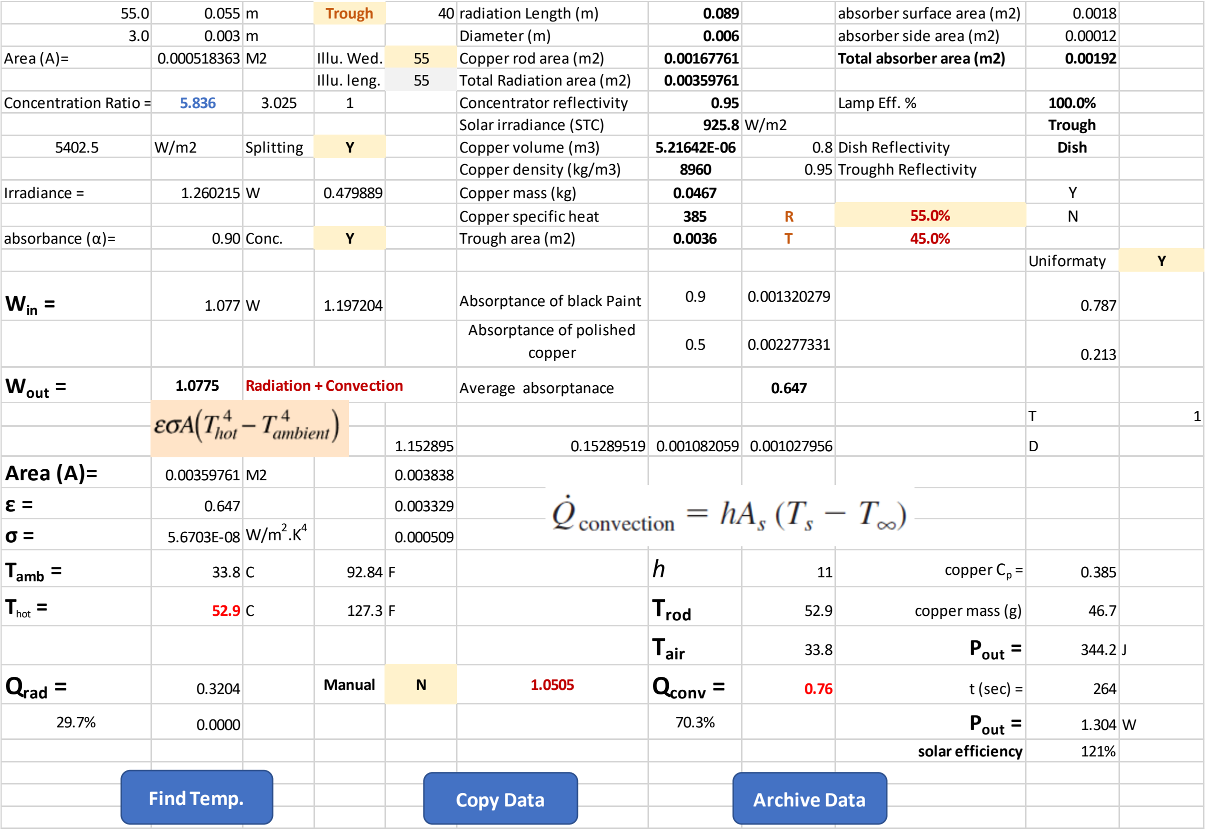

55.0	0.055	m	Trough	40	radiation Length (m)	**0.089**		absorber surface area (m2)	0.0018	
3.0	0.003	m			Diameter (m)	**0.006**		absorber side area (m2)	0.00012	
Area (A)=	0.000518363	M2	Illu. Wed.	55	Copper rod area (m2)	**0.00167761**		**Total absorber area (m2)**	**0.00192**	
			Illu. leng.	55	Total Radiation area (m2)	**0.00359761**				
Concentration Ratio =	**5.836**	3.025	1		Concentrator reflectivity	**0.95**		Lamp Eff. %	**100.0%**	
					Solar irradiance (STC)	**925.8**	W/m2		**Trough**	
5402.5	W/m2	Splitting	**Y**		Copper volume (m3)	**5.21642E-06**	0.8	Dish Reflectivity	**Dish**	
					Copper density (kg/m3)	**8960**	0.95	Troughh Reflectivity		
Irradiance =	1.260215	W	0.479889		Copper mass (kg)	**0.0467**			Y	
					Copper specific heat	**385**	**R**	**55.0%**	N	
absorbance (α)=	0.90	Conc.	**Y**		Trough area (m2)	**0.0036**	**T**	**45.0%**		
									Uniformaty	**Y**
W_{in} =	1.077	W	1.197204		Absorptance of black Paint	0.9	0.001320279		0.787	
					Absorptance of polished copper	0.5	0.002277331		0.213	
W_{out} =	**1.0775**	**Radiation + Convection**			Average absorptanace		**0.647**			
	$\varepsilon\sigma A\left(T_{hot}^4 - T_{ambient}^4\right)$								T	1
				1.152895	0.15289519	0.001082059	0.001027956		D	
Area (A)=	0.00359761	M2		0.003838						
ε =	0.647			0.003329	$\dot{Q}_{\text{convection}} = hA_s\left(T_s - T_\infty\right)$					
σ =	5.6703E-08	$W/m^2.K^4$		0.000509						
T_{amb} =	33.8	C	92.84	F		h	11	copper C_p =	0.385	
T_{hot} =	**52.9**	C	127.3	F		**T_{rod}**	52.9	copper mass (g)	46.7	
						T_{air}	33.8	**P_{out} =**	344.2	J
Q_{rad} =	0.3204		**Manual**	**N**	**1.0505**	**Q_{conv} =**	**0.76**	t (sec) =	264	
29.7%	0.0000					70.3%		**P_{out} =**	1.304	W
								solar efficiency	121%	
	Find Temp.				Copy Data			Archive Data		

Figure 2: *Theoretical model to predict absorber final temperature.*

Appendix 4.3:

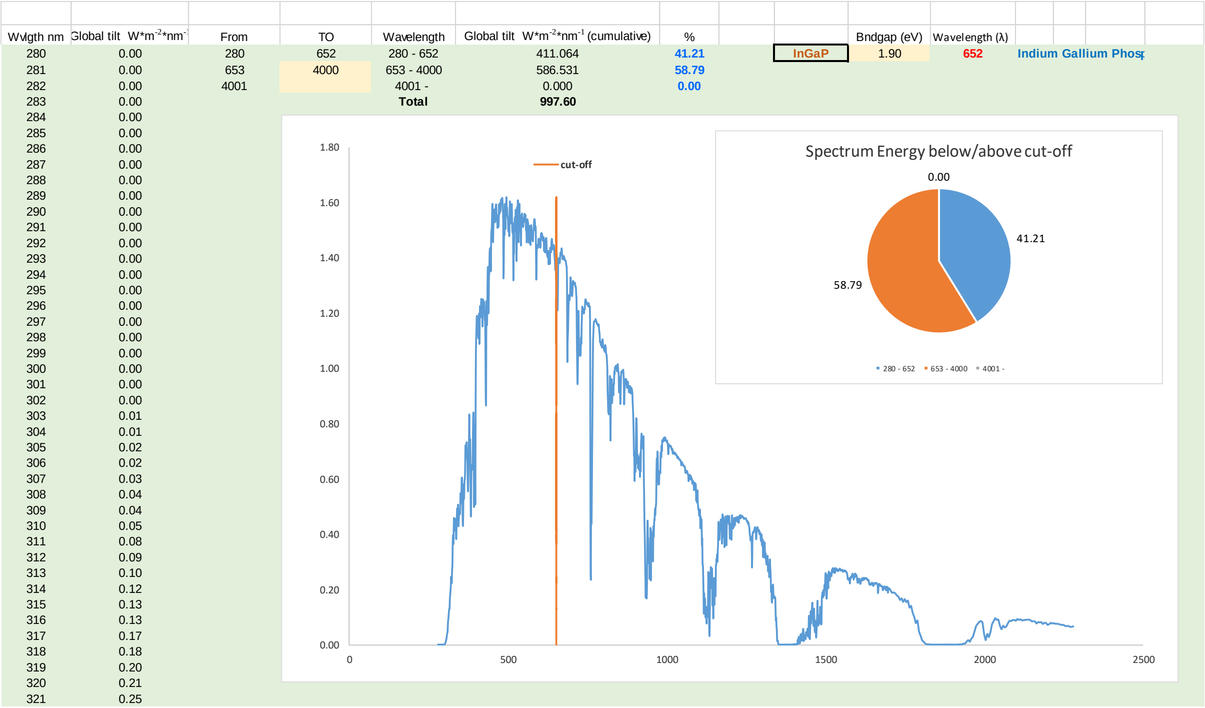

Wvlgth nm	Global tilt W*m^{-2}*nm^{-}
280	0.00
281	0.00
282	0.00
283	0.00
284	0.00
285	0.00
286	0.00
287	0.00
288	0.00
289	0.00
290	0.00
291	0.00
292	0.00
293	0.00
294	0.00
295	0.00
296	0.00
297	0.00
298	0.00
299	0.00
300	0.00
301	0.00
302	0.00
303	0.01
304	0.01
305	0.02
306	0.02
307	0.03
308	0.04
309	0.04
310	0.05
311	0.08
312	0.09
313	0.10
314	0.12
315	0.13
316	0.13
317	0.17
318	0.18
319	0.20
320	0.21
321	0.25

From	TO	Wavelength	Global tilt W*m^{-2}*nm^{-1} (cumulative)	%
280	652	280 - 652	411.064	41.21
653	4000	653 - 4000	586.531	58.79
4001		4001 -	0.000	0.00
		Total	**997.60**	

	Bndgap (eV)	Wavelength (λ)	
InGaP	1.90	652	Indium Gallium Phosp

Figure 5: *ASTM G173-03 used to find energies above cut-off point of different semiconductor materials.*

Appendix 4.4:

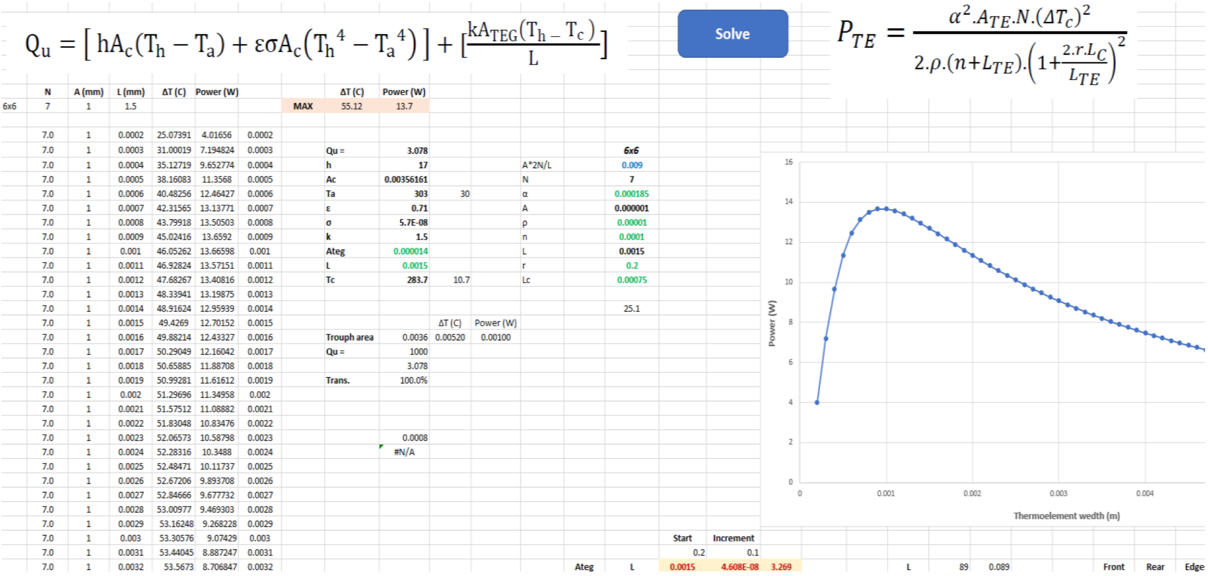

$$Q_u = \left[\, hA_c(T_h - T_a) + \varepsilon\sigma A_c\left(T_h{}^4 - T_a{}^4\right) \right] + \left[\frac{kA_{TEG}(T_h - T_c)}{L}\right]$$

$$P_{TE} = \frac{\alpha^2.A_{TE}.N.(\Delta T_c)^2}{2.\rho.(n+L_{TE}).\left(1+\frac{2.r.L_C}{L_{TE}}\right)^2}$$

	N	A (mm)	L (mm)	ΔT (C)	Power (W)	
6x6	7	1	1.5			
	7.0	1	0.0002	25.07391	4.01656	0.0002
	7.0	1	0.0003	31.00019	7.194824	0.0003
	7.0	1	0.0004	35.12719	9.652774	0.0004
	7.0	1	0.0005	38.16083	11.3568	0.0005
	7.0	1	0.0006	40.48256	12.46427	0.0006
	7.0	1	0.0007	42.31565	13.13771	0.0007
	7.0	1	0.0008	43.79918	13.50503	0.0008
	7.0	1	0.0009	45.02416	13.6592	0.0009
	7.0	1	0.001	46.05262	13.66598	0.001
	7.0	1	0.0011	46.92824	13.57151	0.0011
	7.0	1	0.0012	47.68267	13.40816	0.0012
	7.0	1	0.0013	48.33941	13.19875	0.0013
	7.0	1	0.0014	48.91624	12.95939	0.0014
	7.0	1	0.0015	49.4269	12.70152	0.0015
	7.0	1	0.0016	49.88214	12.43327	0.0016
	7.0	1	0.0017	50.29049	12.16042	0.0017
	7.0	1	0.0018	50.65885	11.88708	0.0018
	7.0	1	0.0019	50.99281	11.61612	0.0019
	7.0	1	0.002	51.29696	11.34958	0.002
	7.0	1	0.0021	51.57512	11.08882	0.0021
	7.0	1	0.0022	51.83048	10.83476	0.0022
	7.0	1	0.0023	52.06573	10.58798	0.0023
	7.0	1	0.0024	52.28316	10.3488	0.0024
	7.0	1	0.0025	52.48471	10.11737	0.0025
	7.0	1	0.0026	52.67206	9.893708	0.0026
	7.0	1	0.0027	52.84666	9.677732	0.0027
	7.0	1	0.0028	53.00977	9.469303	0.0028
	7.0	1	0.0029	53.16248	9.268228	0.0029
	7.0	1	0.003	53.30576	9.07429	0.003
	7.0	1	0.0031	53.44045	8.887247	0.0031
	7.0	1	0.0032	53.5673	8.706847	0.0032

	ΔT (C)	Power (W)
MAX	55.12	13.7

Qu =	3.078				*6x6*
h	17			A*2N/L	0.009
Ac	0.00356161			N	7
Ta	303	30		α	0.000185
ε	0.71			A	0.000001
σ	5.7E-08			ρ	0.00001
k	1.5			n	0.0001
Ateg	0.000014			L	0.0015
L	0.0015			r	0.2
Tc	283.7	10.7		Lc	0.00075
					25.1
		ΔT (C)	Power (W)		
Trouph area	0.0036	0.00520	0.00100		
Qu =	1000				
	3.078				
Trans.	100.0%				
	0.0008				
	#N/A				

		Start	Increment								
		0.2	0.1								
Ateg	L	0.0015	4.608E-08	3.269	L	89	0.089	Front	Rear	Edge

Figure 6: *Excel sheet developed to optimize for thermoelement length for TEG modules.*

Appendix 4.5:

9x9

NS:

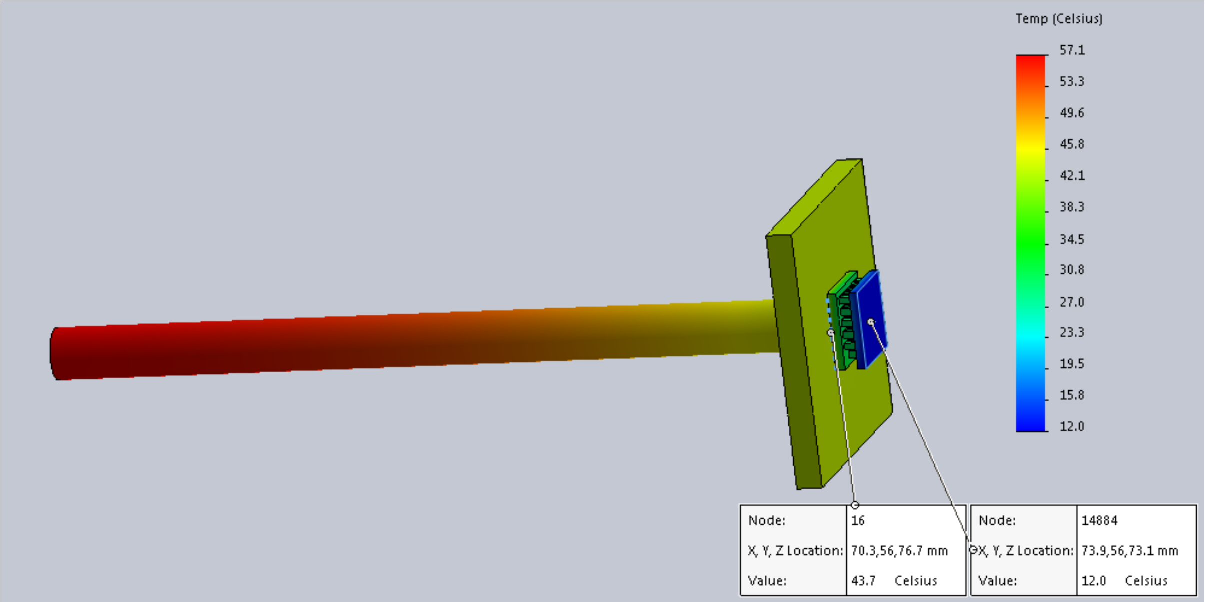

Node: 16
X, Y, Z Location: 70.3,56,76.7 mm
Value: 43.7 Celsius

Node: 14884
X, Y, Z Location: 73.9,56,73.1 mm
Value: 12.0 Celsius

WS:

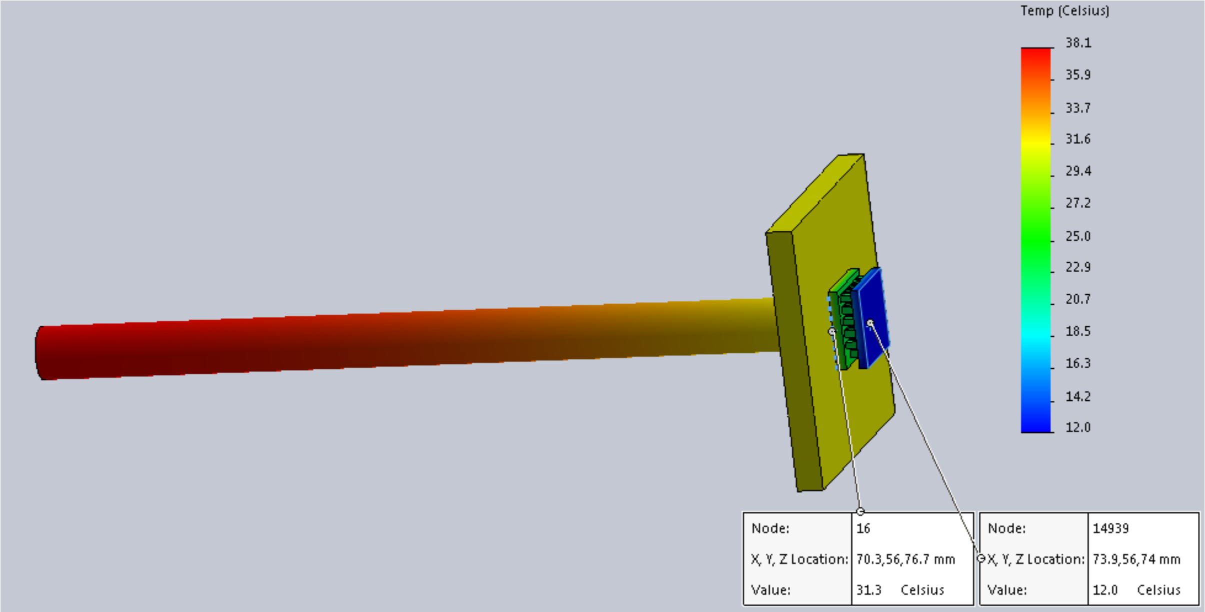

Node: 16
X, Y, Z Location: 70.3,56,76.7 mm
Value: 31.3 Celsius

Node: 14939
X, Y, Z Location: 73.9,56,74 mm
Value: 12.0 Celsius

Figure 7: *Module 9x9 SolidWorks thermal simulation for hot side temperature.*

15x15

NS:

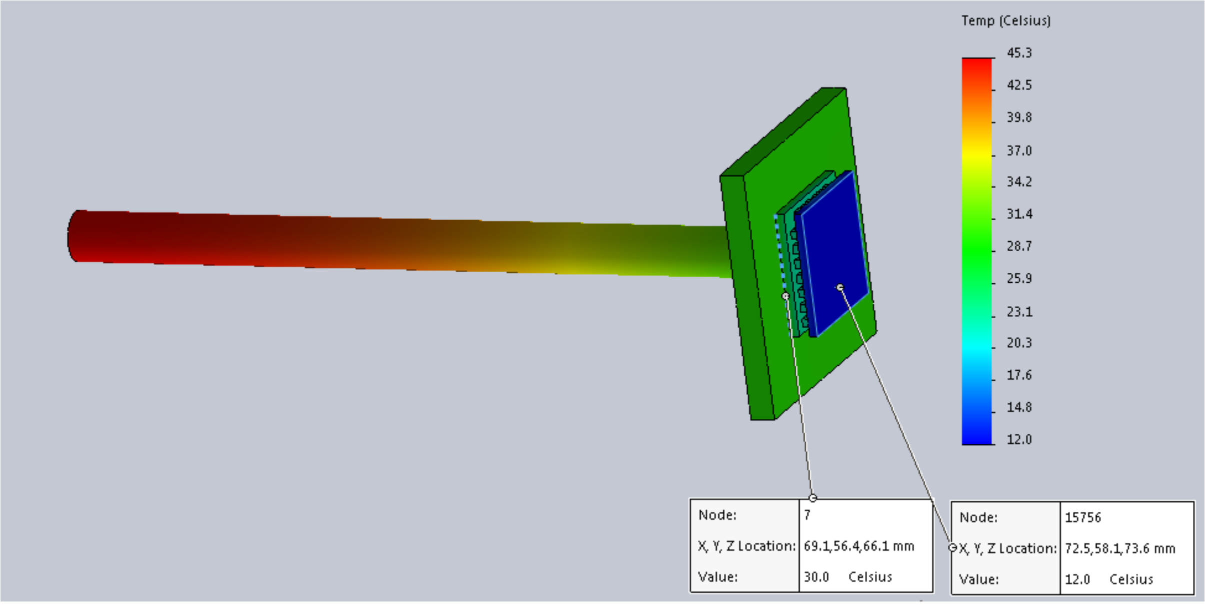

Node: 7
X, Y, Z Location: 69.1,56.4,66.1 mm
Value: 30.0 Celsius

Node: 15756
X, Y, Z Location: 72.5,58.1,73.6 mm
Value: 12.0 Celsius

WS:

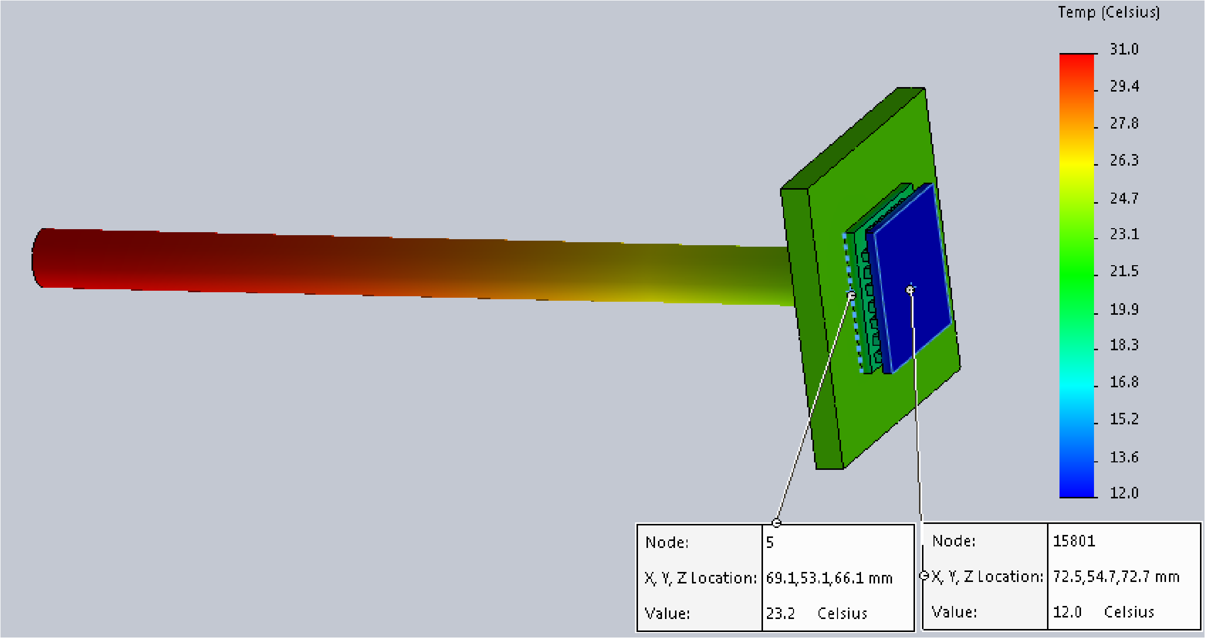

Node: 5
X, Y, Z Location: 69.1,53.1,66.1 mm
Value: 23.2 Celsius

Node: 15801
X, Y, Z Location: 72.5,54.7,72.7 mm
Value: 12.0 Celsius

Figure 8: *Module 15x15 SolidWorks thermal simulation for hot side temperature.*

20x20

NS:

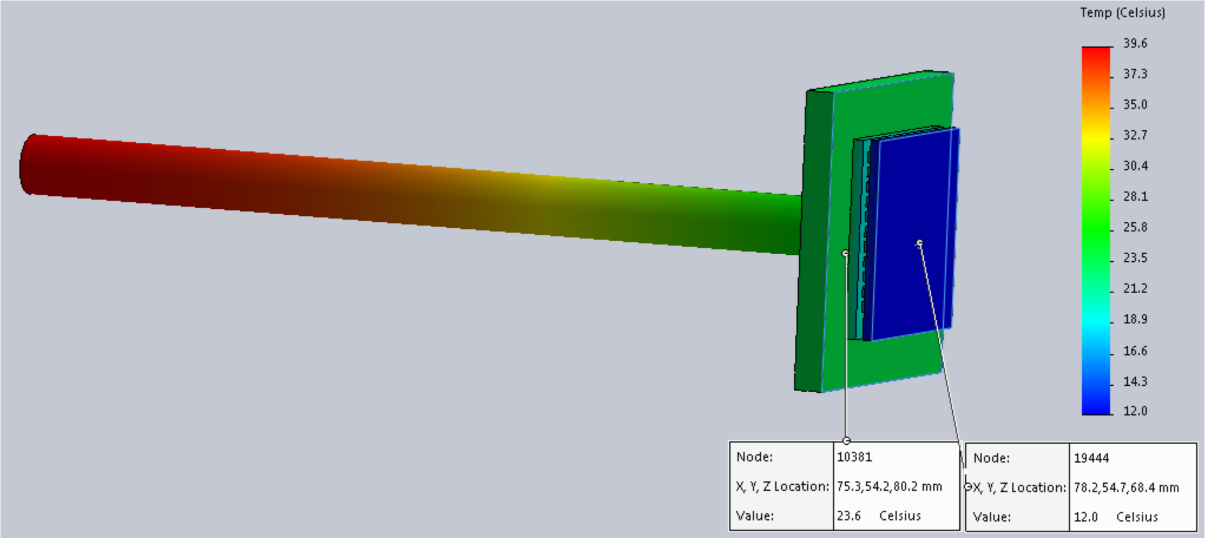

Node: 10381
X, Y, Z Location: 75.3,54.2,80.2 mm
Value: 23.6 Celsius

Node: 19444
X, Y, Z Location: 78.2,54.7,68.4 mm
Value: 12.0 Celsius

WS:

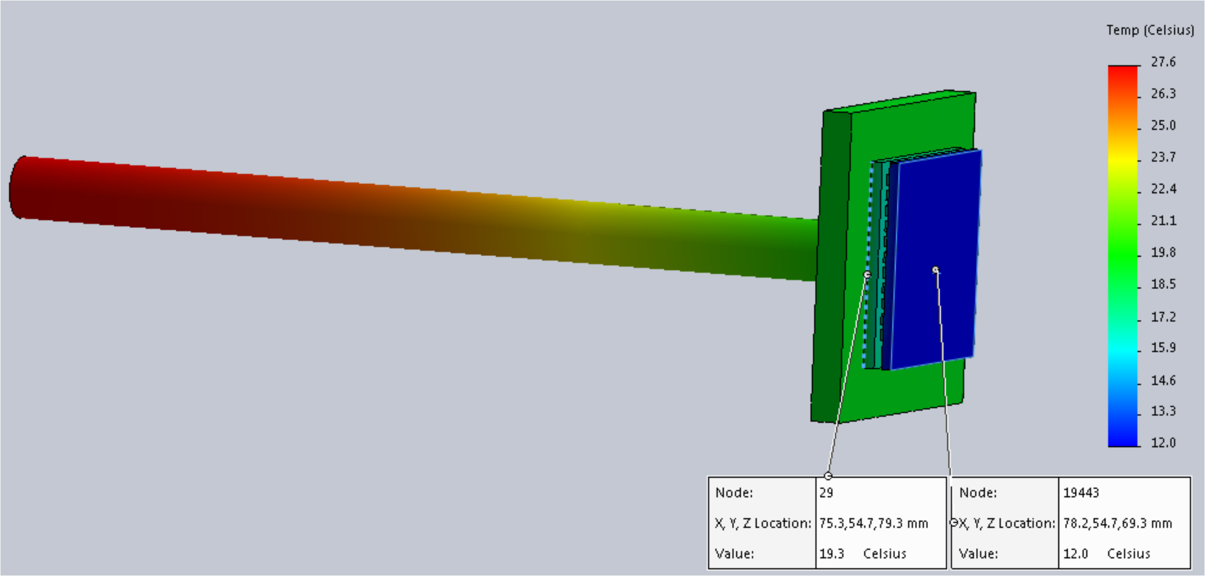

Node: 29
X, Y, Z Location: 75.3,54.7,79.3 mm
Value: 19.3 Celsius

Node: 19443
X, Y, Z Location: 78.2,54.7,69.3 mm
Value: 12.0 Celsius

Figure 9: *Module 20x20 SolidWorks thermal simulation for hot side temperature.*

30x30

NS:

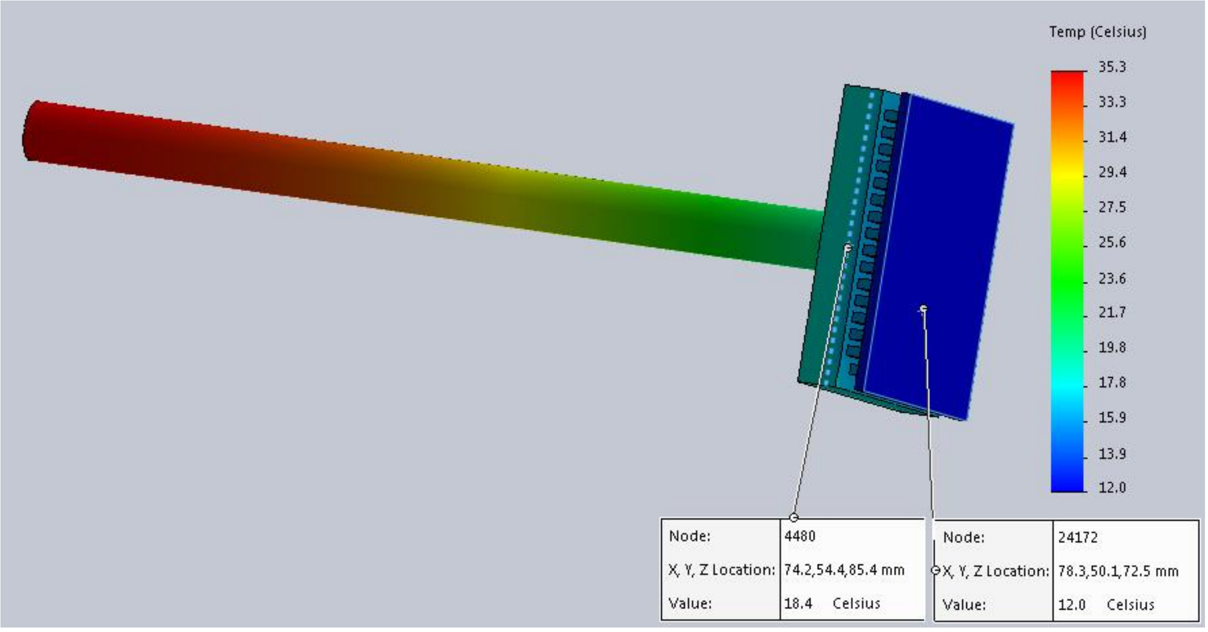

Node: 4480
X, Y, Z Location: 74.2,54.4,85.4 mm
Value: 18.4 Celsius

Node: 24172
X, Y, Z Location: 78.3,50.1,72.5 mm
Value: 12.0 Celsius

WS:

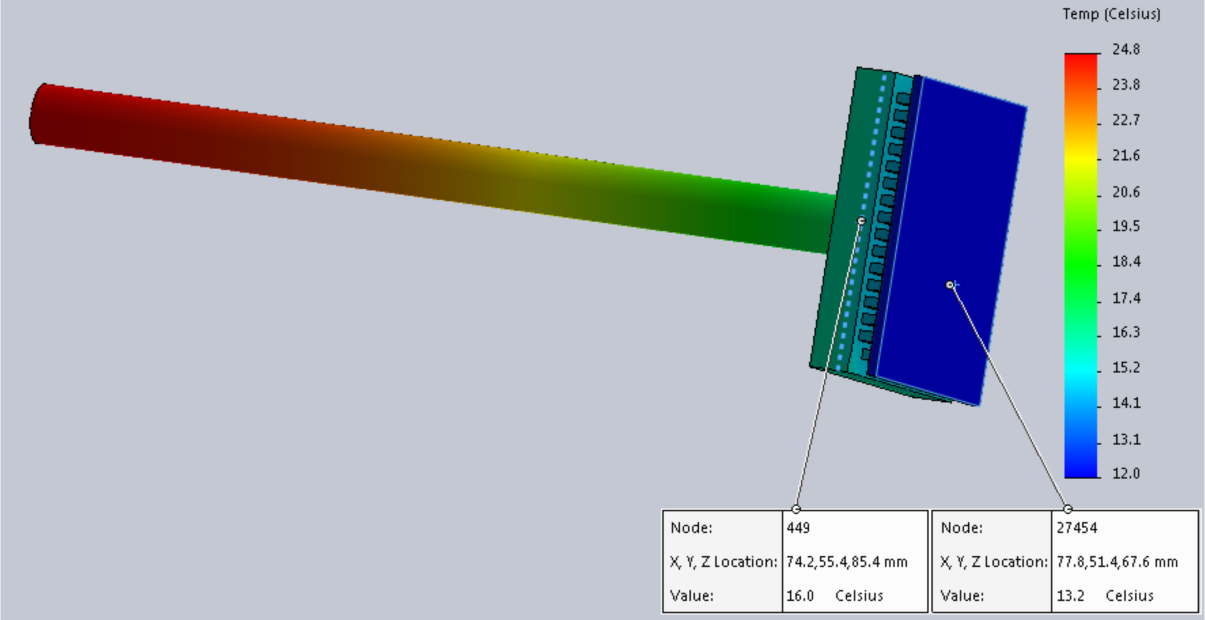

Node: 449
X, Y, Z Location: 74.2,55.4,85.4 mm
Value: 16.0 Celsius

Node: 27454
X, Y, Z Location: 77.8,51.4,67.6 mm
Value: 13.2 Celsius

Figure 10: *Module 30x30 SolidWorks thermal simulation for hot side temperature.*

Appendix 4.6:

I-V curve for InGaP cell after splitting

V	I	P(W)
1.345978	1.86E-05	2.51E-05
1.340942	0.001623	0.002176
1.335907	0.002948	0.003938
1.330872	0.004083	0.005433
1.325836	0.004926	0.00653
1.320801	0.006128	0.008094
1.315765	0.006854	0.009019
1.31073	0.007571	0.009924
1.305695	0.008105	0.010583
1.300659	0.008636	0.011233
1.295624	0.009015	0.01168
1.290588	0.00943	0.01217
1.285553	0.009711	0.012484
1.280518	0.010028	0.012841
1.275482	0.01022	0.013036
1.270447	0.010486	0.013322
1.265411	0.010629	0.01345
1.260376	0.010834	0.013655
1.255341	0.010919	0.013707
1.250305	0.01109	0.013866
1.24527	0.011151	0.013886
1.240234	0.011276	0.013985
1.235199	0.011301	0.013959
1.230164	0.01142	0.014048
1.225128	0.011438	0.014013
1.220093	**0.011536**	**0.014075**
1.215057	0.01153	0.014009
1.210022	0.011621	0.014062
1.204987	0.011618	0.014
1.199951	0.011694	0.014033
1.194916	0.011673	0.013948
1.18988	0.011749	0.01398
1.184845	0.011731	0.013899
1.17981	0.011792	0.013912
1.174774	0.011758	0.013813
1.169739	0.011829	0.013836
1.164703	0.011804	0.013748
1.159668	0.011859	0.013753
1.154633	0.011819	0.013647

Appendix 4.7:

I-V curve for module 15x15 after splitting

V	I	P (WS)
0.158977539	0	0
0.151947021	0.005523987	0.000839353
0.136932373	0.01862793	0.002550767
0.132141113	0.023298218	0.003078652
0.127197266	0.027565552	0.003506263
0.122283936	0.03182373	0.003891531
0.116729736	0.037604736	0.004389591
0.111846924	0.042297363	0.00473083
0.106842041	0.047537231	0.005078975
0.101776123	0.05279541	0.005373312
0.096679688	0.058013916	0.005608767
0.09173584	0.063232422	0.005800679
0.086669922	0.068481445	0.005935282
0.081756592	0.073669434	0.006022962
0.076599121	0.078887939	0.006042747
0.071594238	0.084106445	0.006021537
0.066589355	0.089294434	0.005946059
0.061584473	0.094482422	0.00581865
0.056518555	0.099700928	0.005634952
0.051483154	0.104888916	0.005400012
0.046469116	0.110046387	0.005113758
0.041439819	0.115264893	0.004776556
0.036416626	0.120452881	0.004386488
0.031378174	0.125640869	0.003942381
0.026351929	0.13079834	0.003446789
0.021328735	0.135955811	0.002899766
0.016299438	0.141143799	0.002300565
0.011260986	0.14630127	0.001647497
0.00625	0.15145874	0.000946617
0.001211548	0.156616211	0.000189748